UNIVERSITY OF SOUTHAMPTON

FACULTY OF NATURAL AND ENVIRONMENTAL SCIENCES

Chemistry

Silicon nanowires for high energy lithium-ion battery negative electrodes

by

Jacob Alexander Locke

Thesis for the degree of Doctor of Philosophy

July 2015

Abstract

Samples of silicon nanowire materials, produced by Merck KGaA *via* a batched supercritical fluid method, were evaluated within composite electrodes for use as the active component in future lithium-ion battery negative electrodes. A comprehensive literature review of silicon based negative electrodes with a focus on silicon based composite type electrodes is provided. Characterisation of the nanowire materials was conducted via electron microscopy. Composite type electrodes were prepared utilising poly-acrylic acid as a binder material. Insight into the interaction of poly-acrylic acid with batch-1 nanowire material was achieved via a FTIR spectroscopy study, evidence for the formation of a binding interaction was observed.

Composite electrodes containing nanowire material were electrochemically evaluated via the use of half-cells. The performance of the nanowire material samples was found to be significantly different and attributed to the use of differing precursor chemicals for synthesis. The structural variation of silicon nanowire particles within a composite electrode was investigated throughout an initial cycle and extended cycling. The electrochemical performance of composite electrodes containing the nanowire materials was found to depend critically on the composite electrode formulation and the electrolyte solution used. The rate performance was also observed to be influenced by the electrode formulation, suggesting the electronic and ionic conductivity of the composite electrode to be the rate limiting factors of the composite electrodes tested. Through the optimisation of composite electrode formulation and electrolyte, extended cycling at a capacity of over 600 mA h $g^{-1}_{(Composite)}$ for 200 electrochemical cycles at a C-rate of C/10 was achieved, the highest number of cycles reported for SFLS silicon nanowire materials to date.

Acknowledgements

First and foremost I would like to thank Prof. John Owen for his support and guidance throughout my postgraduate studies. I would like to thank the EPSRC and Merck KGaA for providing funding for the project; specifically I would like to thank Dr. Lichun Chen for his support of the project and generous provision of materials. I would like to thank all of the members of the Owen group, past and present, for their friendship, advice and help. I am thankful for all of the friendships made during my studies which provided necessary distraction and an opportunity to relax; I will miss afternoon tea time debates and Friday evening drinks. I would like to especially thank Dr. Matthew Roberts for his advice and support when I originally joined the Owen group.

I would like to thank Prof. John Drennan for providing the opportunity to conduct experiments at the University of Queensland as well as his advice and hospitality during my visit. I would also like to thank Dr. Graeme Auchterlonie, Ron Rasch and Dr. Kim Sewell for sharing their knowledge and providing advice and guidance when conducting electron microscopy studies. I would also like to thank all of the staff at the Centre for Microscopy and Microanalysis for their welcome and hospitality during my visit.

Finally, I would like to thank my family for their support and patience throughout my studies, especially Amy.

List of Symbols

A = Area of electrode (m^2)
C = Capacitance (F)
C = C-rate (h^{-1})
C_{dl} = Double layer capacitance (F)
D = Diffusion coefficient ($cm^2\ s^{-1}$)
d = Distance between crystal planes (m)
E = Cell potential (V)
e = Charge of an electron (1.602×10^{-19} C)
E_0 = Amplitude (variable units)
F = Faradays constant (96485 C mol^{-1})
f = Frequency (Hz)
G = Gibbs free energy (kJ mol^{-1})
h = Planck's constant (6.626×10^{-34} N m s)
I = Current (A)
j = √-1
L = Inductance (H)
l = Distance between electrodes (m)
M = Mass of active material (g)
m_0 = Rest mass of an electron (9.11×10^{-31} kg)
m_e = Moles of electrons (mol)
M_m = Mass of material (g)
M_w = Molecular mass of material (g)
n = Number of electrons
$Q_{Measured}$ = Measured capacity (mA h)
$Q_{Specific}$ = Specific capacity (mA h g^{-1})
Q_T = Theoretical capacity (mA h g^{-1})
R = Cell resistance (Ω)
R = Resistance (Ω)
r = Resolution (m)
R_{ct} = Charge transfer resistance (Ω)
R_u = Uncompensated resistance (Ω)
t = Time (s)
V = Accelerating voltage (V)
Z = Impedance (Ω)
Z' = Real component of impedance (Ω)
Z'' = Imaginary component of Impedance (Ω)
μ = Chemical potential (J mol^{-1})
μ = Refractive index
θ = Incident angle (degrees)
λ = Wavelength (m)
σ = Conductivity of electrolyte (S m^{-1})
ω = Radial frequency (rad s^{-1}) or (2πf)
ϕ = Phase shift (degrees)

List of Abbreviations

AC – alternating current
AFM – Atomic force microscopy
BET – Brunauer–Emmett–Teller (surface area calculation method)
BF – Bright field
BSE – Back scattered electrons
CPE – Constant phase element
CVD – Chemical vapour deposition
DEC – Diethyl carbonate
DF – Dark field
DME – Dimethoxy ethane
EC - Ethylene carbonate
EDS – Energy dispersive X-ray spectroscopy
EELS – Electron energy loss spectroscopy
EF – Energy filtered
EIS – electrochemical impedance spectroscopy
EMC – Ethyl methyl carbonate
FEC – Fluoroethylene carbonate
FTIR – Fourier transformed infrared spectroscopy
GIC – Graphite intercalation compound
LIB – Lithium-ion battery
LP30 – Electrolyte solution of 1 M $LiPF_6$ in EC: DMC (1:1, w/w)
MPS – mono-phenylsilane
NaCMC – Sodium carboxymethyl cellulose
NMP – N-methyl-2-pyrrolidone
OCV – open circuit potential
PAA – Poly-acrylic acid
PC – Propylene carbonate
PE – Poly-ethylene
PFA – Perfluoroalkoxy alkane
ppm – parts per million
PVDF – Poly-vinylidene fluoride
SAED – Selected area electron diffraction
SBR – Styrene butadiene rubber
SE – Secondary electrons
SEI – Solid electrolyte interphase
SEM – Scanning electron microscopy (microscope)
SFLS – Supercritical fluid liquid solid (nanowire synthesis mechanism)
SS – Stainless steel
TEM – Transmission electron microscopy (microscope)
VC – Vinylene carbonate
VMP – Variable multi-channel potentiostat
XRD – X-ray diffraction

Table of Contents

Chapter 1: Introduction

1.1 Project context

The rechargeable lithium-ion battery is the energy storage solution of choice for the majority of mobile applications. The ubiquitous use of lithium-ion battery technology in everyday life is due to the high gravimetric and volumetric energy density of the system. The high energy density allows for compact, lightweight energy storage for devices such as mobile telephones and laptop computers.

New mobile device technology and the goal of economical fully electric vehicles with a range comparable to that of internal combustion engine powered vehicles, provide demand for the development of new higher energy density battery systems. Lithium-ion batteries utilising traditional materials are reaching the practical limit of energy density after over 25 years of incremental improvement (**Figure 1-1**).

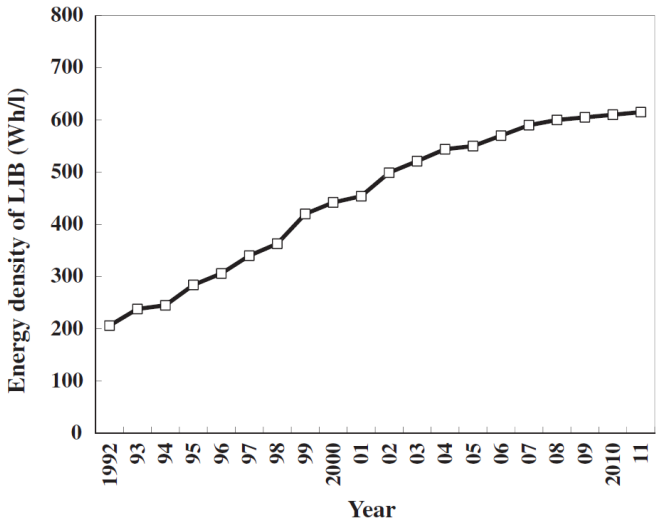

Figure 1-1 – Energy density of lithium-ion batteries between 1992 and 2011, reproduced from reference [1] with permission.

Research into new lithium-ion battery materials is required to allow for higher energy density systems to become realised. The negative electrode of the lithium-ion battery is a crucial component which needs to be addressed to significantly improve the performance of future lithium-ion batteries. Silicon holds promise as a high energy density negative electrode material, theoretically silicon could allow for a 9 fold increase in the amount of energy stored per unit mass and per unit volume compared to currently used graphite based negative electrodes [2]. Practical silicon based negative electrodes that satisfy such high energy density and the necessary stability requirements of a commercially viable electrode have yet to be realised.

1.2 Aim

The aim of this project was to evaluate silicon nanowire material, produced *via* a batched supercritical fluid method by Merck KGaA, for possible use as the active component within the negative electrode of a future high energy density lithium-ion battery.

The project was started after consideration of a number of characteristics of the silicon nanowire material:

- The material is produced in powder form which allows for compatibility with existing commercial electrode manufacturing methods.
- The nanowire morphology provides nanoscale dimensions along two axes, reported to be important for accommodation of stress associated with volume change, whilst also providing a reduced surface area compared to spherical nanoparticles of similar diameter, important when considering side reactions.
- The high aspect ratio of the nanowire particles may be beneficial for maintaining composite electrode structure, porosity and electronic and ionic conductivity throughout the composite.
- The patented production method allows for a significant amount of material to be produced (~ 1 g per batch), with the possibility to scale up the process.

1.3 Background to the lithium-ion battery

1.3.1 Brief history of lithium-ion battery development

Lithium battery technology was initially motivated due to the fact that lithium is both the most electropositive and the lightest metal (equivalent weight of 6.94 g mol^{-1}), properties which enable the production of high energy density storage systems [3]. High energy density lithium metal batteries were first developed in the 1970's as primary systems [3]. The high voltage of these systems required non-aqueous electrolytes. Electrolytes consisting of a lithium salt dissolved in mixtures of propylene carbonate (PC) and dimethoxy ethane (DME) were developed for use in lithium - carbon monoflouride primary cells. Successful secondary systems were not possible until the discovery of intercalation compounds which could be used as the positive electrode, transition metal compounds containing a layered structure were found to be able to reversibly host lithium ions, the most notable are the family of compounds Li_xMO_2 (where M = Co, Ni or Mn) [3,4,5] discovered in the 1980's (**Figure 1-2**).

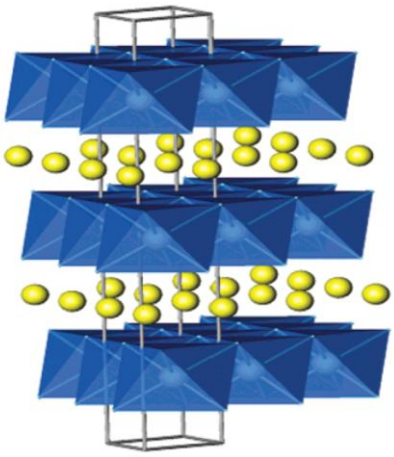

Figure 1-2 – Layered structure of $LiTiS_2$, $LiVSe_2$, $LiCoO_2$, $LiNiO_2$ and $LiNi_yMn_yCo_{1-2y}O_2$ showing lithium ions (yellow) between the transition metal oxide/sulphide sheets. Reprinted with permission from reference [6]. Copyright 2004 American Chemical Society.

A major safety issue for early reversible cells was one of short circuits caused by dendritic lithium formed during the recharging process as lithium metal was plated. This major problem was overcome with the use of a second, negative intercalation type electrode, leading to the design concept of the modern 'lithium-ion' or 'rocking-chair' battery. In 1991 SONY™ introduced the first commercial lithium-ion battery to market [7]. The first commercial lithium-ion battery consisted of a negative electrode containing soft carbon as the active material of the negative electrode, a positive electrode containing $LiCoO_2$ and an electrolyte consisting of 1M $LiPF_6$ in a mixture of PC and DEC (diethylene carbonate). A large effort was made to increase the energy density of the first commercial cell which had an energy density of 200 Wh l^{-1} and 80Wh kg^{-1} [7].

A breakthrough came with the successful utilisation of graphitic carbon as a negative intercalation electrode (**Figure 1-3**) [8]. Graphite enabled higher energy density systems to be produced due to the greater charge storage capacity and the lower voltage during lithium reaction compared to soft carbons. Reversible intercalation of lithium ions into the structure of graphite was achieved after a lengthy struggle with problems of exfoliation caused by co-intercalation of electrolyte solvent molecules between the layers of graphite. Solvent intercalation was overcome *via* the utilisation of ethylene carbonate (EC) as an electrolyte solvent, EC was found to decompose at the surface of the graphite forming a passivating layer which prevented both further solvent intercalation and further solvent decomposition [9]. The layer of electrolyte breakdown products formed at the surface allowed for lithium transport between the electrolyte and the graphite structure, enabling reversible lithium intercalation and extended charge/discharge cycling of the electrode.

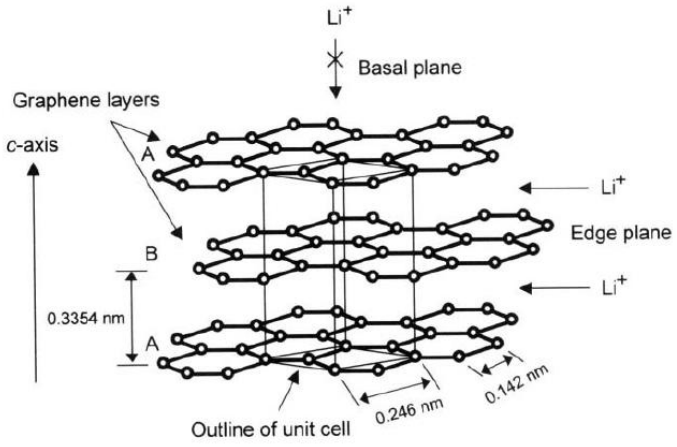

Figure 1-3 – Hexagonal crystal structure of graphite showing the ABAB stacking of graphene sheets and the unit cell. Lithium ions are able to intercalate between the graphene layers *via* the edge plane. Reprinted from reference [10] with permission.

The term solid electrolyte interphase (SEI) was coined by Peled in 1979 and used to describe a layer of electrolyte breakdown products formed on the surface of lithium metal electrodes exposed to organic electrolytes [11]. The electrolyte breakdown layer produced on the surface of the graphite electrode was also described as a form of solid electrolyte interphase (SEI) layer. *Via* adoption of EC containing electrolyte solutions and a graphitic carbon based negative electrode, the energy density of the commercial SONY™ lithium-ion battery was able to be increased to 400 Wh l^{-1} and 165 Wh kg^{-1} [7]. Later incremental developments to the chemistry, materials and packaging have allowed for further increases in energy density to be obtained.

1.3.2 Operation

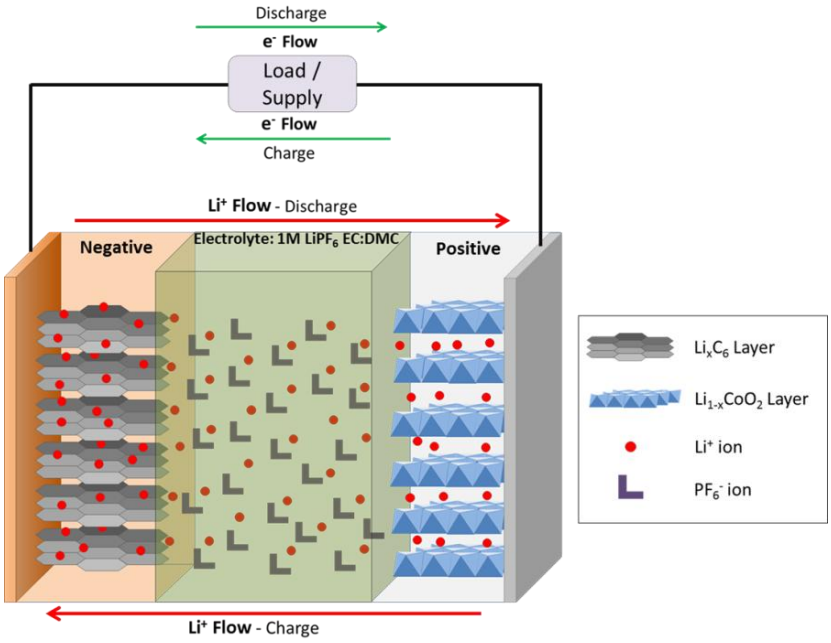

Figure 1-4 – Diagram of graphite - $LiCoO_2$ lithium-ion cell.

A simplified schematic of a lithium-ion battery is displayed in **Figure 1-4**. At the negative electrode lithium ions can reversibly insert between the layers of the graphite structure at an average voltage of around 0.2 V vs. Li/Li^+. The voltage profile of a graphite negative electrode during initial lithium insertion is displayed in **Figure 1-5**. Initially an SEI passivation layer must be formed on the surface of graphite *via* reduction of the electrolyte. The capacity produced between roughly 1.5 V and around 0.25 V (solid black line) in **Figure 1-5** corresponds to formation of the SEI passivation layer. The irreversible capacity highlighted in **Figure 1-5** as 65 mA h g^{-1} includes the amount of charge involved in SEI formation.

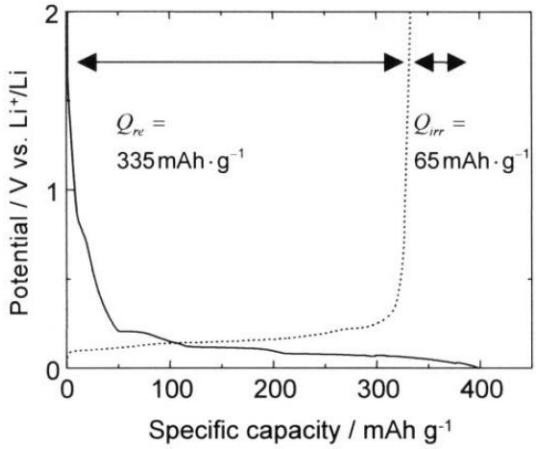

Figure 1-5 – Charge/discharge profile of natural graphite powder throughout the first cycle in 1 M $LiClO_4$ / EC + DEC (1:1 by volume). Reprinted from reference [10] with permission.

Below 0.25 V (**Figure 1-5**) the stepped voltage profile corresponds to the formation of a number graphite intercalation compounds (GIC) (**Figure 1-6**). Initially stage 4 is formed, once stage 4 has been produced then formation of stage 3 becomes favourable, insertion continues until stage 1 is produced throughout the active material. Upon extraction the reverse sequence occurs. Formation of stage 1 corresponds to the formation of a GIC with the formula LiC_6 (**Figure 1-6b**) and assuming full reaction to LiC_6 the theoretical capacity of graphite is 372 mA h g^{-1}.

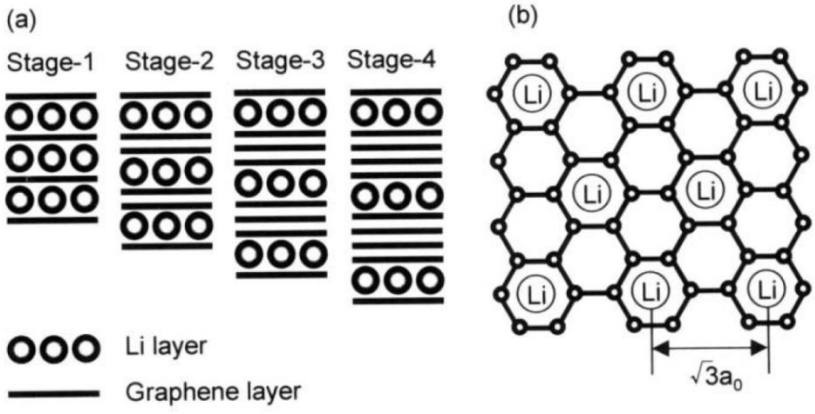

Figure 1-6 – a) Stage structures of GICs and b) In-plane structure of stage 1 Li-GIC corresponding to LiC_6. Reprinted from reference [10] with permission.

At the positive electrode lithium ions are able to reversibly insert within the layered structure of cobalt oxide. The voltage profile during full extraction of lithium from the structure of $LiCoO_2$ is displayed in **Figure 1-7a**. The theoretical capacity of $LiCoO_2$ assuming complete lithium removal is 274 mA h g^{-1}. $LiCoO_2$ was however found to produce a stable reversible performance when half of the lithium was removed equivalent to the formation of $Li_{0.5}CoO_2$, **Figure 1-7b**. Extracting around half of the lithium from the structure of $LiCoO_2$ results in a practical capacity of 137 mA h g^{-1} at an average voltage of around 4.0 V vs. Li/Li^+ (**Figure 1-7b**)

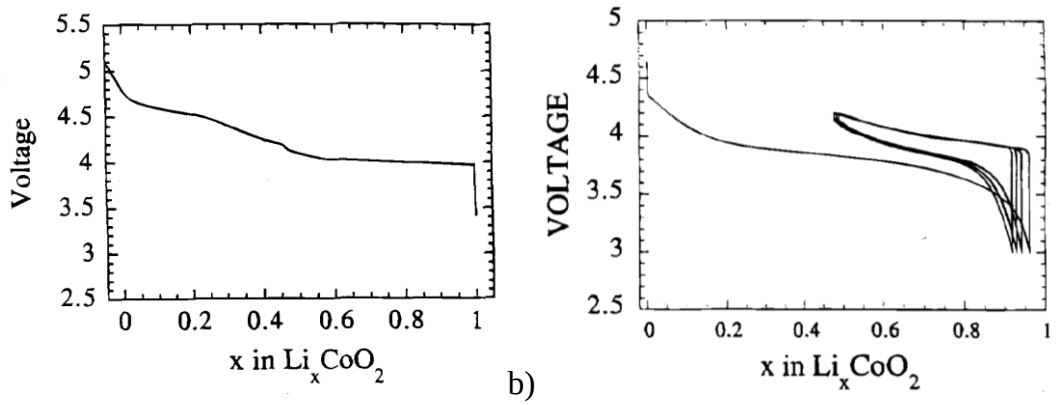

Figure 1-7 – a) Variation in potential as lithium is electrochemically de-intercalated from $LiCoO_2$ to CoO_2 as the electrochemical cell is charge to 5.2 V. b) Subsequent electrochemical cycling of lithium cobalt oxide to 4.2 V. Reproduced from reference [12] by permission of The Electrochemical Society.

Within the structure of $LiCoO_2$, lithium ions form layers between CoO_2 sheets which contain edge sharing CoO_6 octahedra (**Figure 1-8**). The lithium ions occupy octahedral sites between the CoO_2 layers. The structure allows for two dimensional lithium transport pathways parallel to the layered structure. The electronic structure of $LiCoO_2$ consists of octahedral Co^{3+} ions (d^6) in a low spin state, lithium ion and electron removal result in the formation of Co^{4+} (d^5) , electron removal and insertion with the $Co^{3/4+}$ redox couple provide the high voltage of around 4 V vs. Li/Li^+ [13].

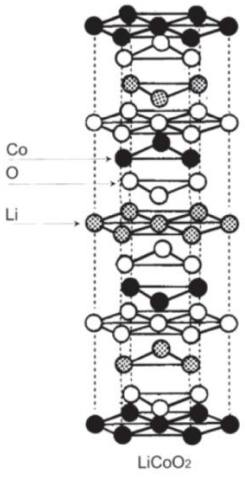

Figure 1-8 – Idealised layered structure of lithium cobalt oxide, lithium = grey, oxygen = white and cobalt = black. Reprinted from reference [14] with permission.

The voltage profile of a lithium ion cell is displayed in **Figure 1-9** (a). Lithium ion batteries are constructed in the discharged state with lithium initially contained within the positive lithium cobalt oxide material. Once constructed lithium-ion batteries must first be charged, during the charge process lithium ions are partially extracted from the positive electrode and inserted into the graphite negative electrode.

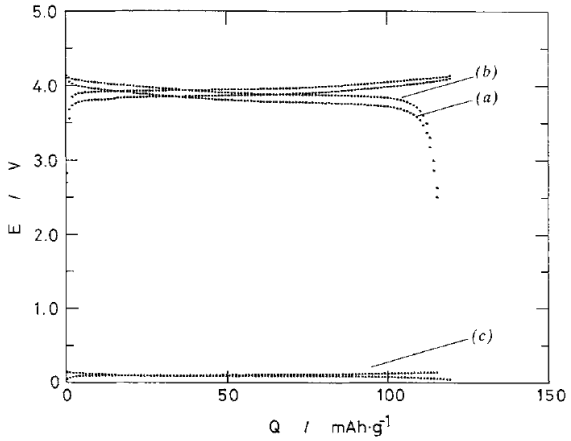

Figure 1-9 – Lithium-ion (shuttlecock) cell which consists of graphite and $LiCoO_2$ fabricated in the discharged state; (a) is the terminal voltage; (b) and (c) are the working voltage of the positive and negative electrode, respectively, against an auxiliary lithium electrode. Electrolyte used was 1M $LiClO_4$ in EC/DME (1:1 by volume) solution. Reproduced from reference [15] by permission of The Electrochemical Society.

The reversible redox reaction which occurs at the negative electrode can be described by **Equation 1-1**

$$Li_xC_6 \underset{Charge}{\overset{Discharge}{\rightleftarrows}} xLi^+ + xe^- + C_6$$

Equation 1-1

The reversible redox reaction which occurs at the positive electrode can be described by **Equation 1-2**

$$Li_{1-x}CoO_2 + xLi^+ + xe^- \underset{Charge}{\overset{Discharge}{\rightleftarrows}} LiCoO_2$$

Equation 1-2

The overall reversible redox reaction for the lithium-ion cell can be described by **Equation 1-3**.

$$Li_{1-x}CoO_2 + Li_xC_6 \underset{Charge}{\overset{Discharge}{\rightleftarrows}} LiCoO_2 + C_6$$

Equation 1-3

When in a charged (high energy) state there is a thermodynamic driving force for the cell to become discharged. The driving force corresponds to the difference in electrochemical potential between the two electrode materials. When required an external circuit may be completed, resulting in a flow of electrons and lithium ions from the negative to the positive electrode which provides an electrical current that can be utilised to conduct work.

1.3.3 The electrolyte and SEI formation

The electrolyte plays a crucial role within a lithium ion battery, allowing for both the transfer of lithium ions between the electrodes and the formation of stable passivation layers at the surface of the electrodes. The electrolyte used in lithium-ion batteries usually consists of a lithium salt dissolved in organic carbonate solvents. The solvents used in the majority of commercial lithium-ion battery electrolytes consist of organic carbonates (**Figure 1-10**).

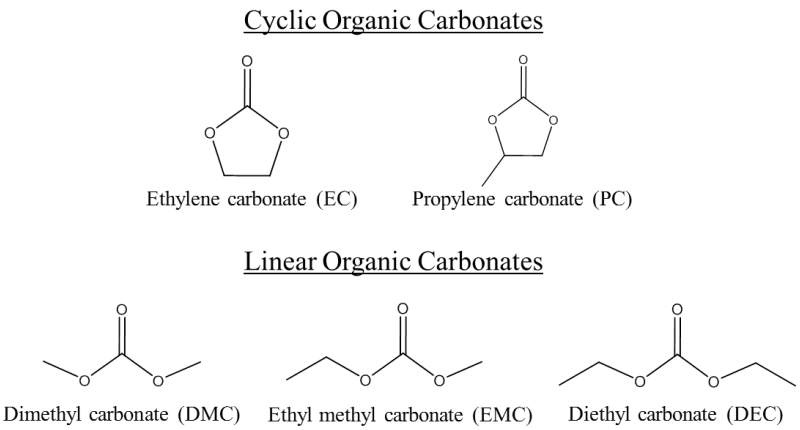

Figure 1-10 – Chemical structure of electrolyte solvents commonly used in lithium-ion batteries.

Mixtures of cyclic and liner carbonates are used to produce a solvent mixture with suitable physical and chemical properties (**Figure 1-10**). Cyclic carbonates display high dielectric constants which enable relatively high concentrations of lithium salt to be dissolved, however cyclic carbonates also display relatively high viscosities. Linear carbonates display low dielectric constants but are included to reduce viscosity of the electrolyte (**Table 1-1**).

Table 1-1 – Physical properties of common electrolyte solvents. M_w = molecular weight, T_m = melting point, T_b = boiling boint, η = viscosity, ε = dielectric constant T_f = flash point, d = density. Adapted with permission from reference [16]. Copyright 2004 American Chemical Society.

Solvent	M_w	T_m / ˚C	T_b / ˚C	η / cP (25˚C)	ε (25˚C)	Dipole Moment / Debye	T_f / ˚C	d / gcm^{-3} (25˚C)
EC	88	36.4	248	1.90 (40˚C)	89.78	4.61	160	1.321
PC	102	-48.8	242	2.53	64.92	4.81	132	1.200
DMC	90	4.6	91	0.59 (20˚C)	3.107	0.76	18	1.063
EMC	104	-53	110	0.65	2.958	0.89	-	1.006
DEC	118	-74.3	126	0.75	2.805	0.96	31	0.969

The most commonly used lithium salt is lithium hexafluorophosphate ($LiPF_6$). $LiPF_6$ displays an optimum combination of properties required of electrolyte salts, relatively high dissociation and good mobility (**Figure 1-11**) which allow for high conductivity electrolyte solutions to be produced (**Figure 1-12**).

Average ion mobility:

$LiBF_4 > LiClO_4 > LiPF_6 > LiAsF_6 > LiTf > LiIm$

Dissociation constant:

$LiTf < LiBF_4 < LiClO_4 < LiPF_6 < LiAsF_6 < LiIm$

Figure 1-11 – Comparison of the ionic mobility and dissociation constant of common lithium salts proposed for use in lithium-ion batteries. LiTf = lithium trifluoromethane sulfonate, LiIm = lithium bis(trifluoromethane sulfonyl) imide. Reprinted with permission from reference [16]. Copyright 2004 American Chemical Society.

$LiPF_6$ based electrolytes also allow for the passivation of aluminium foil current collectors commonly used at the positive electrode [16]. The high conductivity of electrolyte solutions produced utilising $LiPF_6$ allows for the fast transport of Li^+ ions within the lithium ion battery. Fast transport of lithium ions between the electrodes in high conductivity electrolytes allows for fast charge and discharge of lithium-ion batteries enabling use in high power applications.

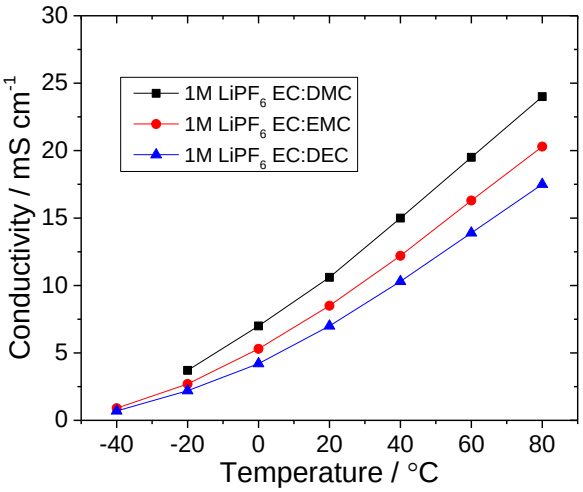

Figure 1-12 – Conductivity of 1 M $LiPF_6$ in binary solvent mixtures 1:1 by weight. Data obtained from reference [14].

The other function of the electrolyte is to ensure the formation of a stable passivation layer at the surface of electrodes. The passivation layer allows for the operation of the electrodes at voltages ordinarily outside of the stability window of the electrolyte solutions used. An early model of the passivation layer formed at the surface of negative electrodes highlights the complexity of the layer formed (**Figure 1-13**). The SEI passivation layer has been reported to be composed of a number of components all produced *via* the reduction of species present within the electrolyte including lithium salt, carbonate solvents and impurities (H_2O, O_2, etc.).

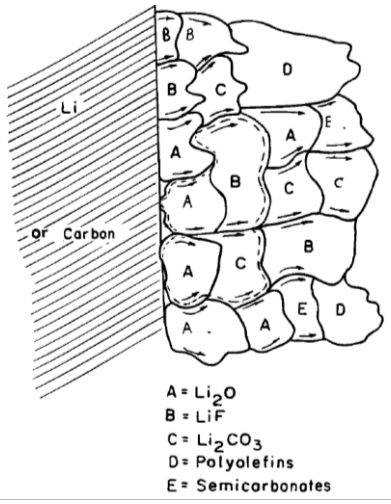

Figure 1-13 – Mosaic type model of the SEI layer formed at the surface of the negative electrode in a lithium-ion battery employing an electrolyte consisting of $LiPF_6$ dissolved in carbonate based solvents. Lithium transport was suggested to occur along the grain boundaries. Reproduced from reference[17] by permission of The Electrochemical Society.

A vast array of reaction products have been reported to be present within SEI layers including both organic and inorganic substances [16]. It is generally agreed that on the initial reduction of graphite based electrodes in standard electrolyte solutions that the predominant electrolyte reduction products are mainly made up of the lithium alkyl carbonates (**Figure 1-14**) as well as the inorganic components LiF and $Li_xPF_yO_z$ [18]. The composition and structure of the SEI layer have been found to be dynamic, varying in composition and structure with time, cycle number and temperature [19].

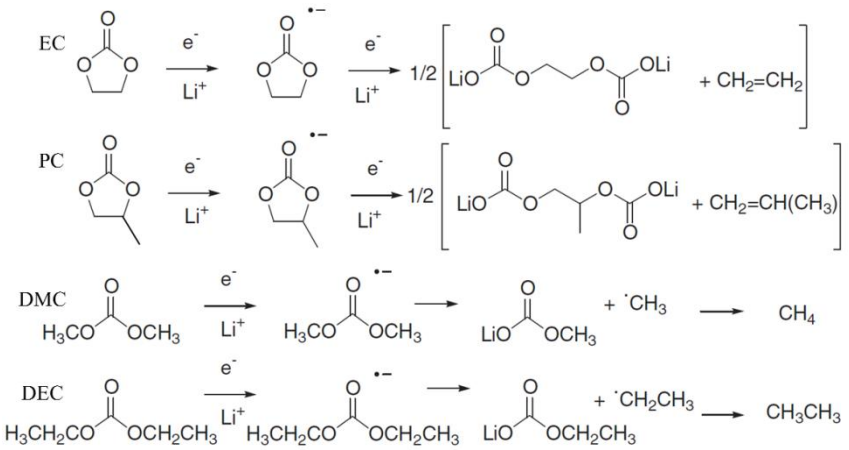

Figure 1-14 – Reduction mechanisms of common electrolyte solvent molecules. The second step in the mechanism of DMC and DEC was reported as unclear. Methane and ethane gases were detected. It was proposed that the alkyl radical may abstract H· or that a second electron transfer could result in the generation of carbanion R: - which reacts with acidic species forming an alkane. Reproduced from reference [20] by permission of The Electrochemical Society.

Electrolyte breakdown layers have been reported to form at the positive electrode *via* oxidation of the electrolyte [16]. The term SEI has not been applied the layers formed at the positive electrode as the transport of lithium ions through the layers has not been established.

1.3.4 Fundamental concepts

1.3.4.1 Lithium-ion cell voltage

The voltage of a lithium-ion cell is related to the free energy available *via* the redox reaction between the electrodes, ΔG. The cell potential is related to the free energy of reaction *via* **Equation 1-4**

$$E = -\frac{\Delta G}{nF}$$

Equation 1-4

E = cell potential, ΔG = change in free energy, n = number of electrons, F = Faradays constant (96485 C mol-1).

The free energy, Δ*G*, can be described by **Equation 1-5**, the difference in the chemical potential of lithium at the surface of the positive and negative electrodes.

$$\Delta G = \mu^{Positive} - \mu^{Negative}$$

Equation 1-5

ΔG = free energy of reaction μ = chemical potential of redox species at each electrode

Since the free energy can be described as the difference in chemical potential of the redox species at the positive and the negative electrode, the equilibrium cell potential of a lithium ion battery can be described by **Equation 1-6** [13].

$$E = -\frac{(\mu_{Li}{}^{LiCoO_2} - \mu_{Li}{}^{Graphite})}{nF}$$

Equation 1-6

E = cell potential μ = chemical potential of lithium at each electrode, n = number of electrons (1 as 1 electron is transferred per lithium) F = Faradays constant (96485C mol^{-1})

The chemical potential of lithium within the graphite negative electrode is close to that of lithium metal ($\mu_{Li}^{Metal} = 0$). The chemical potential of $\mu_{Li}^{Li1\text{-}xCoO2}$ is significantly below that of graphite, resulting in a negative Gibbs free energy for the transfer of lithium from the negative electrode to the positive electrode and a high cell potential (> 3 V) [21].

1.3.4.2 Capacity

Capacity, the technical term used within battery research for charge, can be subdivided into two commonly used terms, the theoretical capacity of an active material and the measured specific capacity of a material or an electrode.

The theoretical capacity of a material is equivalent to the theoretical maximum amount of charge which is stored per unit mass or volume of the material. The value is characteristic of the material. The convention in battery science is to display capacity in the form of mA h g^{-1}. The theoretical capacity of a material can be calculated with the units of mA h g^{-1} using **Equation 1-7**.

$$Q_T = \frac{m_e F}{M_w x\, 3.6}$$

Equation 1-7

Q_T = theoretical capacity (mA h g^{-1}), m_e = moles of electrons passed (mol), F = Faradays constant (96485 C mol^{-1}), M_w = molar mass of material (g)

The moles of electrons passed correspond to the moles of lithium ions passed. The specific capacity of a material is the capacity that can be practically obtained. **Equation 1-8** is used to calculate the specific capacity per gram of material.

$$Q_{Specific} = \frac{Q_{Measured}}{M_m}$$

Equation 1-8

$Q_{Specific}$ = specific capacity (mA h g^{-1}), $Q_{Measured}$ = measured capacity (mA h), M_m = mass of material (g)

1.3.4.3 Rate capability

The ability of a battery to discharge or charge over various timescales is known as the rate performance. As the rate of discharge/charge increases the efficiency of the reaction will decrease. The amount of charge that can be transferred at increased (dis)charge rates is a measure of the performance of an electrode or battery.

Standardised rates of charge/discharge are used to allow for comparison between various materials, electrode designs and cells. The term C-rate is used to represent the standardised rate of charge or discharge. Discharging a cell at a rate of 1 C is equivalent to passing a current which would result in the complete discharge of a cell within one hour assuming the theoretical capacity of the material could be achieved. C-rate is defined by **Equation 1-9**.

$$C = \frac{I}{M \times Q_T}$$

Equation 1-9

C = C-rate (h^{-1}), I = applied current (mA), M = mass of active material (g), Q_T = theoretical capacity of active material (mA h g^{-1})

Common battery testing is conducted within the range of 0.01 C to 10 C, 0.01 C represents a (dis) charge time of 100 hours and 10 C represents (dis) charge within 6 minutes. The definition of C-rate can also sometimes be interpreted to correspond to the current required to discharge an

electrode or battery in 1 hour under constant current conditions, however this interpretation does not allow for simple comparison between *C*-rate values.

1.3.5 Commercial lithium-ion batteries

1.3.5.1 Cell types

Commercial lithium-ion batteries are usually produced in one of three designs, cylindrical, prismatic or a polymer/pouch type [22]. The design of the battery depends on the requirements of the application. All commercial cells have common features, including the use of a non-aqueous electrolyte, a microporous polyolefin separator and composite type electrodes attached to metal foil current collectors.

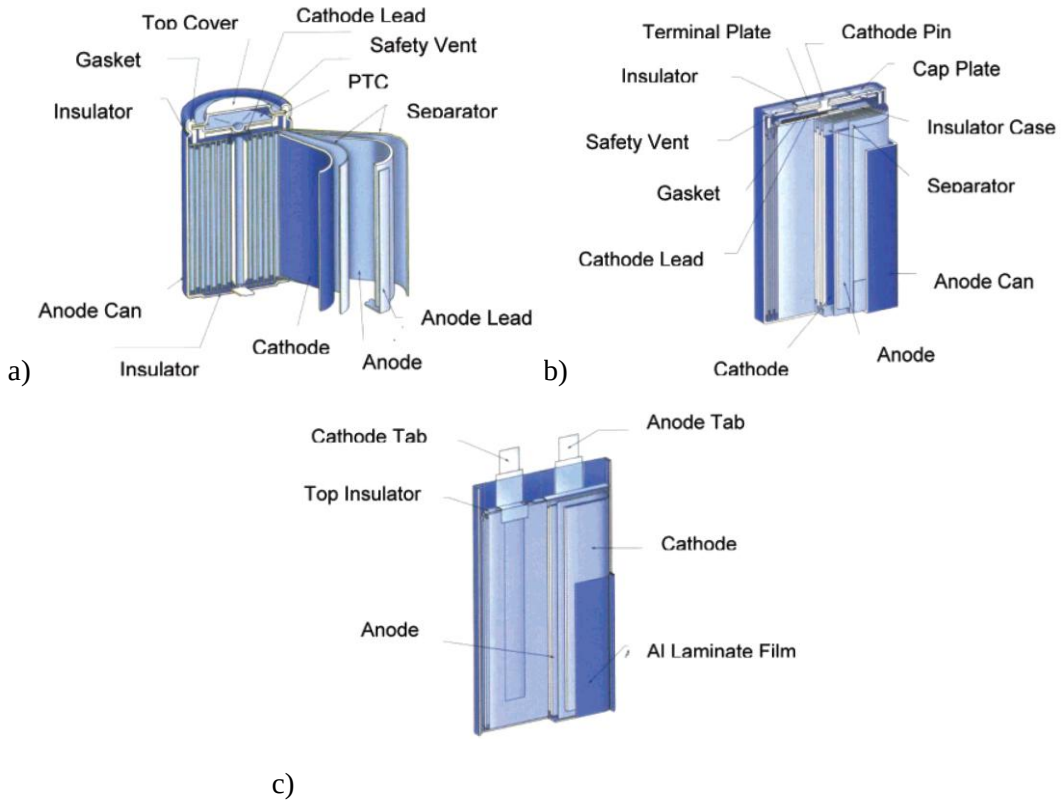

Figure 1-15 – Commercial lithium-ion battery designs a) cylindrical b) prismatic c) polymer/pouch. Reprinted with permission from reference [22] Copyright 2004 American Chemical Society.

1.3.5.2 Battery production

Composite electrodes are formed from a slurry paste or ink which usually contains a number of components including the electrochemically active material, normally in the form of a powder, a conductive additive, and a binder dissolved in an appropriate solvent. The slurry paste or ink is applied as a coating to the surface of a metal foil, which will act as a current collector. The composite electrode is then dried, pressed and shaped prior to being assembled into a cell. The same process is used to form both the positive and negative electrodes. The process of creating

the composite electrodes is usually conducted on a mass scale *via* roll to roll processing (**Figure 1-16**).

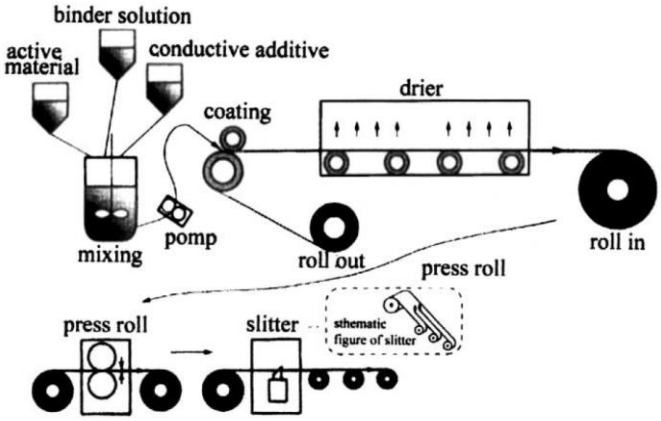

Figure 1-16 – Diagram displaying the manufacturing process of lithium-ion battery composite electrodes. Reprinted from reference [23] with permission.

Within a cell the composite electrodes are separated by a microporous polyolefin membrane which acts as a separator to ensure electronic isolation of the two electrodes. Polyolefin separators are used as they display high strength and allow for automated winding or folding of the electrode stack (**Figure 1-17**). The electrolyte solution is usually added in the final stages of production. The electrolyte solution is drawn into the separator and held within the pores *via* capillary action. The pore structure of commercial separators can be observed in **Figure 1-17**.

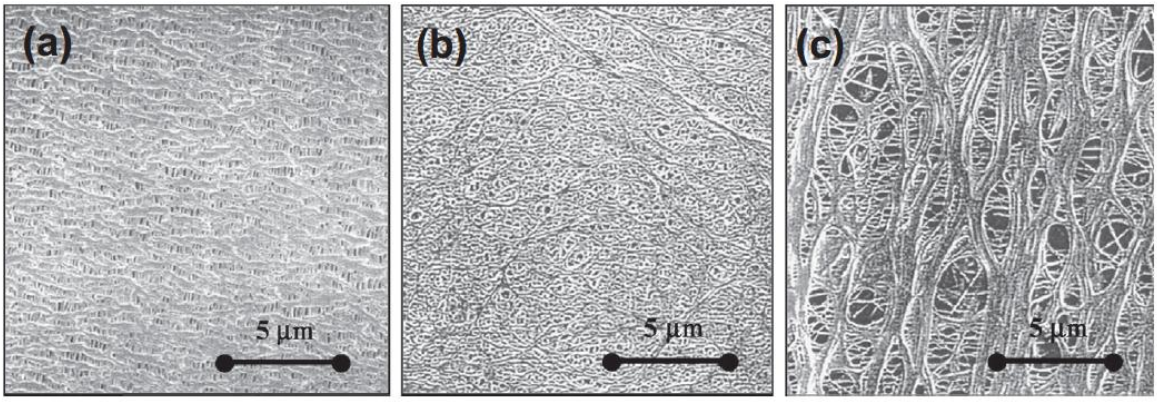

Figure 1-17 – Plan view of the pore characteristics of microporous separator membranes (a) Dry-process one component system (b) wet process two component system and (C) wet process three component system. Reprinted from reference [1] with permission.

The design of lithium-ion cells has been dictated by the significantly lower ionic conductivity of the non-aqueous electrolytes used with lithium-ion batteries. The low conductivity of the electrolyte requires the separation between the positive and negative electrode to be as small as possible and for the area of the electrodes to be as great as possible in order to produce a cell with a low resistance. The resistance of the cell can be defined by **Equation 1-10**.

$$R = \frac{l}{A\sigma}$$

Equation 1-10

R = cell resistance (Ω), σ = conductivity of the electrolyte (S m^{-1}), l = distance between electrodes (m), A = area of electrodes (m^2)

From **Equation 1-10** it can be noted that with constant conductivity of the electrolyte, reducing the distance between the electrodes and increasing the geometric area of the electrodes results in a reduction of cell resistance. Low resistance is achieved in commercial lithium-ion batteries *via* the use of thin (< 100 μm) large area composite electrodes at both the positive and negative electrodes and a thin microporous separator (~25 μm), typically the bipolar electrode stack is < 250 μm thick.

1.4 Silicon as a future high capacity negative electrode material

Silicon is a leading candidate to replace graphite in the negative electrode of future high energy density lithium-ion batteries. As well as the highest theoretical capacity of known materials, silicon benefits from the fact that it is abundant and environmentally benign, allowing for the possibility of low production and disposal costs, key attributes required for widespread commercial use [2].

1.4.1 Early research into silicon negative electrodes

Research into alloying type electrode materials began when in 1971 Dey reported on the reactivity of a range of metals (including Al and Sn) during electrochemical alloying with lithium, utilising organic electrolyte systems and operating at room temperature [24]. Early research conducted on the electrochemical alloying of lithium with silicon was however conducted at between 360 and 480°C using eutectic molten salt electrolytes [25, 26].

The first investigation into the use of silicon as an electrode for lithium batteries was published by S-C. Lai, a high lithium content alloy was reported to form *via* the electrochemical reaction of lithium ions with silicon, a capacity of 2.12 A h g^{-1} (of silicon) was reported [25]. Lai determined the stoichiometry of a number of lithium silicide compounds formed during galvanostatic removal of lithium from a thermally prepared lithium-silicon alloy. The compounds were reported to be Li_5Si, $Li_{4.1}Si$, $Li_{2.8}Si$ and Li_2Si [25]. Similar work investigating the lithium-silicon alloy system at elevated temperature was conducted by Sharma and Seefurth [26, 27]. A later study confirmed four distinct crystalline alloy compounds and determined the stoichiometry of the compounds in the lithium-silicon system at 415 °C to be: $Li_{12}Si_7$ ($Li_{\sim 1.7}Si$) , Li_7Si_3 ($Li_{\sim 2.3}Si$), $Li_{13}Si_4$ ($Li_{3.25}Si$) and $Li_{22}Si_5$ ($Li_{4.4}Si$) [28]. The voltage profile of a silicon electrode during lithium insertion displayed characteristic two phase voltage plateaux corresponding to formation of the silicide phases (**Figure 1-18**).

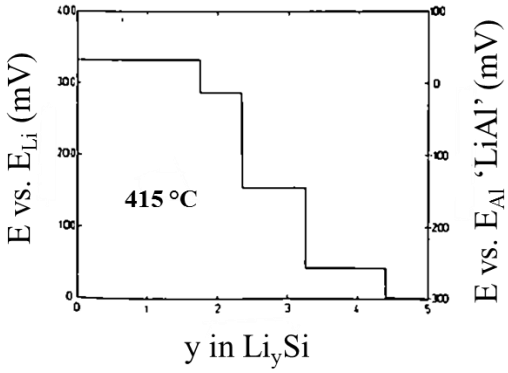

Figure 1-18 – Voltage profile of a silicon electrode during electrochemical alloying with lithium conducted at 415°C. Figure reproduced from reference [28] with permission.

The discovery of the lithium rich lithium silicide alloy phases and their subsequent characterisation suggested that the theoretical capacity of silicon electrodes, corresponding to formation of $Li_{22}Si_5$, was an astounding 4200 mA h g^{-1} of silicon, higher than any material other than lithium metal itself.

1.4.2 Understanding the electrochemical reaction of lithium with silicon at room temperature

The electrochemical reaction of lithium with silicon at room temperature has been widely studied for use in modern lithium-ion batteries. Early ambient temperature studies found that the crystalline lithium silicide phases previously observed during electrochemical lithiation of silicon at elevated temperatures did not form, instead formation of an amorphous lithium silicide phase occurred [29], **Figure 1-19** compares the voltage profile of a silicon electrode during lithium insertion at 415 °C and room temperature.

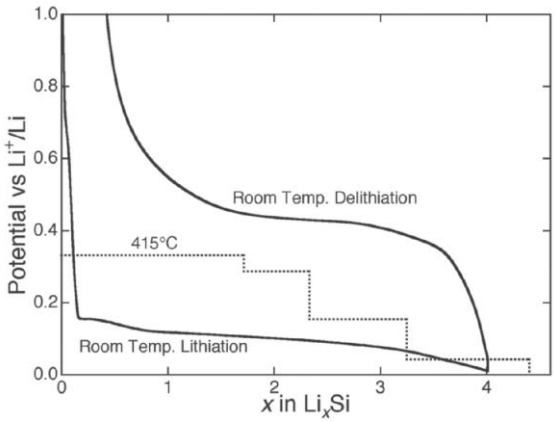

Figure 1-19 – Comparison of voltage profile of a silicon electrode during lithiation and delithiation conducted at 415°C and room temperature. Figure reproduced from reference [30] with permission.

During lithiation, at high lithium concentrations (below ~50 mV vs. Li/Li^+) the amorphous lithium silicon alloy phase was reported to convert to a crystalline phase, $Li_{15}Si_4$ [31, 32,33]. Recent work has observed that it is possible to form an over-lithiated $Li_{15+\delta}Si_4$ phase at potentials below ~30 mV vs. Li/Li^+, δ has been suggested to correspond to around 0.16 [34]. The $Li_{15+\delta}$ Si_4 phase was found to be the final phase formed during lithium insertion at room temperature instead of the $Li_{22}Si_5$ phase found at elevated temperatures. The $Li_{15}Si_4$ phase represents a theoretical capacity of silicon at room temperature of 3579 mA h g^{-1}. The overall electrochemical reaction of lithium with silicon at room temperature during electrochemical reaction can be represented by **Equation 1-11**, assuming formation of $Li_{15}Si_4$.

$$3.75\ Li^{+} + 3.75e^{-} + Si \rightleftarrows Li_{3.75}Si$$

Equation 1-11

A large potential hysteresis between lithium insertion and lithium extraction is characteristic of the reversible reaction of lithium with silicon at room temperature, work to understand the cause has found that stress variation during reaction contributes to the hysteresis *via* an alteration of the Gibbs free energy and hence the insertion and extraction potential during electrochemical reaction [36*]. Other suggested causes which may contribute to the observed hysteresis include sluggish kinetics, and silicon-silicon bond breaking.

1.4.2.1 The electrochemical reaction of lithium with crystalline silicon

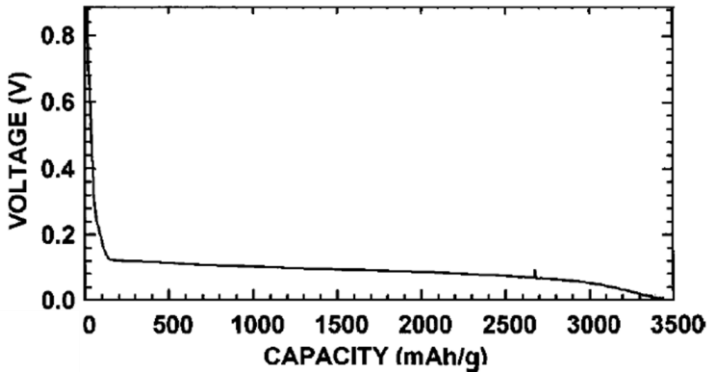

Figure 1-20 – Voltage profile of a crystalline silicon electrode during electrochemical alloying with lithium at room temperature. Reproduced from reference [31] by permission of The Electrochemical Society.

Figure 1-20 displays a typical voltage profile of a crystalline silicon electrode during initial electrochemical reaction with lithium. Crystalline silicon is the most readily available form of silicon and most widely investigated. The crystal faces associated with the diamond cubic structure of crystalline silicon are displayed in **Figure 1-21**. Lithium has been reported to preferentially react with crystalline silicon in the <110> direction [35].

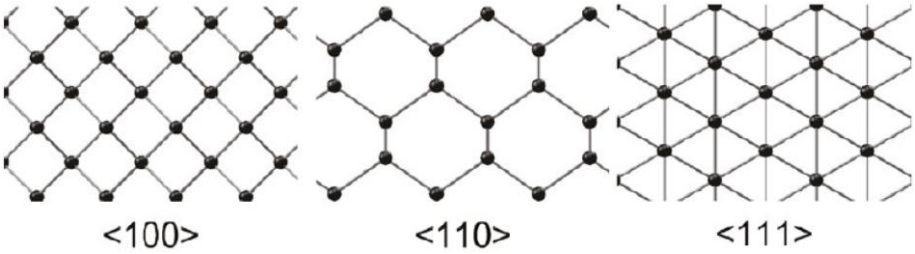

Figure 1-21 – Crystal faces of silicon, silicon atoms are displayed as dots and bonds as lines. Reprinted with permission from reference [35]. Copyright 2011 American Chemical Society.

Assuming the active material consists of particles of crystalline silicon the electrochemical reaction forms an amorphous lithium silicide phase at the particle surface, producing a phase boundary between amorphous lithiated silicon and unreacted crystalline silicon. Further electrochemical reaction results in the consumption of crystalline silicon, causing the

amorphous-crystalline phase boundary to move towards the centre of the particle. The phase boundary has been reported to progress at the fastest rate in the <110> direction [35]. The pseudo-two phase reaction results in a sloping voltage plateau during lithium insertion into crystalline silicon (**Figure 1-20**). The preferential reaction in the <110> direction has been shown to cause anisotropic volume expansion as displayed in **Figure 1-22**.

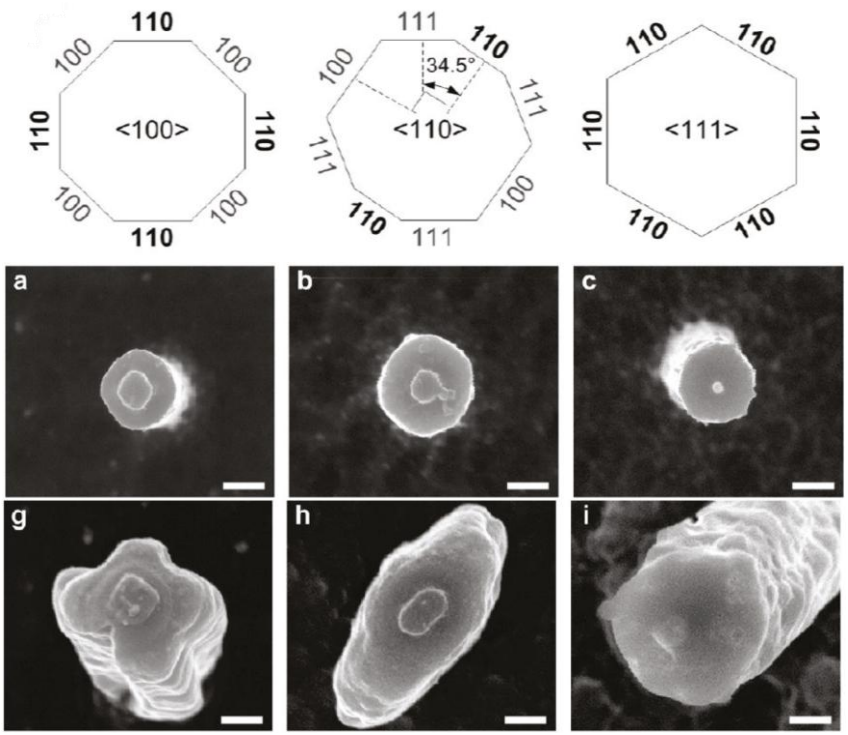

Figure 1-22 – Diagram displaying the corresponding crystal directions of pillars (a, b, c), Plan view of pillars of silicon with different crystal directions before (a, b, c) and after (g, h, i) electrochemical lithiation. Scale bar = 200nm. Reprinted with permission from reference [35]. Copyright 2011 American Chemical Society.

A detailed description of the local lithium environments present during lithium insertion into crystalline silicon has been reported by Key *et al.*[34]. A summary of the process based upon the reported results are described in what follows, **Figure 1-23** is a schematic of the insertion and extraction processes [36].

The reaction of lithium with crystalline silicon initiates at around 0.125 V vs. Li/Li^+, it has been reported that initially lithium inserts into the crystalline silicon structure and as the number of lithium atoms increase silicon-silicon bonds begins to break apart. Lithium disrupts the silicon lattice forming amorphous lithium silicide, within the amorphous lithium silicide, regions of high lithium content lithium silicide and regions of low lithium content phase are formed.

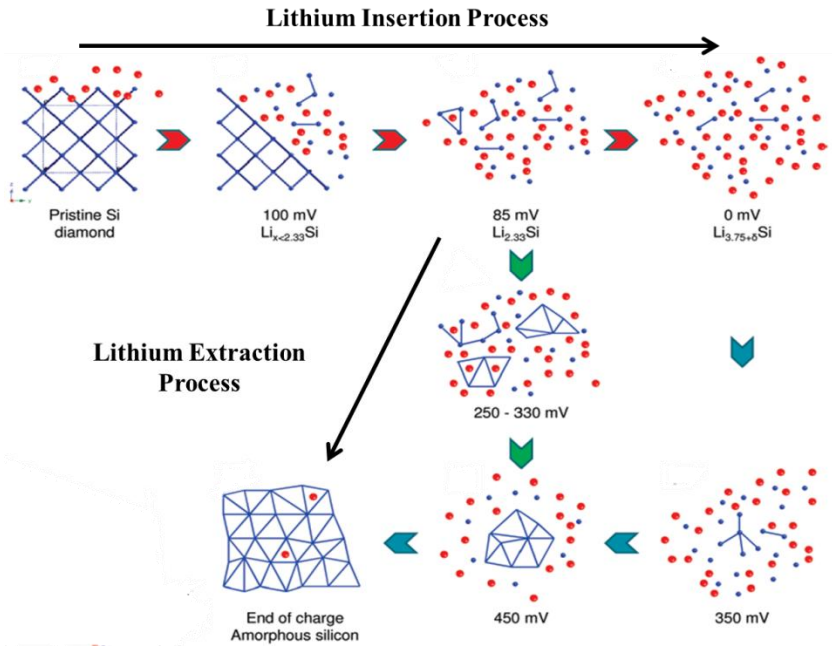

Figure 1-23 – Schematic diagram of the mechanism of lithium insertion into crystalline silicon. Adapted with permission from reference [36]. Copyright 2011 American Chemical Society.

As lithium insertion continues, competing reactions occur as lithium is either inserted into previously formed low lithium content alloy regions or is inserted into crystalline silicon regions further breaking up the crystalline silicon lattice, forming further low lithium content amorphous lithium silicide. Crystalline silicon is broken apart leaving only small silicon clusters. Only once the crystalline silicon has been broken up is lithium insertion into the silicon clusters able to proceed, finally forming isolated silicon atoms surrounded by lithium. Silicon clusters may remain unlithiated at this stage. The $Li_{15}Si_4$ crystalline phase can form in the regions of high lithium concentration. Finally further lithium insertion into the $Li_{15}Si_4$ crystalline phase may occur forming the over lithiated phase, $Li_{15+\delta}Si_4$, at maximum lithium insertion (~0 V vs. Li/Li^+).

The mechanism of lithium extraction from lithiated silicon is dependent on the extent to which silicon was lithiated. If lithiated to a maximum concentration at which an over lithiated crystalline phase was produced then initial lithium extraction occurs from the $Li_{15+\delta}Si_4$ phase resulting in formation of $Li_{15}Si_4$. Further lithium extraction then occurs from the $Li_{15}Si_4$ crystalline phase at a potential of around 0.45 V vs. Li/Li, resulting in the nucleation and growth of an amorphous silicon phase. If however lithium insertion was ceased prior to formation of the crystalline $Li_{15}Si_4$ phase then lithium extraction occurs initially from high lithium content amorphous silicide phase (~0.25V vs. Li/Li^+) resulting in the growth of silicon clusters and the formation of a lower lithium content amorphous silicide phase from which lithium extraction would then occur (~0.42 V vs. Li/Li^+). Lithium extraction from the low lithium content amorphous phase finally results in the formation and growth of an amorphous silicon phase.

1.4.2.2 Lithium insertion into amorphous silicon

After the first electrochemical cycle the structure of the silicon active material becomes amorphous [37]. The mechanism of the second cycle insertion process of lithium into amorphous silicon occurs in a significantly different way to crystalline silicon. The potential at with lithium initially inserts into amorphous silicon is higher (~0.3 V vs. Li/Li^+) than during insertion into crystalline silicon (~0.1V vs. Li/Li^+), representing a lower energy barrier to lithium silicide formation. The mechanism of lithium insertion into amorphous silicon has recently been reported by Ogata *et al.* [38]. **Figure 1-24** displays a schematic explaining the rate and potential dependant mechanism of the electrochemical reaction of lithium with amorphous silicon. A brief description of the mechanism assuming a low rate of lithium insertion and extraction is described in the following paragraph.

During initial insertion (~300 mV) the amorphous silicon phase is converted to a low lithium content amorphous lithium silicide phase throughout. Once the low lithium content amorphous lithium silicide phase has formed, the formation of a higher lithium content lithium silicide phase occurs (~180 mV). During the second insertion process all low lithium content amorphous lithium silicide is converted to high lithium content amorphous lithium silicide phase. Once high lithium content lithium silicide had been produced throughout crystallisation of meta-stable $Li_{15}Si_4$ occurs upon continued lithium insertion (below ~50 mV). Once crystallisation of meta-stable $Li_{15}Si_4$ has occurred further lithium insertion results in the formation of the over lithiated crystalline phase, $Li_{15+\delta}Si_4$ (below ~30 mV). Extraction of lithium follows the same mechanism as that of lithium extraction during the first cycle.

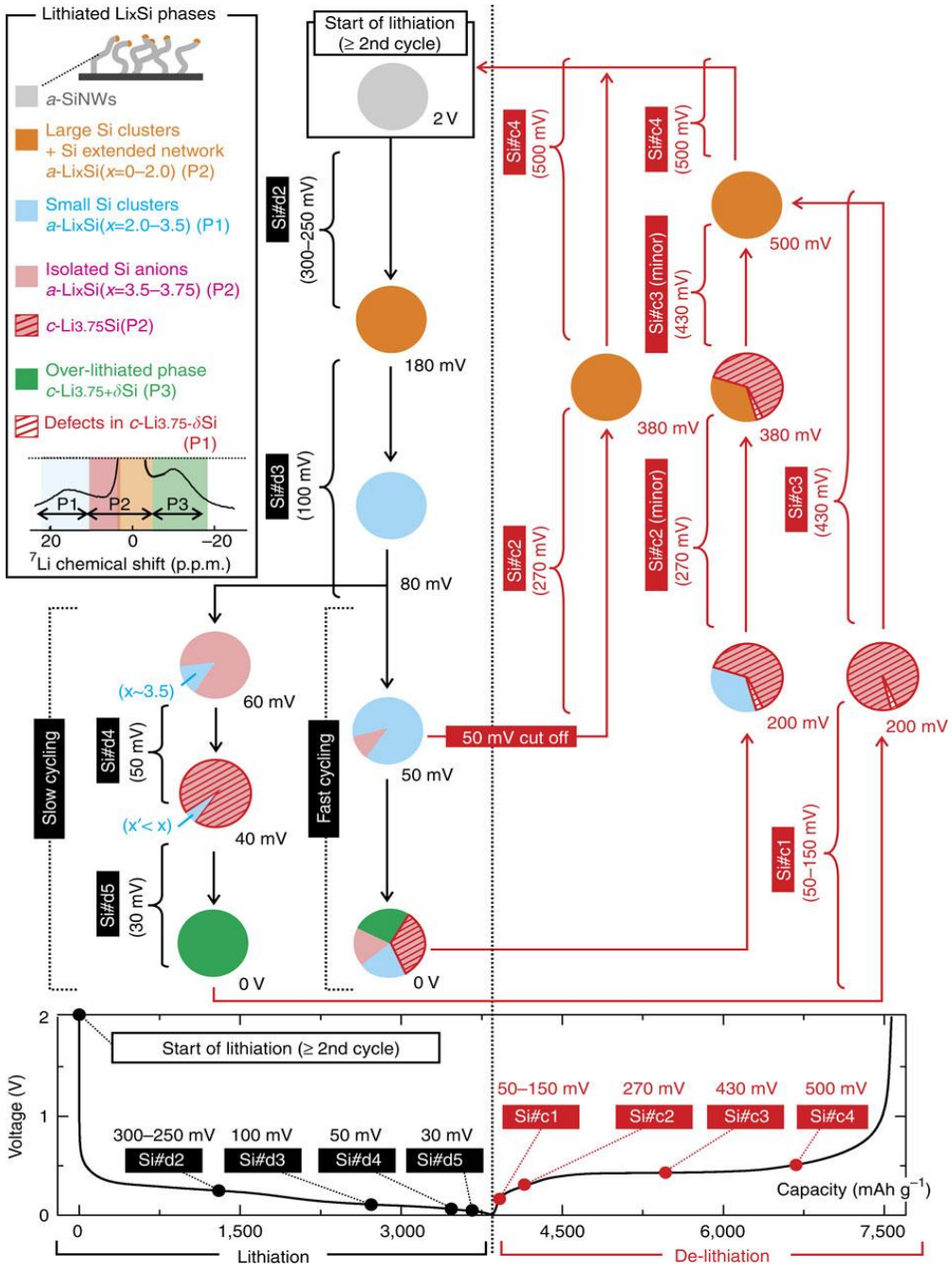

Figure 1-24 – Phase transformations for the amorphous silicon nanowires on lithiation and de-lithiation showing the dependence of the phase evolutions on the rate of cycling. Figure reproduced from reference [38] with permission.

1.5 Development of silicon based composite electrodes

1.5.1 Early studies

Research into the incorporation of silicon as an additional active material in traditional graphitic carbon based composite negative electrodes was conducted in the 1990's. Materials containing silicon were formed either *via* pyrolysis of poly-siloxanes [39,40] or *via* a CVD process forming nano-sized particles of silicon dispersed within 'pre-graphitic' disordered carbon [41]. These studies applied common composite electrode preparation techniques routinely used for graphite and carbon based materials. The technique involved the preparation of an electrode slurry mixture by dissolving a PVDF binder in NMP to which a conductive additive and the active material were added. The slurry mixture was then applied to a metal foil and dried, forming a composite electrode. Results demonstrated that silicon containing carbon materials could provide reversible capacities of around 600 $mAhg^{-1}$ at a potential below 1 V vs Li/Li^{+}. The results suggested stable cycling of silicon within composite electrodes was possible and that incorporation of silicon into carbon based electrodes may provide an approach to increasing the capacity of negative electrodes.

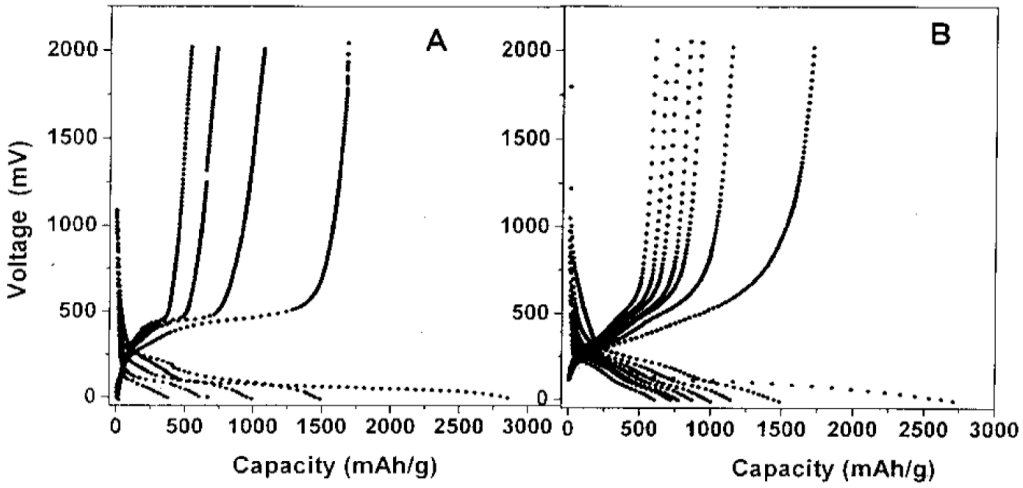

Figure 1-25 – The discharge and charge curves of a cell using (A) normal Si (micron scale powder) and (B) nano-Si as anode active materials. The cell is Si/ 1 M $LiPF_6$, in ECDEC (1:1)/Li. The current density is 0.1 mA / cm^2. The cells were cycled between 0.0 and 2.0 V. Reproduced from reference [42] by permission of The Electrochemical Society.

A report by Li *et al.* was the first to use silicon as the only major active component of a composite electrode [42]. It was noted that the large volume expansion and contraction experienced by silicon particles during electrochemical cycling was a major cause of the poor reversibility of silicon based composite electrodes. The effect of silicon particle size on the performance was investigated *via* comparison of composite electrodes containing micron and nano-sized particles **Figure 1-25**. Results suggested reversible cycling was possible and notably

that the cycle life of electrodes containing nano-sized particles was significantly greater than micron sized particles (**Figure 1-25**). The results agreed with the conclusions of an earlier report by Yang *et al.*[43] which suggested reducing the particle size of tin and tin-antimony composite electrodes provided an improvement in the cycle life performance of alloying type electrode materials.

Significantly improved performance of composite electrodes containing carbon-coated silicon powder was reported by Yoshio *et al.* [44, 45, 46]. The improvement was suggested to be due to suppression of electrolyte breakdown as well an improved electrical contact network, however a capacity decay of 5 - 10 mA h g^{-1} per cycle was observed. The work highlighted the effect of protecting the silicon particles from the electrolyte *via* a carbon-coating layer. A further paper by Yoshio *et al.* evaluated electrodes containing carbon-coated silicon particles under capacity limited conditions and with varying water content of the electrolyte [47]. Results suggested that water content in the electrolyte had a negative impact on the cycle life of electrodes and that lithium was accumulating in the electrodes during cycling due to incomplete lithium extraction, electrolyte breakdown after the initial cycle was also noted to contribute to poor reversibility. Regions of accumulated lithium were termed 'dead spots', and were suggested to be electronically isolated lithiated silicon no longer participating in the electrochemical reaction. Capacity limitation was demonstrated to improve the cycle life of electrodes; the improvement was suggested to be due to the reduced volume change experienced by the silicon particles and the composite electrode structure.

An important investigation into the structural changes occurring within silicon based composite electrodes was conducted by Obrovac and Christensen [31], formation of a crystalline $Li_{15}Si_4$ phase was identified, the associated volume increase during insertion was later calculated to be around 280 % [48]. The cycling stability of a composite electrode was determined to improve if formation of the crystalline $Li_{15}Si_4$ phase was avoided and electrodes were cycled within the amorphous range (>70 mV vs. Li/Li^+), as displayed in **Figure 1-26**.

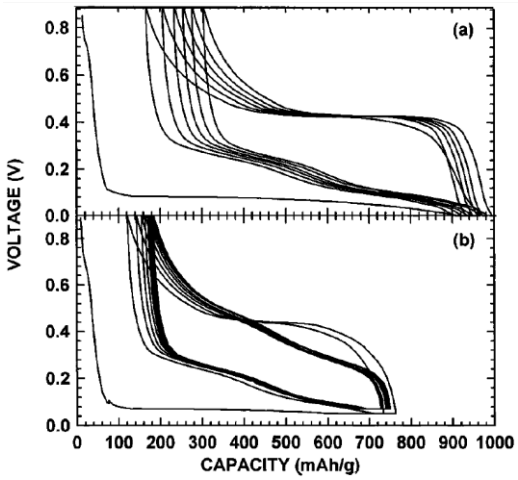

Figure 1-26 – a) Voltage curve of $Ni_{30}Si_{70}$ discharged to 0 V. b) The voltage curve of $Ni_{30}Si_{70}$ discharged to 50 mV for the first two cycles, then to 70 mV for later cycles. Reproduced from reference [31] by permission of The Electrochemical Society.

It was reported by Ryu *et al.* [49] that the cycle life and capacity fade of silicon based composite electrodes could be improved by increasing the conductive additive content and by increasing the pressure applied to the electrode stack. A large increase in the resistance of cells during the lithium extraction process was observed. The capacity fade was therefore suggested to be caused by a loss of electrical contact to lithiated silicon particles during de-alloying. The use of elastomeric binders was suggested as a possible method to allow electrical contact to be maintained during expansion and contraction. Particle contraction and isolation was later confirmed by Timmons and Dahn who directly observed interparticle movement within a composite electrode containing a-$Si_{0.64}Sn_{0.36}$ powder *via* an in-situ optical technique [50]. Particle isolation was suggested to contribute to the observed capacity fade of silicon based composite electrodes. The use of cycling procedures and new binder systems which reduce or accommodate particle movement were suggested as methods to improve the cycle life of silicon based electrodes.

A large number of other studies which evaluate the use silicon based materials as negative electrodes have been conducted and are reviewed by Kasavajjula *et al.* [51] and Larcher *et al.*[2], common problems have been described and an extensive range of methods aimed to improve the performance of composite electrodes have been developed.

1.5.2 Summary of the failure mechanisms of silicon based composite electrodes

Many reports into the performance of silicon based negative electrodes have been conducted and common failure mechanisms have been identified.

- Volume expansion

The source of the poor reversibly of silicon based electrodes is broadly agreed to stem from the large volume change which silicon inherently undergoes during lithium insertion and subsequent extraction (280%) [31]. Cracking and pulverisation of silicon particles has been observed and suggested to result in the electronic isolation of active material [52, 53]. The volume change of silicon particles has also been suggested to be responsible for fracturing and disruption of the SEI passivation layer at the surface of silicon particles.

- SEI formation / continual passivation

Insertion and extraction of lithium from silicon occurs in a potential region outside the stability window of commonly used electrolyte solutions. Passivation of the surface occurs *via* reduction of the electrolyte. As particles expand and contract during cycling, if the surface passivation layer becomes damaged or fresh surfaces become exposed to the electrolyte then further passivation must occur. Passivation consumes electrons, lithium salt ions and solvent. Passivation reduces the efficiency of the insertion-extraction process and has been suggested to contribute to the electronic and ionic isolation of particles. The high reactivity of the lithium silicide phases towards the electrolyte have also been reported to result in further electrolyte breakdown *via* reaction of Li_xSi with the electrolyte in a 'self-discharge' type process [34,54].

- Loss of electrical connectivity throughout the electrode

The dynamic nature of the active material during lithium insertion and extraction, combined with continual passivation of the surface of the particles, has been suggested to cause loss of the electrical contact between individual particles within an electrode [49]. Electronic isolation of particles can result in irreversible capacity, reduced capacity and a subsequent increase of applied current density to remaining active particles.

- Loss of ionic connectivity throughout the electrode

Products of electrolyte breakdown have been suggested to hinder the mass transport of lithium ions within composite electrodes [55]. Lithium transport within the composite electrode is gradually reduced as electrolyte breakdown products are continually formed, reducing the porosity and effectively isolating active material particles from the electrolyte [56].

1.5.3 Improving the performance of silicon based composite electrodes

1.5.3.1 Nanoscale dimensions

Pulverisation of large crystalline particles during initial lithium insertion has been suggested as a major cause of instability, leading to particle isolation and further passivation. An example of fractured particles is displayed in **Figure 1-27**. Recent studies have shown that the pulverisation of silicon particles can be prevented if the dimensions of the particles are reduced to the nanoscale.

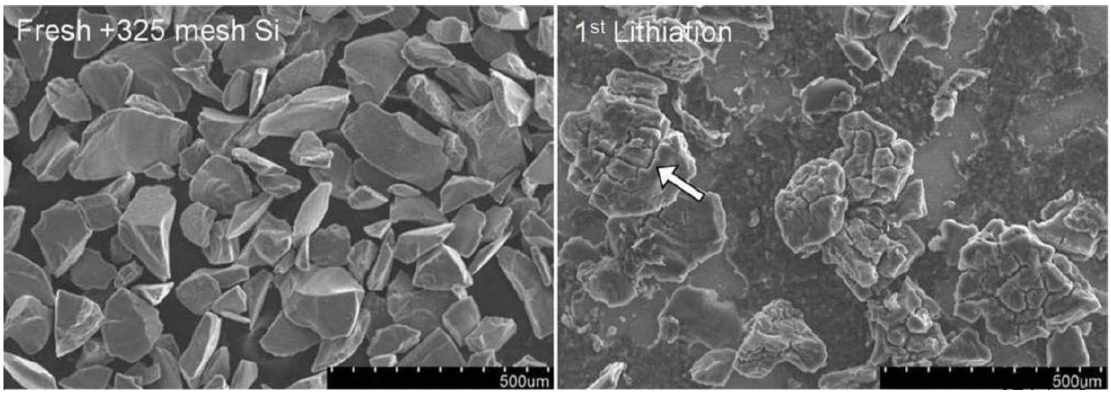

Figure 1-27 – SEM images of micron scale silicon particles before and after lithium insertion, significant cracking and fracturing of the silicon particles is observed. Reproduced from reference [52] by permission of The Electrochemical Society.

A critical size of around 150 nm in diameter has been reported as the limit above which spherical silicon particles are observed to fracture [57]. A diameter of below around 240 nm has been reported to allow for low fracture rates in silicon pillars and a diameter of below around 300 nm has been reported for silicon nanowires during lithium insertion [58,59].

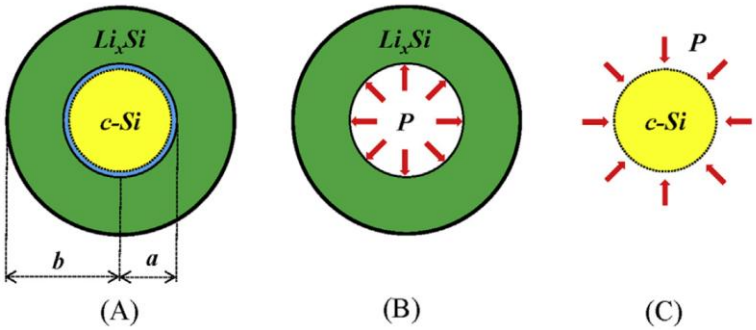

Figure 1-28 – Schematic of lithiation of a crystalline Si nanopillar (A) At a given time, pristine silicon core and Li_xSi alloy shell. The thin layer (blue colour) stands for the atomistically sharp phase boundary where lithiation occurs at the given time duration. (B) Stress state of the lithiated Si alloy shell. (C) Stress state of pristine Si core. Figure reproduced from reference [60] with permission.

The mechanism of crack formation has been investigated and a model which explains the observed behaviour has been described [60]. Formation of the moving phase boundary between amorphous lithium silicide and crystalline silicon phases has been suggested to create a build-up of hoop stress in the outer lithiated silicon phase, **Figure 1-28**. The build-up of energy can be

easily released in larger particles *via* the formation of a crack or fracture, however in smaller particles the energy cannot easily be lost *via* fracturing due to conflicting surface energy gains which would occur if a crack were to form [57].

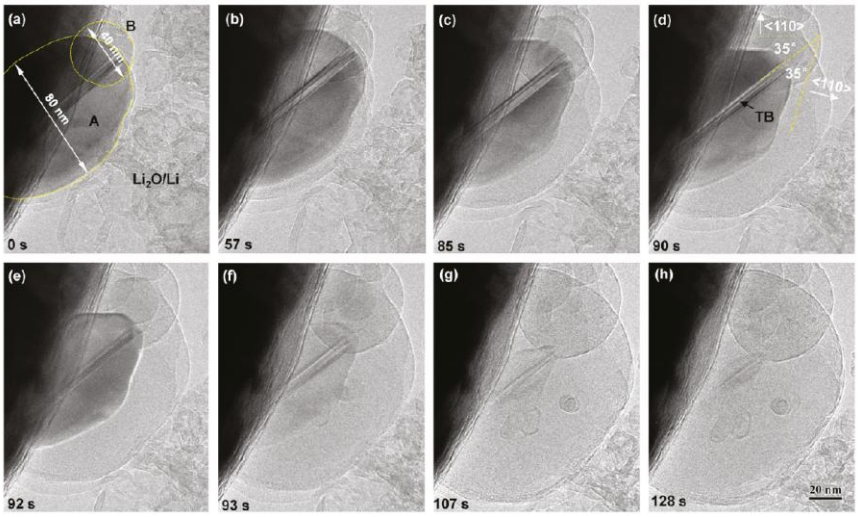

Figure 1-29 – Electrochemical lithiation of two small SiNPs below the critical size and without fracture. (a) Two pristine particles marked by "A" and "B". No cracking or fracture was observed for the two lithiated nanoparticles. The lithiation completed in about 2 min, no cracks formed despite the high lithiation rate. Figure reproduced from reference [57] with permission.

In-situ TEM experiments have recently demonstrated the lithiation of silicon nanoparticles which successfully avoid fracture during lithium insertion (**Figure 1-29**). Preferential lithium insertion in the <110> direction and the fast movement of the sharp two-phase boundary in the <110> direction was directly observed throughout the series of images.

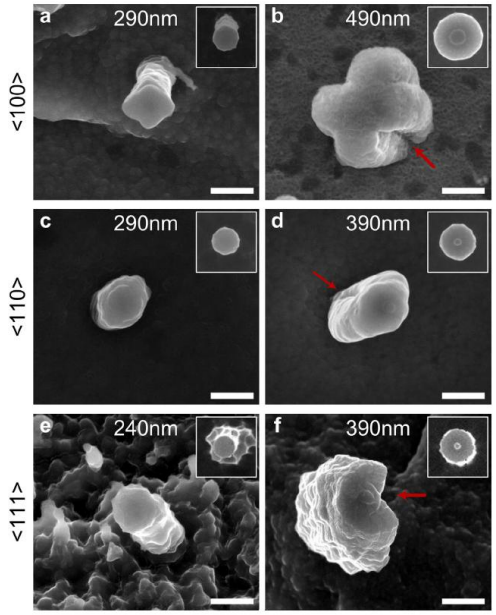

Figure 1-30 – Images of silicon pillars of differing growth direction in the lithiated state, insets display the pillars prior to lithiation. The first column displays pillars originally below the critical diameter and the second shows pillars originally above the critical diameter. The red arrows highlight the formation of cracks. Scale bar = 200nm. Figure reproduced from reference [60] with permission.

Directional fracture has been observed in crystalline silicon pillars above a critical diameter limit (**Figure 1-30**), analysis of the fracture patterns of silicon pillars post lithium insertion allowed for a model of stress evolution to be developed [61]. The preferential reaction of lithium with silicon in the <110> direction was calculated to cause significant directional stresses to build within particles (**Figure 1-31**). The regions of the pillars exposed to the greatest stress were observed to be located between {110} faces. The calculated regions of high stress were observed to correspond well with the observed location of fractures in lithiated silicon pillars.

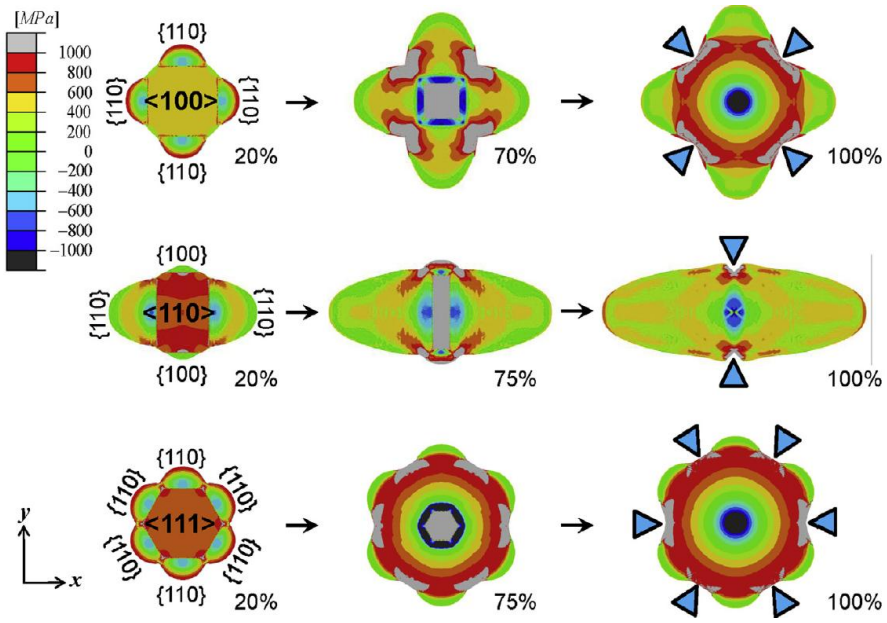

Figure 1-31 – Calculation of the hoop stress developed in silicon pillars during lithium insertion, locations of greatest stress are highlighted by blue arrows and display the calculated location for crack formation. Figure reproduced from reference [60] with permission.

From fundamental research and analysis conducted on the mechanical properties of nanoscale silicon particles it is now known that nanoscale dimensions can prevent the fracture of crystalline silicon particles during lithium insertion. The longer term stability of nanoscale particles over extended expansion-contraction cycles is however currently not well understood. Upon extended cycling of silicon nanoparticles, evolution of particle structures have been described including formation of pores, particle agglomeration and 'welding' of individual nanoparticles [62,63].

1.5.3.2 Binder development

A significant area of research for silicon based composite electrodes has been the development and use of new binder materials. Moving away from PVDF binder (**Figure 1-32**) traditionally used for graphite based negative electrodes has allowed for significant performance improvements in silicon based composite electrodes.

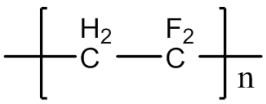

Figure 1-32 – Structure of PVDF

The significant role played by the binder within lithium alloy type composite electrodes was first highlighted by Wachtler *et al.* in 2001 [64]. Electrode processing methods, which resulted in varying PVDF binder distribution and morphology, were observed to have a significant impact on the cycle life performance of silicon based composite electrodes. In 2002 and 2003 Chen, Christensen and Dahn published papers which investigated PVDF-TFE-P [65], an elastomeric, highly extendible binder in composite electrodes containing a-$Si_{0.64}Sn_{0.36}$ [66, 67,68]. Previous research had suggested that elastomeric binders capable of allocating the volume changes that occur during cycling may improve the cycle life, however, only a marginal improvement was observed.

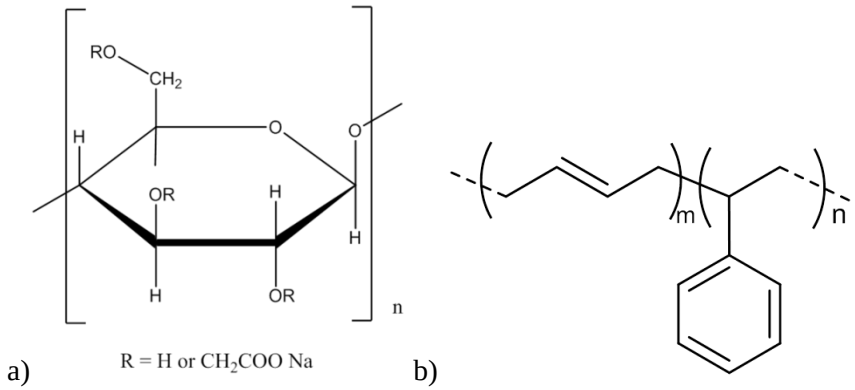

Figure 1-33 – Structure of a) sodium carboxymethyl cellulose (NaCMC) and b) styrene-butadiene-rubber (SBR)

A large step forward in binder development occurred in 2005 when Liu *et al.* tested a modified elastomeric binder containing a 1:1 mixture of styrene-butadiene-rubber (SBR) and Sodium carboxymethyl cellulose (NaCMC) (**Figure 1-33**). Electrode slurry pastes were produced in the form of a water emulsion of SBR with added NaCMC. A significant observation was the swelling ratio of the binders in PC after 45 hours. Traditional PVDF binders were shown to swell significantly whereas SBR/NaCMC displayed no signs of swelling. The adhesion strength of SBR/NaCMC to the copper current collector was measured to be much greater than that of PVDF. Results of electrochemical testing displayed a significant improvement in the cycling performance obtained using the SBR/NaCMC binder. The difference in the performance binders was suggested to be due to the differences in the microscopic mechanical properties of the binders during operation.

Li *et al.* later reported the largely improved performance of silicon powder based composite electrodes bound using pure NaCMC [69]. NaCMC was highlighted as an environmentally friendlier binder that could allow for aqueous processing, avoiding the use of organic solvents. Stress strain analysis found CMC to be stiff and brittle polymer extending only 5-8% before breaking, the results contradicted the previous elastomeric model used to explain improved cycle life stated by Chen *et al.* [68, 66]. Li *et al.* suggested that the use of NaCMC in silicon composite electrodes may also allow for the formation of a more favourable SEI layer [70].

A report published by Lestriez *et al.* [71] on the binding mechanism of CMC in silicon based composites, compared pure CMC and CMC/Poly(ethylene-co-acrylic acid) (PEAA) as binders. It was found that when prepared at a pH of 3 pure CMC produced the best performance. The influence of pH was suggested to result from an extension of CMC chains during slurry preparation. The improvement in performance was attributed to the extended polymer confirmation conformation and an efficient CB-CMC-Si network. The group later published further analysis which suggested an esterification reaction between CMC and the surface oxide of silicon particles (**Figure 1-34**) was promoted at pH 3 [72]. The first example of extremely stable silicon based composite electrodes was demonstrated, *via* capacity limited cycling at 960 mA h g^{-1} (of electrode), more than 700 cycles were achieved.

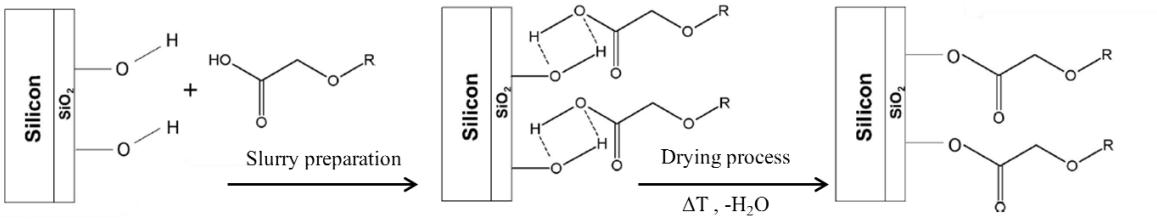

Figure 1-34 – Silicon - binder interaction and ester bond formation mechanism proposed by Hochgatterer *et al.* Reproduced from reference [73] by permission of The Electrochemical Society.

A model to account for the improvement in the performance of silicon based composite electrodes utilising CMC binders was described by Beattie *et al.* [74]. Results suggested that a lower wt. % of nano silicon particles dispersed within an electrode containing higher than usual wt. % of CMC and carbon black allowed for significantly improved cycle life performance. Various ratios of components were tested. A cell with a cycle life of 160 cycles was demonstrated with a capacity of around 2000 mA h g^{-1} (of silicon) for electrode formulations with silicon content of 33 wt. % or lower. The more dispersed nature of the silicon particles within the composite was suggested to provide room for expansion without the particles becoming aggregated or electronically disconnected.

Hochgatterer *et al.* tested various other cellulose based binders and concluded that NaCMC displayed the best performance, highlighting that a higher degree of substitution of NaCMC

(increase in number acetate type groups per monomer unit) improved the performance of composite electrodes [73]. A esterification reaction mechanism by which NaCMC bonded to the hydrolysed silicon oxide surface of silicon nanoparticles was also reported [73], confirming previous reports by Lestriez *et al.* [72].

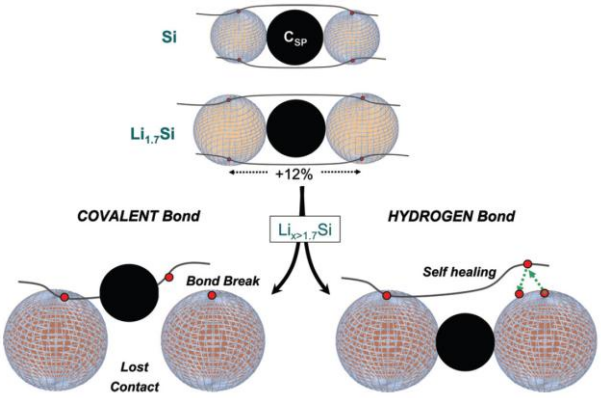

Figure 1-35 – Schematic of binding mechanisms of CMC based binders and possible self-healing *via* hydrogen bond formation. Reproduced from reference [75] by permission of The Electrochemical Society.

A further model was provided by Bridel *et al.* [76, 75] which suggested that a hydrogen bonding interaction between CMC and silicon was the cause of stable cycling when large volume expansion occurred and that a self-healing type process prevented the breaking of the CMC chains during volume change (**Figure 1-35**). Increasing the chain length of CMC was also reported to provide improved performance, the porous texture of composite electrodes produced using CMC was also highlighted as crucial to the electrochemical stability. A number of other cellulose based binders were tested and found to be inferior. Stable cycling of electrodes for 100 cycles was demonstrated with a capacity of over 3000 mA h g^{-1} (of silicon). A later report conducted by Maver *et al.* investigated the bond formed between NaCMC bound to an AFM tip and a silicon surface and under various conditions and concluded that covalent ester type bonding between the silicon surface and CMC molecules provided a strong bond which allowed for a large extension of the polymer chain [77].

A large number of reports into the influence of binders on the performance of silicon containing composite electrodes have been conducted, improvements have been reported with PVDF after heat treatment [78], Poly(amide imide) [79] and Nafion [80], however the results were less impressive than those obtained with NaCMC. A review of polymer binders which have been used to produce composite electrodes has been provided by Bernard Lestriez [81].

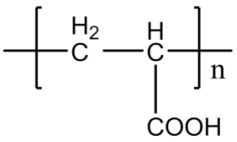

Figure 1-36 – Structure of poly-acrylic acid

Poly-acrylic acid (**Figure 1-36**) and poly-acrylates were later highlighted to provide increased performance over CMC binders [82]. The first reported use of an acrylic binder was in 2006 by Chen *et al.* however results published suggested that a modified acrylic/ NaCMC binder outperformed a pure acrylic based binder [83]. Magasinki *et al.* later described experiments comparing PAA, NaCMC and PVDF using carbon coated nanosilicon powder as the active material, results displayed improved coulombic efficiency and capacity during galvanostatic cycle life testing for PAA bound composite electrodes [82]. Li *et al.* later reported similar improvements for an $Sn_{30}Co_{30}C_{40}$ alloy compound using lithium poly-acrylate as a binder, results displayed significant gains in cycle life performance over CMC bound electrodes [84].

Further analysis of sodium poly-acrylate as a binder for silicon based composite electrodes was conducted by Komaba *et al.*, the performance was found to be superior to NaCMC and PVDF [85]. The Improved performance of PAA bound composites was suggested to be due to a dense film morphology maintaining a conductive network during volume changes accompanied by a low swelling ratio in electrolyte solvents. Another significant observation was the suppression of electrolyte breakdown, suggesting improved SEI formation contributed to improve reversibility and coulombic efficiency.

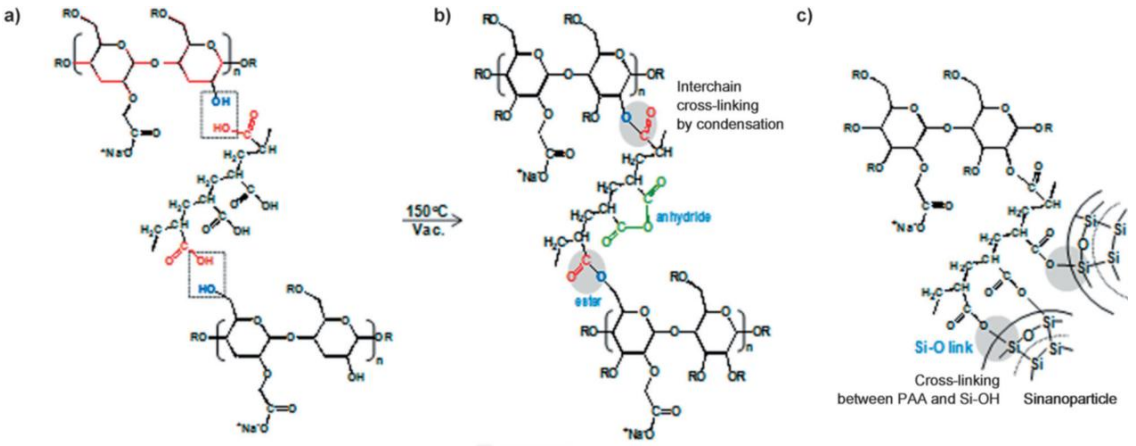

Figure 1-37 – a) Poly (acrylic acid) (PAA) and sodium carboxymethyl cellulose (NaCMC) before heating. b) Cross-linked binder (c-PAA-CMC) formed by condensation between PAA and CMC. c) Chemical binding between silicon nanoparticles and c-PAA-CMC. The OH moieties of a SiO_2 native layer on the Si surface react with the COOH groups of PAA forming a cross-linked binder. Figure reproduced from reference [86] with permission.

Mixtures of PAA and NaCMC have been shown to provide improved performance as a binder for composite electrodes containing nanoparticles of silicon when compared to the performance

of the individual polymer binders. The mixture was reported to form a cross-linked structure formed *via* condensation reactions occurring both between polymer chains of CMC and PAA and also between PAA and the surface of silicon particles during drying (**Figure 1-37**) [86]. The cross-linked structure of the binder was suggested as the reason for the improved electrochemical stability.

Recently alginate binders (**Figure 1-38**) have been reported to display improved performance over both CMC and PAA based binders. Over 1250 cycles (with capacity limitation) were demonstrated using an alginate based binder [87]. Kovalenko *et al.* suggested that ionic conductance through the polymer (around 10^{-8} S cm^{-1}) provided by ordered carboxylic groups allowed for the improved performance and stability [87]. A thin layer of binder between the silicon particle surface and the electrolyte combined with the mechanical properties of the binder were suggested to contribute to the observed performance. An electrode pore volume large enough to accommodate the volume expansion of silicon was also reported to be necessary to obtain stable cycling.

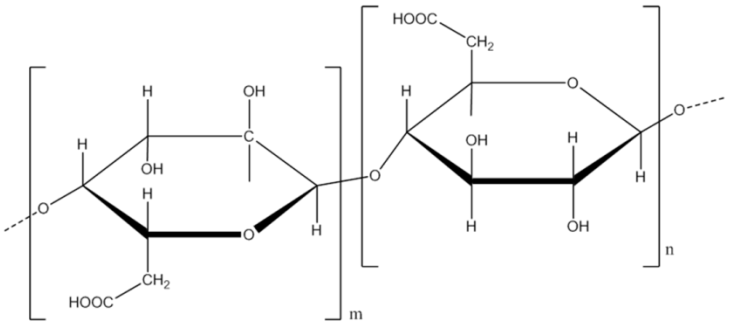

Figure 1-38 – Structure of Alginic-acid (Alg)

Recently specifically designed and synthesised polymers have allowed for the performance of silicon based composites to be further improved. Examples of advanced binder materials include electronically conducting polymers [88, 89, 90], a self-healing polymer [91], and a crack preventing polymer formed from a mixture of gum-arabic and PAA [92]. Electronically conductive binders remove the need for additional conductive additives in the composite electrode, reducing the overall electrode volume and mass. Liu *et al.* have developed the binder, PFFOMB, a polymer specifically designed to be electronically conducting over the potential region of lithium insertion and extraction from silicon [88]. Composite electrodes utilising PFFOMB polymer have displayed outstanding performance, a capacity of over 2000 mA h g^{-1} for over 600 cycles was reported. The performance was suggested to be due to the polymers ability to accommodate the volume change whilst retaining electrical conductivity throughout the electrode. Recently polymers with electronically conducting side chains have also been reported to significantly improve the performance of silicon based composite electrodes and

allow for extended cycling [93]. A very recent review of polymer binders investigated for use with silicon based composite electrodes has been provided by Mazouzi *et al.*[94].

1.5.3.3 Electrolyte stability, SEI formation and additives

Electrolyte systems and the accompanying SEI forming reactions have been thoroughly investigated for carbon based negative electrodes; an understanding of the electrolyte-surface interaction was required to allow for the successful use of graphite. Early testing of silicon based electrodes was conducted in electrolyte systems developed for use with graphite based negative electrodes. Common standard electrolytes used generally consisted of a $LiPF_6$ dissolved in a mixture of short chain (DMC, DEC, EMC) carbonates with ethylene carbonate (EC). The large difference in the volume change experienced by graphite and silicon particles was suggested to be the reason electrolytes that worked well for graphite based electrodes did not work for silicon based electrodes [55]. Upon full lithium insertion into graphite the interlayer spacing increases by around 10 % [95], however the volume expansion associated with silicon has been reported to be around 280 % [48].

The influences of SEI formation, composition and stability have been determined to be crucial to the performance of large volume change electrodes. Cracking, breaking or delaminating of the SEI layer will cause exposure of non-passivated surfaces to the electrolyte forcing further passivation to occur. The repetition of this process during subsequent cycles has been proposed as major cause of growth of the SEI layer contributing to the inefficiency observed during cycling of silicon based composite electrodes [96].

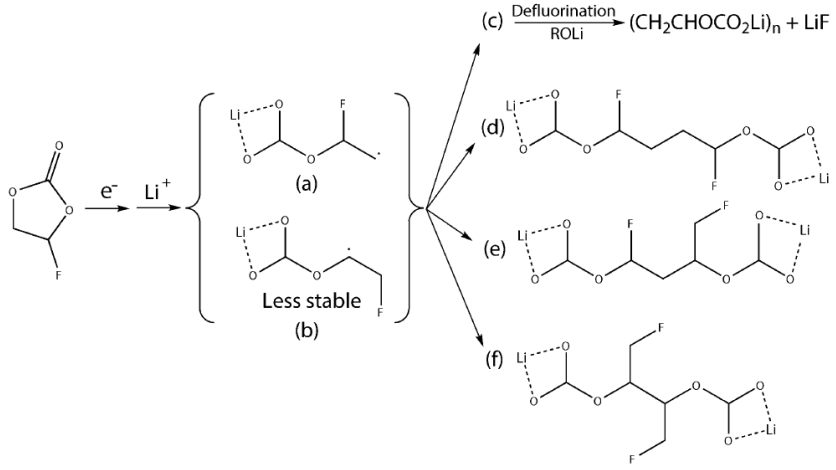

Figure 1-39 – Proposed reduction reaction of FEC. ROLi is the reduction product of alkyl carbonates and serves as a strong base to help remove HF. Figure reproduced from reference [97] with permission.

Most notably FEC (**Figure 1-39**) and VC (**Figure 1-40**) have recently become commonly used solvents/additives in electrolytes used to test silicon based negative electrodes [98]. The use of fluoroethylene carbonate as a solvent has been demonstrated to allow for significant

improvement in the cycling stability of silicon based composite electrodes [99]. Both FEC (**Figure 1-39c**) and VC (**Figure 1-40**) have been reported to undergo polymerisation at the surface of silicon particles, the polymerisation process has been suggested to be responsible for producing a thin SEI layer capable of withstanding the volume changes and allowing for improved passivation of the electrode during cycling. Recently electrolyte systems of 1 M $LiPF_6$ in FEC: DEC [100], 1 M $LiPF_6$ FEC: DMC [101] and 1 M $LiPF_6$ EC: DEC + 10% FEC + 2% VC [102] have been have been demonstrated to allow for the enhanced performance of silicon based electrodes. The influence of FEC and VC solvent content within electrolyte solutions has recently been reported by Nguyen and Lucht [103].

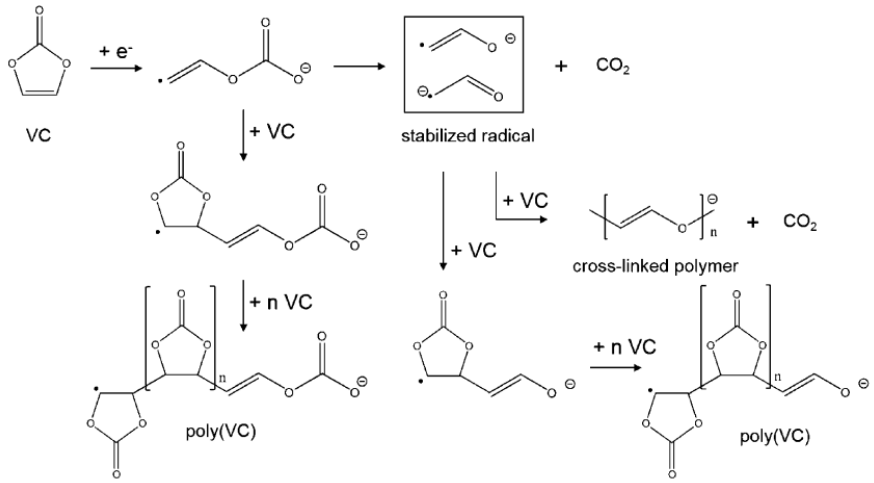

Figure 1-40 – Proposed mechanism for the reduction of VC. Adapted with permission from reference [104]. Copyright 2015 American Chemical Society.

A large number of reports of electrolyte additives used in lithium-ion batteries have been reviewed by Zhang *et al.* [105]. Additives specifically highlighted to improve the performance of silicon based negative electrodes include FEC [106], VC [107], Succinic anhydride [108] and Silane based additives [109]. Succinic anhydride has been reported to polymerise at potentials above usual SEI formation and was suggested to aid in formation of a more stable SEI layer. Silane compounds have been used as electrolyte additives and as surface functionalization compounds. Silane compounds have been reported to promote formation of thinner more stable SEI layers [109, 110, 111, 112].

1.5.3.4 Limiting the utilisation of active material

Capacity limitation and voltage limitation have both been employed as methods to improve the performance of silicon based electrodes [113, 48]. Voltage limitation is easily produced within an experimental cell configuration however within a commercial lithium-ion cell precise control of the voltage of a single electrode is significantly more difficult, requiring additional circuitry and a reference potential [114]. Capacity limitation however can be practically introduced into a

commercial lithium-ion cell *via* balancing of the ratio of active material within the positive and negative electrodes.

Limitation of the capacity of silicon based electrodes has been applied with significant success. For silicon based electrodes a limitation in the capacity corresponds to a limitation in the volume expansion and the associated degradation mechanisms such as SEI passivation layer failure.

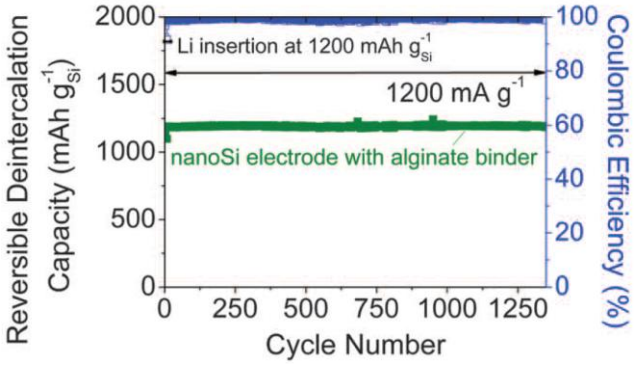

Figure 1-41 – Electrochemical performance of alginate-based nano-Si electrode (electrode density = 0.50 g/cm3, weight ratio of Si: C = 3:1). Reversible Li-extraction capacity and CE of the nano-Si electrodes versus cycle number for Li insertion level fixed to 1200 mA h g^{-1}$_{(Silicon)}$. Figure reproduced from reference [87] with permission.

A number of studies have demonstrated capacity limited cycling of silicon based composite electrodes, Mazouzi *et al.* have demonstrated over 700 cycles [72] and Kovalenko *et al.* have demonstrated over 1250 cycles [87] (**Figure 1-41**). When using nanoparticles, advanced binder systems and capacity limitation, loss of electronic contact is thought not to be the significant mechanism of capacity fade. The major cause of electrode performance degradation has been suggested to be due to a build-up of electrolyte breakdown products caused by side reactions within the composite which gradually restrict lithium transport [56] (**Figure 1-42**).

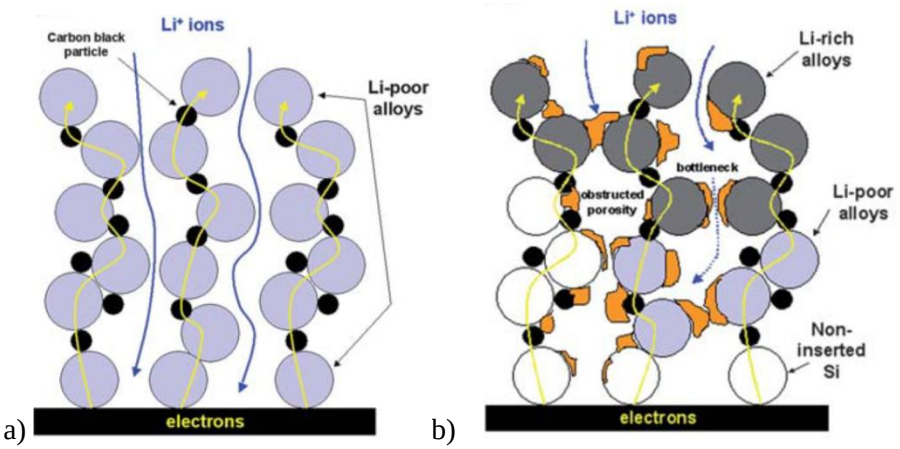

Figure 1-42 – Sketch of the non-homogeneous lithium insertion into the composite electrode at the end of discharge, in the fresh state (a) and in the aged state (b). Figure reproduced from reference [56] with permission.

1.5.3.5 Advanced particle morphology

Further improvements to the performance of silicon based composite electrodes have been reported *via* the intricate design of silicon active material particles. The development of internal space within particles of active material has been reported to allow for volume expansion of silicon without a large volume expansion of the particle as a whole.

Development of porous and 'void space' type silicon structures has occurred within the literature, initially three dimensional porous silicon particles were prepared *via* chemical reduction of a silica template (**Figure 1-43**) [115]. The porous particles displayed a stable high capacity which was attributed to the porous structure acting as a 'buffer' alleviating the volume expansion of the silicon. Similar results were reported for silicon nanotube particles coated with carbon [116]. The improvement was also suggested to be due to accommodation of the volume expansion *via* the internal free space which allowed for the formation of a stable outer surface SEI layer.

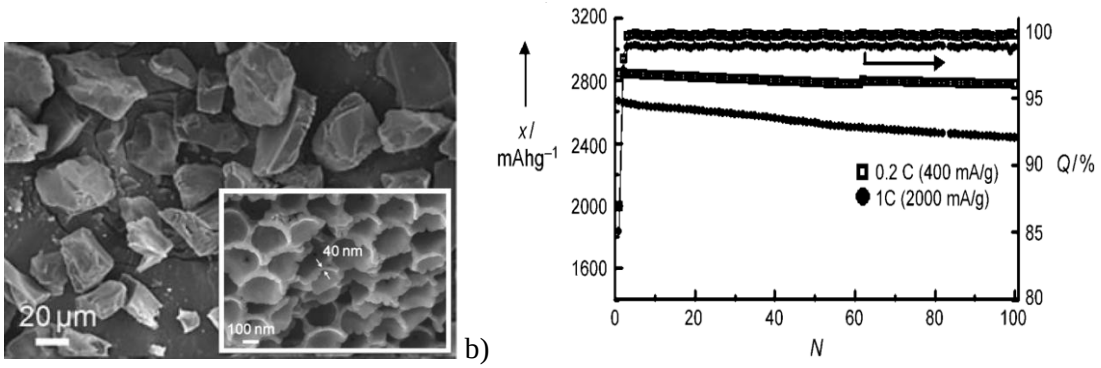

Figure 1-43 – a) SEM images of 3D porous c-Si particles. Inset, an image of a cross-sectioned particle. b) plot of charge capacities versus cycle number of the 3D porous c-Si particles cycled at different rates (0.2 C and 1 C) between 0 and 1.5 V in coin-type half cells. x=charge capacity, N=cycle number, Q=coulombic efficiency. Figure reproduced from reference [115] with permission.

Hollow silicon particles have been investigated for use as an active material [117]. Calculations suggested that the particles would experience reduced stress during volume expansion and as such would be more stable throughout cycling. Stable high capacity was observed which slowly decreased over 700 cycles. The stable performance was attributed to morphology and formation of a stable SEI layer formed on the outside surface of the particles.

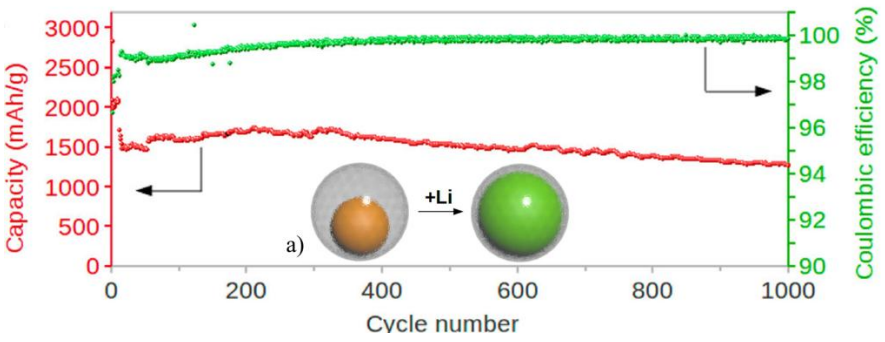

Figure 1-44 – a) Schematic of an individual silicon@void@shell particle displaying volume expansion without bursting the carbon shell or disrupting the SEI layer. b) Delithiation capacity and CE of the first 1000 galvanostatic cycles between 0.01−1 V (alginate binder). The rate was C/10 for one cycle, then C/3 for 10 cycles, and 1C for the later cycles. Adapted with permission from reference [118]. Copyright 2012 American Chemical Society.

Increased stability of was later achieved *via* the use of 'yolk-shell' type particles (**Figure 1-44a**) [119,118]. A void space between a silicon nanoparticle and a carbon shell was produced to allow space for silicon to expand and contract during reaction whilst also allowing for the formation of an SEI layer on the outside of the carbon shell. The design was suggested to prevent cracking and breaking of the SEI layer caused by the volume expansion of the silicon nanoparticle within. Stable cycling of 1000 cycles was demonstrated at a *C*-rate of 1 *C*. Sodium alginate binder was used to bind the composite electrode and VC was added to the electrolyte.

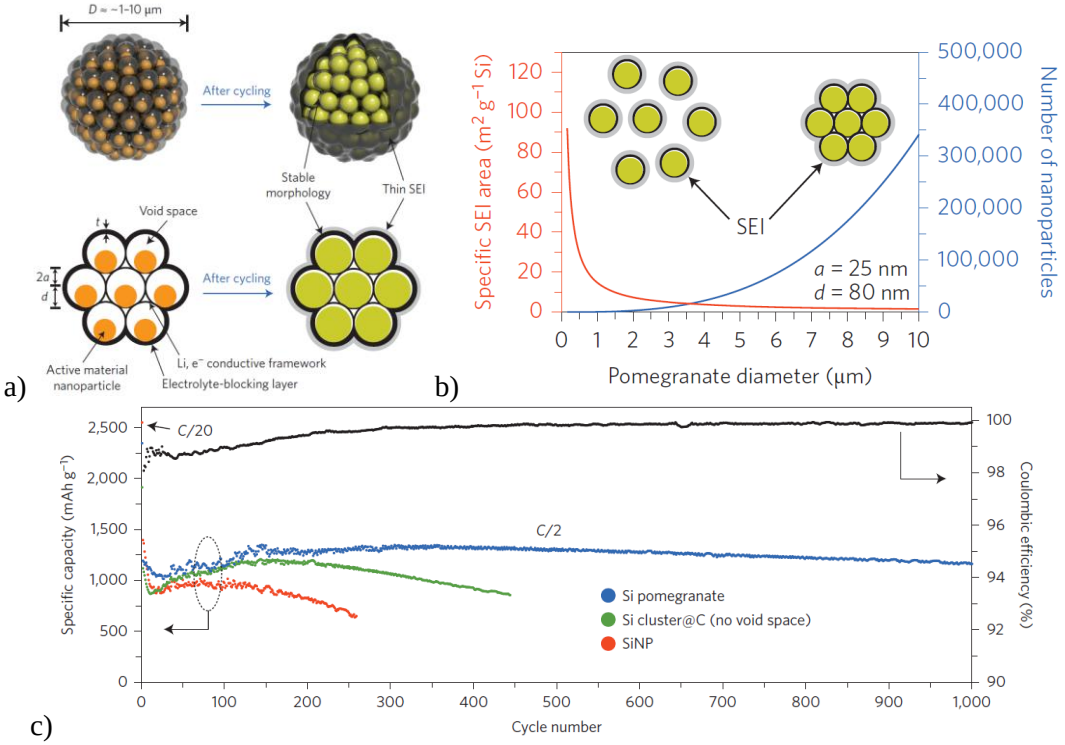

Figure 1-45 – a) Schematic of pomegranate particle design. b) Calculated surface area in contact with electrolyte and number of primary nanoparticles in one pomegranate particle versus its diameter. c) Reversible delithiation capacity for 1,000 galvanostatic cycles of silicon pomegranate and other structures. Active material loading was 0.2 mg cm^{-2}. C/20 for the first cycle and C/2 for later cycles. (1C = 4.2 A g^{-1} active material.) Figure reproduced with permission from reference [120]

Agglomerations of yolk-shell particles, named pomegranate type particles, were later produced by the same group [120]. The structure allowed for a large reduction in the surface area exposed to the electrolyte, reducing SEI layer formation. The pomegranate particles were also reported retain a near constant volume during reaction, preventing loss of electrical contact due to particle motion and retention of a stable SEI layer. The extended cycling demonstrated that the particles were able to retain capacity when cycled at C/2, the electrolyte used to test the electrode was 1M $LiPF_6$ EC: DEC + 1% VC composites were produced utilising a traditional PVDF binder.

1.6 Composite electrodes containing silicon nanowire materials

This section reviews the use of silicon nanowires as the active material within composite electrodes. The term 'silicon nanowire' covers quite a broad range of particles however generally includes silicon particles with a width and depth axis of below around 300 nm and a length axis of greater than 10x the width and depth. Silicon nanowires produced *via* a number of methods have been investigated for use as the active material of the negative electrode for lithium-ion batteries.

1.6.1 Early studies

The first report to investigate electrochemical lithium insertion into silicon nanowires was conducted by Zhang *et al.* in 1999 [121]. Silicon nanowires formed *via* laser ablation were investigated as an electrode material. Electrodes were produced *via* simple dispersion onto a copper foil. Electrochemical testing utilising a lithium counter / reference electrode and 1 M $LiPF_6$ dissolved in EC: DMC as an electrolyte. Ex-situ analysis of the electrode indicated the particles merged during lithium insertion. Large irreversible capacity was reported and an amorphous phased was observed after reaction with lithium.

A report by Li *et al.* in 2000 investigated the structural evolution of silicon nanowires produced *via* laser ablation at room temperature [122]. Electrodes were formed *via* dispersion and compression of the material onto copper foil. Ex-situ XRD, Raman spectroscopy and TEM were utilised to study the structure of silicon nanowires during electrochemical reaction. Results provided evidence of the destruction of the crystalline silicon structure resulting in the formation of an amorphous phase, after lithium extraction locally ordered structure was reported and crystalline silicon was reported to have reformed during lithium extraction. Recrystallization of silicon during extraction has not been corroborated by later studies and the reported results conflict with many other reports. The reported presence of crystalline silicon may instead have been caused by the inactivity of a number of particles resulting in crystalline silicon remaining in the samples throughout analysis.

1.6.2 Recent studies

Recently studies investigating the electrochemical performance of silicon nanowire materials can be divided by nanowire fabrication method, metal assisted chemical etching (MACE) and supercritical solution synthesis (SFLS).

1.6.2.1 Metal assisted chemical etching based synthesis

Xu and Flake investigated the performance of silicon nanowires produced *via* MACE within a composite electrode (**Figure 1-46a**) [123]. The synthesis process was previously described by Peng et al [124]. Graphite and carbon black were used as conductive additives and PVDF was used as a binder. Results of electrochemical tests suggested that a crystalline to amorphous transition occurred during the first cycle. Poor capacity retention was observed and attributed to the physical loss of contact between particles within the electrode (**Figure 1-46b**). Further investigations by the same group found that surface modification of the silicon nanowire particles significantly affected the electrochemical performance [112]. An improvement in the performance of electrodes, attributed to beneficial SEI layer formation, was reported when trimethoxysilane was added to the electrolyte.

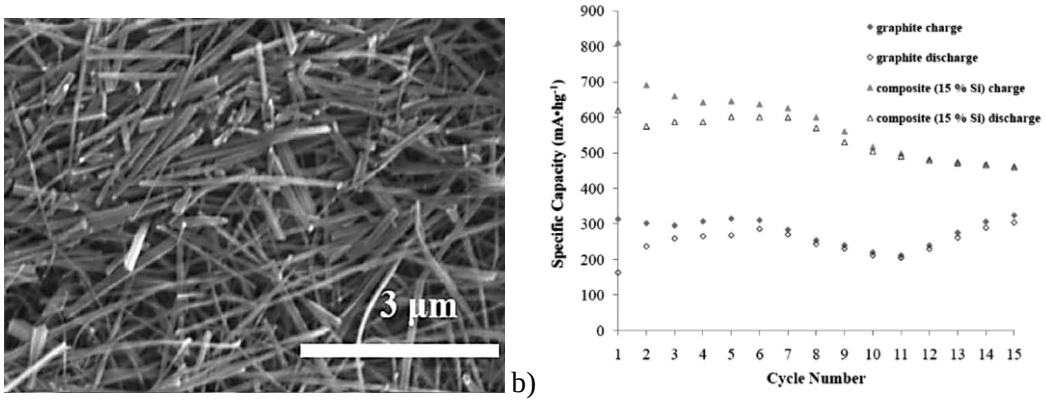

Figure 1-46 – a) SEM image of separated silicon nanowires after electroless fabrication and centrifugation (100–200 nm diameter and 10 µm long). b) Specific capacities of silicon nanowire composite anode and graphite. Electrodes were cycled utilising 1 M $LiPF_6$ in EC: DMC. Reproduced from reference [123] by permission of The Electrochemical Society.

The electrochemical evaluation of porous single crystalline silicon nanowires, produced *via* metal assisted etching of p-doped silicon wafers (resistivity of < 5 Ω cm^{-1}), has been reported by Wang *et al.* [125]. Graphene was used as a conductive additive and NaCMC as a binder. Results demonstrated that the porous silicon nanowire material significantly outperformed commercial silicon nanoparticle material. It was also demonstrated that composite electrodes utilising graphene as a conductive additive outperformed electrodes produced utilising carbon black as a conductive additive.

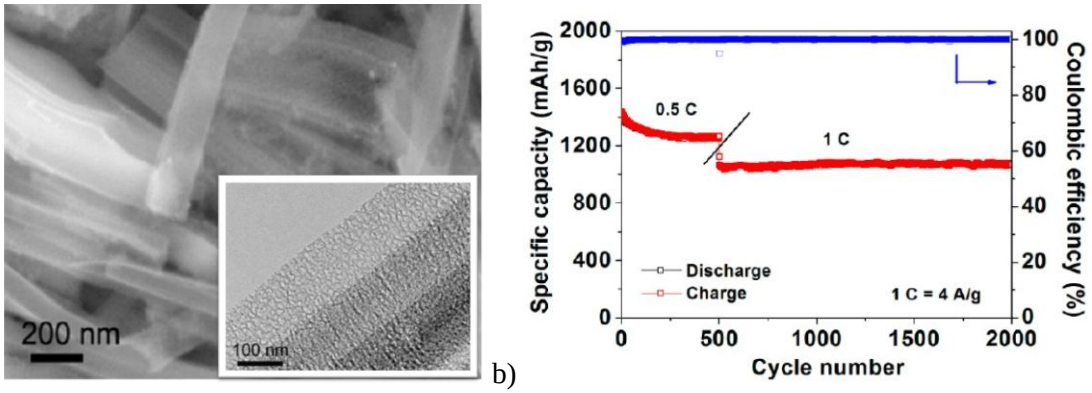

Figure 1-47 – a) SEM and TEM images of porous Si nanowires etched with 0.02 M $AgNO_3$. b) Charge/discharge capacity of a porous silicon nanowire electrode at current rates of 2 A/g (0.5 C) and 4 A/g (1 C). Reprinted with permission from reference [126]. Copyright 2012 American Chemical Society.

Ever higher stability of porous silicon nanowire material has recently been reported by Ge *et al.* [126]. Porous nanowire material (**Figure 1-47a**) produced *via* metal assisted chemical etching of a boron doped silicon wafer (<100>, < 5 Ω cm^{-1}) was tested utilising carbon black as a conductive additive and sodium alginate as a binder. 2000 cycles at a rate of 1 *C*, 4 A g^{-1} were reported (**Figure 1-47b**). The stable high rate performance was attributed to the porous structure accommodating the volume change during cycling. The use of an alginate binder was also found to be crucial to obtain stable performance.

1.6.2.2 Supercritical solution based synthesis

Research into supercritical solution synthesis of silicon nanowires *via* the supercritical fluid liquid solid (SFLS) type mechanism has been pioneered by the group of Brian Korgel [127, 128]. The developed synthesis methods have allowed for the controlled production of various nanowire type materials. Variation in composition and structure of the resulting nanowire materials have been achieved *via* control of synthesis conditions, seed materials and precursor materials [129]. The work conducted by the Korgel group includes investigation into the performance of various silicon nanowire material types within composite electrodes for use as the negative electrode of a lithium-ion battery.

In 2010, Chan *et al.* investigated the electrochemical performance of composite electrodes containing silicon nanowires produced *via* a supercritical route utilising mono-phenylsilane (MPS) as a silicon precursor and gold nanoparticles as seed crystals for nanowire growth (**Figure 1-48a**) [130]. Composite electrodes incorporated silicon nanowire material, a carbon conductive additive and NaCMC binder. Electrochemical analysis suggested that the electrodes containing silicon nanowire material displayed superior performance compared to electrodes containing silicon nanoparticles. Carbon-coating of the silicon nanowire material and the use of

MWCNT were observed to improve the performance (**Figure 1-48b**). The superior performance of silicon nanowire material was suggested to be due to the improved interconnection of silicon nanowires particles compared to silicon nanoparticles.

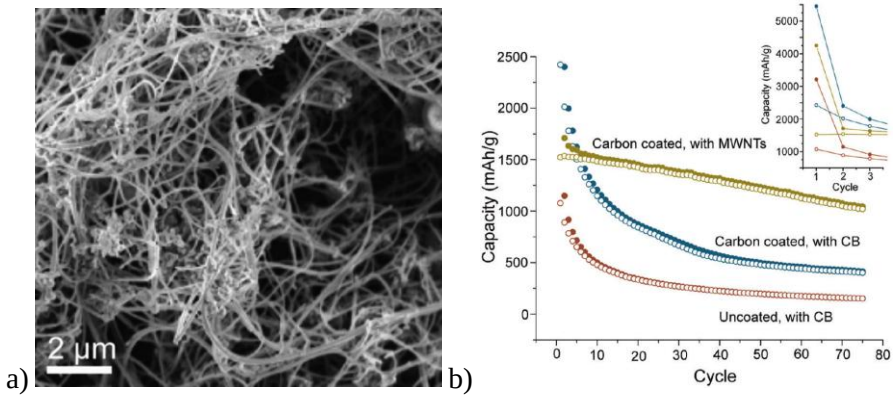

Figure 1-48 – a) SEM image of as-grown SFLS SiNWs. b) Capacity vs. cycling data for SFLS SiNWs uncoated and mixed with carbon black, carbon-coated and mixed with carbon black, and carbon-coated and mixed with multiwalled carbon nanotubes The first cycle is inset. Reprinted with permission from reference [131]. Copyright 2010 American Chemical Society.

A number of other reports have investigated the performance of SFLS type silicon nanowire material within composite electrodes. Various binders have been tested including PVDF (annealed) [100], NaCMC [130], NaAlginate [100], PAA [132] and mixtures of PAA with NaAlginate [133]. The seed material used to form the silicon nanowire material has been reported to play an important role in the electrochemical performance of SFLS material. Reports have suggested that gold seed material present within a sample was detrimental to the long term stability and rate performance (**Figure 1-49**) [100] no specific explanation of the detrimental influence of gold was provided. Tin seed material has been suggested to improve the rate performance of SFLS silicon nanowire based electrodes [134,133].

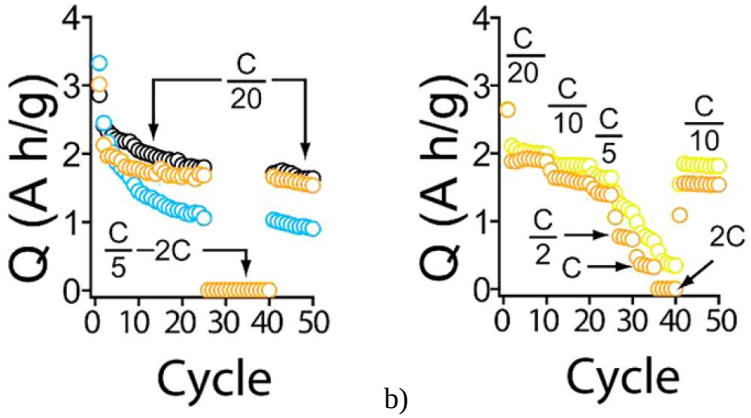

Figure 1-49 – Cycling data of composite electrodes containing silicon nanowire material produced *via* SFLS utilising gold seed crystals and trisilane precursor a) nanowire material including gold seed material, b) silicon nanowire material after gold removal, composite electrodes using Na Alginate binder, the colours represent various electrolyte solutions tested: Blue= EC: DMC, Black=EC: DEC, Orange=FEC: DMC, Yellow = FEC: DEC. Reprinted with permission from reference [100]. Copyright 2012 American Chemical Society.

The electrolyte has also been reported to play a crucial role in the long term performance of SFLS silicon nanowire based composite electrodes (**Figure 1-49**). An electrolyte of 1M $LiPF_6$ FEC: DEC has been reported improve the long term performance of SFLS based composite electrodes [100].

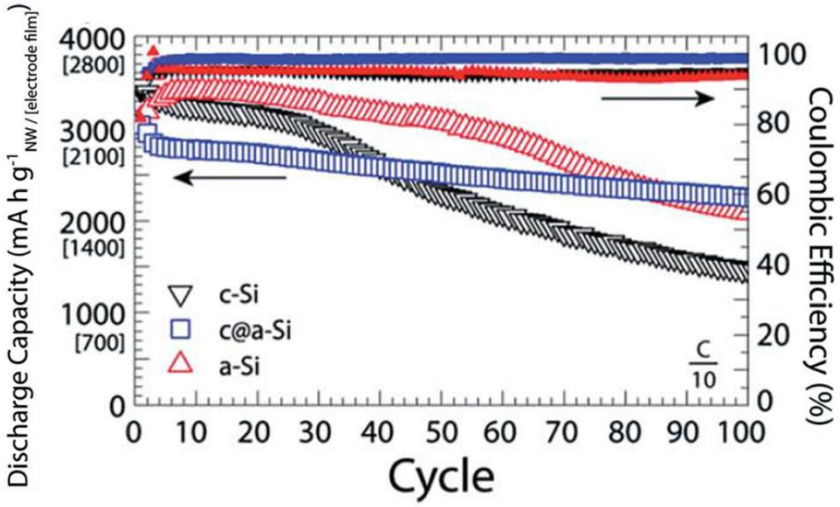

Figure 1-50 – Cycle life performance of a composite electrodes containing types of tin seeded SFLS silicon nanowire material (trisilane precursor), conductive carbon and PAA-NaAlg binder, cycled at 0.1 C utilising 1 M $LiPF_6$ in FEC: DEC as an electrolyte. Reproduced from reference [133] by permission of the Royal Society of Chemistry.

The greatest performance recently reported for composite electrodes containing silicon based SFLS type nanowire material is displayed in **Figure 1-50**, a reversible capacity of ~2500 mA h g^{-1} was obtained in the 100th cycle when cycled at a C-rate of 0.1C, a capacity of > 1500 mA h g^{-1} at a rate of 1 C was also reported, the composite electrode was produced utilising partially amorphous SFLS silicon nanowire particles, conductive carbon and a binder mixture of PAA and NaAlg. Electrodes were cycled utilising an electrolyte of 1 M $LiPF_6$ in EC: DEC + 5% FEC (**Figure 1-50**) [134]. The combination of the inclusion of tin and an amorphous silicon shell was suggested to allow for the improved rate performance and the use of PAA and NaAlg was suggested to form a cross-linked binder which contributed to the electrochemical stability of the composite electrode.

1.7 Organisation of thesis

The reviewed literature surrounding silicon based electrodes provided initial direction for an investigation into the performance of the batched SFLS material provided by Merck KGaA. The decision to evaluate the material via incorporation into a composite type electrode was taken. The key areas expected to be of significant importance to the performance based upon the literature survey were: the binder material and chemistry, the structural stability of the nanowire particles, the stability of the composite electrode structure and the electrolyte solution used.

The following 7 chapters detail investigations made into the performance of SFLS nanowire material. The chapters contain:

Chapter 2 – Details of experimental procedures and characterisation methods.

Chapter 3 – Initial characterisation of batch-1 and batch-2 SFLS silicon nanowire material and an FTIR investigation into the interaction of poly-acrylic acid with batch-1 material.

Chapter 4 – Initial electrochemical characterisation of composite electrodes containing batch-1 material, including impedance measurements obtained throughout the initial cycle.

Chapter 5 – Investigation into the structural changes of SFLS silicon nanowire material occurring within the initial electrochemical cycle of a composite electrode.

Chapter 6 – Investigation into the effect of electrode formulation on the performance of SFLS based electrodes. The effect of capacity and voltage limitation on the performance of electrodes is determined.

Chapter 7 – Investigation into the influence of electrolyte on the performance of composite electrodes. Ex-situ SEM and TEM study into the variation of composite electrode and active material structure throughout extended cycling. The rate performance of composite electrodes was also evaluated.

Chapter 8 – Conclusions and proposed further work.

1.8 Chapter references

1 G. Pistoia, Lithium-Ion Batteries: Advances and Applications, Elsevier, 2014.

2 D. Larcher, S. Beattie, M. Morcrette, K. Edström, J.-C. Jumas and J.-M. Tarascon, J. Mater. Chem., 2007, **17**, 3759.

3 J. M. Tarascon and M. Armand, Nature, 2001, **414**, 359–67.

4 K. Mizushima, P. C. Jones, P. J. Wiseman and J. B. Goodenough, Mater. Res. Bull., 1980, **15**, 783–789.

5 M. M. Thackeray, W. I. F. David, P. G. Bruce and J. B. Goodenough, Mater. Res. Bull., 1983, **18**, 461–472.

6 M. S. Whittingham, Chem. Rev., 2004, **104**, 4271–301.

7 Y. Nishi, J. Power Sources, 2001, **100**, 101–106.

8 R. Yazami and P. Touzain, J. Power Sources, 1983, **9**, 365–371.

9 R. Yazami, Electrochim. Acta, 1999, **45**, 87–97.

10 Z. Ogumi and M. Inaba, Advances in Lithium-Ion Batteries, Kluwer Academic Publishers, 2002.

11 E. Peled, J. Electrochem. Soc., 1979, **126**, 2047.

12 G. G. Amatucci, J. M. Tarascon and L. C. Klein, Electrochem. Soc., 1996, **143**, 1114–1123.

13 P. G. Bruce, Chem. Commun., 1997, 1817.

14 D. Linden and T. B. Reddy, Handbook of Batteries, McGraw-Hill, 2002.

15 T. Ohzuku, J. Electrochem. Soc., 1993, **140**, 2490.

16 K. Xu, Chem. Rev., 2004, **104**, 4303–417.

17 E. Peled, J. Electrochem. Soc., 1997, **144**, L208.

18 M. Nie, D. Chalasani, D. P. Abraham, Y. Chen, A. Bose and B. L. Lucht, J. Phys. Chem. C, 2013, **117**, 1257–1267.

19 P. Verma, P. Maire and P. Novák, Electrochim. Acta, 2010, **55**, 6332–6341.

20 D. M. Seo, D. Chalasani, B. S. Parimalam, R. Kadam, M. Nie and B. L. Lucht, ECS Electrochem. Lett., 2014, **3**, A91–A93.

21 J. R. Owen, Chem. Soc. Rev., 1997, **26**, 259–267.

22 M. Winter and R. J. Brodd, Chem. Rev., 2004, **104**, 4245–69.

23 M. Wakihara, Mater. Sci. Eng. R Reports, 2001, **33**, 109–134.

24 a. N. Dey, J. Electrochem. Soc., 1971, **118**, 1547.

25 S.-C. Lai, J. Electrochem. Soc., 1976, **123**, 7–8.

26 R. a. Sharma, J. Electrochem. Soc., 1976, **123**, 1763.

27 R. N. Seefurth, J. Electrochem. Soc., 1977, **124**, 1207.

28 C. J. Wen and R. A. Huggins, J. Solid State Chem., 1981, **37**, 271–278.

29 P. Limthongkul, Y.-I. Jang, N. J. Dudney and Y.-M. Chiang, Acta Mater., 2003, **51**, 1103–1113.

30 M. T. McDowell, S. W. Lee, W. D. Nix and Y. Cui, Adv. Mater., 2013, **25**, 4966–85.

31 M. N. Obrovac and L. Christensen, Electrochem. Solid-State Lett., 2004, **7**, A93.

32 Y. Wang and J. Dahn, J. Electrochem. Soc., 2006, **153**, A2314.

33 J. Li and J. R. Dahn, J. Electrochem. Soc., 2007, **154**, A156.

34 B. Key, R. Bhattacharyya, M. Morcrette, V. Seznéc, J.-M. Tarascon, C. P. Grey, V. Sezne and D. P. J. Verne, J. Am. Chem. Soc., 2009, **131**, 9239–49.

35 S. W. Lee, M. T. McDowell, J. W. Choi and Y. Cui, Nano Lett., 2011, **11**, 3034–3039.

36 B. Key, M. Morcrette, J.-M. Tarascon and C. P. Grey, J. Am. Chem. Soc., 2010, 503–512.

36* V. a. Sethuraman, V. Srinivasan, A. F. Bower and P. R. Guduru, 2011, 21.

37 P. Limthongkul, Acta Mater., 2003, **51**, 1103–1113.

38 K. Ogata, E. Salager, C. J. Kerr, a E. Fraser, C. Ducati, a J. Morris, S. Hofmann and C. P. Grey, Nat. Commun., 2014, **5**, 3217.

39 A. M. Wilson, J. N. Reimers, E. W. Fuller and J. R. Dahn, Solid State Ionics, 1994, **74**, 249–254.

40 J. R. Xing, Weibing; Wilson, A. M. Eguchi, K; Zank , G ; Dahn, J. Electrochem. Soc., 1997, **144**, 2410.

41 A. Wilson, B. Way and J. R. Dahn, J. Appl. …, 1995, **77**, 2363–2369.

42 H. Li, Electrochem. Solid-State Lett., 1999, **2**, 547.

43 J. Yang, M. Wachtler, M. Winter and J. O. Besenhard, Electrochem. Solid-State Lett. , 1999, **2** , 161–163.

44 T. Umeno, K. Fukuda, H. Wang, N. Dimov, T. Iwao and M. Yoshio, Chem. Lett., 2001, 1186–1187.

45 N. Dimov, K. Fukuda and T. Umeno, 2003, **114**, 88–95.

46 M. Yoshio, H. Wang, K. Fukuda, T. Umeno, N. Dimov and Z. Ogumi, J. Electrochem. Soc., 2002, **149**, A1598.

47 N. Dimov, Electrochim. Acta, 2003, **48**, 1579–1587.

48 M. N. Obrovac and L. J. Krause, J. Electrochem. Soc., 2007, **154**, A103.

49 J. H. Ryu, J. W. Kim, Y.-E. Sung and S. M. Oh, Electrochem. Solid-State Lett., 2004, **7**, A306.

50 a. Timmons and J. R. Dahn, J. Electrochem. Soc., 2006, **153**, A1206.

51 U. Kasavajjula, C. Wang and a Appleby, J. Power Sources, 2007, **163**, 1003–1039.

52 K. Rhodes, N. Dudney, E. Lara-Curzio and C. Daniel, J. Electrochem. Soc., 2010, **157**, A1354.

53 S. Kalnaus, K. Rhodes and C. Daniel, J. Power Sources, 2011, **196**, 8116–8124.

54 G. M. Veith, L. Baggetto, R. L. Sacci, R. R. Unocic, W. E. Tenhaeff and J. F. Browning, Chem. Commun. (Camb)., 2014, **50**, 3081–4.

55 J. R. Szczech and S. Jin, Energy Environ. Sci., 2011, **4**, 56.

56 Y. Oumellal, N. Delpuech, D. Mazouzi, N. Dupré, J. Gaubicher, P. Moreau, P. Soudan, B. Lestriez and D. Guyomard, J. Mater. Chem., 2011, **21**, 6201.

57 X. Liu, L. Zhong, S. Huang, S. Mao, T. Zhu and J. Huang, ACS Nano, 2012, 1522–1531.

58 S. Woo, M. T. Mcdowell, L. A. Berla, W. D. Nix and Y. Cui, 2012.

59 I. Ryu, J. W. Choi, Y. Cui and W. D. Nix, J. Mech. Phys. Solids, 2011, **59**, 1717–1730.

60 I. Ryu, S. W. Lee, H. Gao, Y. Cui and W. D. Nix, J. Power Sources, 2014, **255**, 274–282.

61 S. W. Lee, M. T. McDowell, L. a. Berla, W. D. Nix and Y. Cui, Proc. Natl. Acad. Sci., 2012.

62 J. W. Choi, J. McDonough, S. Jeong, J. S. Yoo, C. K. Chan and Y. Cui, Nano Lett., 2010, **10**, 1409–13.

63 K. Karki, E. Epstein, J.-H. Cho, Z. Jia, T. Li, S. T. Picraux, C. Wang and J. Cumings, Nano Lett., 2012, **12**, 1392–7.

64 M. Wachtler, M. R. Wagner, M. Schmied, M. Winter and J. O. Besenhard, J. Electroanal. Chem., 2001, **510**, 12–19.

65 Z. Chen, L. Christensen and J. R. Dahn, J. Appl. Polym. Sci., 2004, **91**, 2949–2957.

66 Z. Chen, L. Christensen and J. R. Dahn, J. Electrochem. Soc., 2003, **150**, A1073.

67 Z. Chen, L. Christensen and J. R. Dahn, J. Appl. Polym. Sci., 2004, **91**, 2958–2965.

68 Z. Chen, L. Christensen and J. R. Dahn, Electrochem. commun., 2003, **5**, 919–923.

69 J. Li, R. B. Lewis and J. R. Dahn, Electrochem. Solid-State Lett., 2007, **10**, A17.

70 M. Gaberscek, M. Bele, J. Drofenik, R. Dominko and S. Pejovnik, Electrochem. Solid-State Lett. , 2000, **3** , 171–173.

71 B. Lestriez, S. Bahri, I. Sandu, L. Roue and D. Guyomard, Electrochem. commun., 2007, **9**, 2801–2806.

72 D. Mazouzi, B. Lestriez, L. Roué and D. Guyomard, Electrochem. Solid-State Lett., 2009, **12**, A215.

73 N. S. Hochgatterer, M. R. Schweiger, S. Koller, P. R. Raimann, T. Wöhrle, C. Wurm and M. Winter, Electrochem. Solid-State Lett., 2008, **11**, A76.

74 S. D. Beattie, D. Larcher, M. Morcrette, B. Simon and J.-M. Tarascon, J. Electrochem. Soc., 2008, **155**, A158.

75 J.-S. Bridel, T. Azaïs, M. Morcrette, J.-M. Tarascon and D. Larcher, J. Electrochem. Soc., 2011, **158**, A750.

76 J.-S. Bridel, T. Azaïs, M. Morcrette, J.-M. Tarascon and D. Larcher, Chem. Mater., 2010, **22**, 1229–1241.

77 U. Maver, A. Žnidaršič and M. Gaberšček, J. Mater. Chem., 2011, **21**, 4071.

78 J. Li, L. Christensen, M. N. Obrovac, K. C. Hewitt and J. R. Dahn, J. Electrochem. Soc., 2008, **155**, A234.

79 N.-S. Choi, K. H. Yew, W.-U. Choi and S.-S. Kim, J. Power Sources, 2008, **177**, 590–594.

80 R. R. Garsuch, D.-B. Le, A. Garsuch, J. Li, S. Wang, A. Farooq and J. R. Dahn, J. Electrochem. Soc., 2008, **155**, A721.

81 B. Lestriez, Comptes Rendus Chim., 2010, **13**, 1341–1350.

82 A. Magasinski, B. Zdyrko, I. Kovalenko, B. Hertzberg, R. Burtovyy, C. F. Huebner, T. F. Fuller, I. Luzinov and G. Yushin, ACS Appl. Mater. Interfaces, 2010, **2**, 3004–10.

83 L. Chen, X. Xie, J. Xie, K. Wang and J. Yang, J. Appl. Electrochem., 2006, **36**, 1099–1104.

84 J. Li, D.-B. Le, P. P. Ferguson and J. R. Dahn, Electrochim. Acta, 2010, **55**, 2991–2995.

85 S. Komaba, N. Yabuuchi, T. Ozeki, Z. Han, K. Shimomura, H. Yui, Y. Katayama and T. Miura, 2012, 1380–1389.

86 B. Koo, H. Kim, Y. Cho, K. T. Lee, N.-S. Choi and J. Cho, Angew. Chemie Int. Ed., 2012, n/a–n/a.

87 I. Kovalenko, B. Zdyrko, A. Magasinski, B. Hertzberg, Z. Milicev, R. Burtovyy, I. Luzinov and G. Yushin, Science, 2011, **334**, 75–9.

88 G. Liu, S. Xun, N. Vukmirovic, X. Song, P. Olalde-Velasco, H. Zheng, V. S. Battaglia, L. Wang and W. Yang, Adv. Mater., 2011, **23**, 4679–83.

89 M. Gu, X. Xiao, G. Liu, S. Thevuthasan and D. R. Baer, 2014, 1–7.

90 H. Wu, G. Yu, L. Pan, N. Liu, M. T. McDowell, Z. Bao and Y. Cui, Nat. Commun., 2013, **4**, 1943.

91 C. Wang, H. Wu, Z. Chen, M. T. McDowell, Y. Cui and Z. Bao, Nat. Chem., 2013, **5**, 1042–8.

92 M. Ling, H. Zhao, X. Xiaoc, F. Shi, M. Wu, J. Qiu, S. Li, X. Song, G. Liu and S. Zhang, J. Mater. Chem. A, 2015, **3**, 2036–2042.

93 S.-J. Park, H. Zhao, G. Ai, C. Wang, X. Song, N. Yuca, V. S. Battaglia, W. Yang and G. Liu, J. Am. Chem. Soc., 2015, 150213162931005.

94 D. Mazouzi, Z. Karkar, C. Reale Hernandez, P. Jimenez Manero, D. Guyomard, L. Roué and B. Lestriez, J. Power Sources, 2015, **280**, 533–549.

95 Y. Qi, H. Guo, L. G. Hector and A. Timmons, J. Electrochem. Soc., 2010, **157**, A558.

96 B. Liang, Y. Liu and Y. Xu, J. Power Sources, 2014, **267**, 469–490.

97 X. Chen, X. Li, D. Mei, J. Feng, M. Y. Hu, J. Hu, M. Engelhard, J. Zheng, W. Xu, J. Xiao, J. Liu and J. G. Zhang, ChemSusChem, 2014, **7**, 549–554.

98 S. Dalavi, P. Guduru and B. L. Lucht, J. Electrochem. Soc., 2012, **159**, A642.

99 Y.-M. Lin, K. C. Klavetter, P. R. Abel, N. C. Davy, J. L. Snider, A. Heller and C. B. Mullins, Chem. Commun. (Camb)., 2012, **48**, 7268–70.

100 A. M. Chockla, T. D. Bogart, C. M. Hessel, K. C. Klavetter, C. B. Mullins and B. A. Korgel, J. Phys. Chem. C, 2012, **116**, 18079–18086.

101 V. Etacheri, O. Haik, Y. Goffer, G. a. Roberts, I. C. Stefan, R. Fasching and D. Aurbach, Langmuir, 2012, **28**, 965–976.

102 M. Gauthier, D. Reyter, D. Mazouzi, P. Moreau, D. Guyomard, B. Lestriez and L. Roué, J. Power Sources, 2014, **256**, 32–36.

103 C. C. Nguyen and B. L. Lucht, J. Electrochem. Soc., 2014, **161**, 1933–1938.

104 B. Zhang, M. Metzger, S. Solchenbach, M. Payne, S. Meini, H. a. Gasteiger, A. Garsuch and B. L. Lucht, J. Phys. Chem. C, 2015, 11338–11348.

105 S. Zhang, J. Power Sources, 2006, **162**, 1379–1394.

106 N.-S. Choi, K. H. Yew, K. Y. Lee, M. Sung, H. Kim and S.-S. Kim, J. Power Sources, 2006, **161**, 1254–1259.

107 L. Chen, K. Wang, X. Xie and J. Xie, J. Power Sources, 2007, **174**, 538–543.

108 G.-B. Han, M.-H. Ryou, K. Y. Cho, Y. M. Lee and J.-K. Park, J. Power Sources, 2010, **195**, 3709–3714.

109 Y.-G. Ryu, S. Lee, S. Mah, D. J. Lee, K. Kwon, S. Hwang and S. Doo, J. Electrochem. Soc., 2008, **155**, A583.

110 S.-W. Song and S.-W. Baek, Electrochem. Solid-State Lett., 2009, **12**, A23.

111 H. Choi, C. C. Nguyen and S.-W. Song, Bull. Korean Chem. Soc., 2010, **31**, 2519–2526.

112 W. Xu, S. S. S. Vegunta and J. C. Flake, J. Power Sources, 2011, **196**, 8583–8589.

113 W.-R. Liu, M.-H. Yang, H.-C. Wu, S. M. Chiao and N.-L. Wu, Electrochem. Solid-State Lett., 2005, **8**, A100.

114 V. L. Chevrier, L. Liu, D. B. Le, J. Lund, B. Molla, K. Reimer, L. J. Krause, L. D. Jensen, E. Figgemeier and K. W. Eberman, J. Electrochem. Soc., 2014, **161**, A783–A791.

115 H. Kim, B. Han, J. Choo and J. Cho, Angew. Chem. Int. Ed. Engl., 2008, **47**, 10151–4.

116 M. Park, M. G. Kim, J. Joo, K. Kim, J. Kim, S. Ahn, Y. Cui and J. Cho, Nano Lett., 2009, **9**, 3844–7.

117 Y. Yao, M. T. McDowell, I. Ryu, H. Wu, N. Liu, L. Hu, W. D. Nix and Y. Cui, Nano Lett., 2011, **11**, 2949–54.

118 N. Liu, H. Wu, M. T. McDowell, Y. Yao, C. Wang and Y. Cui, Nano Lett., 2012, **12**, 3315–21.

119 S. Chen, M. L. Gordin, R. Yi, G. Howlett, H. Sohn and D. Wang, Phys. Chem. Chem. Phys., 2012, **14**, 12741–5.

120 N. Liu, Z. Lu, J. Zhao, M. T. McDowell, H.-W. Lee, W. Zhao and Y. Cui, Nat. Nanotechnol., 2014, **9**, 187–92.

121 G. W. Zhou, H. Li, H. P. Sun, D. P. Yu, Y. Q. Wang, X. J. Huang, L. Q. Chen and Z. Zhang, Appl. Phys. Lett., 1999, **75**, 2447.

122 H. Li, X. Huang, L. Chen, G. Zhou, Z. Zhang, D. Yu, Y. J. Mo and N. Pei, Solid State Ionics, 2000, **135**, 181–191.

123 W. Xu and J. C. Flake, J. Electrochem. Soc., 2010, **157**, A41.

124 K.-Q. Peng, Y.-J. Yan, S.-P. Gao and J. Zhu, Adv. Mater., 2002, **14**, 1164.

125 X.-L. Wang and W.-Q. Han, ACS Appl. Mater. Interfaces, 2010, **2**, 3709–13.

126 M. Ge, J. Rong, X. Fang and C. Zhou, Nano Lett., 2012, **12**, 2318–23.

127 J. D. Holmes, K. P. Johnston, C. R. Doty and B. A. Korgel, Science (80-.)., 2000, **287**, 1471–1473.

128 P. S. Shah, T. Hanrath, K. P. Johnston and B. a. Korgel, ChemInform, 2004, **35**, 9574–9587.

129 H. Y. Tuan, D. C. Lee and B. a. Korgel, Angew. Chemie - Int. Ed., 2006, **45**, 5184–5187.

130 C. K. Chan, R. N. Patel, M. J. O'Connell, B. a. Korgel and Y. Cui, ACS Nano, 2010, **4**, 1443–1450.

131 C. K. C. K. Chan, R. N. R. N. Patel, M. J. O'Connell, B. a. B. a Korgel, Y. Cui, M. J. O'Connell, B. a. B. a Korgel and Y. Cui, ACS Nano, 2010, **4**, 1443–50.

132 T. D. Bogart, D. Oka, X. Lu, M. Gu, C. Wang and B. a Korgel, ACS Nano, 2014, **8**, 915–22.

133 T. D. Bogart, X. Lu, M. Gu, C. Wang and B. a. Korgel, RSC Adv., 2014, **4**, 42022–42028.

134 A. M. Chockla, K. C. Klavetter, C. B. Mullins and B. a. Korgel, Chem. Mater., 2012, **24**, 3738–3745.

Chapter 2: Experimental techniques

2.1 General methods

All chemicals were available within the laboratory, provided by the industrial sponsor or acquired from leading suppliers.

2.1.1 Nanowire material synthesis – conducted by Merck KGaA

Two batches of silicon nanowires produced *via* a supercritical fluid synthesis route were supplied in powder form by the industrial sponsor. The material synthesis procedure was stated by the industrial sponsor and has been recently published [1]. The synthesis procedures are briefly described here.

2.1.1.1 Batch-1 synthesis – trisilane precursor

A reagent solution was prepared inside a glove box by mixing trisilane (Si_3H_8) and gold nanoparticles capped with dodecanethiol in toluene to a concentration of 1.68 M trisilane, the silicon to gold molar ratio was 44:1. The reagent was anaerobically handled because of extreme pyrophoricity of trisilane. The freshly prepared reagent was loaded into a valve system attached to a reactor set up. It was passed by using a precision pump into a cylindrical titanium reactor at a flow rate of 3 ml/min. The reactor cylinder was preheated and maintained at a temperature of 430˚ C and a pressure of 1450 psi (with toluene). The reagent pump was shut off after 2 min of flowing and the reactor was sealed from the rest of the system as it was air cooled. After cooling, the product was dispersed in ethanol and collected *via* centrifugation (8000 rpm, 10 min.). The resulting powder was collected in toluene and kept as a suspension.

2.1.1.2 Batch-2 synthesis – mono-phenylsilane (MPS) precursor

A reagent solution was prepared inside a glove box by mixing MPS together with Au nanoparticles capped with dodecanethiol at a silicon to gold molar ratio of 600:1 and diluted with anhydrous toluene to achieve an MPS concentration of 200 mM. Nanowires were then grown in a preheated sealed titanium reactor at 410 °C and 1200 psi. After cooling, the product was dispersed in ethanol and collected *via* centrifugation (8000 rpm, 10 min.). The resulting powder was collected in toluene and kept as a suspension.

2.1.2 Preparation of silicon nanowire based composite electrode

2.1.2.1 Slurry method utilising poly-acrylic acid as a binder

Poly-acrylic acid (Avg. 100,000 Mw, 35 wt. % in H_2O, Sigma-Aldrich) was added to a PE container and diluted with deionised water. Silicon nanowire material was added to the solution and the mixture was dispersed *via* ultra-sonication. Acetylene black conductive additive was then added to the mixture and dispersed *via* ultra-sonication. The mixture was then stirred for 1

hour and additional solvent may have been added at this stage. The mixture dispersed in solvent was then subjected to ultra-sonication to further disperse the particles. Following ultra-sonication the mixture was subjected to homogenisation using a high speed shear stirrer (IKA), 15000 rpm for 5 minutes. Finally the mixture was heated to 90 °C to remove excess solvent whilst simultaneously stirred. The slurry mixture was then cast onto pre-roughened copper foil (125 µm thick, Temper rolled, >99.99 % purity, Advent Research Materials Ltd.) utilising a K bar hand coater (RK PrintCoat Instruments Ltd.) and dried at ambient temperature. Once dry, test electrodes were produced by punching 1 cm^2 circular disks from the coated foil. The punched electrodes were then further dried under vacuum at 120°C for 12 hours and weighed prior to incorporation into an electrochemical cell.

Composite electrodes containing ball milled (5 hours, 10: 1, ball: powder w/w, set to 20 Hz, Retsch) silicon powder (325 mesh, Sigma-Aldrich) were produced *via* a similar method. Binders were investigated including sodium carboxymethyl cellulose (Avg. 700,000 Mw Sigma Aldrich D.S. 0.9) and sodium alginate (medium viscosity, Sigma-Aldrich). PVDF (Solef®3150, Solvay) was also tested as a binder in composite electrodes utilising ball-milled silicon powder, in this case NMP was used as a solvent and a glass container was used to prepare the slurry mixture.

2.1.2.2 Method development

Accurately assessing the electrochemical properties of composite electrodes is dependent on obtaining an accurate mass measurement. A common method used to calculate composite electrode mass was to punch 1 cm^2 circular metal foil disks, measure the individual mass values and calculate an average mass of a foil disk of with an associated error. The average disk mass is then subtracted from any future punched electrodes to find the mass of the composite electrode layer present and hence the mass of active material can then be calculated. This method is suitable if the mass of the composite electrode is significantly larger than the error in mass measurement for the foil disks. When calculated it was found that the mass of the metal disks could vary by as much as 2 mg. The mass of composite electrodes was calculated to vary between 1.5 and 0.3 mg and so a more accurate method of mass measurement was required to allow for accurate data to be collected.

A new method was devised to improve the accuracy of mass measurement. The obvious solution of simply applying slurry to individually pre-weighed metal disks was found to prevent formation of an even composite electrode layer. To overcome the problem a custom designed jig was produced to hold 1 cm^2 metal disks and to allow for an evenly spread slurry film to be cast over the surface. The method allowed the mass of each individual composite electrode to be determined accurately.

2.1.3 Electrochemical cell construction

Cell design is an important consideration when conducting electrochemical experiments, the materials, size and geometry can all have a significant impact on the results obtained. Cells commonly used in lithium-ion battery research include custom designed cells either made of glass or steel, commercial coin cells or Swagelok cells. It was found that the Swagelok cell design provided the best combination of properties to allow for the collection of accurate, reproducible and comparable data.

2.1.3.1 Swagelok cell design

The Swagelok cell housing, ferrules and connectors used throughout this work were purchased directly from the manufacturer. The cells were manufactured out of PFA polymer. Pistons, springs and current collectors were manufactured from stainless steel by the on-site workshop. **Figure 2-1** displays a diagram of the components used to construct electrochemical cells utilising Swagelok components.

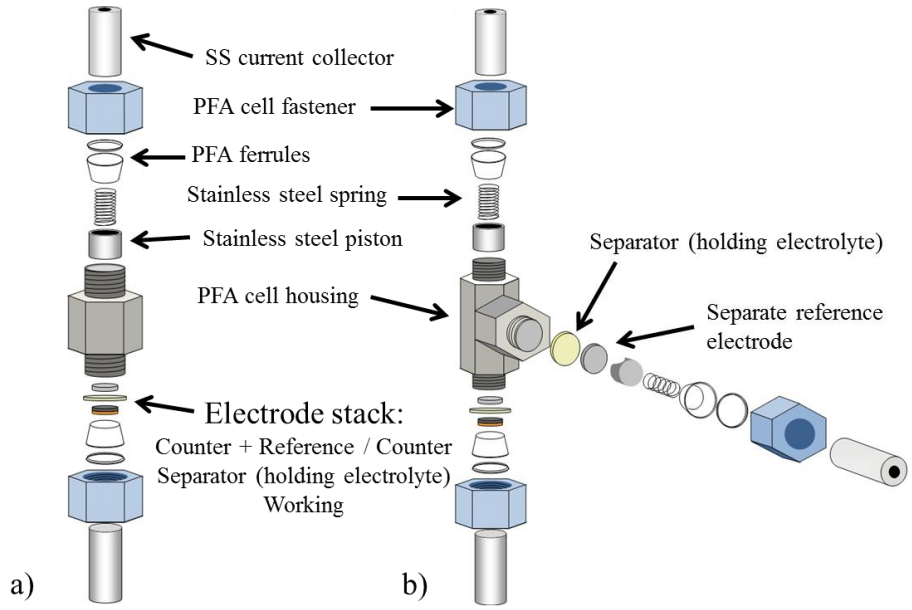

Figure 2-1– Schematic of Swagelok type cells a) two electrode b) three electrode.

The electrode stack consisted of the composite electrode, a polypropylene separator and counter electrode consisting of lithium metal. Silicon based composite electrodes were tested by incorporation into either two or three electrode Swagelok cells. The dried composite electrodes were transferred under vacuum into a glove box containing argon gas (Ultrashield 99.999 %) with oxygen gas and moisture levels below 10 ppm and were incorporated into cells as in **Figure 2-1**.

Celgard 2500 poly-propylene separator material was used to separate electrodes and to hold the electrolyte, 12.5 mm diameter disks were punched from a roll of separator sourced from the

manufacturer. Separator disks were saturated with 3 drops of electrolyte prior to use. The electrolyte used if not otherwise described was a 1 M solution of lithium hexafluorophosphate dissolved in a 1:1 weight ratio of ethylene carbonate and dimethyl carbonate (1 M $LiPF_6$ EC: DMC), commonly referred to as LP30. Lithium metal counter/reference or reference electrodes were produced by punching a 1 cm^2 disk of lithium foil (150 µm Thick) from a roll supplied by Rockwood Lithium GmbH.

2.1.4 Electrochemical testing - Swagelok cell

Constructed cells were transferred out of the glove box and tested and stored inside a temperature controlled chamber set to 25°C. Electrochemical cells were connected to a VMP2 multi-channel potentiostat (Princeton Applied Research) for electrochemical characterisation.

2.2 Gold removal from silicon nanowire material

Gold removal was conducted by following a procedure described by Chockla *et al.*[2]; the procedure consists of two stages, etching any oxide present on the surface of the nanowire material particles followed by the dissolution of gold. An amount of nanowire material was dispersed in chloroform ($CHCl_3$). The dispersion was then transferred to a solution of HF: EtOH: H_2O (45% HF) to etch any oxide layer present at the surface of the nanowire material. The mixture was stirred for 30 minutes. The mixture was then allowed to phase separate. The top aqueous layer was removed and the remaining chloroform layer containing the nanowire material was washed once with ethanol and then twice with water. The chloroform layer was centrifuged at 8000 rpm for 10 minutes. The nanowire material collected was dispersed in fresh chloroform.

The etching of oxide from the surface occurred *via* the general reaction:

$$SiO_{2(S)} + 4HF_{(aq)} \rightarrow SiF_{4(g)} + 2H_2O_{(l)}$$

Equation 2-1

Nanowire material dispersed in chloroform was then added to a solution of aqua regia, prepared utilising 37 % hydrochloric acid (HCl) and 70 % nitric acid (HNO_3) in a ratio of 1:3 (HNO_3 was slowly added to HCl, while care was taken to prevent contact with any organic material). The mixture was stirred for 2 hours, the mixture was then allowed to phase separate, the nanowire material was present within the aqueous top layer, and the chloroform layer was removed. The aqueous layer was centrifuged and the nanowire material was collected and dispersed in fresh de-ionised water, this was repeated twice. The nanowire material was then dispersed and washed in ethanol. The nanowire material was then collected and dried at 70°C under vacuum.

The general reaction of gold with aqua regia can be described by the following [3]:

$$Au_{(S)} + 3{NO_3}^-_{(aq)} + 6{H^+}_{(aq)} \rightarrow 2{Au^{3+}}_{(aq)} + 3NO_{2(g)} + 3H_2O_{(l)}$$

Equation 2-2

$${Au^{3+}}_{(aq)} + 4{Cl^-}_{(aq)} \rightarrow {AuCl_4}^-_{(aq)}$$

Equation 2-3

2.3 Preparation of electrolyte solutions

Electrolyte solutions other than LP30 (BASF) were prepared in-house. Carbonate solvents (FEC, DEC, EMC, DMC) were purchased in the purest form available from Sigma-Aldrich. Solvents were stored in sealed polyethylene containers and dried using molecular sieves within the glove box. Electrolyte solutions were prepared prior to use, lithium hexafluorophosphate ($LiPF_6$, Sigma-Aldrich, battery grade ≥99.99 %) was dissolved in mixtures of carbonate solvents. Once prepared the solutions were stored in polyethylene containers inside the glove box.

2.4 Characterisation methods

2.4.1 Electrochemical characterisation *via* constant current chronopotentiometry

All potential values quoted within this work are measured vs. a lithium reference potential unless otherwise stated.

2.4.1.1 Theory

Constant current chronopotentiometry involves the application of a constant current to an electrode whilst the potential of the electrode is measured versus a reference potential. Galvanostatic cycling is the common name given to a constant current chronopotentiometry technique used within battery research to simulate the charge and discharge of an electrochemical cell or battery.

Galvanostatic cycling of an electrochemical cell consists of a constant current applied to an electrode at which an electro-active species is either oxidised or reduced. The potential of the electrode is measured versus a known reference potential. The reversible redox potential of lithium ($Li \leftrightarrow Li^+ + e^-$, -3.05 V vs. SHE) is a commonly used reference potential in lithium battery research. After either a specified period of time/charge has passed or the voltage of the electrode reaches a specified limit, the current is reversed and reverse reaction occurs. The combination of an oxidation and reduction, or reduction and oxidation process relating to the charge and discharge of an electrode is commonly called an electrochemical cycle. Electrodes are 'cycled' under various conditions to investigate the properties of electrodes and electrochemical systems as a whole. Data is usually reported in the form of E vs. Q. dQ/dE vs. E is also a common method of displaying data; the units of dQ/dE correspond to Farads and usually termed pseudo-capacitance.

2.4.1.2 Method

Galvanostatic cycling of either 2 or 3 electrode cells was conducted utilising a VMP potentiostat (VMP2 Biologic, (Princeton Applied Research)). The potentiostat was used to apply either a positive or negative current to the working electrode of the cell and to monitor the voltage of the electrode with respect to a reference potential. Calculation of the current to be applied to an electrode was conducted in order to cycle the electrode at a specific C-rate. All reported C-rates were calculated based upon the theoretical capacity of the active material. The mass used to calculate the C-rate was that of the nanowire material under examination, nanowire materials were known to contain a proportion of non-active material. The actual applied C-rate was therefore likely to be higher than that calculated as the tested nanowire material were not completely pure silicon.

2.4.2 Electrochemical impedance spectroscopy (EIS)

2.4.2.1 Theory

EIS is used to probe the current response of an electrochemical system to an applied small amplitude AC voltage signal over a range of frequencies. Analysis of the variation in the current response as a function of frequency allows for the investigation of electrochemical processes occurring over various timescales.

The applied small amplitude AC voltage signal can be represented by **Equation 2-4**.

$$E(t) = E_0 \sin(\omega t)$$

Equation 2-4

E (t) = Potential at time t, E_0 = amplitude ω = radial frequency ($2\pi f$), t = time, f = frequency

The response signal can be represented by **Equation 2-5**. Examples of applied and response signals are displayed in **Figure 2-2**.

$$I(t) = I_0 \sin(\omega t + \phi)$$

Equation 2-5

I (t) = current at time t, I_0 = amplitude ω = radial frequency ($2\pi f$), t = time, f = frequency, ϕ = phase

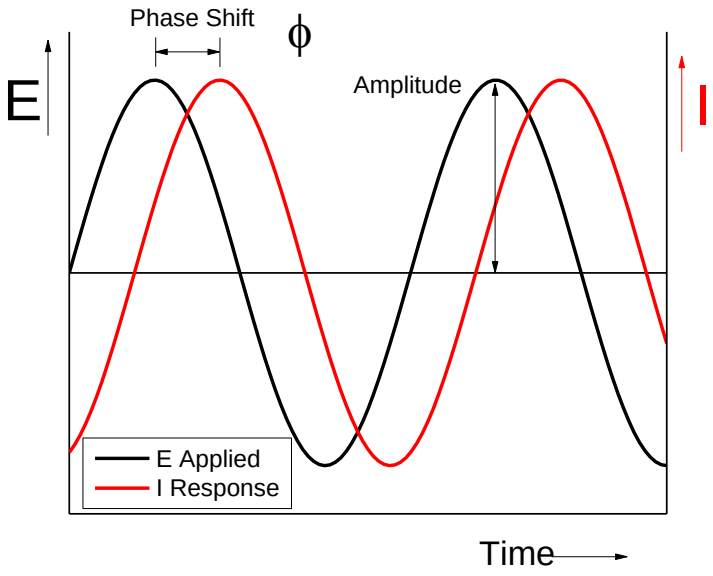

Figure 2-2 – Example of an applied small amplitude AC perturbation signal and response signal

The impedance, Z, is defined by **Equation 2-6**.

$$Z = \frac{E_t}{I_t} = \frac{E_0 \sin(\omega t)}{I_0 \sin(\omega t + \phi)} = Z_0 \frac{\sin(\omega t)}{\sin(\omega t + \phi)}$$

Equation 2-6

Z= impedance, E_t = potential at time t, I_t = current at time t, E_0 = applied signal amplitude, I_0 = response signal amplitude, ω = radial frequency ($2\pi f$), t = time, f = frequency, ϕ = phase, Z_0 = magnitude of impedance

Using Euler's formula, Z can be displayed in complex notation as displayed in **Equation 2-7.**

$$Z = Z_0(cos\phi + j \sin\phi) = Z' + j\,Z''$$

Equation 2-7

Z= impedance, Z_0 = magnitude of impedance, j = √-1, ϕ = phase, Z' =real component of impedance Z'' = Imaginary component of impedance

The impedance can be plotted on a complex plane plot in terms of Z' and Z'' as displayed in **Figure 2-3**.

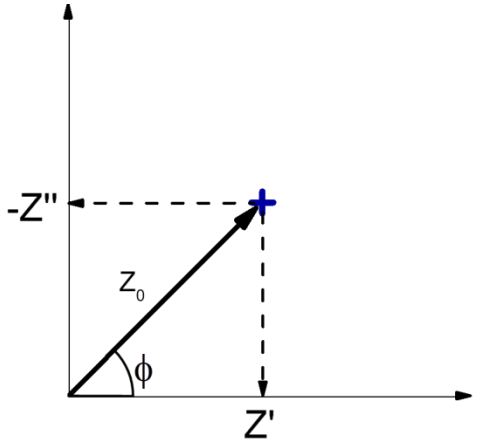

Figure 2-3 – Complex plane plot displaying impedance. Z' = real component, Z'' = imaginary component, Z_0 = magnitude of impedance, ϕ = phase

Impedance spectra are commonly displayed using Nyquist (Z' vs. -Z'') and Bode plots (Z vs. frequency and ϕ vs. frequency). The impedance response of system under investigation is commonly modelled using a simplified equivalent circuit. Equivalent circuits are produced from simple components of known impedance response. The impedance of a resistor corresponds directly to the resistance (**Equation 2-8**).

$$Z_R = R$$

Equation 2-8

Z_R = impedance of a resistor, R = resistance (Ω)

The impedance of a capacitor is purely imaginary and varies as a function of frequency (**Equation 2-9**).

$$Z_C = \frac{1}{j\omega C}$$

Equation 2-9

Z_C = impedance of a capacitor, $j = \sqrt{-1}$, ω = radial frequency ($2\pi f$), C = capacitance (F)

The impedance of an inductor is also purely imaginary and varies as a function of frequency (**Equation 2-10**).

$$Z_I = j\omega L$$

Equation 2-10

Z_I = impedance of an inductor, $j = \sqrt{-1}$, ω = radial frequency ($2\pi f$), L = inductance (H)

For components in series the impedance response is additive. For example a resistor and capacitor in series can be represented by **Equation 2-11**.

$$Z_{RC\ series} = R + \frac{1}{j\omega C}$$

Equation 2-11

$Z_{RC\ Series}$ = impedance of a resistor and capacitor in series, R = resistance (Ω), $j = \sqrt{-1}$, ω = radial frequency ($2\pi f$), C = capacitance (F)

For components in parallel the inverse impedance is additive. The impedance response of a resistor and capacitor in parallel is described by **Equation 2-12**

$$Z_{RC\ parallel} = \frac{R}{1 + j\omega RC}$$

Equation 2-12

$Z_{RC\ Parallel}$ = impedance of a resistor and capacitor in parallel, R = resistance (Ω), $j = \sqrt{-1}$, ω = radial frequency ($2\pi f$), C = capacitance (F)

The Nyquist plot of common circuit elements are displayed in **Figure 2-4**.

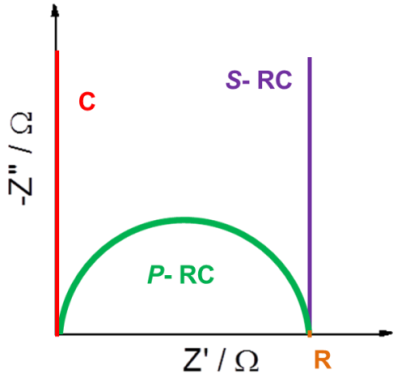

Figure 2-4 – Nyquist plot displaying the impedance response of simple circuit elements. C- capacitor, R- resistor, *P*-RC - parallel resistor capacitor combination, *S*-RC - series resistor capacitor combination. The displayed responses represent the impedance as a function of frequency.

A constant phase element (CPE) provides the response of a non-ideal capacitor and is sometimes used to model impedance spectra in which a capacitor type response does not fit the data. The CPE can be represented by **Equation 2-13** and can be displayed on Nyquist plot as in **Figure 2-5**.

$$Z_{CPE} = \frac{1}{Q(j\omega)^n}$$

Equation 2-13

Z_{CPE} = impedance of a CPE, Q = capacitance (when n =1) ($s^n\ \Omega^{-1}$), $j = \sqrt{-1}$, ω = radial frequency ($2\pi f$), n = varies between 0 and 1 (0 = resistor, 1 = capacitor)

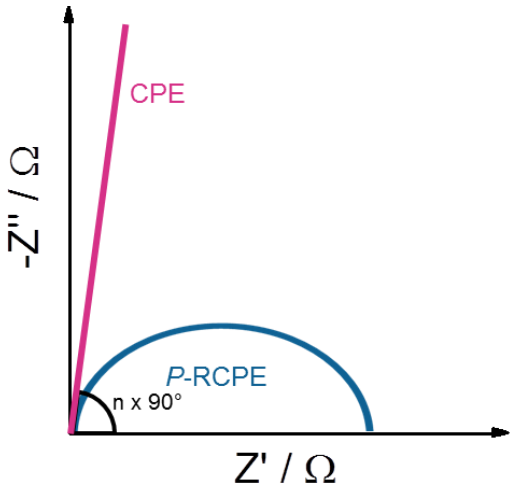

Figure 2-5 – Nyquist plot displaying the impedance response of a CPE (pink) and a parallel combination of a resistor with a CPE (blue) showing a depressed semicircle (P-RCPE).

According to **Equation 2-13**, Q represents a capacitor if n is equal to 1 and a resistor when n equals 0. At intermediate n values CPE cannot be equated to a capacitor; however the capacitance of a parallel combination of a resistor and CPE can be calculated from the R-CPE time constant see **Equation 2-14** to **Equation 2-17**.

$$RQ = \tau^n$$

Equation 2-14

R = Resistance, Q = ($s^n\ \Omega^{-1}$), τ = time constant (s), n = varies between 0 and 1

The time constant of a capacitor in parallel with a resistor is defined by **Equation 2-15**.

$$\tau = RC$$

Equation 2-15

R = Resistance, τ = time constant (s), C = capacitance

Combining **Equation 2-14** and **Equation 2-15** gives **Equation 2-16**.

$$RQ = (RC)^n$$

Equation 2-16

R = Resistance, Q = ($s^n\Omega^{-1}$), C = capacitance, n = varies between 0 and 1

The capacitance of a parallel resistor CPE circuit element can then be calculated using **Equation 2-17**.

$$C = \frac{(RQ)^{\frac{1}{n}}}{R}$$

Equation 2-17

R = Resistance, Q = ($s^n\Omega^{-1}$), C = capacitance, n = varies between 0 and 1

The theory of EIS described was obtained from a number of sources [4,5,6,7].

2.4.2.2 Method

Impedance measurements were obtained using a VMP potentiostat with built in EIS analyser and EC-Lab software (VMP2 Biologic, (Princeton Applied Research)). Three electrode Swagelok type cells were used and cells were allowed to rest for at least 1 hour prior to measurement. A sinusoidal potential perturbation with an amplitude of 10 mV was used to probe the cell, various frequency ranges were used (usually 100 kHz to 0.1 Hz). Measurements were obtained in triplicate and averaged automatically by the software. Ten points were measured per decade. The obtained data was then analysed using Z-View software (Scribner associates Inc.). Data was fitted to simple equivalent circuits.

2.4.3 Electron microscopy

Electron microscopy allows for the imaging of samples at magnification levels greater than traditional visible light microscopes allow. The resolution (directly related to the quality of image achievable at a given magnification) of a microscope is defined by the Raleigh criterion (**Equation 2-18**). The resolution is defined as the smallest distance between two discernible individual points.

$$r = \frac{0.61\lambda}{\mu \sin\beta}$$

Equation 2-18

r = resolution (m), λ = wavelength of radiation (m) , μ = refractive index of the viewing medium, β = semi angle of collection (μ sin β can be approximated to 1 for light microscopes)

Electron microscopes allow the wavelength of the electron to be controlled and reduced far beyond that of photons used within light microscopes (roughly 390 – 700nm). The wavelength of electrons is governed by the de Broglie equation, and is dependent on the momentum of the electron. The wavelength of an electron can be reduced by increasing its momentum, commonly

achieved in electron microscopes with the application of a potential gradient, increasing the kinetic energy of the electron. The wavelength of an electron beam can be related to the accelerating voltage *via* **Equation 2-19**.

$$\lambda = \frac{h}{(2\, m_0\, eV)^{\frac{1}{2}}}$$

Equation 2-19

λ = wavelength (m), h = Planck's constant (6.626 x 10^{-34} N m s), m_0 = rest mass of electron (9.11 x10^{-31} Kg), eV = kinetic energy of electron (electron charge (1.602 x 10^{-19}(C)) x accelerating voltage (V)).

Electron microscopy involves the application of small wavelength, high energy electrons to probe samples at increased magnification. High energy electrons interacting with the sample produce a number of emissions (**Figure 2-6**). The emissions occur from the interaction of high energy electrons with the sample and can be used to provide information about the sample.

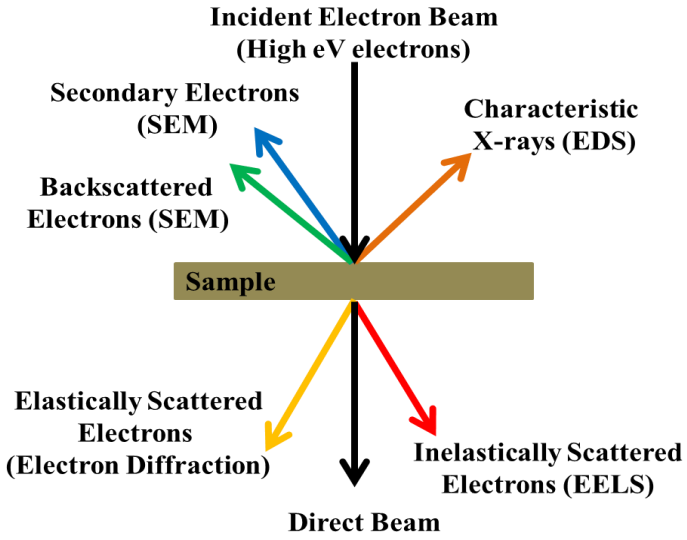

Figure 2-6 – Interaction of a beam of high energy electrons with a sample, common emission types are displayed as coloured arrows. Figure adapted from reference [8].

2.4.3.1 Scanning electron microscopy

2.4.3.1.1 Theory

The scanning electron microscope (displayed in **Figure 2-7a**) consists of an evacuated column through which a beam of a high energy electrons are focused on to and rastered across the surface of a sample. The energy of the electron beam determines the volume of the sample with which it interacts (**Figure 2-7b**). The atomic number of the sample also affects the interaction volume of the sample with the beam of electrons.

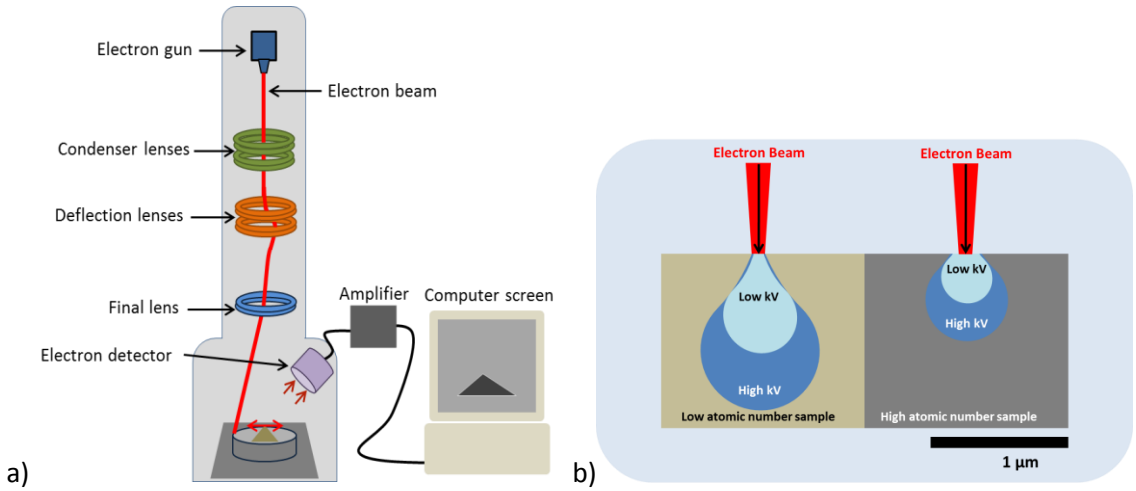

Figure 2-7 – a) Simplified diagram of a scanning electron microscope b) kV dependant interaction volume of electron beam.

Images are produced by the collection of emitted secondary electrons from the surface of the sample. Secondary electrons (SE) are only able to escape from just beneath the surface (a few 100's of nm) of a sample exposed to an electron beam (**Figure 2-8a**). The signal produced by the collection of secondary electrons at a certain location is amplified and combined with data collected over a region of a sample to produce an image.

The structure and composition of the sample can have a large influence on the number of electrons produced, edges and variation in the incident beam angle can allow for additional secondary electrons to be produced, the effect creates contrast in the images produced (**Figure 2-8b**).

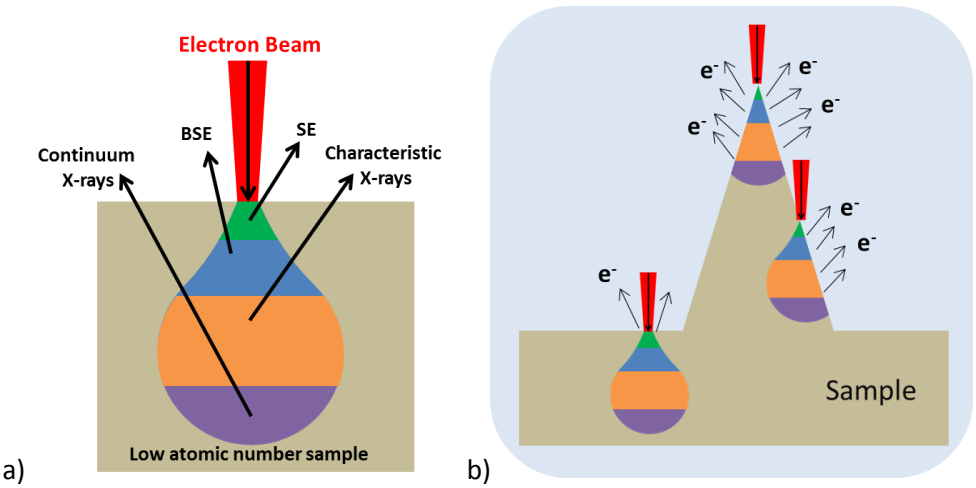

Figure 2-8 – a) Interaction of a high energy electron beam with a sample b) Influence of sample structure on the number and type of emitted electrons and X-ray photons. BSE- backscattered electrons, SE- secondary electrons.

Images can also be produced utilising the emission of backscattered electrons (BSE) from the sample. Backscattered electrons are caused when a high energy electron interacts elastically with the nuclei of an atom within the sample, the probability of the production of back scattered

electrons increases as the atomic number of the nuclei with which the high energy electron interacts increases. The variation in production due to the atomic number of the sample allows for compositional images to be produced in which high atomic number material within the sample will appear brighter than regions containing lower atomic number material.

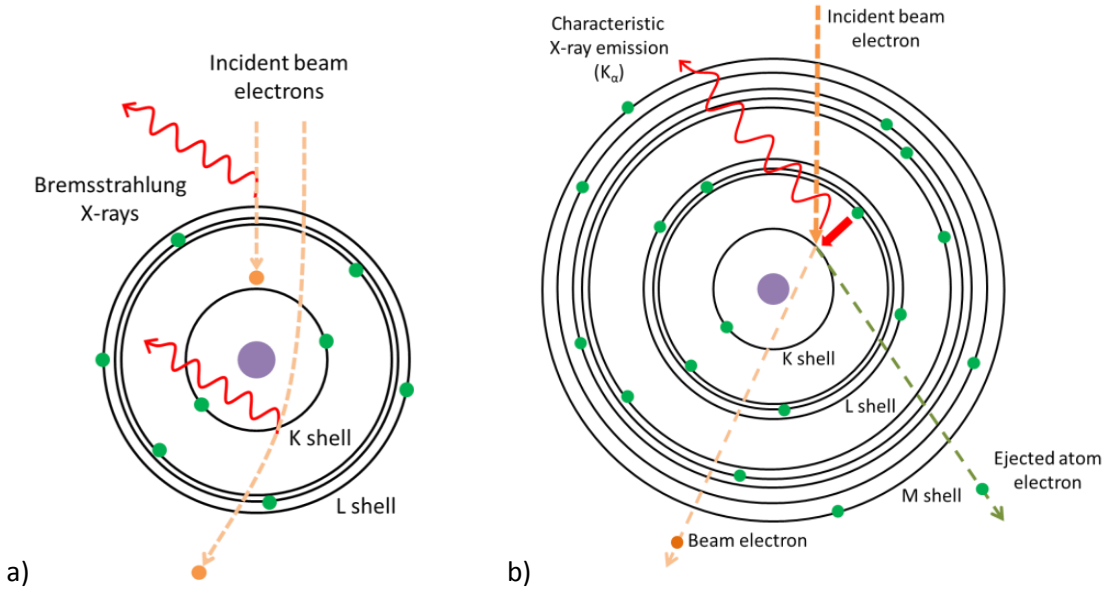

Figure 2-9 – X-ray photon generation mechanisms a) Bremsstrahlung X-ray generation (continuum X-rays), b) Characteristic X-ray generation. [8]**.**

X-rays are produced *via* two main processes which occur when a sample is exposed to a beam of high energy electrons (**Figure 2-9**). Bremsstrahlung X-ray production occurs when high energy electrons experience deceleration or directional change caused by interaction with the nucleus of atoms within a sample. Characteristic X-ray production is caused when a high energy electron interacts with an inner shell electron resulting in the ejection of the electron from the atom. To stabilise the inner shell an electron relaxes from an outer shell and emits a X-ray photon of energy equal to the difference in energy between the energy shells and replaces the emitted electron. The energy of the X-ray photon released is characteristic of the atom from which it was emitted, the measurement of the energy of X-rays produced from a sample allows for the identification of the material from which it was produced. Analysis of the characteristic X-rays produced from a sample allow for the composition of the sample to be determined.

2.4.3.1.2 Method

A JEOL 6500F instrument with an attached EDS detector (Oxford Instruments Inca 300) and JEOL backscatter detector was used to collect images and characterise samples. The sample stage was rotated and tilted during imaging and the probe current and accelerating voltage of the instrument were altered during analysis of the samples. EDS spectra were recorded with an accelerating voltage of greater than double the energy of the characteristic X-ray energy of interest. Samples were prepared *via* a number of methods including bulk powder samples

(greater than 5 microns in thickness to ensure X-ray generation from within the sample), particles of interest suspended on copper TEM grids (utilising a TEM grid sample holder), and composite electrodes (attached to the sample stage *via* conductive carbon tape). JEOL JSM 7800F and JEOL JSM 7100F microscopes equipped with EDS and backscatter detectors were also used.

2.4.3.2 Transmission electron microscopy

2.4.3.2.1 Theory

The transmission electron microscope (TEM) (**Figure 2-10**) differs from the scanning electron microscope (SEM) in that the electrons used to create an image are produced from elastically scattered beam electrons which pass through the sample. The instrument is similar to that of an SEM in that a beam of high energy electrons is directed towards and focused on a sample within an evacuated column.

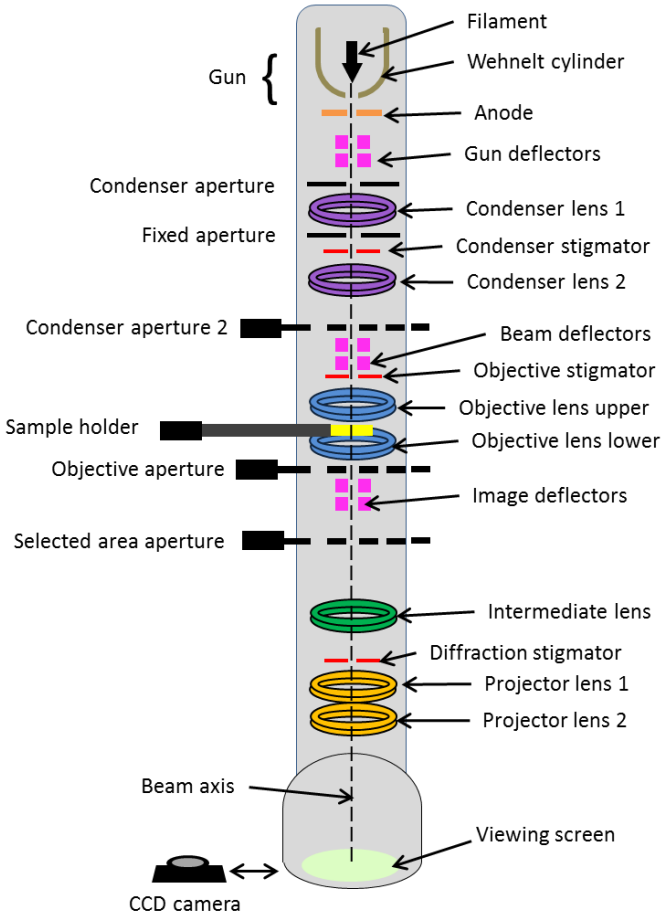

Figure 2-10 – Simplified diagram of a TEM highlighting the major image forming components.

The TEM differs from the SEM in that the TEM contains magnetic lenses which magnify and focus transmitted electrons which have passed through the sample. The beam of electrons used in a TEM is typically over 10 times greater in energy than that found in a SEM, the beam of

electrons is not scanned or rastered across the sample. The higher energy of the electrons used to form the image in a TEM allows for higher resolution images to be produced compared to a SEM. The resolution of images formed within a TEM is around 0.2 nm and is restricted by the focusing ability of the magnetic lenses.

Imaging of samples can be conducted in either bright field or dark field modes. Bright field imaging consists of forms images from the directly transmitted electron beam. Contrast is produced in the image due to differences in the number of transmitted electrons, variation can occur due to differences in thickness or atomic number of the sample. Dark field images are produced using diffracted electrons, images are formed in a similar way to bright field images, although consist only of diffracted electrons. Selection of diffracted beams of electrons produced by the interaction of the incident electron beam with a crystalline material can allow for images to be produced of electrons diffracted from specific crystal planes within the sample. Electron diffraction occurs when the beam of incident electrons interact with the sample and are scattered. The resulting electron diffraction patterns carry the structural information of the crystal from which they originate and are commonly used to observe the crystallinity of samples within the TEM.

Electron energy loss spectroscopy (EELS) is a further common characterisation method associated with TEM instruments. EELS measures the energy of electrons which have lost energy *via* interaction with the sample. The high loss region (>50 eV) of an electron energy loss spectra is used specifically to measure electrons which have lost energy *via* inelastic interactions with the sample. Inner shell ionisation of an atom can be caused by a transfer of energy from a beam electron. The inelastic interaction of a beam electron with the sample results in an energy loss to the beam electron. The energy loss of the beam electron is equal to the ionisation energy of the atom with which it interacted. *Via* analysis of an electron energy loss spectrum the elemental composition of a sample can be determined.

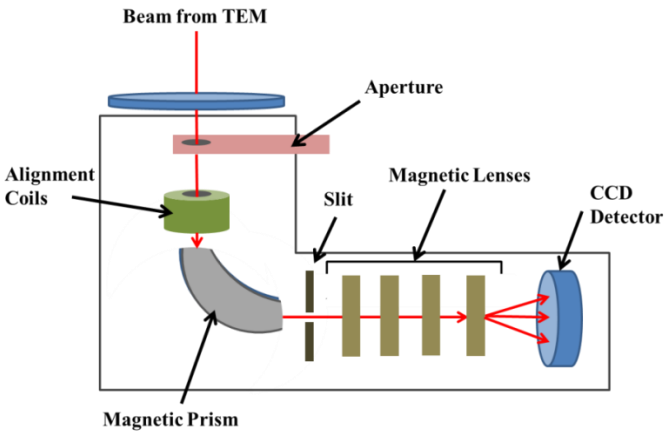

Figure 2-11 – Diagram of a Gatan EEL Spectrometer, the spectrometer is usually attached to a TEM below the viewing screen [8].

The components of an electron energy loss spectrometer are displayed in **Figure 2-11**. The use of a magnetic prism combined with a slit allows for the selection of energy loss electrons of a specific energy. Images can be produced utilising energy loss electrons of a specific energy. The images formed display regions within the sample from which energy loss electrons of the selected specific energy were produced. Images produced *via* this method are called energy filtered (EF) images, or energy filtered transmission electron microscope (EFTEM) images. EFTEM images provide elemental analysis.

2.4.3.2.2 Method

Samples were prepared on copper grids of various mesh size. TEM grids with amorphous carbon and lacey carbon coating layers were also used. Sample TEM grids were prepared *via* dispersion of a powder sample in acetone followed by the application of drops of the dispersion on to a TEM grid. Once dry the process was repeated to obtain a sufficient loading of the sample.

Instruments used include a JEOL 3010 TEM with attached EDS detector (Oxford Instruments Inca 100), Philips Tecnai F20 FEG-STEM with an attached Gatan Image Filter (GIF) and a JEOL 2100 TEM-STEM. Settings were altered to acquire images and characterisation data in various modes.

2.4.4 X-ray diffraction

2.4.4.1 Theory

X-ray diffraction is a technique used primarily to determine the structure of samples. X-rays are reflected *via* interaction with atoms within the sample. When crystalline solids are exposed to X-ray radiation the interaction of X-ray beams with the multiple lattice planes within the crystal gives rise to interference between the reflected waves (**Figure 2-12**). Constructive interference occurs between X-rays when the difference in distance travelled between reflected waves is an integer multiple of the incident wavelength. Interaction of monochromatic X-ray beams with the ordered lattice of crystalline solids results in the constructive interference of reflected X-ray beam at specific incident beam angles. This phenomenon was first described by Bragg [9]. Using Bragg's law, $2d \sin \Theta = n \lambda$, the structure of the diffracting crystal can be determined [10].

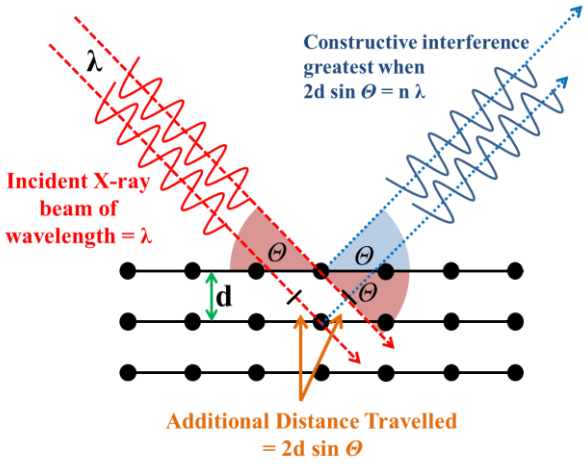

Figure 2-12 – Schematic displaying the principle of X-ray diffraction

Powder X-ray diffraction is a technique commonly utilised to determine the presence and structure of crystalline phases within a powdered sample. Powder X-ray diffraction assumes the random orientation of many particles of material and allows for the collection of the full crystal structure of the material present within the sample without the need to rotate the sample [10].

2.4.4.2 Method

A Bruker D2 Phaser powder X-ray diffractometer with a Copper K_α X-ray source was used to collect X-ray diffraction patterns. Bragg-Brentano geometry was used, 2-theta angle between the X-ray source and detector maintained throughout collection. The collection range was selected between 10 and 80 2-theta degrees. Increments of 0.016 2-theta were used with a step time of between 0.5 and 1 second. Samples were rotated at a rate of 6 rotations per minute. Bruker Eva software was used to interpret collected data. Data was obtained from the inorganic crystal structure database (ICSD) to compare and identify the structure of phases present.

2.4.5 Fourier transformed infrared spectroscopy (FTIR)

2.4.5.1 Theory

FTIR is a common technique used to determine the chemical composition of samples. The principle of the technique is based on the fact that molecules absorb energy at specific wavelengths within the infrared region of the electromagnetic spectrum which correspond to the resonant frequency of molecular vibrations of the molecules within the sample. The frequencies of vibrational modes are determined by the structure of the molecule, specific vibrations modes are dependent on the strength of the bond and the mass of the atoms which vibrate. As a general rule it has been stated that as the strength of the bond increases, the wavelength of the absorption decreases (wave number and energy increase). For a vibrational mode of a molecule to absorb the vibration must correspond to a change in diploe moment.

2.4.5.2 Method

A Perkin-Elmer Spectrometer was used to collect infrared spectra. Samples were prepared *via* KBr palletisation. KBr powder (spectroscopic grade, Sigma-Aldrich) was dried under vacuum at 120 °C for at least 5 hours prior to use. Samples were exposed to ambient conditions and spectra were collected under ambient conditions. Spectra were recorded between 4000-400 cm^{-1} with a resolution of 4 cm^{-1}.

2.5 Chapter references

1 H. Zhou, J. Nanda, S. K. Martha, R. R. Unocic, H. M. Meyer, Y. Sahoo, P. Miskiewicz and T. F. Albrecht, *ACS Appl. Mater. Interfaces*, 2014, **6**, 7607–14.

2 A. M. Chockla, T. D. Bogart, C. M. Hessel, K. C. Klavetter, C. B. Mullins and B. A. Korgel, *J. Phys. Chem. C*, 2012, **116**, 18079–18086.

3 J. Marsden and I. House, *The Chemistry of Gold Extraction*, Society for Mining, Metallurgy, and Exploration, Inc, 2nd edn., 2006.

4 E. Barsoukov and J. R. Macdonald, Eds., *Impedance Spectroscopy: Theory, Experiment, and Applications*, John Wiley & Sons, Inc., 2005.

5 M. E. Orazem and B. Tribollet, *Electrochemical Impedance Spectroscopy*, 2008.

6 A. J. Bard and L. R. Faulkner, *Electrochemical Methods: Fundamentals and Applications*, Wiley, 2nd edn., 2001.

7 M. J. Lacey, UNIVERSITY OF SOUTHAMPTON, 2012.

8 D. B. Williams and C. B. Carter, *Transmission electron microscopy: A textbook for materials science*, 2009.

9 W. H. Bragg and W. L. Bragg, *Proc. R. Soc. A Math. Phys. Eng. Sci.*, 1913, **88**, 428–438.

10 B. Fultz and J. M. Howe, *Transmission Electron Microscopy and Diffractometry of Materials (Third Edition)*, 2007.

Chapter 3: Characterisation of as-received material

3.1 Introduction

This chapter contains two sections. The first section details initial characterisation of the two batches of silicon nanowire material provided by Merck KGaA. Initial electrochemical tests of commercially available binders were conducted (*Appendix 1*), composite electrodes utilising poly-acrylic were found to display the best performance. Further investigation into the use of poly-acrylic acid as a binder was therefore conducted. The second section investigates the possibility of bond formation between poly-acrylic acid and batch-1 material during a drying process.

3.2 Batches of Merck silicon nanowire material

Two samples of batches of silicon nanowire material were provided as brown powders by Merck KGaA. The batches were synthesised *via* a supercritical fluid liquid solid (SFLS) method from different silicon precursors, trisilane (batch-1) and mono-phenylsilane (batch-2) *via* similar procedures to those reported by Korgel *et al.* [1, 2]. Both batches of silicon nanowire material were expected to consist of crystalline silicon nanowires as well as an amount of gold, used as a seed material for nanowire growth. Initial characterisation of the samples was conducted to compare the material to that previously described. An understanding of the morphology was sought so as to gain an understanding of the relationship of the structure to the electrochemical performance.

3.2.1 Batch-1 – trisilane precursor

Batch-1 (1 g, tap density 85 mg cm^{-3}) was supplied and stated to have a high gold content; the molar ratio of silicon to gold used during synthesis was 44:1, equivalent to 16 wt. % gold content. The high gold content was required to obtain nanowire particle morphology when trisilane was used as the precursor. A powder X-ray diffraction measurement was conducted to confirm the crystallinity of the sample and to observe the possible presence of other crystalline phases in the sample. The diffraction pattern shown in **Figure 3-1** clearly shows the presence of silicon and gold as the only crystalline phases. The surface area of the sample was measured to be 30 $m^2 g^{-1}$ *via* the BET method.

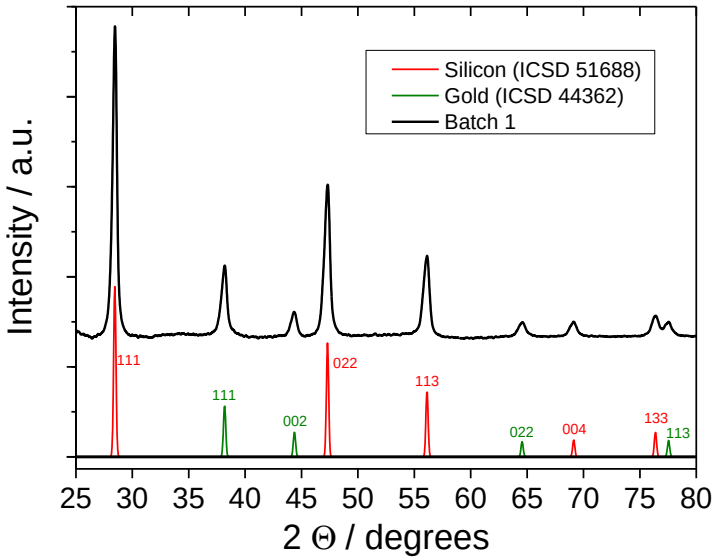

Figure 3-1 – X-ray diffractiogram of batch-1 silicon nanowire material, data from the ICSD data base was matched to the measured data, batch-1 was found to contain a mixture of crystalline silicon and gold phases.

Scanning electron microscope (SEM) imaging was conducted to observe the morphology of the material. **Figure 3-2a and b** displays images of batch-1 material at various magnifications, the material was found to display a highly complex morphology consisting of various particle types

in addition to classical nanowire type particles. Although some particles were essentially straight as expected, the vast majority were twisted, with many particles displaying frequent changes in growth direction. Non-nanowire type particles of material were also observed, such as large (400 nm) spherical particles (blue arrow, Figure 3-2**a**). The spherical particles were assumed to be particles of amorphous silicon, previously reported to form during the synthesis of silicon nanowires from a trisilane precursor [2].

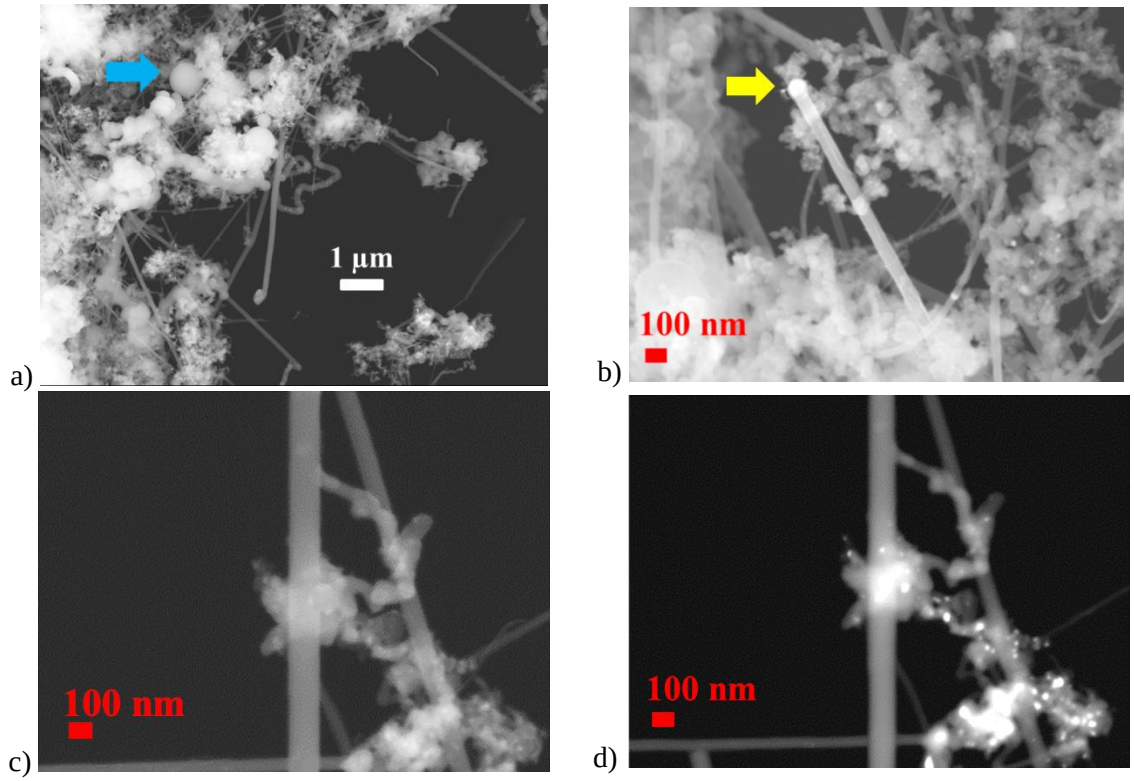

Figure 3-2 – a, b) low, high magnification secondary electron imaging, of as-received silicon nanowires provided by the industrial sponsor. c, d) Region of sample containing twisted particles imaged using secondary electrons (c) and backscattered electrons d).

Regions containing high concentrations of gold were observed in the SEM images as brighter areas at the end of nanowires (highlighted with an arrow in **Figure 3-2b**). The brightness of these regions in the secondary electron images is caused by the contribution of backscattered electrons to the measured signal. Backscattered electron images showed that the twisted regions (**Figure 3-2d**) contained discrete regions of gold distributed along the length of the particles. The high density of gold observed in the twisted regions suggests that the high gold concentration in these particles distorted nanowire growth

Higher magnification imaging of the sample was conducted *via* transmission electron microscopy (TEM) (**Figure 3-3**). The sample was observed to contain both straight (blue arrows) and twisted nanowire particles (yellow arrows). A relatively large distribution in silicon nanowire particle diameter was observed, the majority of particles were less than 100 nm in diameter. Particles of gold previously observed in backscattered SEM images in **Figure 3-2** were

also observed in TEM images, high molecular weight material distinguishable by reduced signal, specifically in **Figure 3-3b (red arrow) and d**.

A thin amorphous layer (<5 nm) was observed to be present on the surface of the particles (**Figure 3-3c, red arrow**). A similar thin layer present on the surface of silicon nanoparticles has been reported to be an oxide layer [1]. An EDS spectrum (**Figure 3-3c (inset))** obtained from the region displayed the presence oxygen which suggested the observed amorphous layer was an oxide layer. Copper and carbon were expected to be present in the spectrum due to the use of a lacey carbon copper TEM grid to mount the sample. Electron diffraction measurements obtained from a region of twisted type particles suggested that the twisted particles were crystalline (**Figure 3-3d**).

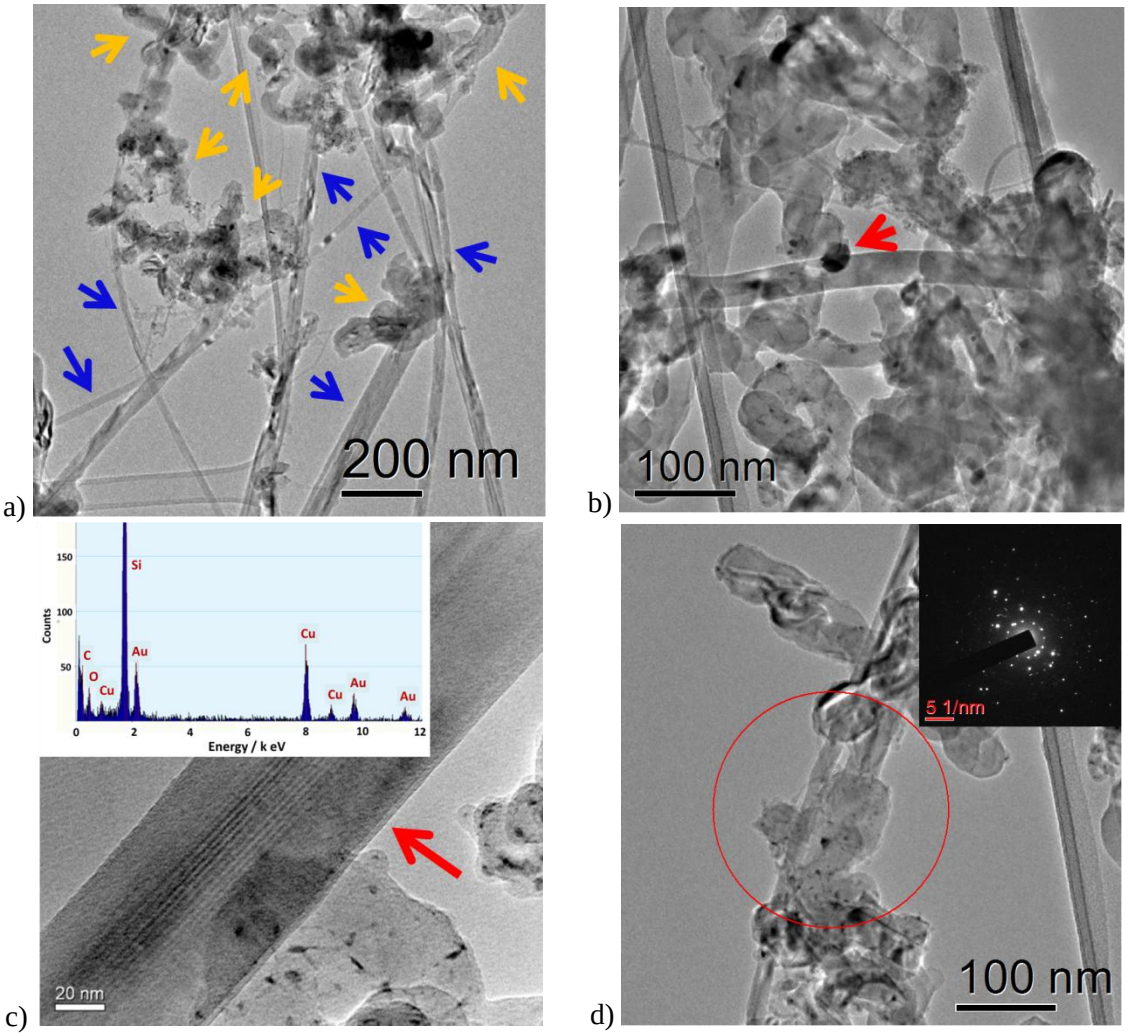

Figure 3-3 – Bright-field (BF) TEM images of as-received batch-1 material. a) straight nanowire particles (blue arrows), and bent nanowire particles (yellow arrows) b) Twisted nanowire particles and a gold seed crystal (red arrow) c) higher magnification image displaying the surface of both twisted and straight nanowire particles an amorphous surface layer was observed (red arrow), Inset EDS spectrum acquired from the sample. d) BF image of region containing both straight and twisted particles. Inset electron diffraction pattern which confirmed crystallinity of both nanowire particle types.

An estimate of the average diameter of the nanowires can be made from the BET specific surface area measurement previously made. Assuming most of the surface area measured was due to nanowires, the diameter can be estimated from **Equation 3-1**:

$$Specific\ surface\ area\ (SSA) = \frac{2\,\pi\,r\,l}{\pi\,r^2\,l\,\rho}$$

Equation 3-1

Therefore,

$$r = \frac{2}{SSA\,\rho}$$

Equation 3-2

SSA = specific surface area ($m^2\ g^{-1}$) ρ = density ($g\ cm^{-3}$), r = nanowire radius, l= nanowire length

Using **Equation 3-2** and substituting a surface area of 30 $m^2\ g^{-1}$ and a density of 2.33 $g\ cm^{-3}$ (density of pure silicon), the diameter of the nanowire particles was calculated to equal ~ 60 nm. The estimation is consistent with the diameter of particles observed by microscopy, and therefore it may be concluded that the proportion of silicon nanowire type particles within the sample is relatively high and accounts for most of the measured surface area. An error due to the gold content of the sample should be noted, the overall influence of gold would be an underestimate of the surface area per gram of silicon nanowire material, resulting in an overestimate of the diameter.

Nanowire material produced using trisilane precursors and gold seed crystals has previously been reported to contain nanowire particles with a growth direction of predominantly <110> with a low ratio of <111> and <112> growth directions also present, twin defects and stacking faults were also reported [1].The morphology of batch-1 generally corresponded to previous reports, although a large proportion of kinked and twisted nanowire particles were present. Similar highly kinked nanowire particles have recently been reported for germanium nanowire samples synthesised *via* a solution route, the cause of structure variation was suggested to be due to temperature variations during growth which affected stacking fault concentration which can give rise to various degrees of kinking [3].

3.2.2 Batch-2 – mono-phenylsilane (MPS) precursor

Batch-2 (~200 mg) was supplied, electron microscopy revealed a material with a similar morphology to that observed in batch-1 (**Figure 3-4**). BET surface measurements were not conducted due to a lack of material. The majority of particles were observed to be long (> 5 μm) straight nanowire type particles with a gold seed crystal at one end. A small proportion of the nanowire particles displayed changes in growth direction. A relatively high concentration of non-nanowire type material was observed throughout the sample, highlighted in **Figure 3-4a** by yellow arrows. Gold seed crystals were observed as bright regions at the end of the silicon nanowire particles (**Figure 3-4b**).

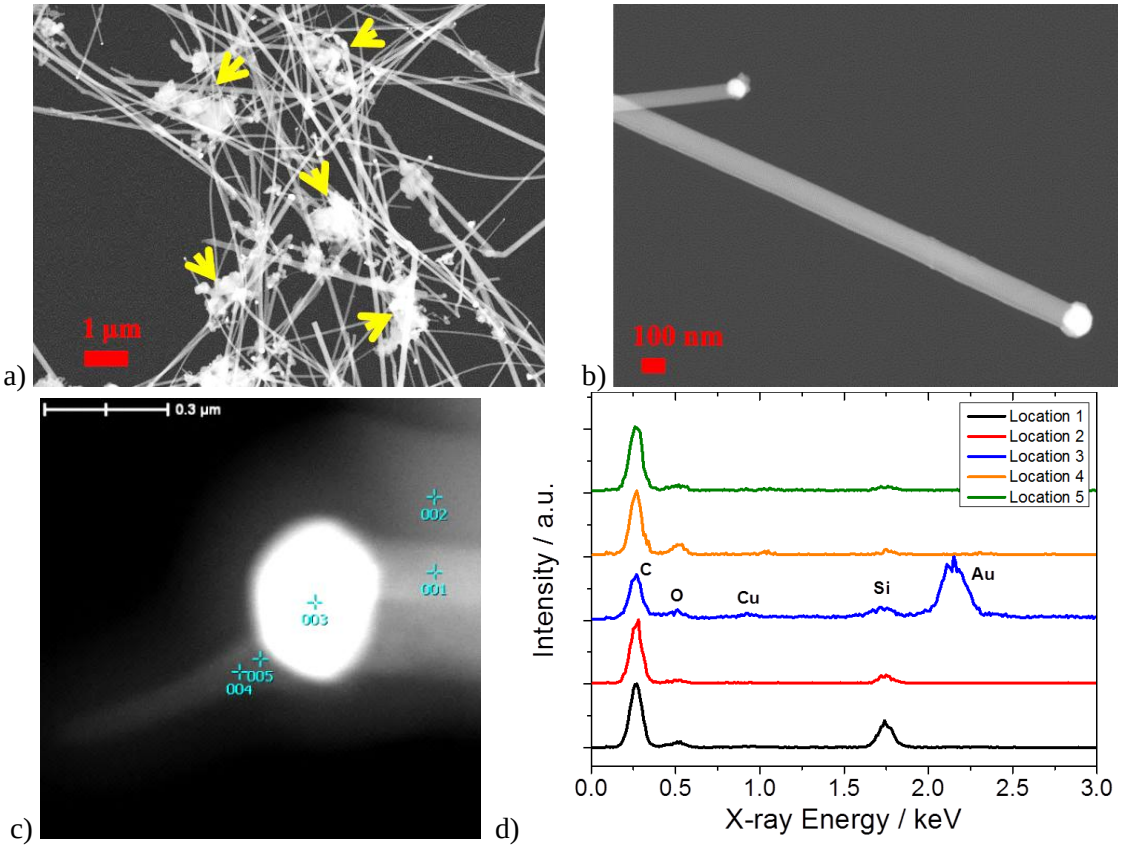

Figure 3-4 – a,b,c) SEM images of batch-2 silicon nanowire material at various magnifications, orange arrows highlight non-nanowire material in image a), d) EDS spectra aquired at 10kV corresponding to locations highlighted in c)

EDS analysis of the particles, **Figure 3-4c and d**, also confirmed that the seed crystals contained gold. The synthesis process utilising MPS has been reported to result in the formation of an amorphous organic poly-phenylsilane shell around the silicon [4]. The amorphous organic shell may be the source of the significant carbon signal observed in **Figure 3-4d**. Copper was present in the spectrum due to the use of a copper grid to mount the sample. An EDS line scan across another nanowire particle (**Figure 3-5**) did not display a large carbon signal which suggested that precursor decomposition products were not present on the surface of every particle.

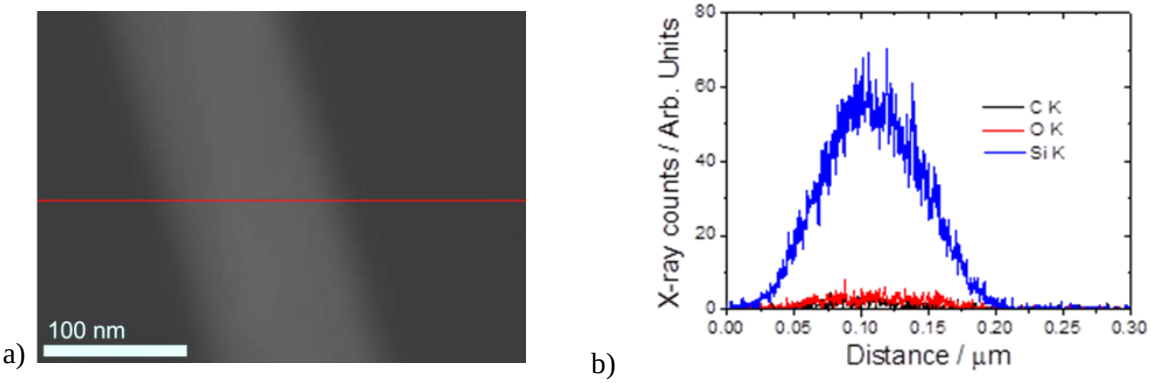

Figure 3-5 –EDS line scan across a silicon nanowire a) image of nanowire with line scan position highlighted in red b) EDS results acquired at an accelerating voltage of 10kV.

TEM analysis of the batch-2 sample was conducted (**Figure 3-6**). Particles were observed to display a distribution of diameters. Non-nanowire material, highlighted by orange arrows in **Figure 3-6a**, was observed throughout the sample. An electron diffraction pattern obtained from the imaged region in **Figure 3-6a**, confirmed the crystallinity of the nanowire particles. A ~5 nm thick amorphous layer was observed to be present at the surface of a particle displayed in **Figure 3-6c**. High densities of stacking faults were observed within the nanowire particle, highlighted by green arrows in **Figure 3-6c**. Stacking faults are commonly reported to occur at (111) planes in silicon nanowires and thin films. Stacking faults running parallel to the growth direction of nanowire particles have been reported in particles with growth directions of <110> and <112> [4b,c].

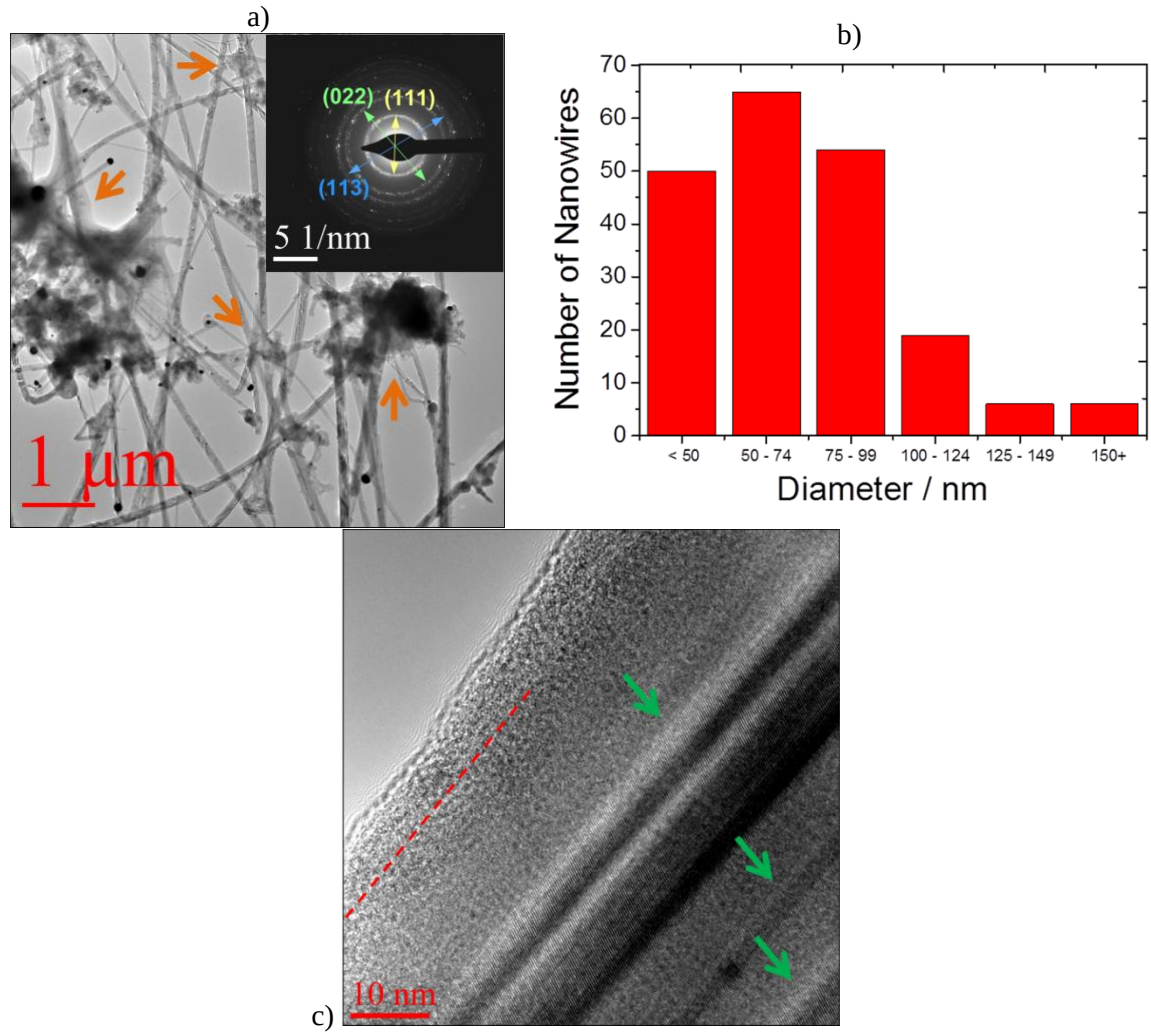

Figure 3-6 – Bright field TEM images a) Image displaying as-received nanowire material non nanowire material is highlighted with orange arrows, a selected area diffraction pattern (SAED) pattern is inset. b) Measured diameter distribution of nanowire particles. c) high magnification image highlighting the amorphous surface layer (red dashed line) and the presence defects within the nanowire particles(green arrows).

The chemical composition of a batch-2 nanowire particle was investigated *via* Energy Filtered TEM (EFTEM) imaging. During imaging growth a bulge of material occurred (**Figure 3-7**).

EFTEM images of the particle were produced at loss energies corresponding to carbon (K-edge), silicon ($L_{2,3}$-edge) and oxygen (K-edge). The contamination layer was found to consist mainly of carbon and oxygen. The source of the carbon signal is suggested to the poly-phenylsilane shell surrounding the nanowires which is present as a breakdown product of the silicon precursor MPS. The shell material appeared to have been melted by the beam and drawn together by surface tension.

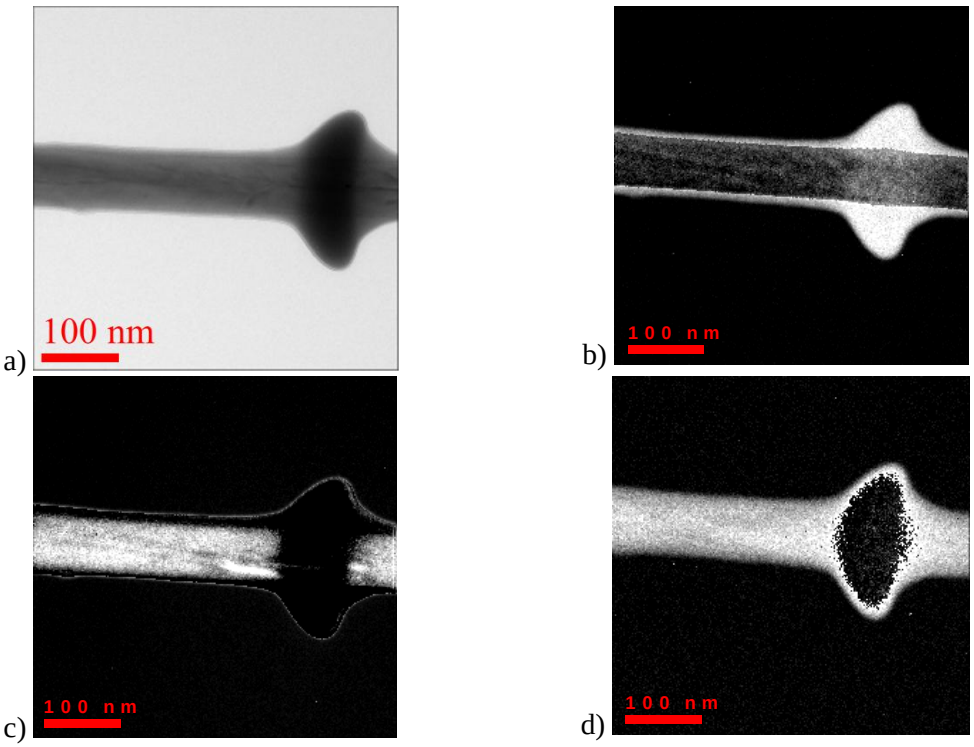

Figure 3-7 – Bright Field and Energy Filtered TEM images of a batch-2 nanowire particle with a bulged area of contamination. a) Bright field image. b) Image formed using signal energy of 304 eV with a filter slit width of 30eV corresponding to the C – K edge. c) Image formed using signal energy of 109 eV with a filter slit width of 20 eV corresponding to the Si –$L_{2,3}$ edge. d) Image formed using signal energy of 542 eV with a filter slit width of 20 eV corresponding to the O – K edge.

The morphology and composition of the batch-2 silicon nanowire material corresponded well with previous reports [2]. Nanowire growth directions of predominantly <111>, with a low ratio of <110> and <112> have been reported for nanowires synthesised utilising MPS as a silicon precursor [2].

3.3 Interfacial chemistry of batch-1 material and poly-acrylic acid binder

3.3.1 Introduction

An understanding of the interaction of active materials with the polymer binder is essential to allow for the electrochemical optimisation of composite electrodes, particularly in the case of binder materials which contain functional groups. The interaction of binder materials with the surface of large volume change materials such as silicon has been reported to play a significant role. For example, covalent bond formation between the oxidised surface of silicon and the carboxylic functional groups of CMC based binders have been reported to significantly influence the electrochemical performance [5]. Silicon nanowires provide a large specific surface area, so that the interface with the binder is present in large concentration, giving large signals in IR and other analysis techniques, so this section was devoted to producing high quality analyses of the interface between silicon nanowires and the binder of choice, poly-acrylic acid (PAA).

PAA consists of a simple saturated carbon backbone with a carboxylic acid functional group present on every second carbon. PAA was recently reported to be an excellent binder for silicon based composite electrodes [6]. Its excellent performance as a binder has been attributed to a low swelling ratio in carbonate based solvents which allows for the retention of the structural integrity of the electrode throughout cycling. It has also been suggested to form an artificial solid electrolyte interface (SEI) layer allowing for the transport of lithium ions through a polymer layer at the surface of active particles [7]. The binder may also act as a solvent-impermeable barrier to protecting the reactive surface of lithiated silicon from the electrolyte.

3.3.2 Chemical changes during drying of PAA

Initially, samples of pure PAA, prepared from an aqueous 35 wt. % solution of PAA (pH of 2.3) *via* drying at either room temperature (RT) or at 120 °C under vacuum (HT), were analysed *via* IR spectroscopy (Figure 3-8).

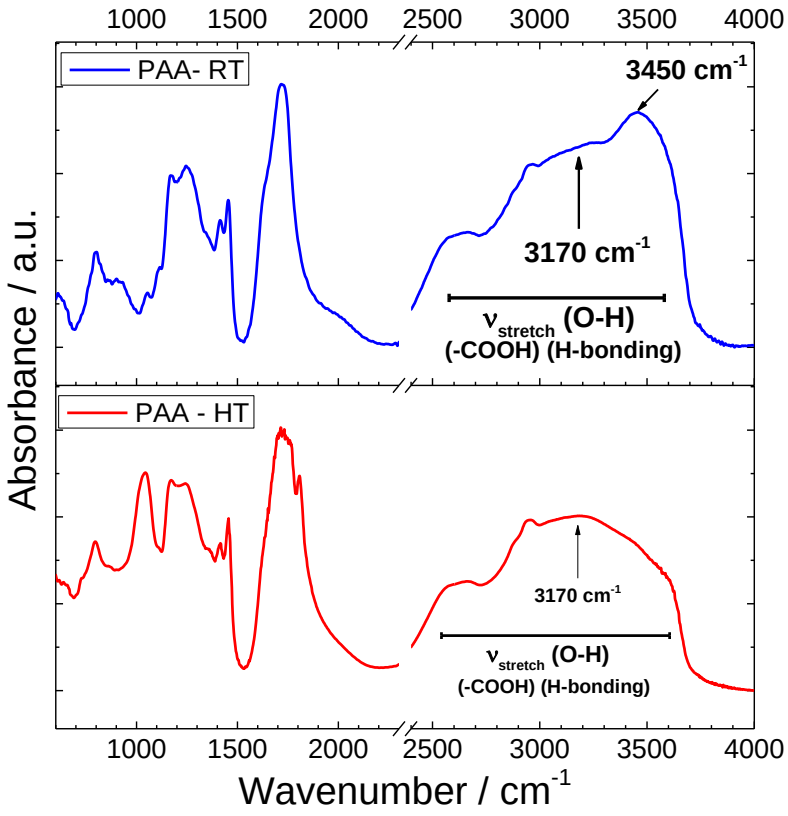

Figure 3-8 – FTIR spectra obtained of poly-acrylic acid dried at room temperature (blue trace - RT) and dried under vacuum at 120 °C (red trace – HT). Spectra were baseline corrected and normalised.

The spectra recorded for a sample of PAA dried at room temperature (blue trace) (**Figure 3-8** and **Figure 3-9**) displayed four major groups of peaks found around 1200 cm^{-1}, 1400 cm^{-1}, 1700 cm^{-1} and a broad peak from 2500-3700 cm^{-1}, the peaks are characteristic of PAA and compare favourably with reports by Dong *et al.* [8], Arndt *et al.*[9] and Kirwan *et al.*[10]. The peaks around 1200 cm^{-1} can be assigned to carboxylic -C-O bond stretching. The peak at 1454 cm^{-1} can be assigned to the scissoring vibrations of $-CH_2$. The broad peak at around 1700 cm^{-1} can be assigned to the carboxylic -C=O bond. The broad nature of the peak has been reported to be due to considerable variation in hydrogen bonding interactions including the formation of dimers [2]. Finally, the large broad peak between 2500 and 3700 cm^{-1} can be assigned to the carboxylic -O-H group. Peaks found at around 2900 cm^{-1} can be assigned to stretching vibrations of -C-H.

Differences between the samples were observed, at higher wavenumber the broad peak centred around 3170 cm^{-1} was observed to be less intense and a peak at around 3450 cm^{-1} was not present in the sample dried at 120 °C under vacuum (**Figure 3-8**). The difference is consistent with the loss of adsorbed water *via* evaporation and the loss of –COOH functionality *via* a condensation reaction.

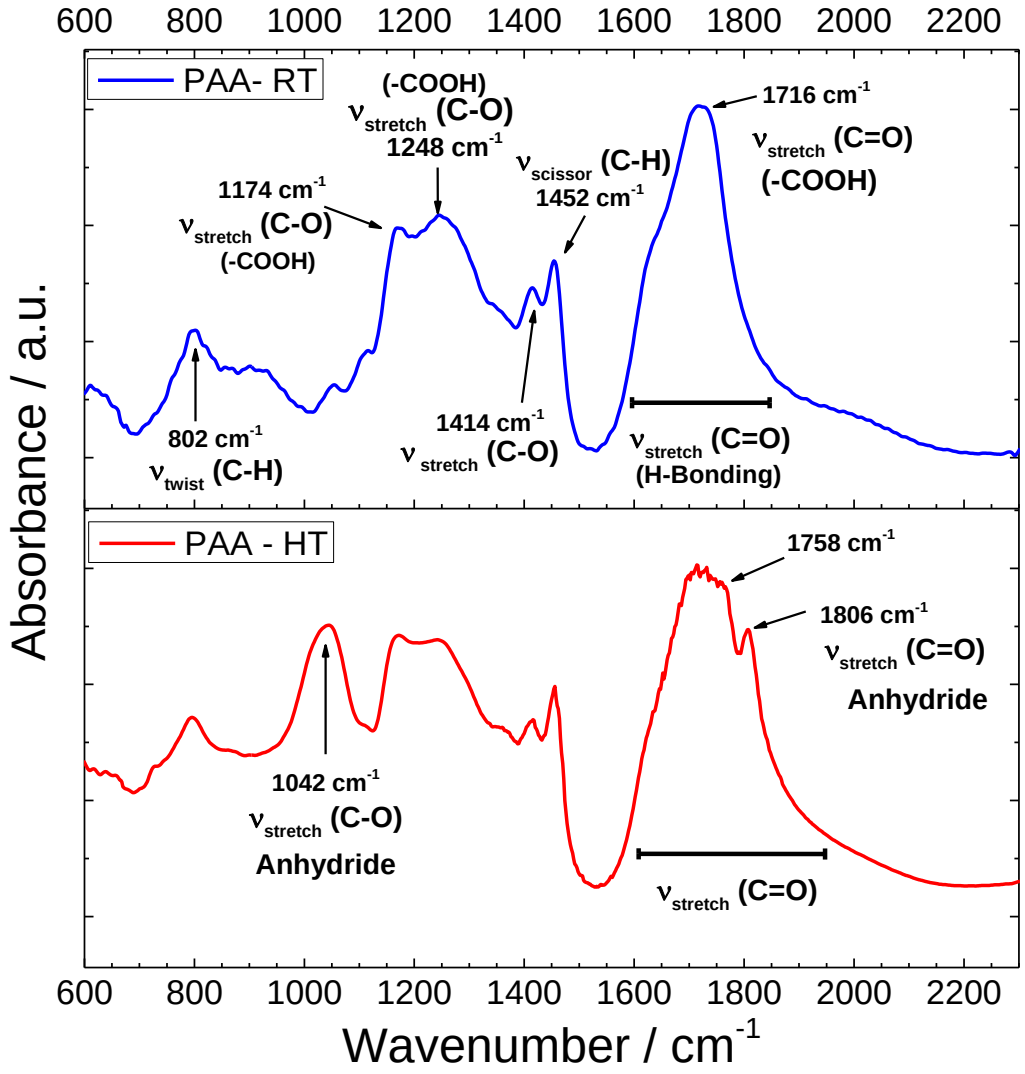

Figure 3-9 – FTIR Spectra obtained of poly-acrylic acid dried at room temperature and dried under vacuum at 120 °C (range displayed 600 – 2300cm^{-1})

Differences at lower wavenumber were also observed (**Figure 3-9**). The spectrum of the sample dried at 120 °C under vacuum shows peaks characteristic of anhydride functionality: C=O stretches at 1806 cm^{-1} and 1758 cm^{-1} and a C-O stretch at 1042 cm^{-1}, suggesting condensation reactions between of a proportion of the carboxylic acid functional groups occurred. Condensation and anhydride formation may result in a proportion of crosslinking between the polymer chains [9].

3.3.3 Chemical changes during drying of PAA + batch-1

The influence of the presence of batch-1 silicon nanowire material on the drying process of PAA was investigated to understand the functionality of poly-acrylic acid expected to be present within a composite electrode utilising PAA as a binder.

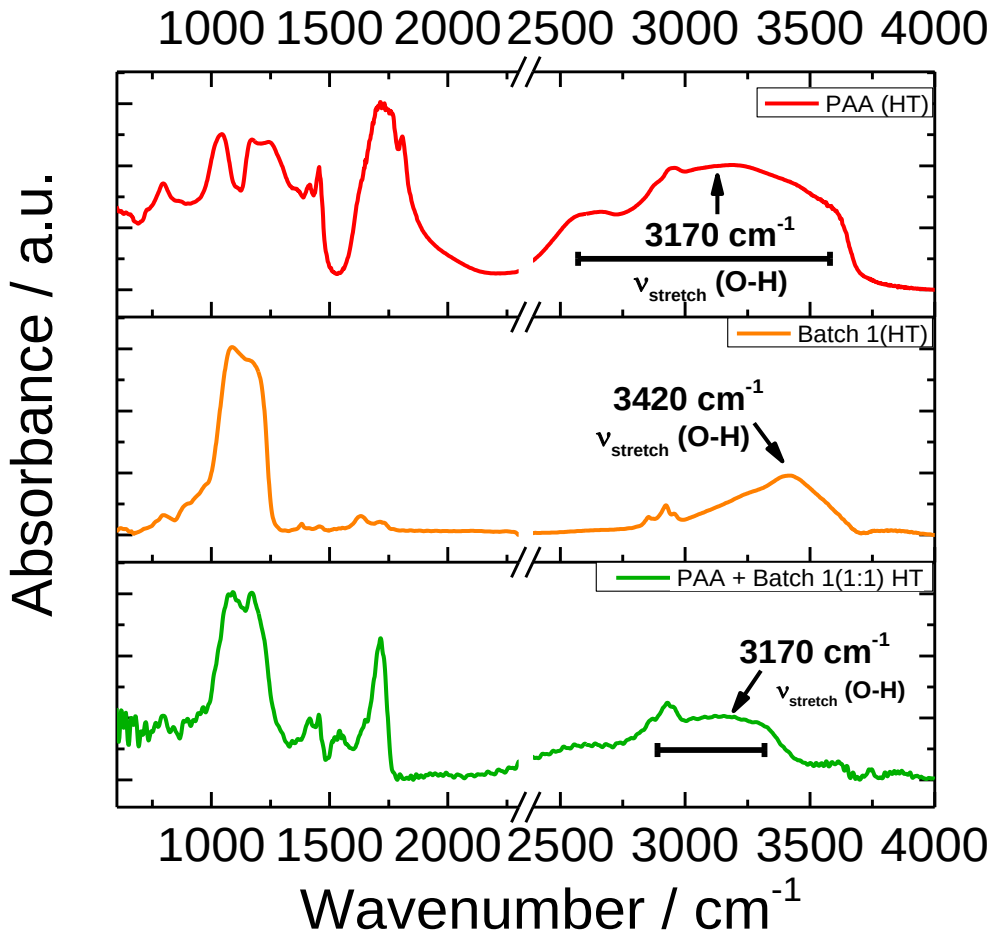

Figure 3-10 – FTIR spectra of aqueous processed PAA, dried at 120°C under vacuum (red), batch-1 silicon nanowire material dried at 120°C under vacuum (orange) and an aqueous processed mixture of poly-acrylic acid and batch-1 silicon nanowire material 1:1 w/w, vacuum dried at 120°C for 16 hours (green).

The IR spectrum recorded for batch-1 silicon nanowire material (orange trace, **Figure 3-10**) is consistent with one obtained from silicon nanoparticles by Bywalez *et al.* [11]. A large Si-O stretch band around 1100 cm^{-1} corresponds to the surface oxide layer previously observed *via* TEM (**Figure 3-3c**). The peak O-H stretch centred around 3420 cm^{-1} is attributed to adsorbed atmospheric H_2O.

Notably *via* comparison of the spectra in Figure 3-10, the spectrum of batch-1 material mixed with PAA and dried at 120 °C under vacuum displayed a significantly less intense and narrower peak centred around 3170 cm^{-1}, suggesting a significant loss of -OH type functionality and hydrogen bonding.

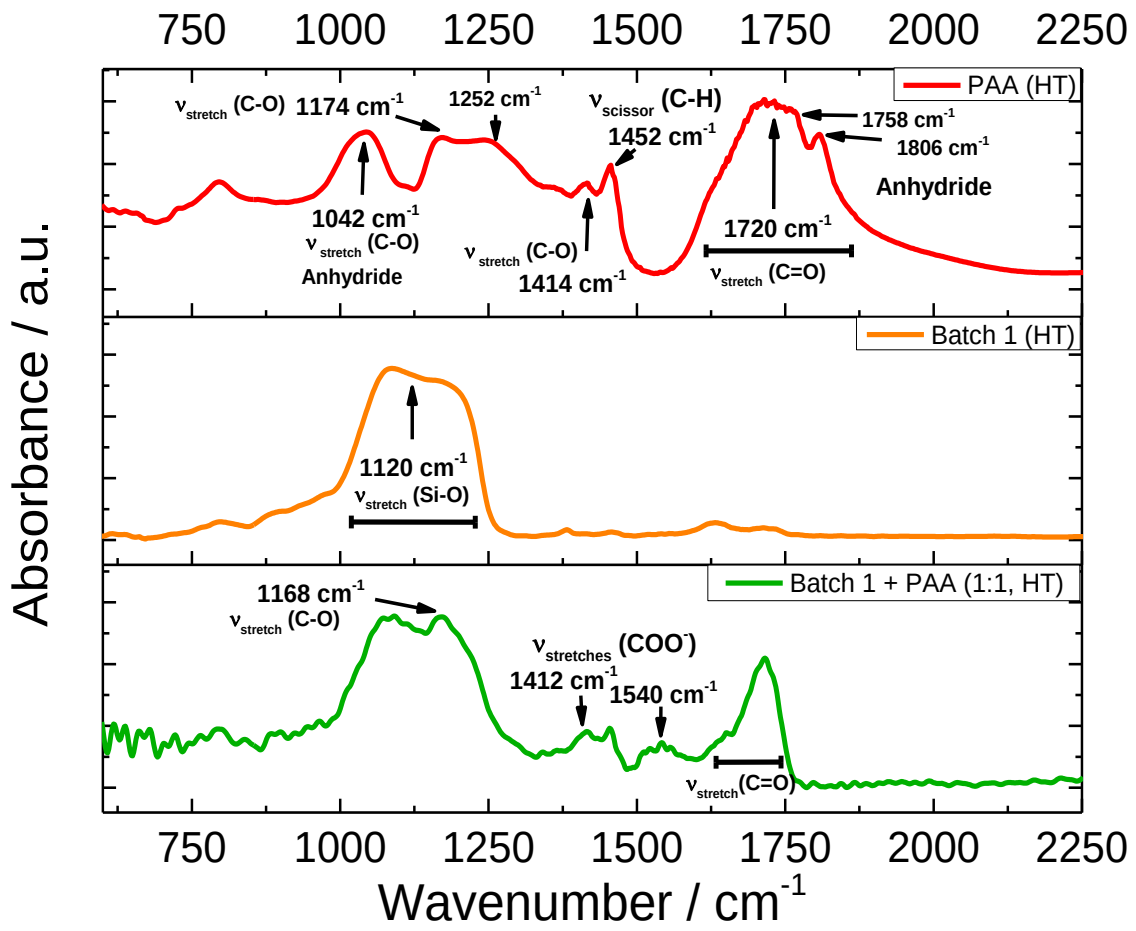

Figure 3-11 – Low wavenumber region of FTIR spectra obtained for aqueous processed PAA dried at 120°C under vacuum (red), batch-1 silicon nanowire material dried at 120°C under vacuum (orange) and an aqueous processed mixture of poly-acrylic acid and batch-1 silicon nanowire material 1:1 w/w vacuum dried at 120°C for 16 hours (green).

Further differences were observed at lower wavenumber in **Figure 3-11** where anhydride peaks (1042 cm^{-1}, 1758 cm^{-1} and 1806 cm^{-1}) previously identified within dried PAA were notably absent in the dried PAA + batch-1 material. Loss of the peak at 1252 cm^{-1} (**Figure 3-11)** and reduction of the –OH peak at 3170 cm^{-1} (**Figure 3-10)** suggest loss of the –COOH functionality, formation of a strong peak at 1168 cm^{-1} (**Figure 3-11**, green trace) was suggested to correspond to a C-O stretching vibration, as similar to the peak observed by Ardnt *et al.* at 1161 cm^{-1} during ester formation [9].

Further, a new peak was observed at ~ 1540 cm^{-1}, and the intensity of the peak at 1412 cm^{-1} increased relative to the peak at 1454 cm^{-1} (–CH_2 scissoring), displayed more clearly in the expanded spectrum in **Figure 3.12**. The peaks may be assigned to the symmetric and asymmetric stretching bands of –COO^- type functionality as previously reported by Kirwan *et al.* [10]. Via utilisation of the binding rules proposed by Deacon and Phillips [11b], peak separation data of the asymmetric and symmetric –COO^- bands associated with PAA at pH 13 (deprotonated, sodium

salt) provided by Kirwan et al.[10], $\Delta \upsilon = 154$ cm^{-1}, and the calculated peak separation observed in this work, $\Delta \upsilon = 128$ cm^{-1} the bonding associated with the peaks is suggested to be bidentate chelating interaction. Similar interaction behaviour was also observed for ball-milled silicon powder mixed with PAA (120 °C, vacuum) (*Appendix 2*).

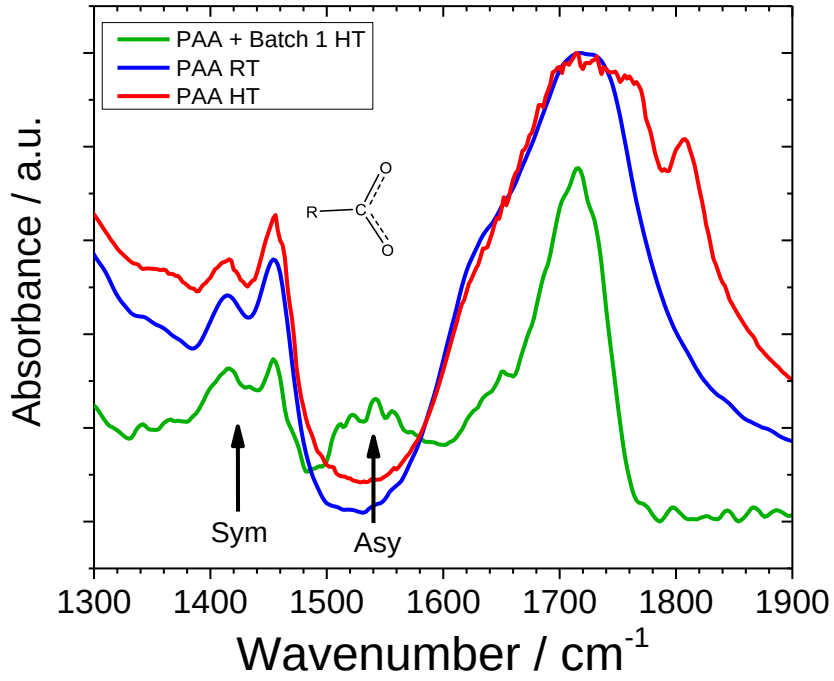

Figure 3-12 – Comparison of IR spectra highlighting peaks suggesting evidence of a bidentate interaction of PAA with batch-1 material.

The observed results suggest anhydride formation did not occur and that a condensation reaction occurred between the PAA -OH groups and -OH groups on the surface silicon result in bonding interactions as depicted in **Figure 3.13**. This brief study illustrates that PAA acts as a functional binder, interacting with the surface of the silicon nanowire material. The study also provides insight into the functionality present within the composite electrode when PAA is used. Further work to quantitatively investigate the functional groups present would be useful to understand the remaining -COOH content.

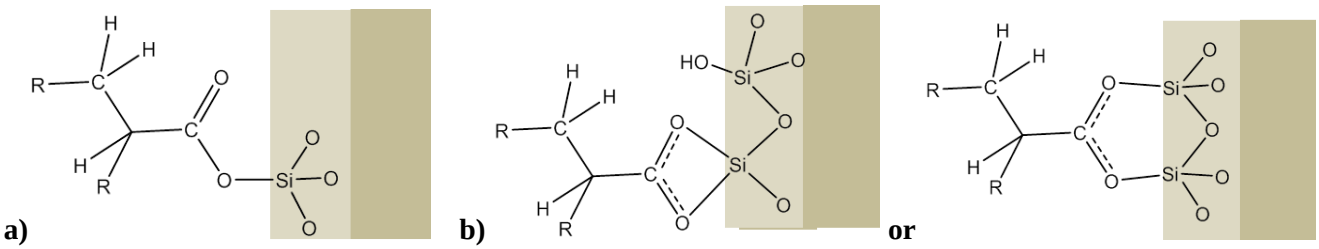

Figure 3-13 – Illustrations of suggested interations formed between polyacrylic acid and silicon nanowire particle after drying of an aqueous mixture at 120°C under vacuum. a) monodentate ester formation b) bidentate interations resulting in a symetrical carbxyolate type group.

3.4 Chapter conclusions

Nanowire batches

Batch-1 material was observed to contain a high proportion of twisted nanowire type particles. The high concentration of twisted nanowire material is suggested to be caused by unstable conditions during synthesis. Batch-2 was observed to contain a higher proportion of straight nanowire particles.

Both batches were observed to contain a proportion of non-nanowire material suggested to be produced *via* breakdown of the silicon precursor during synthesis. Batch-1 was expected to contain amorphous silicon formed *via* uncontrolled thermal breakdown of trisilane. Batch-2 was expected to contain poly-phenylsilane, produced *via* breakdown of the mono-phenylsilane precursor [12]. EFTEM analysis of batch-2 material confirmed the presence of a coating layer at the surface of a nanowire particle which contained a high proportion of carbon correlating well with the expected formation of poly-phenylsilane.

Interaction of PAA with batch-1

Results of an FTIR spectroscopy investigation into the interaction of PAA with batch-1 provided evidence for the formation of a bidentate type interaction and ester bond formation, strong interactions which are likely to enable the structural stability of composite electrodes. Formation of anhydride functionality was completely inhibited when batch-1 material was added to aqueous solutions of PAA prior to drying. A large reduction in the free –OH content of PAA was observed when dried with batch-1 material. The loss of free –OH is important when considering possible side reactions of binder functional groups with the electrolyte solution [13].

3.5 Chapter references

1 A. T. A. Heitsch, V. A. Akhavan and B. A. B. Korgel, *Chem. Mater.*, 2011, **23**, 2697–2699.

2 D. C. Lee, T. Hanrath and B. a. Korgel, *Angew. Chemie - Int. Ed.*, 2005, **44**, 3573–3577.

3 H. Geaney, C. Dickinson, W. Weng, C. J. Kiely, C. a. Barrett, R. D. Gunning and K. M. Ryan, *Cryst. Growth Des.*, 2011, **11**, 3266–3272.

4 A. M. Chockla, J. T. Harris, V. a Akhavan, T. D. Bogart, V. C. Holmberg, C. Steinhagen, C. B. Mullins, K. J. Stevenson and B. a Korgel, *J. Am. Chem. Soc.*, 2011, **133**, 20914–21.

4b C.Cayron, M. Den Hertog, L. Latu-Romain, C. Mouchet, C. Secouard, J.-L. Rouviere, , E. Rouviere, & J.-P. Simonato, *J. Appl. Cryst.*, 2009, **42**, 242-252.

4c F. J. Lopez, E. R. Hemesath, and L. J. Lauhon, *Nano Letters* 2009, **9**, 2774-2779

5 N. S. Hochgatterer, M. R. Schweiger, S. Koller, P. R. Raimann, T. Wöhrle, C. Wurm and M. Winter, *Electrochem. Solid-State Lett.*, 2008, **11**, A76.

6 A. Magasinski, B. Zdyrko, I. Kovalenko, B. Hertzberg, R. Burtovyy, C. F. Huebner, T. F. Fuller, I. Luzinov and G. Yushin, *ACS Appl. Mater. Interfaces*, 2010, **2**, 3004–10.

7 S. Komaba, N. Yabuuchi, T. Ozeki, K. Okushi, H. Yui, K. Konno, Y. Katayama and T. Miura, *J. Power Sources*, 2010, **195**, 6069–6074.

8 J. Dong, Y. Ozaki and K. Nakashima, *Macromolecules*, 1997, **30**, 1111–1117.

9 K.-F. Arndt, A. Richter, S. Ludwig, J. Zimmermann, J. Kressler, D. Kuckling and H.-J. Adler, *Acta Polym.*, 1999, **50**, 383–390.

10 L. J. Kirwan, P. D. Fawell and W. Van Bronswijk, *Langmuir*, 2003, **19**, 5802–5807.

11 R. Bywalez, H. Karacuban, H. Nienhaus, C. Schulz and H. Wiggers, *Nanoscale Res. Lett.*, 2012, **7**, 76.

11b G.B. Deacon, R. J. Phillips, *Coord. Chem. Rev.*,1980, **33**, 227-250.

12 T. D. Bogart, D. Oka, X. Lu, M. Gu, C. Wang and B. a Korgel, *ACS Nano*, 2014, **8**, 915–22.

13 S. F. Lux, I. T. Lucas, E. Pollak, S. Passerini, M. Winter and R. Kostecki, *Electrochem. commun.*, 2012, **14**, 47–50.

Chapter 4: Initial electrochemical characterisation

4.1 Introduction

The chapter describes an initial investigation into the production of composite electrodes containing batch-1 material via the utilisation of PAA as a binder. The electrochemical performance of produced composite electrodes was then investigated via incorporation of composite electrodes into electrochemical cells.

4.2 Fabrication of composite electrodes

4.2.1 Selection of materials

A simple three component system was chosen to evaluate the performance of silicon nanowire material. Acetylene black (Shawinigan Black, 100% compressed Chevron Philips) was selected as a high surface (45 m^2 g^{-1} BET surface area) area conductive carbon (**Figure 4-1**). Acetylene black was selected as it was commercially available and routinely used. Poly-acrylic acid was selected as a binder to evaluate the performance of silicon nanowire material.

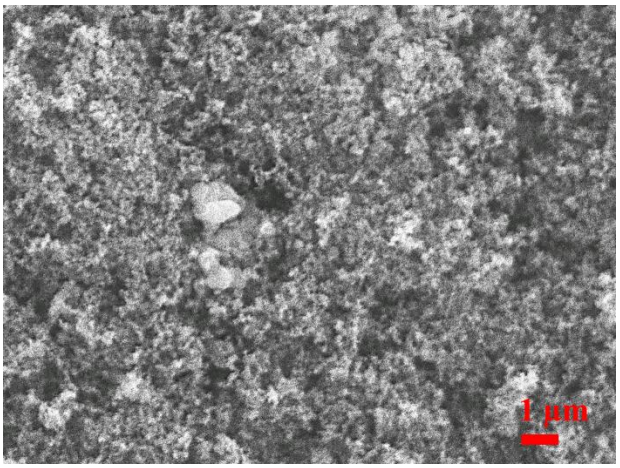

Figure 4-1 - SEM image of acetylene black powder used as a conductive additive. Material consists of <100 nm diameter particles of amorphous carbon, a number of larger particles were also present.

4.2.2 Production of electrodes

The formulation selected for initial electrochemical testing was 37: 37: 26 (batch-1: carbon: poly-acrylic acid) (w/w). The formulation was selected as a report by Beattie *et al.* [1] suggested that a simple reduction in the active material content of composite electrodes containing large volume change active materials gave improved electrode stability. The high content of conductive carbon was used to promote electronic contact between silicon nanowire particles and the current collector. A high content of poly-acrylic acid binder content was also stated to be beneficial to the stable performance of silicon based electrodes [1].

a) 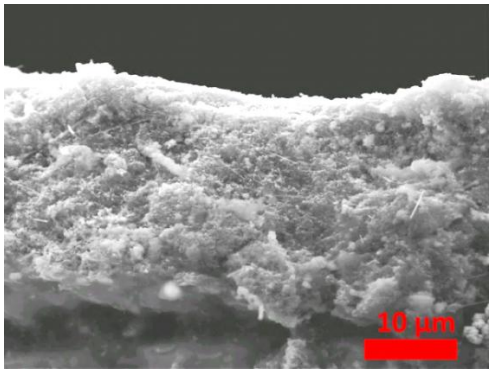

b) 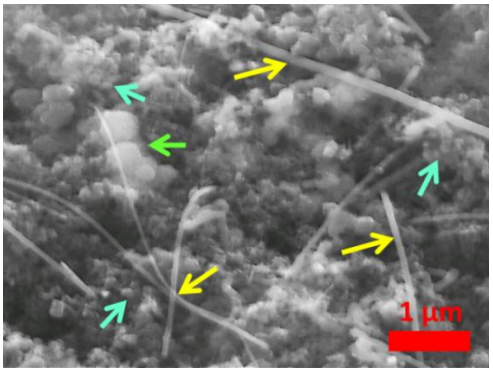

Figure 4-2 – a,b) SEM images of a composite electrode consisting of batch-1 silicon nanowire material, acetylene black conductive additive and poly-acrylic acid binder, average electrode thinkness = 22 µm b) yellow arrows highlight silicon nanowire particles, blue arrows highlight carbon black particles, green arrow highlights particles of amorphous silicon.

SEM images of the cross section of a composite electrode of formulation 37:37:26 are displayed in **Figure 4-2**; the electrodes appear to be homogenous with an even distribution of material throughout the thickness of the electrode. The properties of the composite electrode are displayed in **Table 4-1**.

Table 4-1 – Properties of composite electrodes produced

Mass of composite electrode (mg)	1.38 ±0.02
Average thickness (cm)	0.0022 ± 0.0003
Geometric area (cm^2)	1
Volume (cm^3)	0.0022 ± 0.0003
Density (g cm^{-3})	0.64 ±0.1
*Porosity estimation (%)**	66 ± 7

** assumed densities: carbon black - 1.75 g cm^{-3} (data from supplier), poly-acrylic acid - 1.4 g cm^{-3}(data from reference [2]) and silicon - 2.33 g cm^{-3} (density of batch-1 assumed to be 2.33 g cm^{-3})*

The theoretical performance of the composite electrode was calculated (**Table 4-2**) based upon the known weight ratio of components. The electrochemical properties of PAA and the carbon black conductive additive were measured in control experiments (*Appendix 3*).

Table 4-2 – Calculation of the theoretical capacity of the composite electrode

Component	**Formulation / wt. %**	**Q_T / mA h $g^{-1}_{(Component)}$**	**Capacity Contribution / mA h $g^{-1}_{(Composite)}$**
Batch-1 material	37	3579†	1324
Carbon additive	37	200*	74
Poly-acrylic acid	26	0*	0
			Total : 1398

† - theoretical capacity of silicon if $Li_{15}Si_4$ is the final lithiated phase[3]
** - Capacity of carbon black and PAA based upon control cell data (Appendix 3)*

The maximum capacity of the electrode was calculated to be 1398 mA h g^{-1} assuming batch-1 material contained pure silicon (**Table 4-2**).

4.3 Electrochemical characterisation of a composite electrode

4.3.1 Electrochemical cell configuration

Electrochemical characterisation was conducted utilising Swagelok type cells in a two electrode configuration. Lithium metal was used as a counter electrode due to its ability both to provide lithium ions and act as a reference electrode. The cell configuration used causes the composite electrode to be the positive electrode and lithium metal to be the negative.

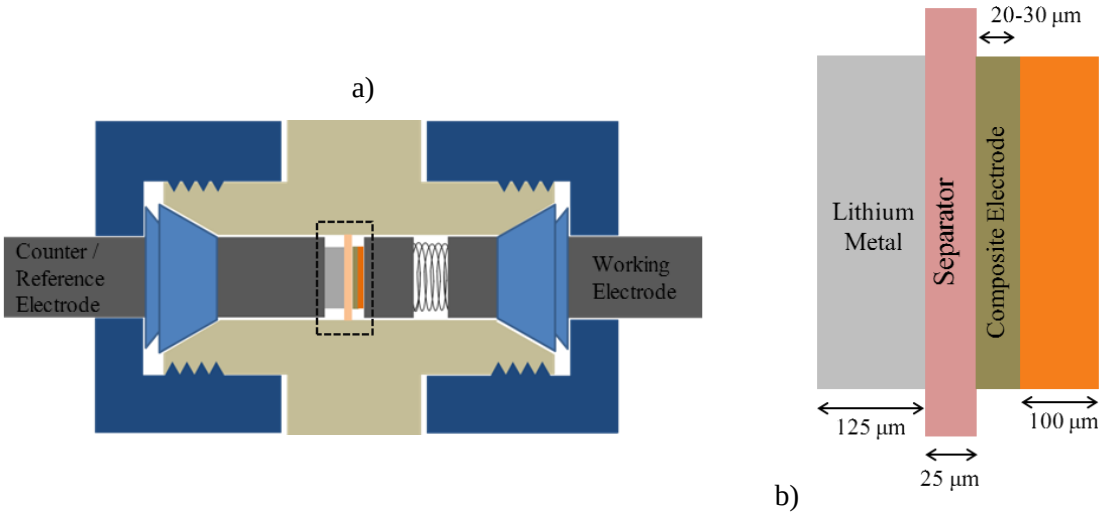

Figure 4-3 – a) Diagram of electrochemical cell used for electrochemical characterisation of composite electrodes b) diagram of electrode stack (marked by dashed region in a)

The thermodynamically favourable reaction (discharge) is that of lithium insertion into the composite silicon electrode. Once fully inserted the cell would be said to be in the discharged state and could then be charged, *via* the application of a current. The charge process would involve removal of lithium from the previously formed lithium silicide phase within the composite electrode, whilst lithium ions are plated onto the lithium metal electrode. The discharge process followed by the charge process for this cell configuration is from here on referred to as a cycle.

4.3.2 Specification of applied current

The rate of lithium insertion and extraction depends on the current applied to discharge and charge the cell. For a given C-rate, the current applied to the cell was calculated using **Equation 4-1**.

$$\mathbf{I} = \boldsymbol{C}\,\mathbf{M}\,\mathbf{Q}_{\boldsymbol{T}}$$

Equation 4-1

I = applied current (mA) , C = C-rate (h^{-1}), M = mass of silicon material (g), Q_T = theoretical specific capacity of silicon (mA h g^{-1})

It is recognised that acetylene black adds some capacity due its high surface area, so that some of the applied current is diverted from the lithium insertion/extraction process. However the amount of additional charge was estimated to be about 6% (*Appendix 3*) of the total measured value and therefore has a negligible effect on a C-rate specified to an accuracy of only around 10%.

a)

M (of electrode) (mg)	1.38
Q_T (of electrode) (mA h g^{-1})	1398
C-rate (h^{-1})	0.05
I (mA)	0.0965

b)

M (of silicon) (mg)	0.51
Q_T (of Silicon) (mA h g^{-1})	3579
C-rate (h^{-1})	0.05
I (mA)	0.0913

Figure 4-4 – Calculation of applied current a) includes carbon contribution (200 mA h g^{-1} of carbon) and binder mass and b) based on mass of silicon within the electrode

The above calculation is useful for an estimation of the expected (dis)charge time assuming theoretical capacity is achieved e.g. a current of 91.3 μA would provide a discharge time of 20 hours assuming the theoretical capacity of 3579 mA h g^{-1} for silicon alone, or around 21 hours if the carbon contributed a capacity of 200 mA h g^{-1}. The presence of non-silicon material within the batches of as received materials results in an artificially high C-rate applied to the electrodes.

4.3.3 The first cycle

The voltage profile of a composite electrode during the first cycle is displayed in **Figure 4-5**. Lithium insertion corresponds to discharge and lithium extraction corresponds to charge of the cell. The capacity achieved during lithium insertion to 0.01 V vs. Li/Li^+ was measured to be around 2 mA h. The reversible capacity achieved during lithium extraction to a voltage of 1 V was only 1.4 mA h, indicating an irreversible capacity of 0.6 mA h.

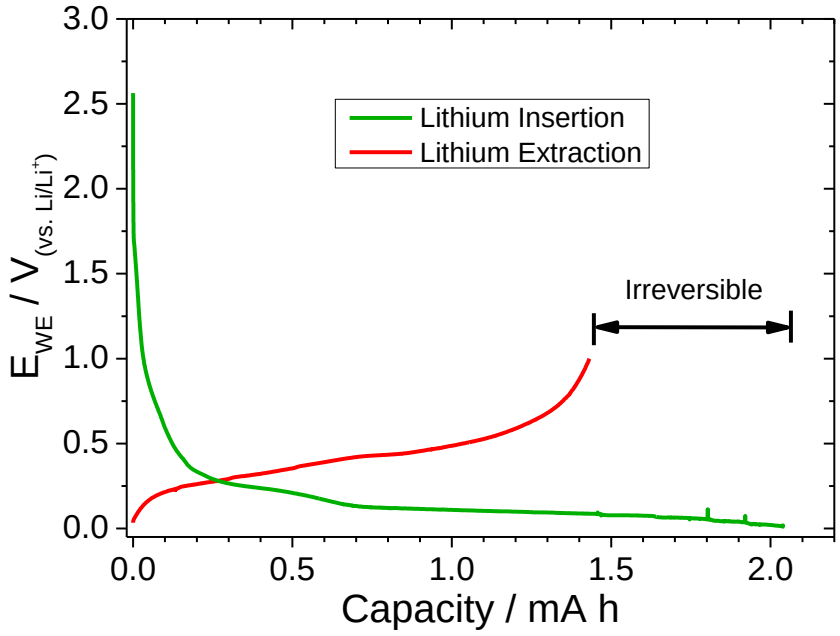

Figure 4-5 – Voltage profile of a composite electrode during the first cycle. An electrolyte solution of 1 M $LiPF_6$ EC: DMC was used. The electrode was cycled at a rate of C/10.

The extraction capacity due to the carbon additive was calculated to correspond to 0.102 mA h assuming a specific capacity of 200 mA h $g^{-1}_{(carbon\ additive)}$. During the initial insertion reaction the capacity attributable to the carbon additive is not clear and hence produces a significant source of error in calculating the capacity due to silicon. All capacity values are presented in **Table 4-3**. The voltage of the working electrode is plotted against common measures of capacity in **Figure 4-6**.

Table 4-3 – Capacity values of the first cycle of a composite electrode. The maximum contribution of the carbon additive to the extraction capacity values is also displayed. Errors are displayed in brackets calculated from errors associated with mass and thickness measurements of the composite electrode (Table 4-1). The geometrical area of the composite electrode was assumed to be 1 cm^2 due to the use of a mechanical 1 cm^2 punch to form the electrodes. The error associated with the potentiostat was assumed to be negligible.

Capacity Values	Insertion	Extraction	Carbon Contribution (Extraction)
Capacity / mA h	2.044	1.432	0.102
Specific Capacity / mA h g^{-1} (batch-1)	4003 (± 2 %)	2804 (± 2 %)	200 (± 2 %)
Specific Capacity / mA h g^{-1}(composite)	1481 (± 2 %)	1038 (± 2 %)	74 (± 2 %)
Areal Capacity / mA h cm^{-2}(electrode)	2.044	1.432	0.102
Volumetric Capacity / mA h cm^{-3}(composite)	946 (± 15%)	651 (± 15%)	46.4 (± 15%)

The capacity value measured during initial insertion was larger than the theoretical capacity previously calculated (1398 mA h $g^{-1}_{(Composite)}$, **Table 4-2**). A proportion of the capacity can be explained by charge passed resulting in the reduction of electrolyte at the surface of silicon and carbon within the electrode, the processes commonly associated with SEI layer formation.

4.3.3.1 Analysis of the voltage profile during the first cycle

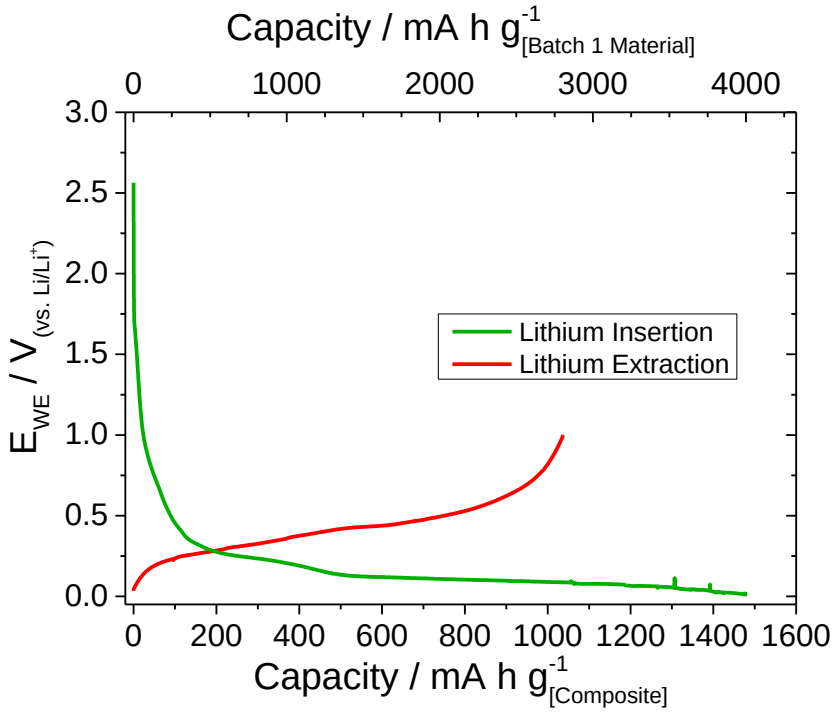

Figure 4-6 – Voltage profile a composite electrode displayed with capacity values in terms of mA h $g^{-1}_{(Composite)}$ and mA h $g^{-1}_{(Batch\text{-}1\ material)}$.

The majority of the charge was passed within the voltage region commonly associated with lithium insertion into silicon (0.4 V- 0.01V (cut-off)). The derivative of the charge passed with respect to voltage is shown in the dQ/dE plot in **Figure 4-7**. The form of the plot resembles a slow scan cyclic voltammogram where the usual distortion due to the IR drop has been largely eliminated by limiting the current to a small value throughout the experiment.

Analysis of the dQ/dE plot during lithium insertion (**Figure 4-7**) suggests a number of stages occur prior to lithium insertion into silicon. The inset in **Figure 4-7** highlights the charge passed above 0.3 V. Initially a rapid drop in the potential of the composite electrode occurred, from a stable open circuit potential of 2.6 V to a value of 1.7 V. The onset of a reaction at 1.7 V is attributed to reduction of either surface species on the composite electrode or contaminants within the electrolyte solution. The high surface area of the carbon additive and the high proportion present within the composite explains the relatively large amount of charge passed above 0.3 V (150 mA h g^{-1}).

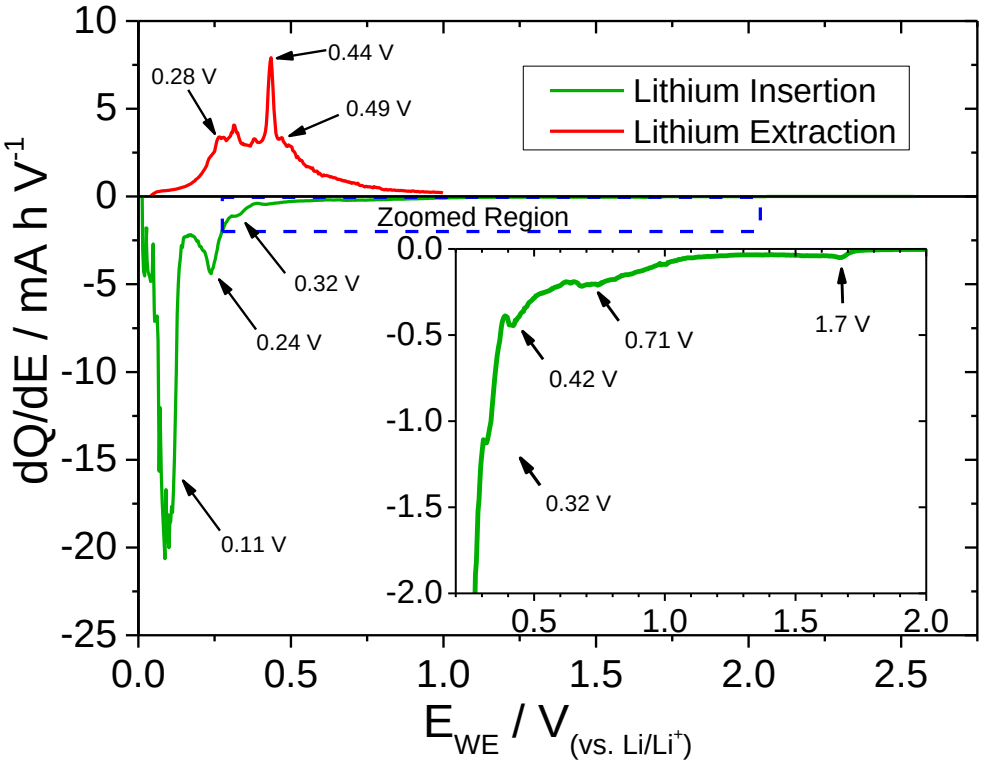

Figure 4-7 – a) dQ/dE plot of the 1st cycle of a composite electrode cycled between 0.01 and 1 V from a starting potential of 2.6 V at open circuit with an applied current of 91.3 µA Inset is a dQ/dE plot of region highlighted in blue.

The potential continued to decrease until around 1.1 V at which point another reaction began, the voltage of this process corresponds to previous reports of the reductive decomposition of the electrolyte [4]. The reaction occurring between 0.38 V and 0.32 V is suggested to be due to the electrochemical reaction of lithium with the surface silicon oxide species present on the surface of the nanowire material, as also previously suggested by Ogata *et al.* [5]. It should be noted that the amorphous carbon conductive additive contributed to the observed charge, the high surface area of the carbon causes a significant proportion of the charge passed during the first cycle insertion to be associated with electrolyte breakdown and reduction of surface species at the carbon electrolyte interface (*Appendix 3*).

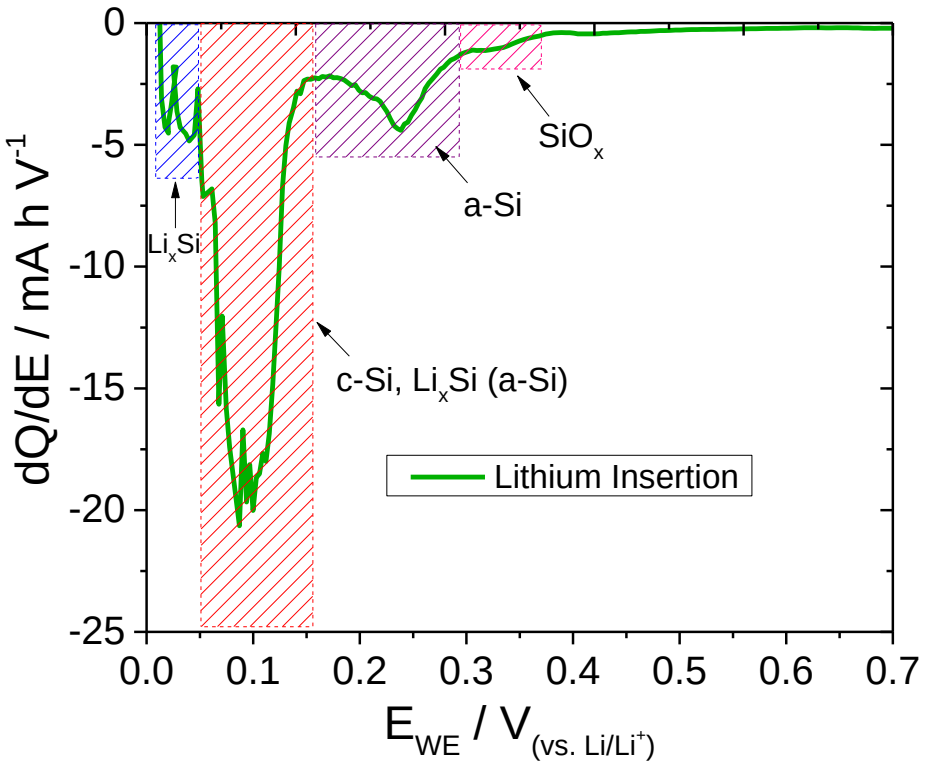

Figure 4-8 – dQ/dE plot of insertion processes occurring below 0.7 V, lithium insertion into various phases present within the electrode are highlighted.

A large amount of charge was observed to pass at around 0.25 V (**Figure 4-8**). The potential of this process does not correspond to lithium insertion into crystalline silicon which commonly has been reported to occur at around 0.1 V. It is suggested that the charge corresponds to lithium insertion into amorphous silicon, commonly reported to occur at around 0.3 V [6]. The presence of the peak suggests that amorphous silicon was present within as-received batch-1 material, confirming the nature of the large spherical particles present within the sample. Charge passed below 0.15 V is assigned to lithium insertion into crystalline silicon, accompanied by further lithium insertion into the previously lithiated amorphous silicon.

The amorphous silicon content was estimated to be around 16 % of the active silicon present within the electrode. The estimation was calculated *via* integration of the region of the dQ/dE plot associated with lithium insertion into amorphous silicon (0.17-0.28 V) and the whole region associated with lithium insertion into silicon (0.004 – 0.3 V). An assumption of formation of Li_2Si in the amorphous silicon phase by 0.17 V and formation of $Li_{3.5}Si$ by 0.01 V was made and suggested to be reasonable based upon the work of Ogata *et al.* [5].

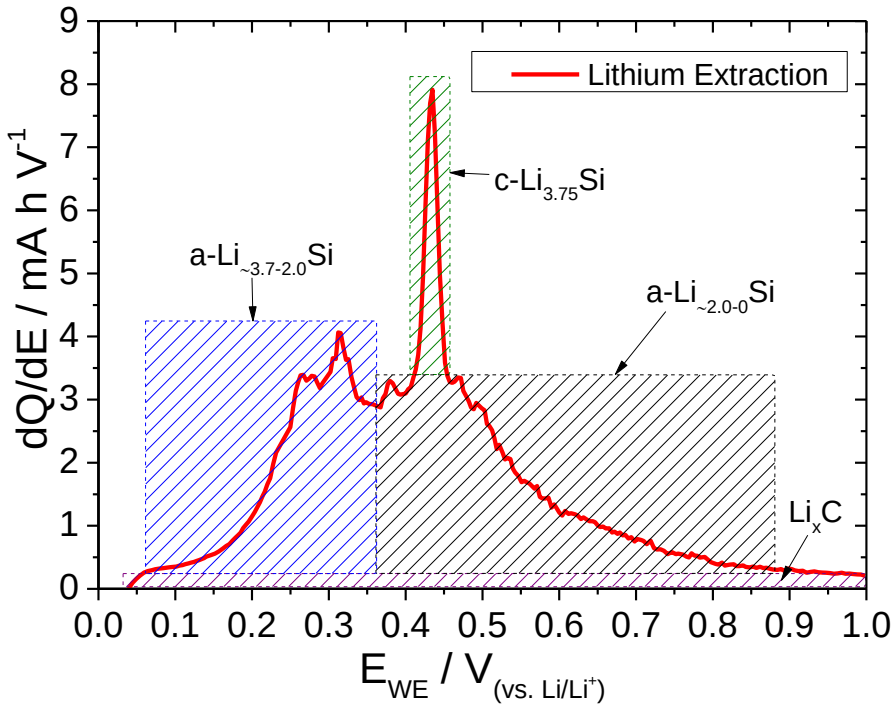

Figure 4-9 – dQ/dE plot of the lithium extraction process, lithium extraction was observed from various highlighted phases. Lithium extraction from Li_xAu and Li_xO phases may also contribute to observed extraction charge however the contribution is expected to be minor.

The dQ/dE plot highlighting lithium extraction processes is displayed in **Figure 4-9**. The observed peaks corresponded well with other reports of lithium extraction from nanowire type electrodes [5]. Lithium is initially extracted from high lithium content amorphous lithium silicide. A small proportion of the charge between ~0.05 V to 1 V will also be caused by lithium extraction from the charged carbon black additive. At 0.44 V, a sharp peak was observed which corresponds to the two phase extraction of lithium from the crystalline $Li_{15}Si_4$ phase. Above 0.46 V extraction of lithium from the remaining amorphous low lithium content phase occurs. Lithium extraction continues from the amorphous lithium silicide phase until all lithium has been extracted leaving an amorphous silicon phase. Lithium silicide phase transitions which correspond to the observed results have recently been described in detail by Ogata *et al.*[5].

4.3.3.2 Impedance analysis of the first cycle

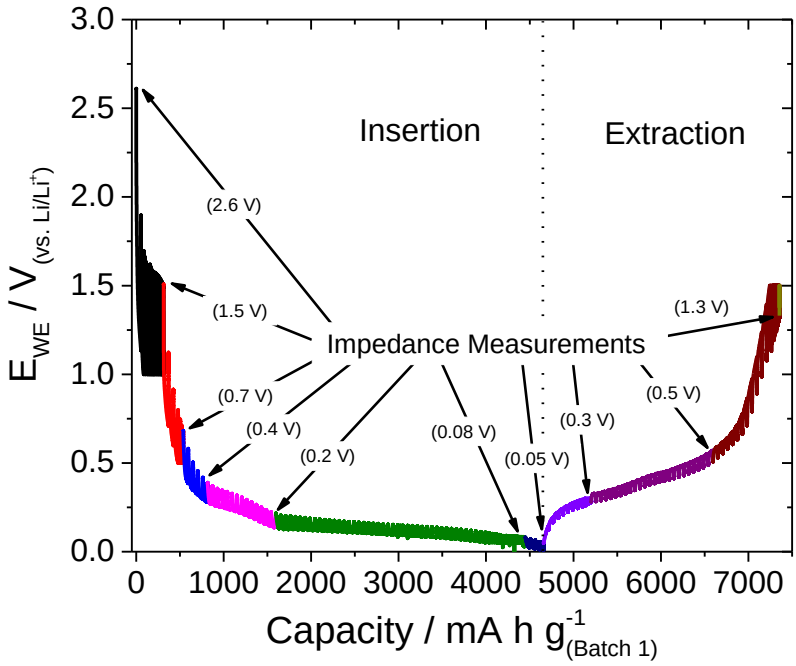

Figure 4-10 – Voltage profile of a composite electrode within a three electrode cell throughout the initial cycle. A pulsed constant current regime was used to conduct the cycle. A current equivalent to 20 C was applied for 20 minutes followed by an open circuit time of 1 hour 40 minutes. Arrows indicate the position of impedance measurements obtained throughout the cycle.

Impedance measurements were made throughout the first cycle of a three electrode cell containing a nanowire based composite electrode (batch-1) as the working electrode (**Figure 4-10**). The impedance spectra obtained throughout the cycle are displayed on Nyquist and Bode plots in **Figure 4-11**.

The greatest variation was observed in the medium-low frequency region of the obtained spectra. In the Nyquist plot the highest frequency arc is attributed to the interfacial resistance between the current collector and the composite electrode layer in parallel with the double layer capacitance of the copper metal substrate [6b]. The high frequency arc was observed to become well defined as the potential of the electrode was decreased below 1.5 V. Initially, as the electrode is reduced the potential decreases from OCV to ~1.5 V, the potential decreases as reduction of surface species and contaminants within the electrolyte occur forming reduction products at the surface of the all electronically conducting surfaces these processes are suggested to result in increased electronic resistance between the current collector and the composite electrode.

A medium frequency arc was observed for impedance spectra recorded between 0.7 V during insertion and 0.5 V during extraction. The medium frequency arc is commonly reported for lithium ion battery electrode materials and associated with a charge transfer resistance in parallel with the double layer charging of the composite electrode surface.

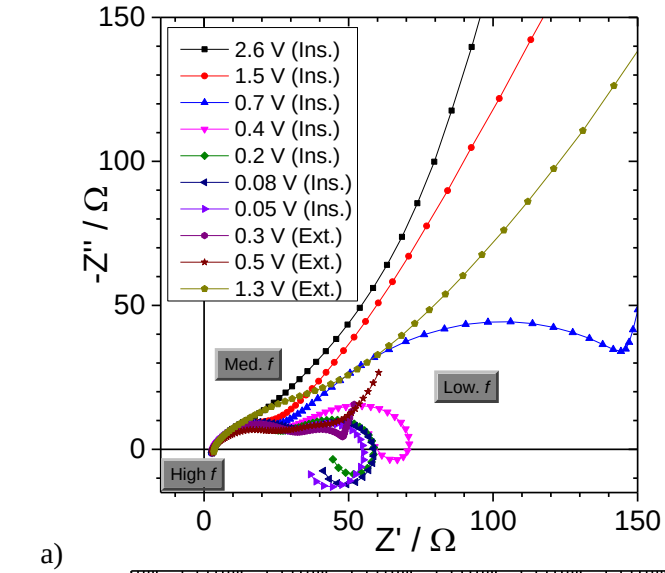

a)

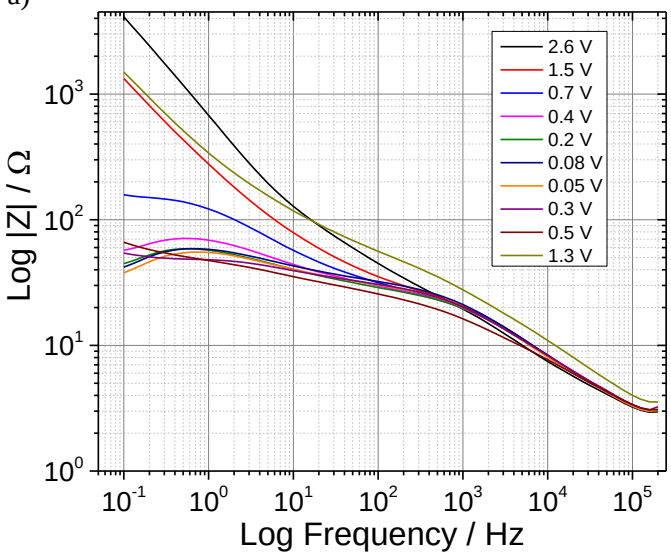

b)

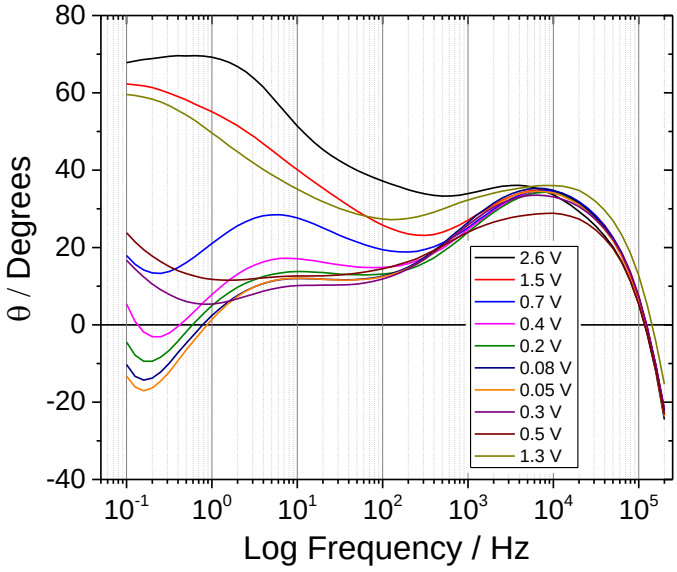

c)

Figure 4-11 – Impedance spectra displayed in the form of a) Nyquist plot, b and c) Bode plot acquired from the cell displayed in Figure 4-10, conducted at various potentials throughout the first insertion and extraction of lithium from a composite electrode over the frequency range 50 kHz to 100 mHz in a three electrode cell configuration at 25°C.

During lithium insertion, formation of a pseudo-inductive loop at medium-low frequency was observed at potentials of 0.4 V and below (**Figure 4-11**a). The presence of pseudo-inductive loops has recently been reported during the analysis of composite electrodes containing nano-silicon particles; the feature was suggested to be caused by a non-conventional SEI formation mechanism [7]. The proposed mechanism involved reduction of a lithium ion and solvent molecule at the surface of the active material, after conventional SEI layer formation had occurred, i.e. beyond the initial cycle and low potential.

A pseudo-inductive loop may be produced when applying an alternating voltage of a certain frequency, if during a half cycle the frequency is low enough for the lowest voltage to be applied for a critical time to trigger a current response which is delayed with respect to the applied voltage. The increased current due to the response will result in a decreased equivalent resistance and the current lag will simulate pseudo-inductive behaviour. Such behaviour has been noted as early as 1965 [8]. The presence of the pseudo-inductive loop suggested that a similar reaction process was occurring at 0.4 V and below during the initial cycle. The high potential at which the pseudo-inductive loop was observed may be due to reaction of high surface area carbon and amorphous silicon with the electrolyte, each known to store lithium at potentials greater than crystalline silicon at potentials around 0.4 V.

At partial extraction (0.3 V) the impedance spectra consisted of two depressed arcs (high and medium frequency) and a diffusional tail at medium-low frequency. The absence of inductive loops in spectra recorded during the lithium extraction process suggests that the same process did not occur; this may be caused by the loss of lithium from the surface of the particles during lithium extraction and the subsequent reduction in the reactivity of the material. Further, if the process responsible for the inductive loop is promoted by cracking or fracturing of the SEI layer as suggested by Radvanyi *et al.* [9] then contraction of the active particles, which is known to occur during lithium extraction, may act to seal and condense the SEI layer formed at the surface possibly ad also contribute to the observed lack of an pseudo-inductive loop. After near complete extraction at 1.3 V, the spectrum no longer displayed well-defined high frequency arcs.

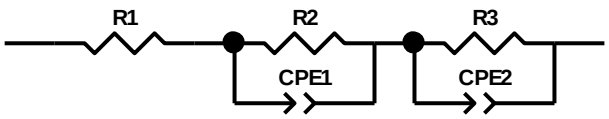

a)

Figure 4-12 – Equivalent circuit used to fit high – medium frequency impedance data recorded throughout the first electrochemical cycle.

Fitting of the spectra obtained between 0.7 V (insertion) and 0.5 V (extraction) over the high-medium frequency range was conducted to investigate the capacitance values and time constants

associated with the two arcs, to confirm the suggested assignment. Fitting was conducted using Z-view™ software and the equivalent circuit displayed in **Figure 4-12**.

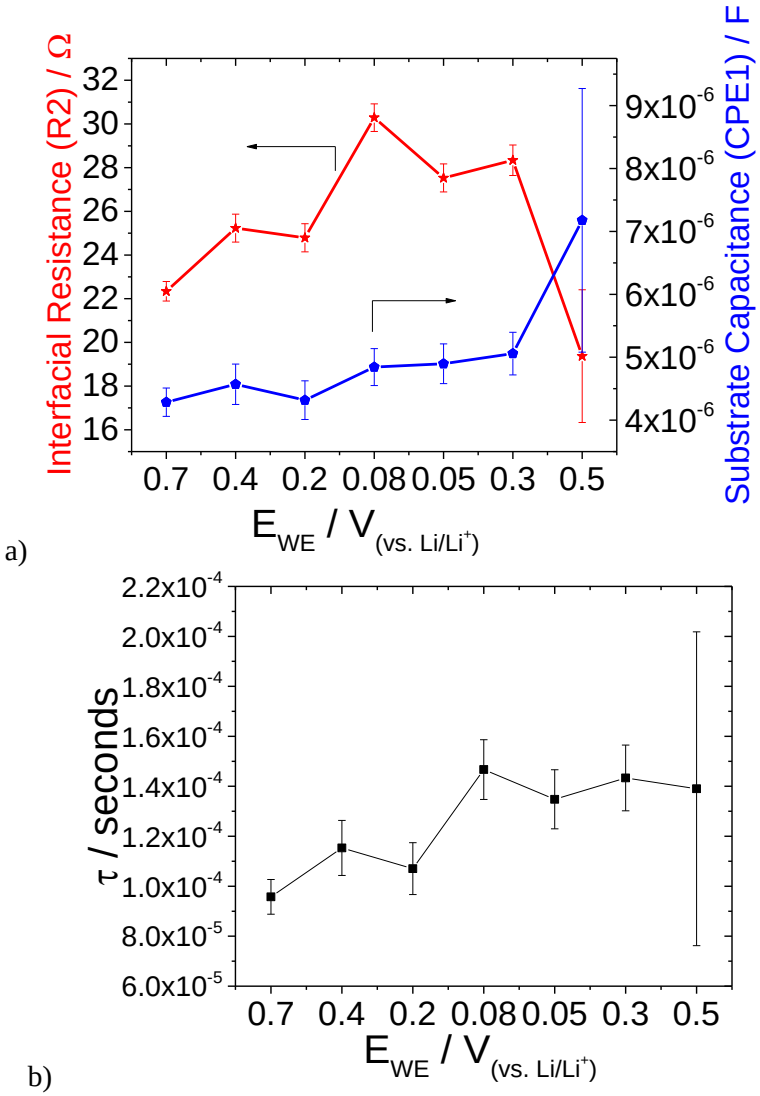

Figure 4-13 – a) Variation of resistance and capacitance associated with the high frequency arc observed in impedance spectra between 0.7 V (insertion) and 0.5 V (extraction) in the first cycle. Calculation of the capacitance of the CPE element was conducted as described in Chapter 2. b) Time constant of parallel R2 (CPE2) element with associated error.

The results of the fitting can be summarised as follows, R1, the uncompensated resistance of the cell, dominated by the ionic conductivity of the electrolyte solution, was observed to be roughly constant at 3 Ω. The high frequency arc of the spectra in **Figure 4-11**a, associated with the electronic resistance at the interface of the copper current collector and the composite film in parallel with the capacitance of the current collector, was modelled by a resistor and CPE in parallel (R2, CPE1). The resistance was observed to vary as a function of electrode potential, **Figure 4-13**, generally the resistance was observed to increase during lithiation and decrease during de-lithiation. A capacitance of around 5 x 10^{-6} F cm^{-2} was calculated from the measured data (**Figure 4-13**), the value corresponds well with capacitance associated with the double layer of a 1 cm^2 copper substrate [9*]. The capacitance value remained relatively constant throughout

the cycle, slight increases may have been produced via the exposure of current collector previously masked from the electrolyte by composite electrode. Larger errors in the fitting of the spectra at 0.5 V during extraction prevent accurate determination of the resistance and capacitance values. The time constant associated with the parallel RCPE element was calculated to be around 1.2 x 10^{-4} seconds (**Figure 4-14b**), the relatively low time constant confirms that the impedance response corresponding to the high frequency arc was associated with a fast process and correlates with the assignment of the double layer charging of the substrate.

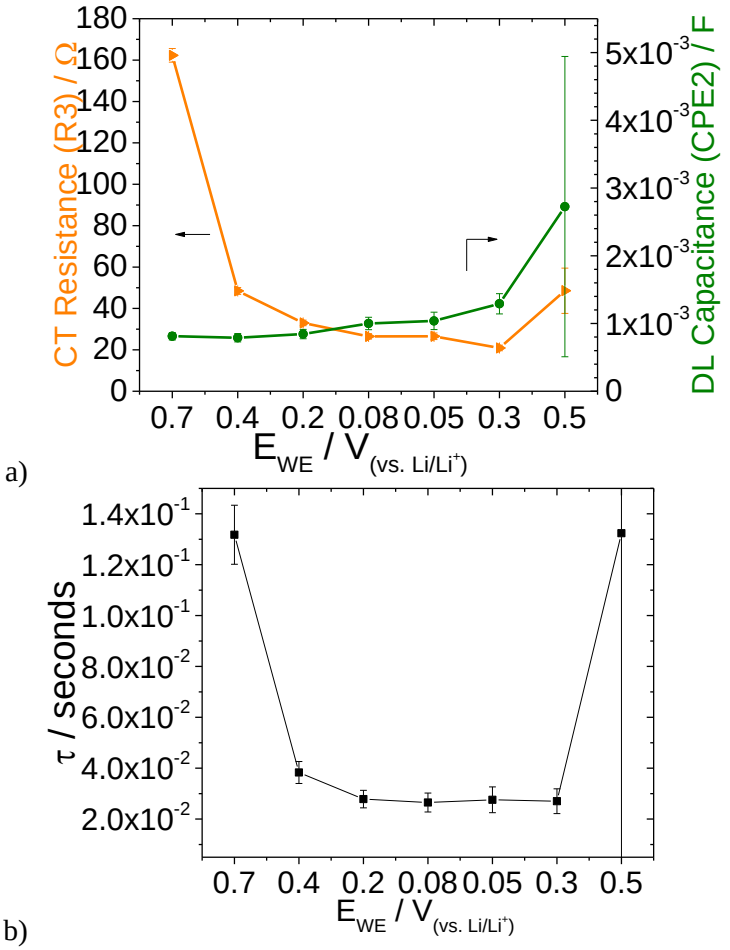

Figure 4-14 – Variation of resistance and capacitance associated with the medium frequency arc observed in impedance spectra between 0.7 V (insertion) and 0.5 V (extraction) in the first cycle. Calculation of capacitance of the CPE element was conducted as described in Chapter 2. b) Time constant of parallel R3 (CPE3) element.

Fitting of the medium frequency arc to the parallel combination of R3 and CPE2 was conducted. The medium frequency arc was associated with the parallel combination of charge transfer resistance and double layer capacitance of the composite electrode, resistance and capacitance values obtained *via* curve fitting of the data are displayed in **Figure 4-14**. The charge transfer resistance was observed to decrease during lithium insertion and further decrease after partial lithium extraction to 0.3 V, above 0.3 V the resistance increased to a value similar to that measured at a potential of 0.4 V prior to lithium insertion. The charge transfer resistance

was expected to decrease as the potential of the composite electrode was reduced closer to the potential of lithium insertion into silicon [10]. Variation in charge transfer resistance has also been associated with the electronic conductivity of the active material [11] and also to changes to the surface area of the active material [12]. The general trend observed complies with the known lithium insertion/extraction process and the associated volume expansion and contraction of silicon particles.

The capacitance was observed to increase throughout the cycle. The variation of the capacitance throughout the cycle was suggested to be due to changes in the electrochemically active surface area of the electrode. The active area of the electrode would be expected to increase during lithium insertion and decrease during extraction as the active particles vary in size. The observed increase during extraction is unexpected and may be explained *via* cracking or pulverisation of particles or *via* new exposure of carbon or active material surface area to the electrolyte; the reduced confidence of the calculated values at 0.5 V should be noted.

Assuming a specific double layer capacitance of 10^{-5} F cm^{-2}, the electrochemical surface area of the electrode can be estimated from the calculated electrode double layer capacitance. The area was calculated to vary from around 80 cm^2 (0.7 V during insertion) to around 120 cm^2 (0.3 V during extraction) throughout the first cycle. These values correspond relatively well to the combined surface area of the nanowire material and carbon additive within the composite electrode, around 465 cm^2, assuming surface areas of 30 m^2 g^{-1} for batch-1 material and 45 m^2 g^{-1} for the carbon additive. The total electrode mass was 1.54 mg of which 0.3 mg was PAA binder which would be expected to significantly reduce the electrochemical surface area of the silicon and carbon constituents. The calculated surface area is therefore suggested to correspond relatively well with the expected surface area, confirming the assignment of the medium frequency.

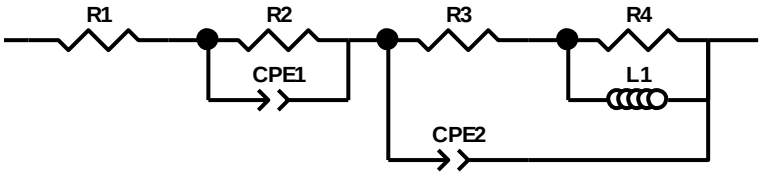

Figure 4-15 – Equivalent circuit used to fit high-medium frequency impedance spectra containing an pseudo-inductive loop, circuit has previously been used to model similar impedance data displaying pseudo-inductive loops at medium frequency [12,7].

Spectra which were observed to contain a pseudo-inductive loop were modelled using the equivalent circuit displayed in **Figure 4-15**. **Figure 4-16** displays the inductance (L1) and resistance (R4) associated with the recorded spectra. The observed trend suggests that as the concentration of lithium increases within the composite electrode the pseudo-inductive response of the electrode increases. Assuming the pseudo-inductive response is associated with a

reduction of a lithium ion and a solvent molecule in an SEI formation process, as suggested by Radvanyi *et al.* [9], the increase in calculated inductance would suggest a greater current response due to the SEI formation reaction at increased lithium concentrations.

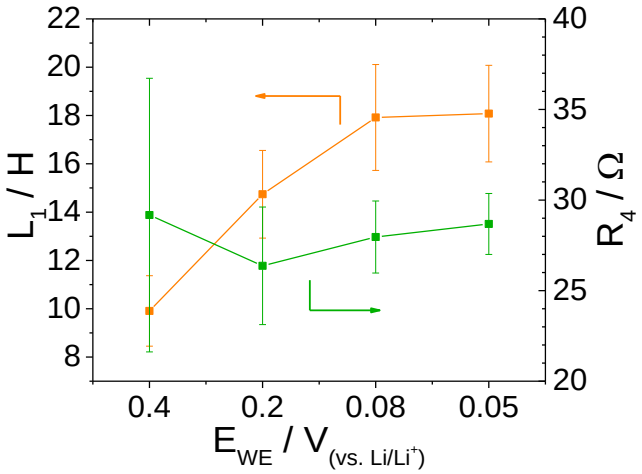

Figure 4-16 – Variation of inductance and resistance associated with the pseudo-inductive loop observed during insertion at potentials below 0.5 V, modelled using circuit elements L1 and R4.

The fact that pseudo-inductance loops were initially observed in the impedance measurements obtained at around 0.4 V suggests the parasitic reduction mechanism occurs throughout the initial cycle lithium insertion process. The impedance measurement taken at 0.4 V was obtained after relaxation from a potential of around 0.25 V. the initial current pulse to 0.25 V may have resulted in the initial lithiation of the amorphous silicon content of the electrode. As such the inductive loop formed at 0.4 V was suggested to be caused by the possibility of electrochemically induced parasitic reactions to occur between the lithiated surface of amorphous silicon and the electrolyte.

Pseudo-inductive loops have been reported to occur in the early stages of de-lithiation [7], pseudo-inductive loops were not observed in the spectra recorded during delithiation in this study. The absence was suggested to be due to the relatively significant amount of lithium extraction conducted prior to the initial impedance measurement during delithiation (0.3 V). The lack of a pseudo-inductive response at higher levels of delithiation may be due to a significant decrease in the surface reactivity of the active material particles. Contraction of the particles which would result in a reduced surface area may also contribute to the observed absence.

An example of fitted data is presented in **Figure 4-17 and Table 4-4.**

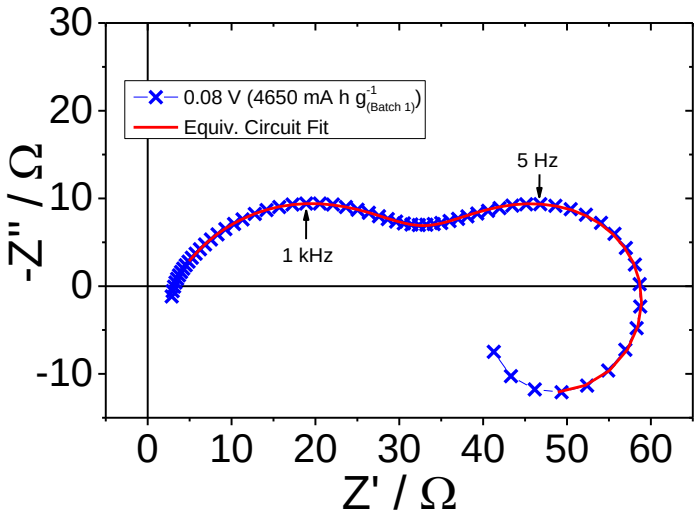

Figure 4-17 – Example fit of impedance data recorded at 0.08 V during insertion utilising the equivalent circuit displayed in Figure 4-15

Table 4-4 – Values obtained *via* curve fitting of impedance data recorded at 0.08 V utilising the equivalent displayed in Figure 4-15.

Element	Value	Error	Error %
R1 (Ω)	2.95	0.21	0.72
R2 (Ω)	30.06	0.17	0.56
CPE-T / Q ($s^n \Omega^{-1}$)	8.68E-5	1.49E-6	1.72
CPE-P (n)	0.67	1.86E-3	0.28
R3 (Ω)	3.18	0.33	10.42
R4 (Ω)	26.56	0.21	0.80
L1 (H)	18.54	0.40	2.16
CPE-T / Q ($s^n \Omega^{-1}$)	3.45E-3	6.33E-5	1.84
CPE-P (n)	0.68	6.69E-3	0.98

χ^2 = 4.2E-5, Weighted sum of squares = 4.10E-3

4.3.3.3 Expansion of composite electrode at 0.01 V

Analysis of SEM images of the composite electrode prior and post lithium insertion (**Figure 4-18**) displayed an average increase of 2 ± 1 µm (7 ± 4 %) in thickness. The low accuracy of the thickness measurement was caused by the lack of easily distinguishable start and end points for measurement and the non-uniform structure of the electrode.

a) 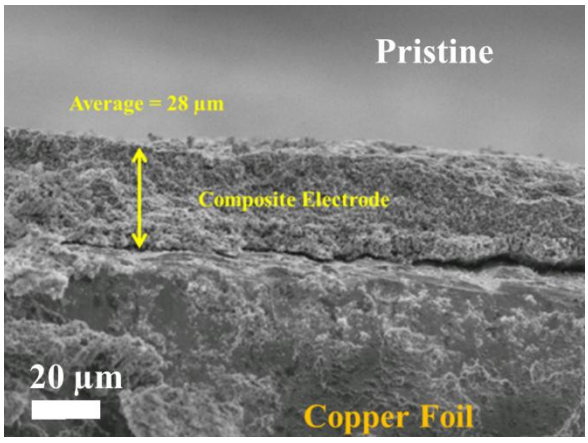

b) 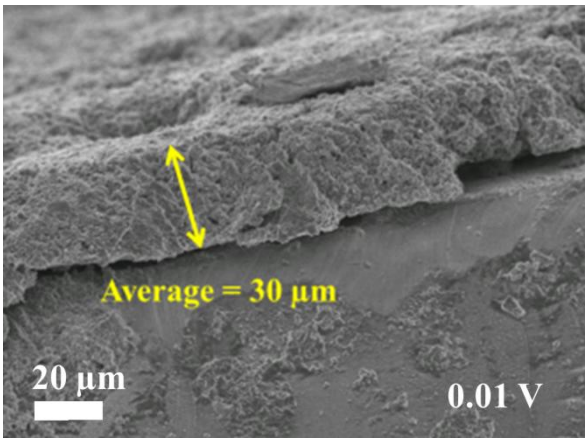

Figure 4-18 – SEM images of produced with an accelerating voltage of 10kV dispalying the thickness of a) a pristine composite electrode b) composite electrode after lithium insertion to 0.01 V (galvanostatic insertion at C/10 to 0.01V then held for 5 h).

Images obtained at maximum lithium insertion suggested that lateral expansion of the composite layer had caused material to extend out over the copper foil current collector. The observed structural change is intuitive when considering an expansion of 7 % in all directions. A 7% increase to 1.13 cm diameter is equivalent to 79 µm. The relatively low volume expansion observed for the composite electrode suggests that expansion of the active material was accommodated within the porous structure of the composite electrode.

4.3.4 The second cycle

The voltage profile of a composite electrode throughout the 2nd cycle is compared with the first cycle in **Figure 4-19**. Above 0.35 V breakdown of electrolyte and charge storage due to carbon are expected to contribute to the observed charge. Below 0.35 V the charge passed is attributed to lithium insertion into amorphous silicon. The region associated with lithium insertion into amorphous silicon (0.25-0.3 V) appears at a slightly higher potential than was observed in the first cycle. The shift in onset potential is likely due to a lower energy barrier associated with lithium insertion into electrochemically disordered amorphous silicon. Below around 0.04 V similar profiles were observed in both the 1st and 2nd cycle insertion processes. The sloping region below 0.04V has been associated with the formation of the crystalline $Li_{15}Si_4$ phase from the previously formed lithium rich phase [5]. Further reaction of lithium with previously unreacted crystalline silicon may also contribute to the charge passed at low potential.

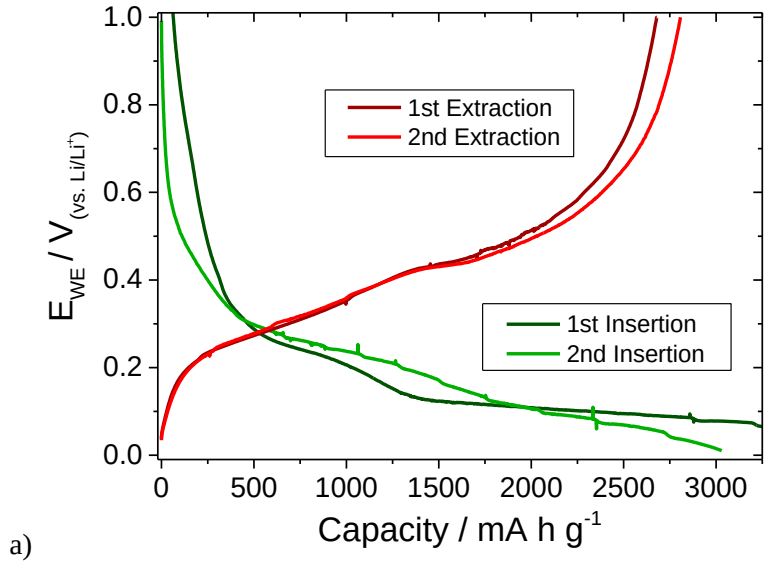

a)

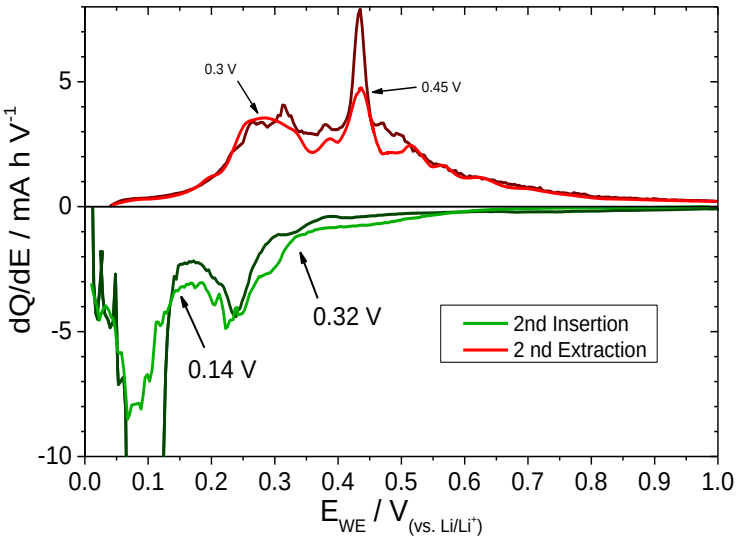

b)

Figure 4-19 - Electrochemical cycling of a half-cell a) voltage profile of the composite electrode as a function of capacity during the first and second cycles b) a dQ/dE plot of the first and second cycles. Cycled at C/10.

The extraction processes displayed in the second cycle were identical to the first cycle. A decrease in the proportion of charge assigned to lithium extraction from the crystalline $Li_{15}Si_4$ phase at around 0.45 V was observed (**Figure 4-19b**), suggesting a reduced proportion of amorphous lithium silicide was converted to crystalline $Li_{15}Si_4$ during the insertion process.

4.3.5 Comparison of impedance measurements obtained in the first and third cycle

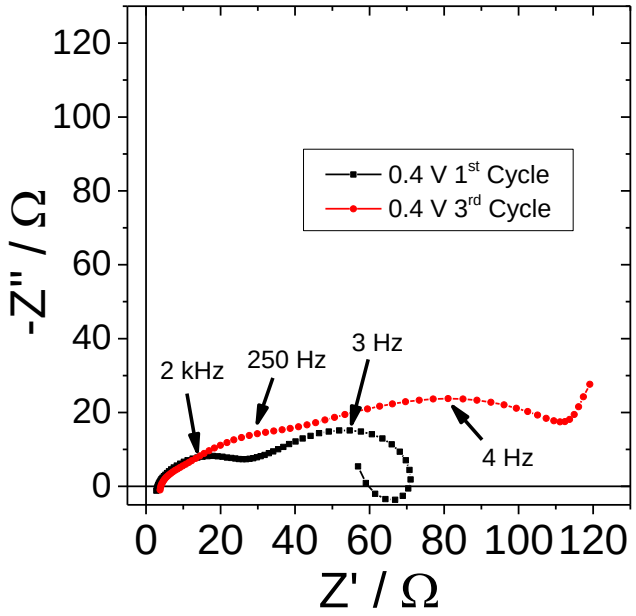

Figure 4-20 – Nyquist plot displaying a comparison of impedance spectra measured in the first and third cycle of a composite electrode. The spectra were recorded after relaxation of 1 hour 40 minutes at around 0.4 V during the insertion process. Spectra were recorded over the frequency range of 200 kHz to 0.1 Hz.

The voltage profile of the composite electrode in the third cycle was observed to be consistent with that of the second cycle. Impedance measurements obtained during lithium insertion at 0.4 V and 0.05 V in the third cycle are compared with measurements obtained in the first cycle (**Figure 4-20**, **Figure 4-21**). *Via* comparison of the impedance data obtained at 0.4 V it was observed that the impedance of the composite electrode had increased significantly (**Figure 4-20**). It was also observed that a pseudo-inductive loop was not present at 0.4 V in the third cycle. The absence of a pseudo-inductive loop suggests that the non-conventional electrolyte breakdown mechanism did not occur at 0.4 V in the third cycle. A possible reason for the lack of an pseudo-inductive response may be due to effective passivation of the active material at 0.4 V by the third cycle.

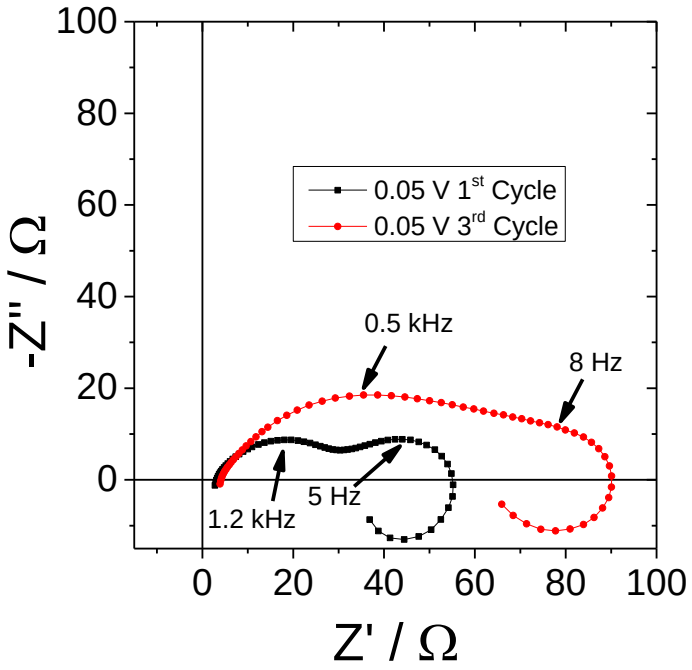

Figure 4-21 – Nyquist plot displaying a comparison of impedance spectra measured in the first and third cycle of a composite electrode. The spectra were recorded after relaxation of 1 hour 40 minutes at around 0.05 V during the insertion process. Spectra were recorded over the frequency range of 200 kHz to 0.1 Hz.

Direct comparison of impedance measurements obtained at 0.05 V during the first and third cycles is presented in **Figure 4-21**. An increase in the SEI resistance was observed. The spectrum displayed a general increase in impedance of the electrode by the 3rd cycle. A pseudo-inductive response was present at 0.05 V in the third cycle suggesting that at high lithium concentration the electrolyte breakdown process still occurred in the third cycle. Fitting of the spectra suggested that the pseudo-inductive response of the electrode at 0.05 V was lower in the third cycle compared to the first (*Appendix 4*). The decrease in pseudo-inductive response suggested a decrease in the amount of charge produced *via* electrolyte breakdown, this may be due to improved passivation of the electrode by the third cycle.

4.3.6 Extended cycling

The voltage profile and reversible capacity of a composite electrode throughout 50 electrochemical cycles are displayed in **Figure 4-22**. The reversible capacity was observed to decrease throughout cycling. By the 50th cycle less than 30 % of the initial reversible capacity was achieved. The decrease in reversible capacity can be associated with the loss in activity of the silicon particles within the composite electrode. The loss of activity could result from a combination of reduced electronic and ionic contact of the silicon particles within the composite electrode.

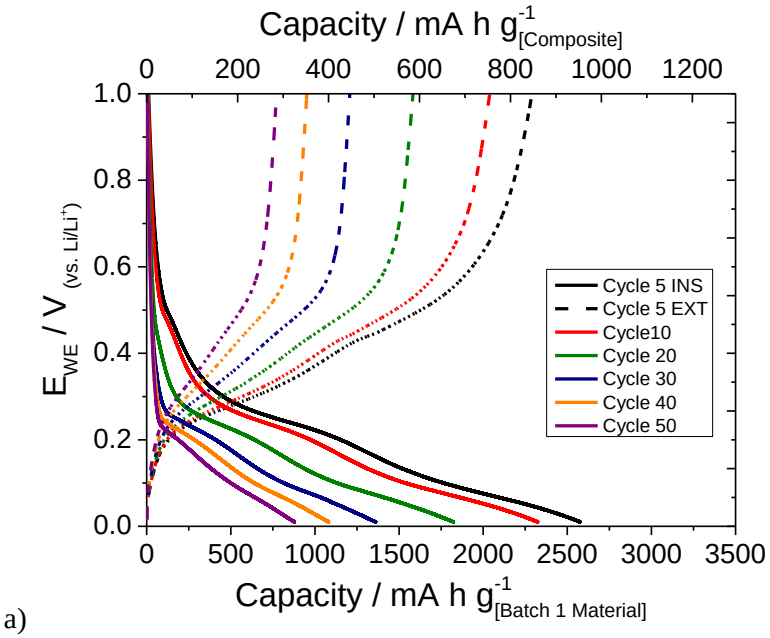

a)

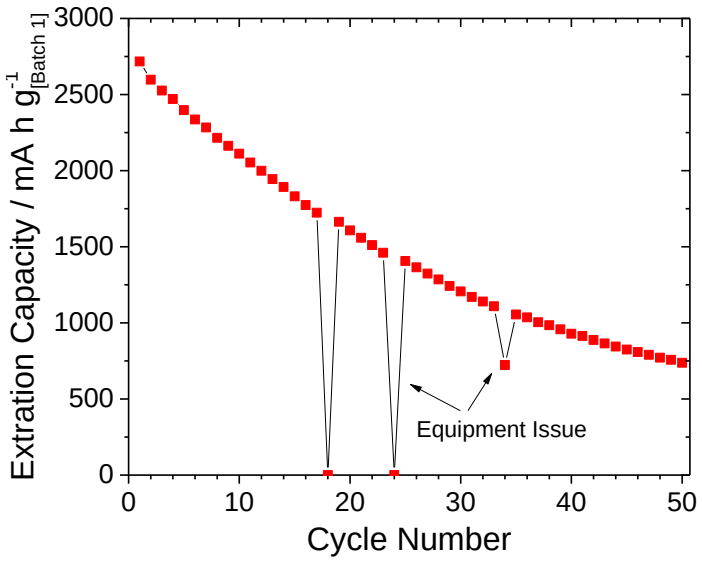

b)

Figure 4-22 – a) Voltage profile of a composite electrode during lithium insertion and lithium extraction highlighting various cycle numbers b) Plot displaying the extraction capacity achieved from a composite electrode over 50 cycles. Cycled at C/10.

Figure 4-23 displays dQ/dE plots of selected cycles voltage profiles, the peak at around 0.43 V associated with lithium extraction from the crystalline $Li_{15}Si_4$ phase was observed to display a disproportionate decrease throughout extended cycling. The decrease suggests that the number of active particles reaching the required concentration for the formation of the crystalline $Li_{15}Si_4$ decreased at a rate greater than the general loss of capacity. By the 20th cycle the reversible capacity has decreased by around 40 %, therefore the current density applied to the active material has increased by the same measure. The reduction in the amount of charge associated lithium extraction from the $Li_{15}Si_4$ phase which was observed to occur during extended cycling is suggested to be caused by the increase in current density applied to active silicon particles as the reversible capacity decreases.

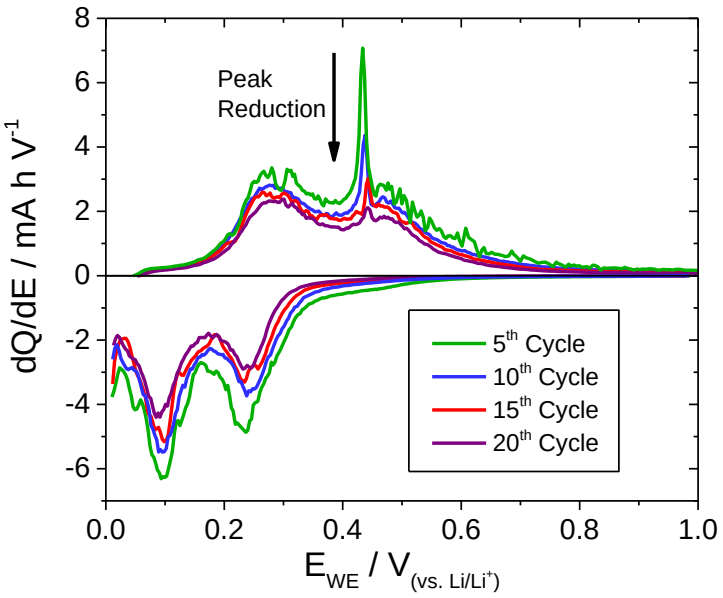

Figure 4-23 – dQ/dE plots highlighting changes to the a) lithium insertion process and b) lithium extraction process over the first 20 electrochemical cycles. Cycled at C/10.

Crystallisation of $Li_{15}Si_4$ requires a high concentration of lithium across a region of lithiated silicon, as the current density is increased the efficiency of lithium transport throughout the composite electrode will be reduced resulting in poor lithium transport to the back of the composite electrode. The high concentration of lithium required for crystallisation of $Li_{15}Si_4$ will therefore be achieved in a lower number of particles. Particles closest to the separator enjoy the most efficient lithium transport and as such would be expected to achieve the highest level of lithiation. Continual electrolyte breakdown processes will also contribute to reduce lithium transport throughout the composite electrode *via* formation of electrolyte breakdown products within the structure of the electrode.

4.4 Chapter conclusions

Initial characterisation

Via electrochemical analysis of composite electrodes containing batch-1 material it was observed that a significant amount of charge was passed at around 0.3 V during the initial lithium insertion reaction. The charge passed at this potential was assigned to lithium insertion into amorphous silicon present within the sample; the percentage of amorphous silicon within batch-1 material was estimated to be around 16 %.

Impedance measurements

Impedance measurements revealed a pseudo-inductive type process occurring in the lithiated composite electrode. Previous reports of similar pseudo-inductive type processes have been suggested to result from a relaxation process due to uneven lithium concentration within active material particles [13]. In this study a current interruption technique was used to cycle an electrode and allow for relaxation of the electrode during cycling which would be expected to result in an even distribution of lithium throughout the active material particles. The fact pseudo-inductive loops were observed suggested that an alternative process caused the pseudo-inductive response. A recent report by Radvanyi *et al.* [7] suggested that a pseudo-inductive response observed for composite electrodes containing nanosilicon active material was associated with an SEI formation/electrolyte breakdown process.

The results observed during the initial and third cycle correlated well with observations reported by Radvanyi *et al.* The pseudo-inductive response observed in this study is therefore suggested to be produced by a reaction between the lithiated surface of the active material and the electrolyte. The reaction results in the oxidation of the active material causing an opposing current flow which produces the inductive type effect, the reaction is activated by the varying potential applied to the electrode. The presence of the inductive loop suggests that a stable SEI layer was not formed during the initial lithium insertion reaction.

Extended cycling

Composite electrodes produced to a formulation of 37:37:26 (batch-1: carbon additive: PAA) displayed initial extraction capacities of 1000 mA h $g^{-1}_{(composite)}$ when cycled between 0.01 and 1.5 V, 70 % of the calculated theoretical capacity. Significant extraction of lithium from crystalline $Li_{15}Si_4$ was not observed suggesting $Li_{15}Si_4$ did not form throughout all particles within the electrode during insertion. The lack of formation of $Li_{15}Si_4$ suggested incomplete reaction of the nanowire particles. Capacity fade observed during extended cycling was attributed to a reduction in activity of silicon particles within the composite electrode throughout cycling. A reversible capacity of 300 mA h $g^{-1}_{(composite)}$ was observed after 50 cycles, 30 % of the initial reversible capacity.

4.5 Chapter references

1 S. D. Beattie, D. Larcher, M. Morcrette, B. Simon and J.-M. Tarascon, *J. Electrochem. Soc.*, 2008, **155**, A158.

2 K. Hiraoka, H. Shin and T. Yokoyama, *Polym. Bull.*, 1982, 303–309.

3 M. N. Obrovac and L. Christensen, *Electrochem. Solid-State Lett.*, 2004, **7**, A93.

4 J. Graetz, C. C. Ahn, R. Yazami and B. Fultz, *Electrochem. Solid-State Lett.*, 2003, **6**, A194.

5 K. Ogata, E. Salager, C. J. Kerr, a E. Fraser, C. Ducati, a J. Morris, S. Hofmann and C. P. Grey, *Nat. Commun.*, 2014, **5**, 3217.

6 T. L. Kulova, a. M. Skundin, Y. V. Pleskov, E. I. Terukov and O. I. Kon'kov, *J. Electroanal. Chem.*, 2007, **600**, 217–225.

6b J-M. Atebamba, J. Moskon, S. Pejovnik, and M. Gaberscek, *J. Electrochem. Soc.*, 2010, **157**, A1218-A1228.

7 E. Radvanyi, K. Van Havenbergh, W. Porcher, S. Jouanneau, J. S. Bridel, S. Put and S. Franger, *Electrochim. Acta*, 2014, **137**, 751–757.

8 F. Gutmann, *J. Electrochem. Soc.*, 1965, **112**, 94–98.

9 E. Radvanyi, W. Porcher, E. De Vito, A. Montani, S. Franger and S. Jouanneau Si Larbi, *Phys. Chem. Chem. Phys.*, 2014, **16**, 17142–17153.

9* P. Lu, C. Li, E. W. Schneider and S. J. Harris, *J. Phys. Chem. C*, 2014, **118**, 896–903.

10 Y. Oumellal, N. Delpuech, D. Mazouzi, N. Dupré, J. Gaubicher, P. Moreau, P. Soudan, B. Lestriez and D. Guyomard, *J. Mater. Chem.*, 2011, **21**, 6201.

11 M. D. Levi, *J. Electrochem. Soc.*, 1999, **146**, 1279.

12 C. Wang, a. J. Appleby and F. E. Little, *Electrochim. Acta*, 2001, **46**, 1793–1813.

13 J. S. Gnanaraj, R. W. Thompson, S. N. Iaconatti, J. F. DiCarlo and K. M. Abraham, *Electrochem. Solid-State Lett.*, 2005, **8**, A128.

Chapter 5: Structural changes of nanowire particles

5.1 Introduction

The volume and structural changes associated with the reversible formation of high lithium content lithium silicide have been suggested as explanations for the poor stability of silicon based electrodes [1]. The volume expansion is however intrinsic to the ability of silicon to store a large amount of lithium within its structure. Nanoscale particles of silicon have been shown to withstand the volume changes and remain intact after lithium insertion and extraction [2]. The following section investigates the structural changes which occur during reaction of SFLS synthesised nanowire material.

This chapter details experiments conducted to develop an understanding of the structural transformation SFLS silicon nanowire particles undergo during the initial cycle. Given that previous reports have mainly described the behaviour of silicon nanowires during electrochemical reactions in unusual situations e.g. within a TEM chamber, the present study was conducted to investigate structural changes of SFLS type silicon nanowires within a composite electrode.

5.2 Investigation into the structural changes during the first cycle

5.2.1 Sample preparation

Composite electrodes were discharged to various cut-off voltages corresponding to various degrees of reaction of lithium then charged to extract lithium prior to opening the cells. The electrodes were them washed with acetonitrile and a dilute nitric acid solution to remove any electrolyte and electrolyte breakdown products then dried. The voltage profiles of the composite electrodes from which samples were obtained are displayed in **Figure 5-1**. A relatively low C-rate of 0.05 C was used to cycle the composite electrodes so as to reduce differences in lithium distribution throughout the composite electrode thickness during reaction.

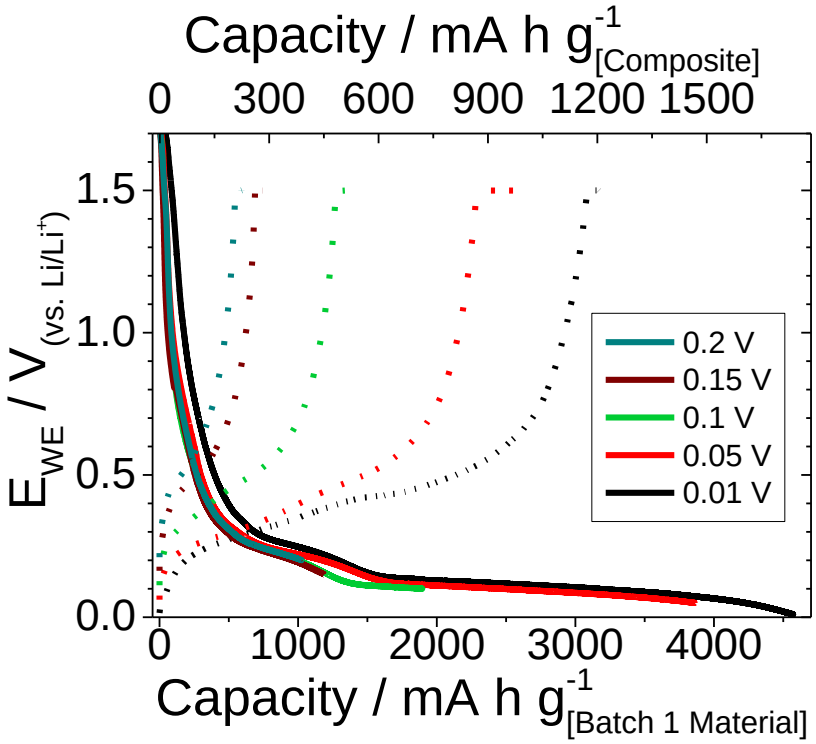

Figure 5-1 – Voltage profiles of the first cycle of composite electrodes containing batch-1 silicon nanowires. Cells were cycled at a rate C/20 to various potentials and then charged to 1.5 V and held for 12 hours.

5.2.2 Imaging of particles removed from composite electrodes with lower cut-off potentials of 0.2 and 0.15 V

SEM images of particles removed from composite electrodes after initial cycles with lower cut of potential of 0.2 V and 0.15 V are displayed in **Figure 5-2a, b** respectively.

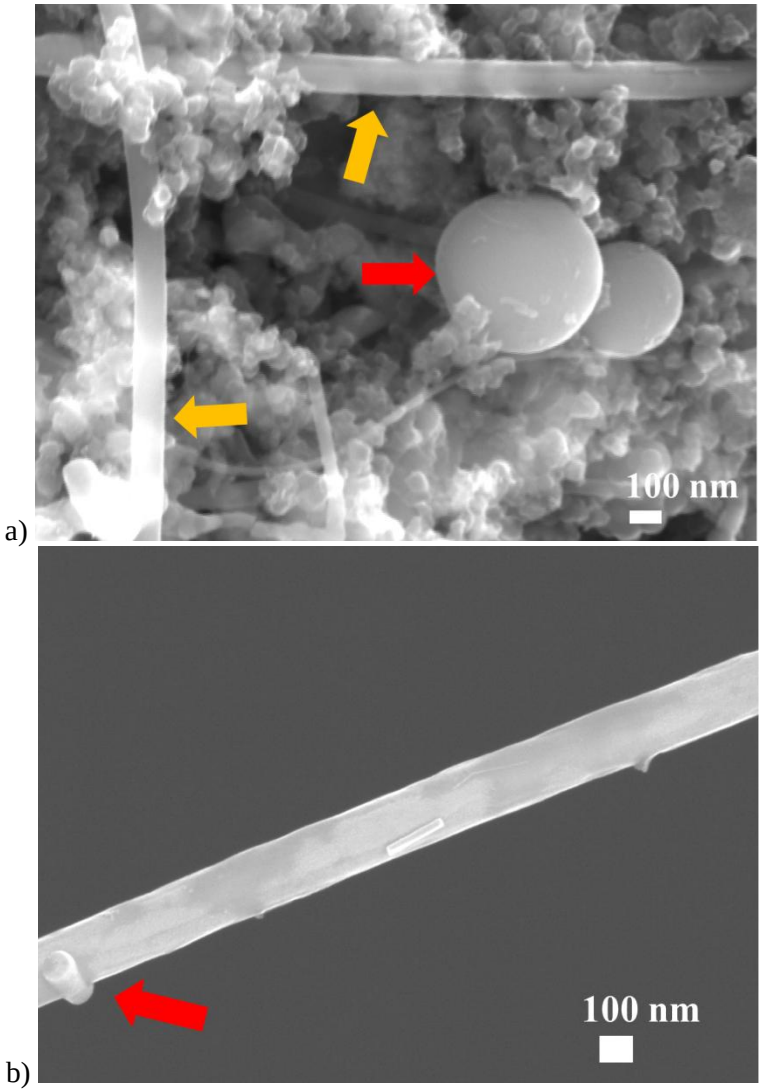

Figure 5-2 – Secondary electron SEM images of a) composite electrode fragment after an initial cycle with a lower cut-off potential of 0.2 V vs. Li/Li+. Red arrow highlights amorphous silicon particles. Orange arrows highlight silicon nanowire particles. b) Nanowire particle after an initial cycle with a lower cut-off potential of 0.15 V vs. Li/Li+. Red arrow highlights incorporation of one nanowire within another. Images acquired at 20 kV.

An image of a fragment of a composite electrode after an initial cycle with a lower cut-off potential of 0.2 V is displayed in **Figure 5-2a**. The structure of nanowire particles within the sample appeared smooth and straight, spherical amorphous silicon particles were observed to appear unchanged (**Figure 5-2a**). Nanowire particles recovered from a composite cycled to 0.15 V **Figure 5-2b** showed some surface roughness and also incorporation of one nanowire within another either during synthesis [3] or *via* 'welding' of silicon during lithium insertion [4]

a) 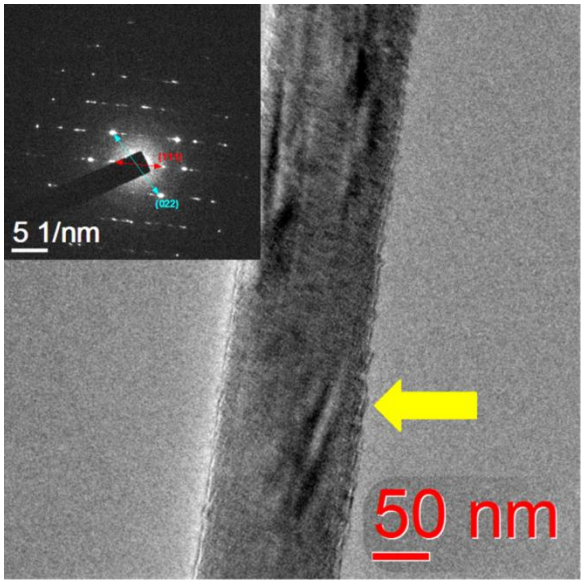

b) 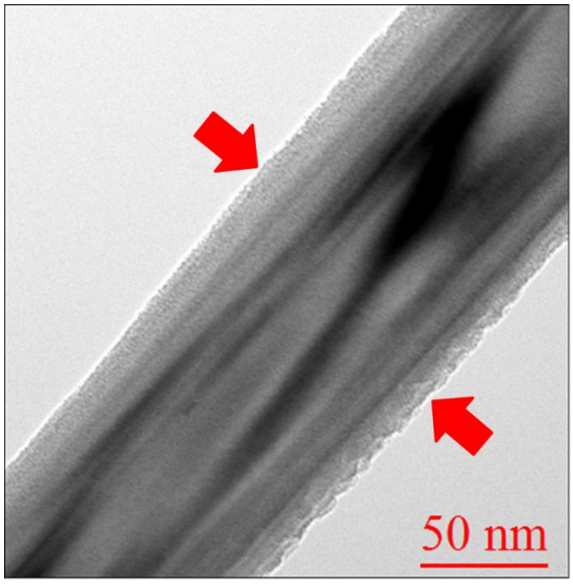

Figure 5-3 – BFTEM Images of nanowire particles removed from a composite electrode after 1 cycle with a lower cut-off voltage of 0.2 V. a) inset SAED pattern obtained from the nanowire imaged in a) the diffraction pattern displays a slight amorphous contribution, yellow arrow highlights the rough surface of the nanowire. b) Higher magnification image of a nanowire particle, red arrows highlight the rough amorphous surface.

TEM Images of nanowire particles removed from composite electrodes after an initial cycle with lower cut-off voltages of 0.2 V and 0.15 V are displayed in **Figure 5-3** and **Figure 5-4**. The difference in degree of reaction between the two samples is small. Nanowire particles from each sample displayed a similar structure.

A rough layer was observed at the surface of the nanowire particles removed from both samples (**Figure 5-3**, **Figure 5-4**). The layer was stable under the electron beam of the TEM suggesting that it was not composed of binder or electrolyte breakdown products. It is suggested that the layer was produced *via* the electrochemical reaction of lithium with a surface oxide layer and the outermost region of the crystalline nanowire structure. The rough surface structure corresponds well with the appearance of lithiated silicon oxide recently reported by Zhang *et al.*[5]. The rough surface was seen to be present along the entire length of nanowire particles, suggesting that electron transfer through the nanowire particles was not limiting.

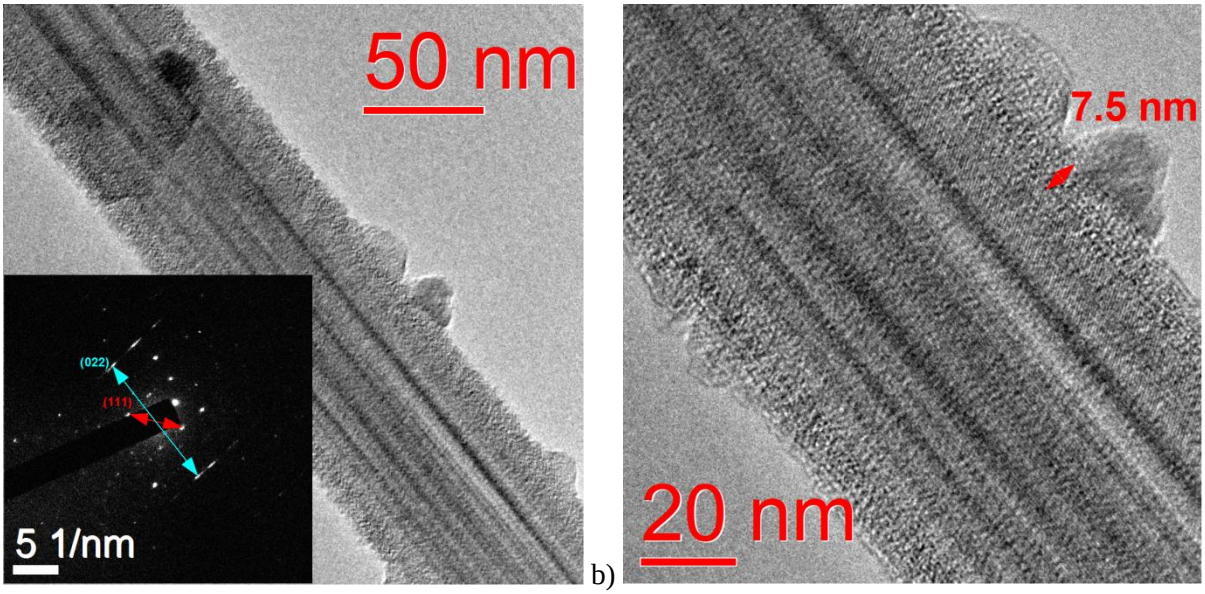

a) b)

Figure 5-4 – BFTEM Images of a nanowire particle removed from a composite electrode after 1 cycle with a lower cut-off voltage of 0.15 V, a) lower magnification image with an SAED pattern obtained from the imaged nanowire. b) Higher magnification image of the nanowire displayed in a) (a red arrow highlights the thickness of an amorphous layer observed at the surface of the nanowire particle)

The absence of structural changes to the crystalline core of both samples confirms that the reduction process observed at around 0.3 V in the voltage profile was not associated with significant reaction of lithium with the crystalline core of the nanowire particles.

5.2.3 Imaging of particles removed from a composite electrode with lower cut-off potentials of 0.1 V

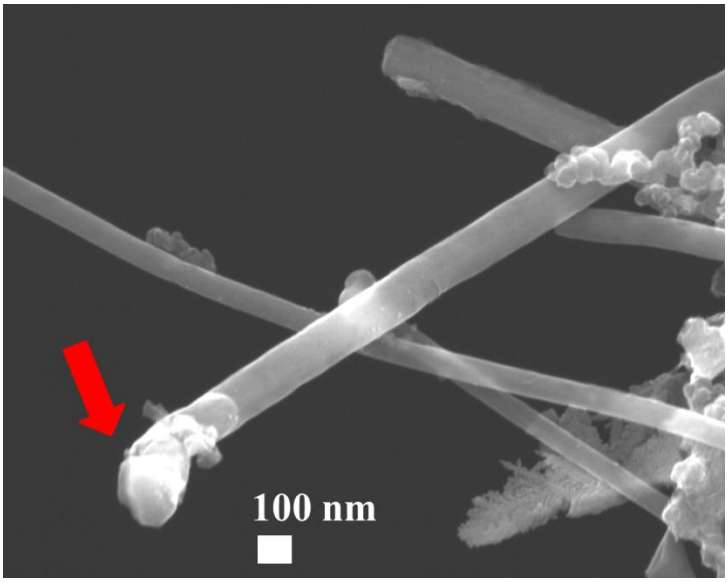

Figure 5-5 – Secondary electron SEM image of nanowire particles after an initial cycle with a lower cut-off potential of 0.1 V vs. Li/Li$^+$. Red arrow highlights the distorted structure of a gold seed particle at the end of a nanowire. Image acquired at 20 kV.

An SEM image of a fragment of a composite electrode after 1 cycle with a lower cut-off voltage of 0.1 V is displayed in **Figure 5-5**. The red arrow highlights the structure of a gold seed at the end of a nanowire particle, the deformation suggesting that the gold seed particle reacted with lithium before 0.1 V, as suggested in section 4.3.3.1.

TEM images of nanowire particles taken from composite electrodes cycled to 0.1 V displayed an amorphous surface layer of around 15 nm at the surface of nanowire particles , a thicker layer than that observed in particles from composites with cut-off potentials of 0.2 or 0.15 V (**Figure 5-6**). An increase in amorphous silicon content was observed by an increase in intensity of amorphous bands in the electron diffraction patterns of the nanowire particles displayed in **Figure 5-6**. The formation of a thicker amorphous region at the surface of the nanowire particles suggests that reaction of lithium with a portion of the crystalline core had occurred. The amorphous layer was observed to be uniform across the surface and along the length of particles suggesting that transport of lithium ions or electrons across the nanowire structure were not rate limiting factors under the conditions used here.

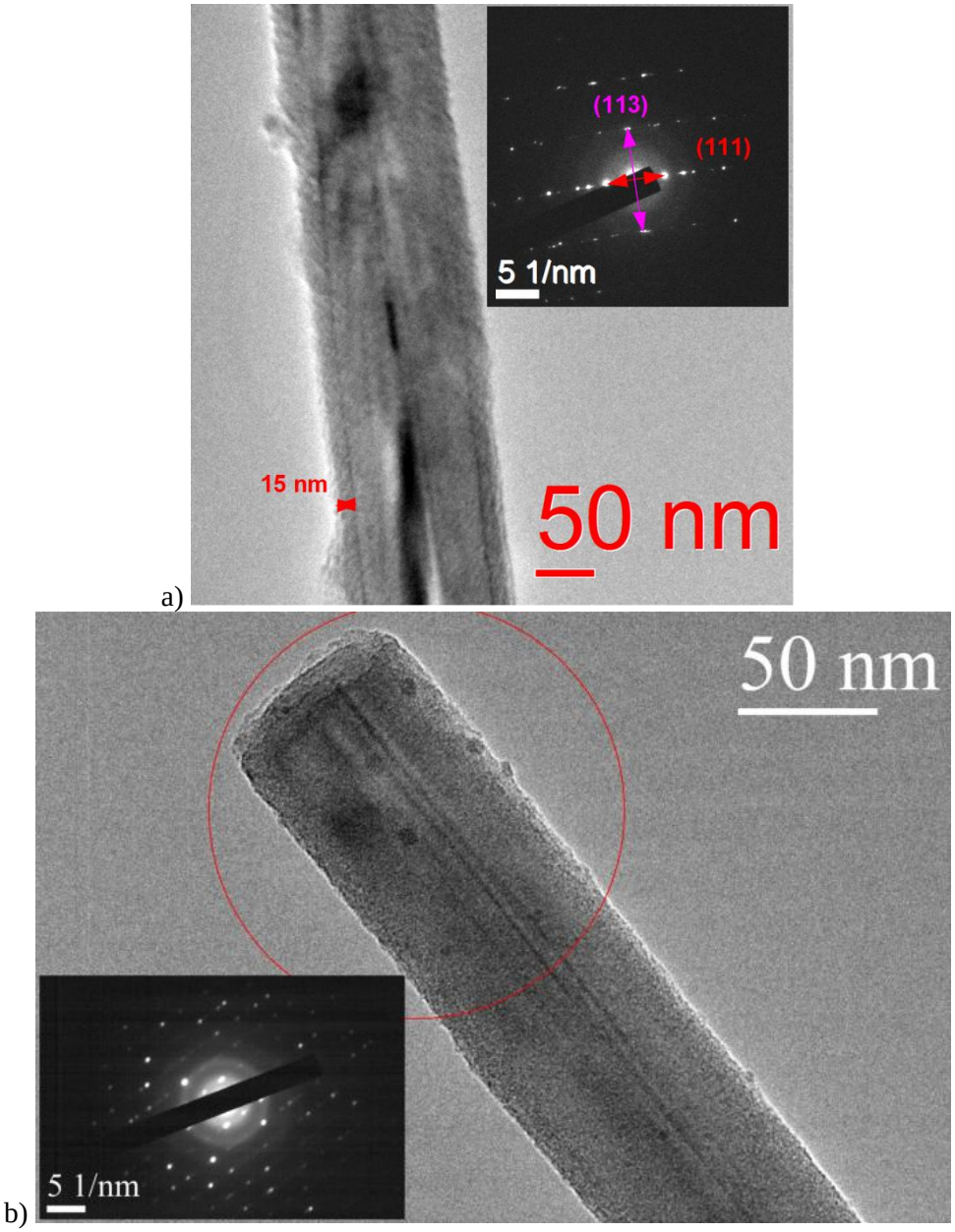

Figure 5-6 – BFTEM images with inset SAED pattern of nanowire particles removed from a composite electrode after 1 cycle with a lower cut-off voltage of 0.1 V. Red arrow in a) displays the thickness of the amorphous region at the surface of the nanowire particle.

A high proportion of nanowire particles were observed to display a different structure; an example of which is displayed in **Figure 5-7**. Amorphous regions where observed to have formed throughout the thickness of some particles, resulting in the formation of a segmented crystalline core. Reaction throughout the thickness of the nanowire occurred at two locations on the particle displayed in **Figure 5-7**, highlighted by red arrows in **Figure 5-7a**. A recent report by Wang *et al.* described similar observations of radial lithiation of silicon nanowires resulting in the formation of crystalline segments, the cause of radial reaction was suggested to be due to the presence of defects within the nanowire structure [6].

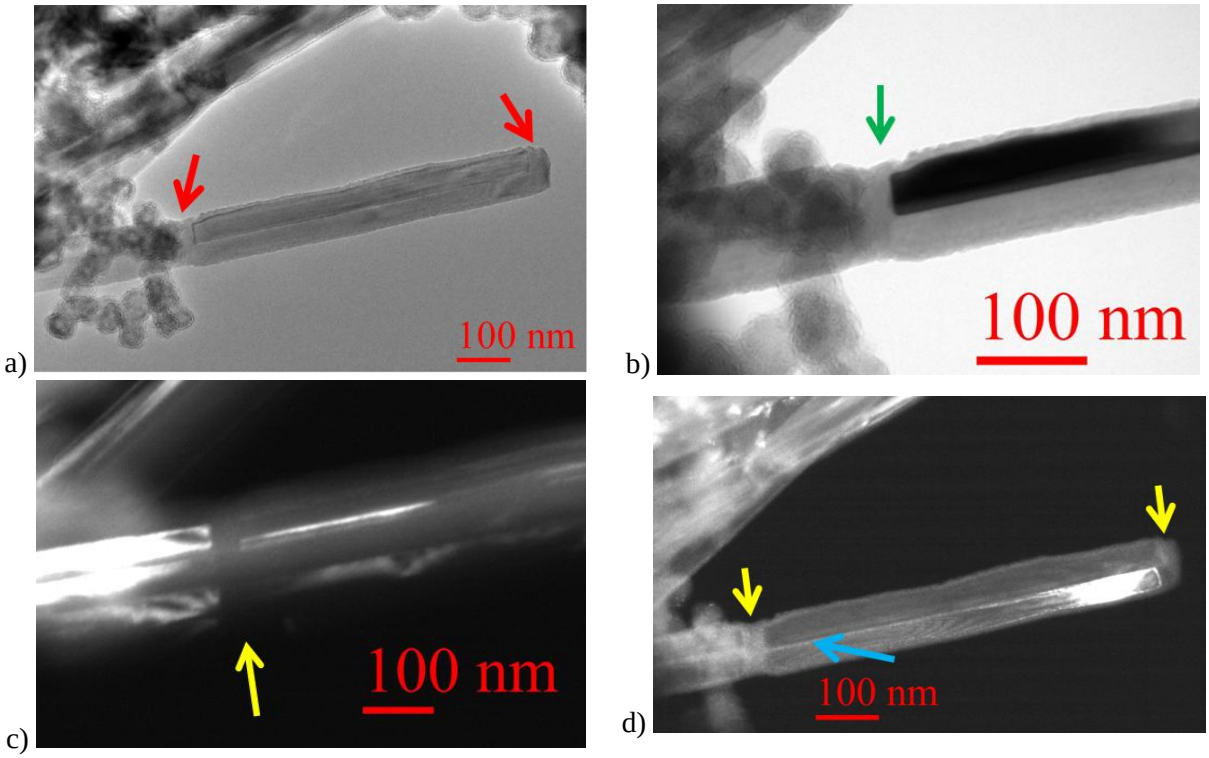

Figure 5-7 – Images of a sample removed from a composite electrode after 1 cycle with a lower cut-off voltage of 0.1V. a) Bright field image, b) higher magnification image of the amorphous region. C) Dark field image highlighting absence of crystallinity. Arrows highlight the presence of amorphous regions throughout the thickness of the nanowire particle. The blue arrow in d) highlights a boundary running along the length of the particle highlighting the twinned nature of the particle.

Figure 5-7b and c, show dark field images, collected from <111> diffraction spots. The clear break of the crystal structure can be observed in the DFTEM images, the crystal appearing as a dark region in b) and a bright region in c). **Figure 5-7d** displays a DFTEM image of the nanowire highlighting the presence of twin crystals which share a mirror plane running parallel to the length direction of the nanowire. Amorphous surface layers are highlighted by yellow arrows, interestingly a region of similar contrast to the amorphous edges was observed running between the interface of the twinned crystals, the amorphous appearance of the region suggested that reaction occurred along the interface between the twinned crystals.

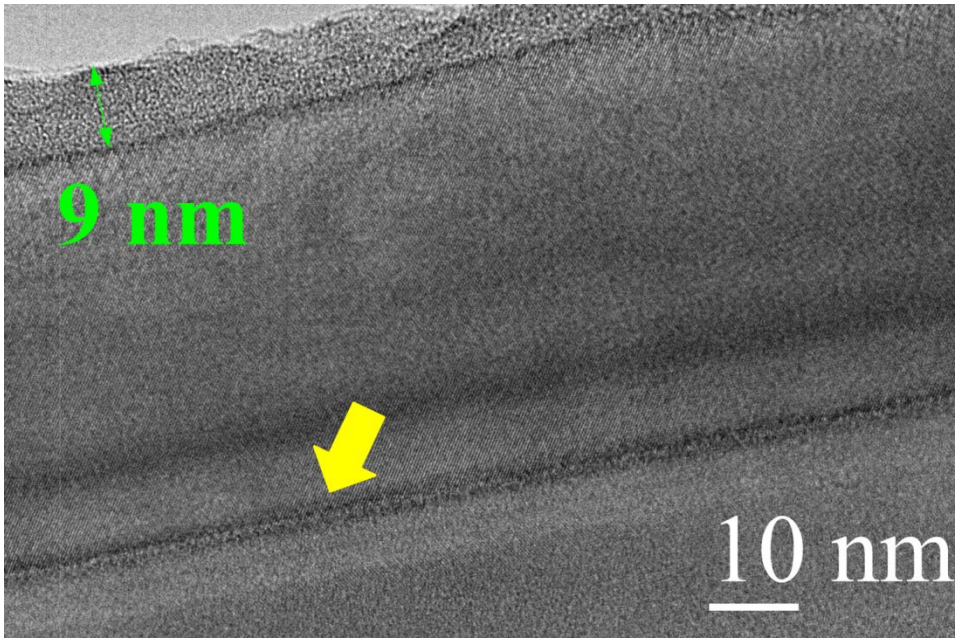

Figure 5-8 – High magnification image of area highlighted by blue arrow in Figure 5-7d. Image displays the amorphous surface layer to be ~9 nm thick (green arrow). The yellow arrow highlights the amorphous region at the twin boundary.

The high magnification image in **Figure 5-8** shows a sharp interface between the crystalline region and the 9 nm amorphous surface layer. A thin amorphous band appeared to be present at the interface between the twinned crystals, highlighted by a yellow arrow. Lattice fringes were observed across the crystalline regions.

5.2.4 Imaging of particles removed from a composite electrode with lower cut-off potentials of 0.05 V

SEM images taken for the cut-off potential of 0.05 V are displayed in **Figure 5-9**. The particles show a much rougher surface with surface cracks running parallel to the length of the particles (highlighted by red arrows in **Figure 5-9**). The images suggest that the structure of a number of nanowire particles did not prevent formation of cracks. Larger diameter particles were observed to display surface cracks. The reduction of nanowire diameter has previously been reported to be critical to the prevent fracture [8]. Despite surface cracks the nanowire particles retained nanowire morphology. Amorphous silicon particles previously observed to be spherical were found to be slightly deformed (**Figure 5-9b**, yellow arrow).

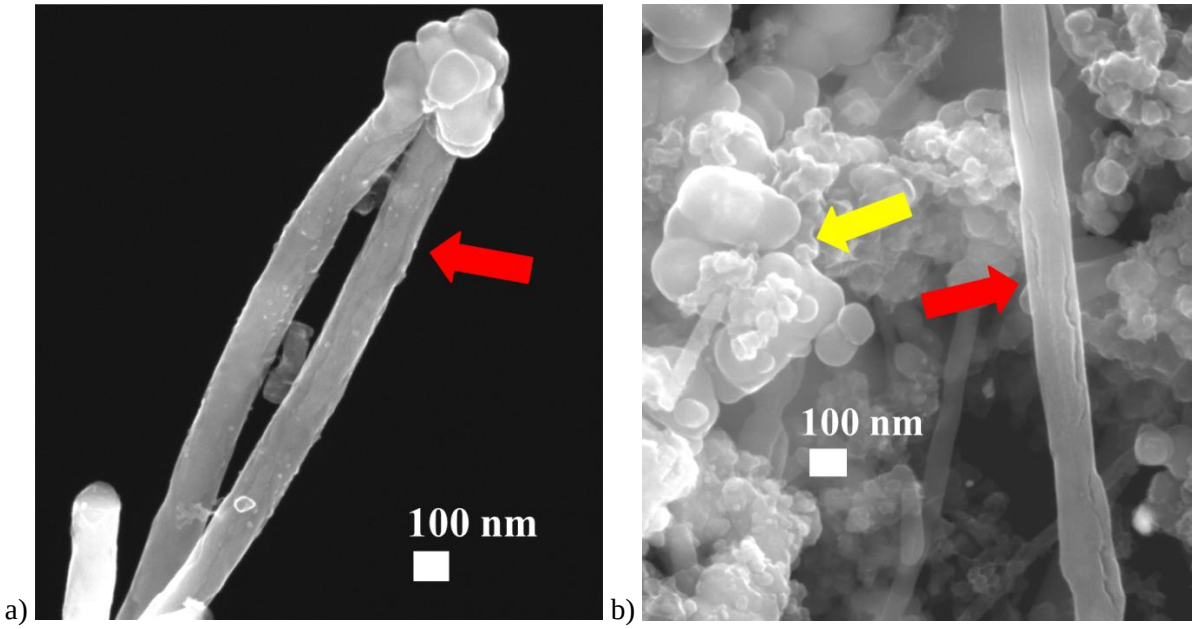

Figure 5-9 – Secondary electron SEM image of nanowire particles after an initial cycle with a lower cut-off potential of 0.1 V vs. Li/Li$^+$. a) Red arrow highlights the rough surface of the nanowire particle. b) Red arrow highlights surface cracks parallel to the length of the particle. Yellow arrow highlights distorted amorphous silicon particles. Images acquired at 20 kV.

TEM images of nanowire particles removed from a composite electrode after 1 cycle with a lower cut-off potential of 0.05V are displayed in **Figure 5-10**, **Figure 5-11** and **Figure 5-12**. The particles displayed a similar structure to particles removed from an electrode with a 0.1V cut-off except that a significantly thicker amorphous layer was observed. Further reaction of the crystalline core appeared to have resulted in formation of a thicker amorphous layer. Interestingly the distance between the separated crystals in the axial direction remained at roughly 20 nm (**Figure 5-10b**), suggesting that axial reaction resulting in amorphous regions throughout the particles occurred at localised defects.

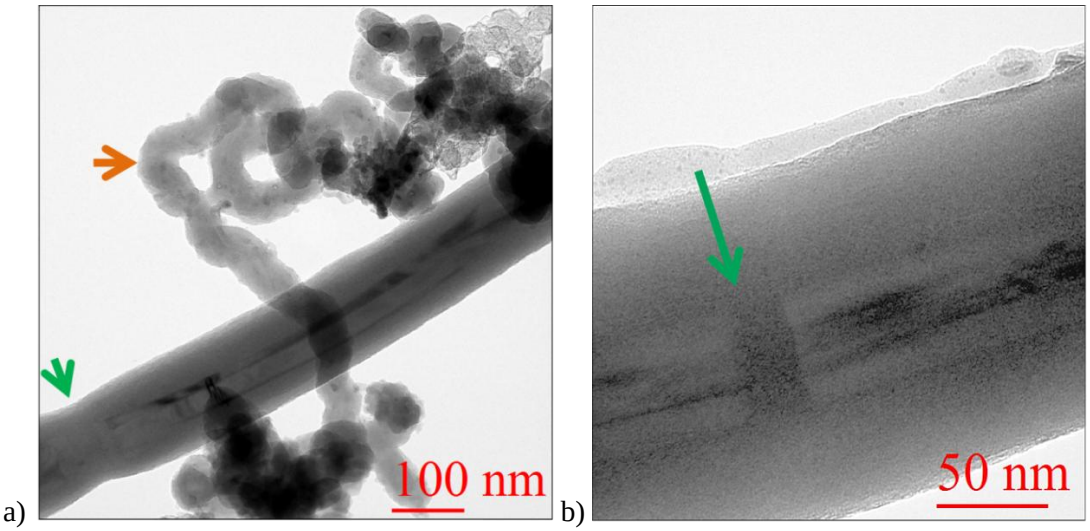

Figure 5-10 – BFTEM images of a nanowire particle removed from a composite electrode after 1 cycle with a lower cut-off voltage of 0.05 V at different magnifications. Green arrows highlight the location of a fracture of the crystalline core of the nanowire particle. The orange arrow highlights a twisted nanowire particle.

Figure 5-11 displays the internal structure of another nanowire, the thickness of amorphous silicon between crystalline fragments of the core was 14 nm, and the thickness of the amorphous surface region was 56 nm. EELS spectra (**Figure 5-11b**) obtained from the highlighted positions in **Figure 5-11a** display the differing bonding environments of silicon. The sharper peak observed at around 96 eV at position 1 confirms the increased crystallinity compared to position 2. The absence of a definable peak at position 2 indicated the amorphous nature of the silicon present at the location [9].

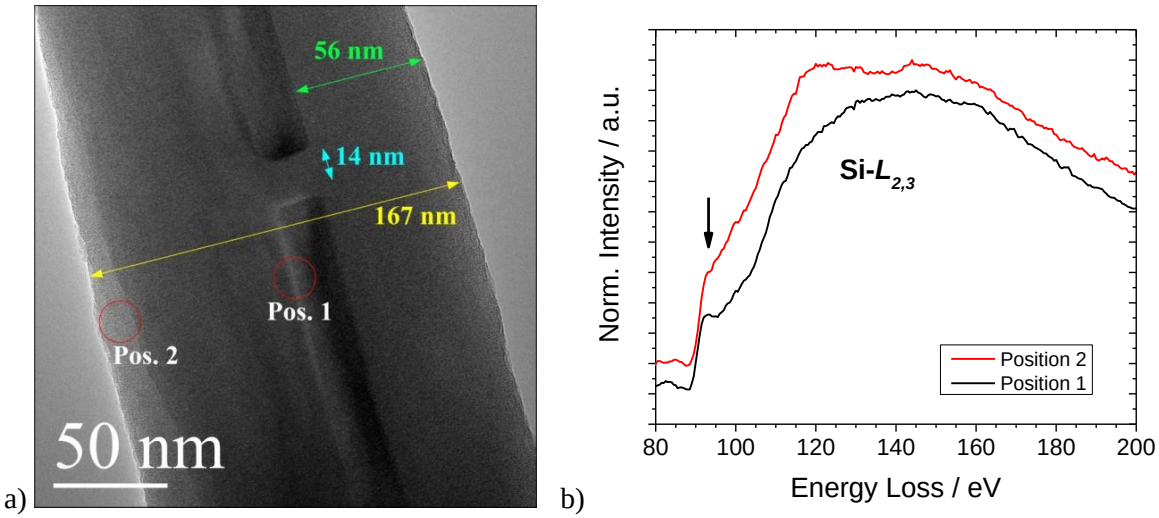

Figure 5-11 – a) BFTEM image of a nanowire particle removed from a composite electrode after 1 cycle with a lower cut-off voltage of 0.05 V. b) EELS spectra corresponding to the Si–$L_{2,3}$ core-loss edge (0.5 eV per channel, average of 10 acquisitions each of 10 seconds) obtained from positions 1 and 2 highlighted in a), black arrow highlights the peak which corresponds to level of crystallinity [9], the intensity of the traces are normalised and offset for clarity.

The amorphous surface layer thickness was also observed to depend on the thickness of the nanowire particle, nanowire particles of similar diameter were observed to display an amorphous layer of around the same thickness (**Figure 5-12**).The amorphous content of the particles was confirmed *via* electron diffraction and observation of the intensity of the rings characteristic of amorphous silicon.

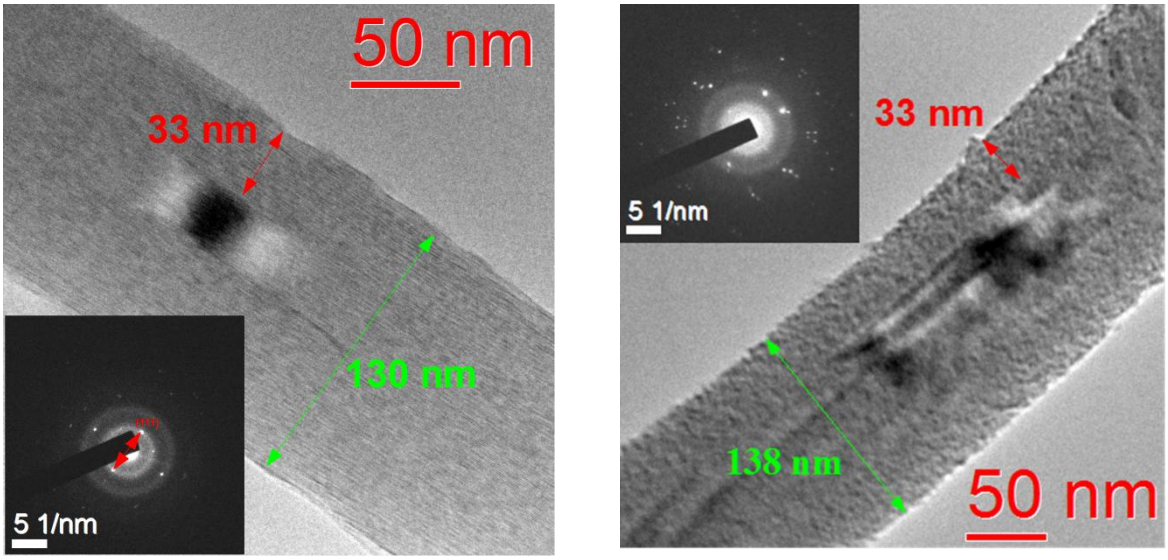

Figure 5-12 – BFTEM images of nanowire particles removed from a composite electrode after 1 cycle with a lower cut-off voltage of 0.05 V. Inset are SAED patterns which highlight the amorphous content of the particles. Red arrows highlight the thickness of the amorphous region of the particles.

5.2.5 Imaging of particles removed from a composite electrode with a lower cut-off potential of 0.01 V

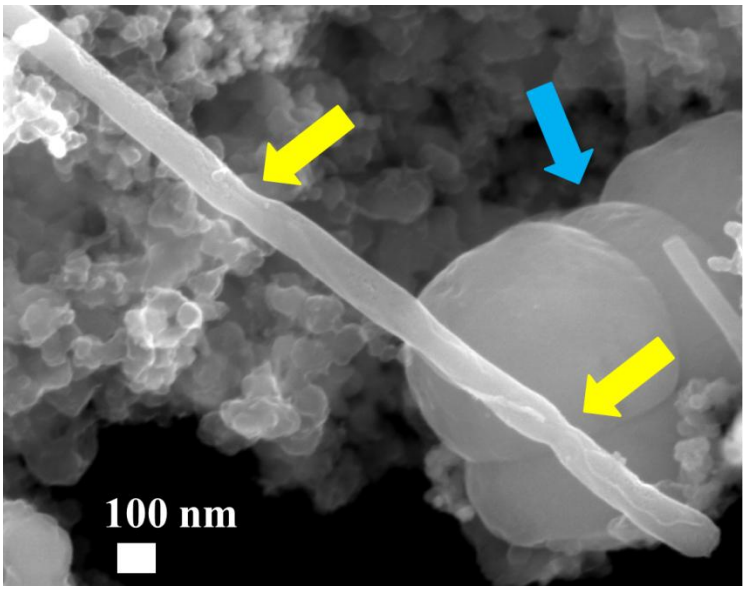

Figure 5-13 – Secondary electron SEM image of nanowire particles after an initial cycle with a lower cut-off potential of 0.01 V vs. Li/Li$^+$. Yellow arrows highlight the location of stretched regions of the nanowire particle. The blue arrow highlights large particles of amorphous silicon. Images acquired at 20 kV.

Figure 5-13, and **Figure 5-14** display images of particles removed from a sample with a lower cut-off potential of 0.01 V. A segmentation effect along the length of the nanowire particles was observed. Yellow arrows highlight stretched regions of the particle which displayed a local decrease in diameter. The deformed structure of amorphous silicon particles were also observed in **Figure 5-13**. Despite the large diameter the particles did not appear to fracture, this observation corresponds with the reported stability of amorphous silicon structures [10]. Further

evidence of the segmentation of nanowire particles is displayed in **Figure 5-14**. The majority of nanowire particles were observed to display a segmented type structure. The length and location of segments appeared to be random. Gold seed particles were not evident at the ends of a number of nanowire particles suggesting that segments of the nanowire may have become detached from the particle.

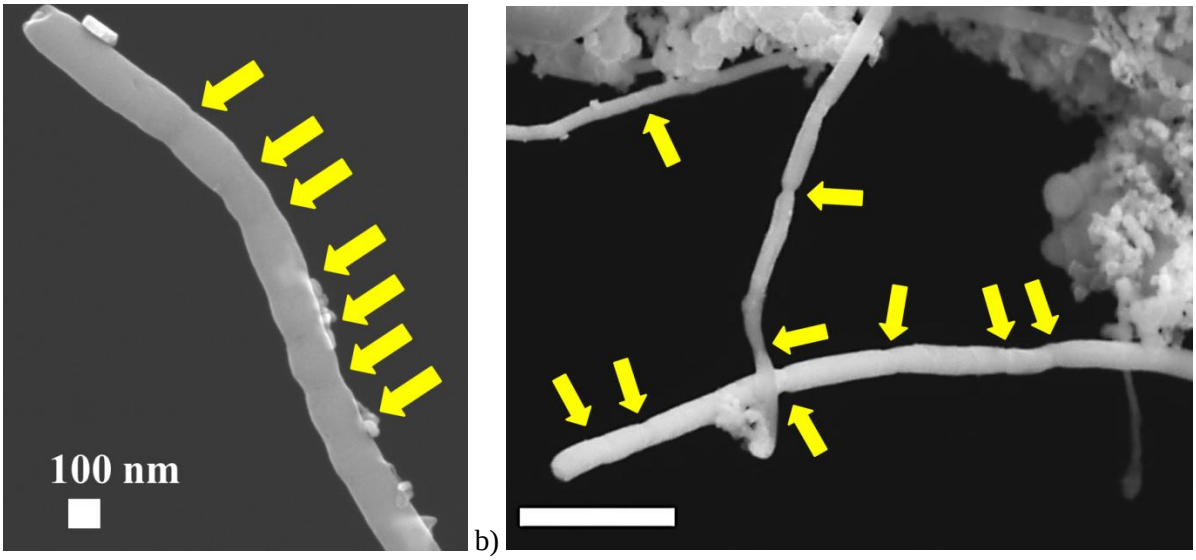

Figure 5-14 – Secondary electron SEM image of a nanowire particle after an initial cycle with a lower cut-off potential of 0.01 V vs. Li/Li$^+$. Yellow arrows highlight the location of stretched regions of the nanowire particle. The nanowire particle displays a segmented structure. Scale bar of image b = 1 µm Images acquired at 20 kV.

TEM imaging of a nanowire from the same sample display the segmented structure at higher magnification (**Figure 5-15)**. The particle was observed to be completely amorphous; no crystalline regions were present within the particle. The nanowire particle was curved and displayed surface roughness. Surface cracks were observed running parallel to the length of the particle. The region of reduced diameter appeared to have formed by a stretching type process. **Figure 5-15b** displays a high magnification image of the stretched region.

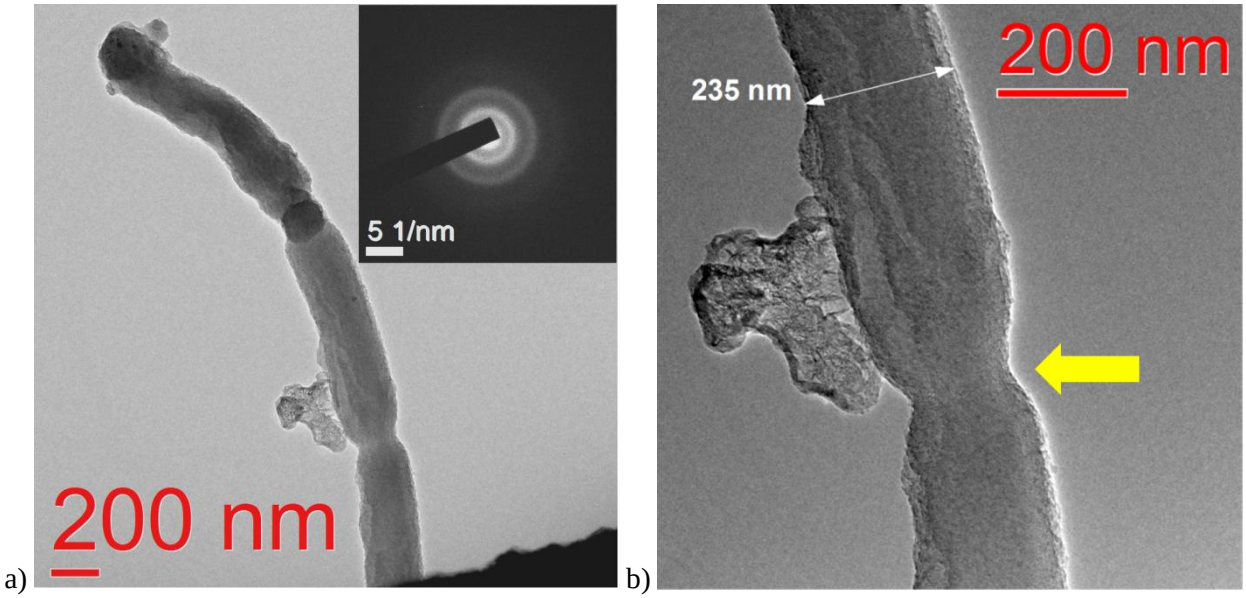

Figure 5-15 – a) Image of a nanowire particle removed from a composite electrode after 1 cycle with a lower cut-off voltage of 0.01V, particle displays the segmentation observed within a high proportion of nanowire particles. b) Higher magnification image of the particle highlighting the connection between two segments (yellow arrow) and the presence of surface cracks.

The segmented structure and reduced diameter of the particle displayed in **Figure 5-10a** corresponded well with the structure of particles observed in previous samples. The stretched region highlighted in **Figure 5-10b** is suggested to originate at a location which was previously (at a lower level of reaction) an amorphous region between two crystalline core fragments.

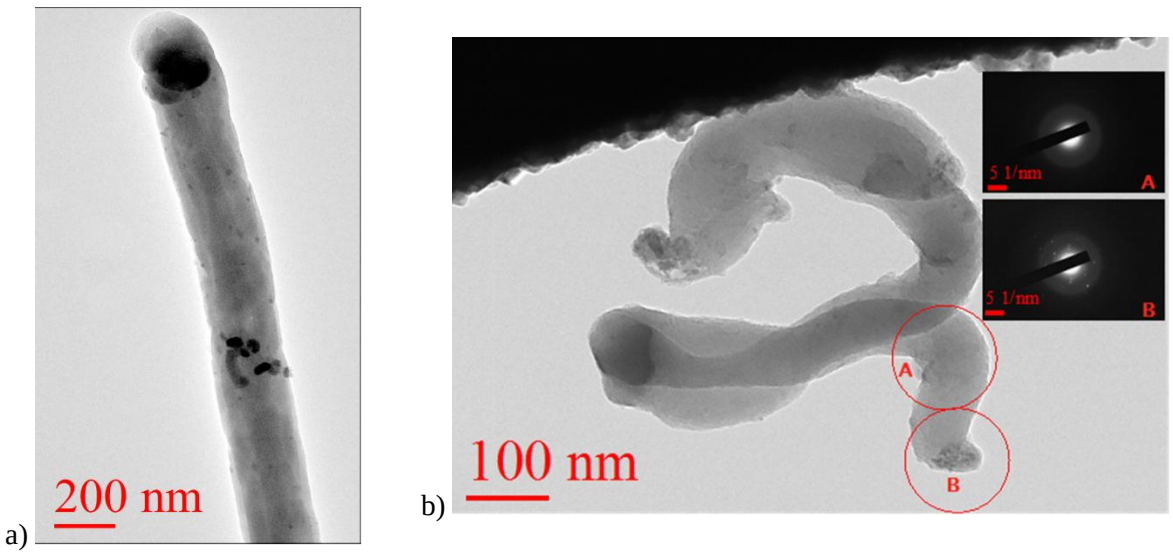

Figure 5-16 – BFTEM Images of nanowire particles removed from a composite electrode after 1 cycle with a lower cut-off voltage of 0.01 V. a) nanowire particle displaying no indication of fracture. b) Nanowire which has split along its length, SAED patterns obtained from the imaged nanowire are inset.

It should be noted not all of the nanowire particles displayed the typical segmented structure. Examples of alternative particle structures are displayed in **Figure 5-16**. **Figure 5-16a** displays a straight amorphous nanowire which did not show any evidence of stretched regions or a

segmented structure along its length. The particle displayed in **Figure 5-16b** was observed to display a twinned structure and a fracture of resulting in the splitting of the particle along a section of its length. The particle was observed generally to be amorphous throughout except for at the location of the fracture as shown by inset electron diffraction patterns. Splitting of nanowire particles during lithium insertion has been reported by Liu *et al.*[11] to occur in [112] orientated nanowires which displayed twinning.

5.3 Summary of observed structural changes

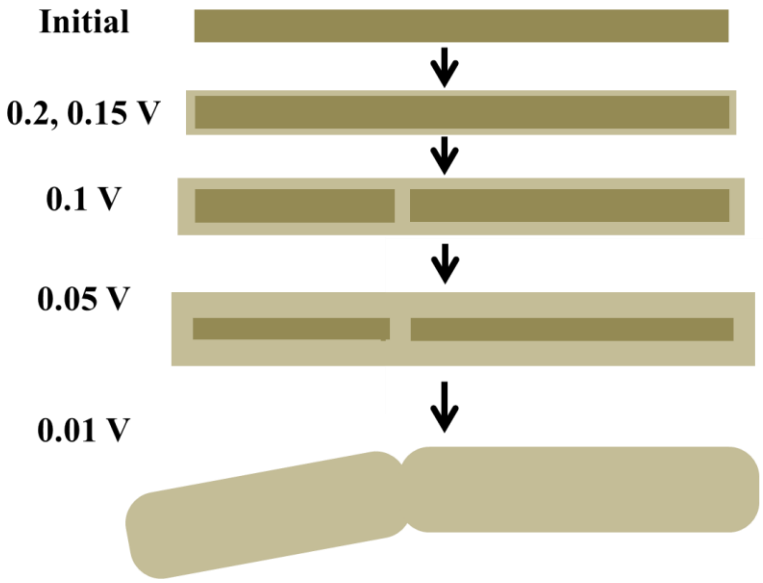

Figure 5-17 – Simplified model of reaction progress observed in the majority of SFLS type nanowire particles taken from composite electrodes after 1 cycle with various lower cut-off potentials. Dark brown represents crystalline silicon, light brown indicates amorphous silicon.
Figure 5-18

Reaction was observed to occur across the surface of the nanowire particles in samples with lower cut-off voltages of 0.2 and 0.15 V. In samples with a lower cut-off of 0.1V reaction was also observed to have occurred throughout the core of nanowire particles at random locations along the length. For amorphisation of the crystalline core to occur as observed lithium ions would have required access to the core at the specific location within the particle. Access to the core may have occurred either *via* the presence of defects running perpendicular to the growth direction of the nanowire, or *via* fracture of crystalline core due to a build-up of stress. Fracture of the crystalline core is suggested to be an unlikely mechanism as fracture of the core would be expected to cause the particle to fracture completely into two fragments, which was not observed. The most likely method by which lithium gained access to the core of the particle at an isolated section along its length is suggested to be *via* defects within the particle.

Previous reports on the electrochemical amorphisation of silicon have suggested preferential reaction along defects within silicon particles [6,12,13]. A detailed study of defects present within the structure of the nanowire particles was not conducted, however, a high density of defects were observed in a number of nanowire particles, and defects are commonly reported to be present within silicon nanowires [14,15]. Once access to the core is established the formation of an amorphous region within the nanowire as observed, could then be explained *via* preferential reaction of lithium with the defected structure.

The growth direction of silicon nanowire particles produced *via* the same synthesis process under similar conditions have previously been reported by Heitsch *et al.* [16], nanowire particles were observed to display growth directions predominantly of <110>, with some particles displaying <111> and <112> . Volume expansion of silicon pillars has been reported to occur preferentially in the <110> direction in crystalline silicon [17]. Assuming the growth direction of the majority of particles in the sample to be <110>, volume expansion would be expected to preferentially occur in the axial and radial <110> directions (**Figure 5-19**).

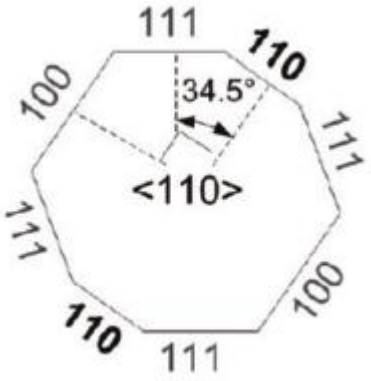

Figure 5-19 - Plan view of a <110> silicon pillar highlighting the exposed crystal faces Reprinted with permission from reference[17]. Copyright 2011 American Chemical Society.

Preferential reaction in the axial direction would initially explain the observed structure of nanowire particles (cycled with a lower cut-off of 0.1 V, **Figure 5-7**) in which the thickness of the axial amorphous region was thicker than the amorphous surface layer. However, particles removed from a composite electrode cycled with a cut-off of 0.05 V displayed formation of amorphous regions in the axial direction of a similar thickness to that observed in particles removed from a composite electrode cycled with a cut-off of 0.1 V, this observation suggests that reaction of the nanowire particles below 0.1 V occurred mainly *via* radial expansion. Axial reaction is therefore suggested to only occur at around 0.1V during insertion and be restricted to specific regions containing defects running normal to the growth direction.

Formation of the segmented amorphous nanowire structure observed in particles removed from an electrode with a lower cut-off of 0.01 V suggested further reaction resulting in a stretching of the segments may have occurred at higher degrees of lithium reaction. Silicon has been reported to undergo plastic flow during lithium insertion and extraction which may also contribute to the observed structural changes during the initial cycle [19, 20]. The mechanical influence of the binder may also act to influence the structural changes observed. The differing response of a number of particles to the insertion and extraction process is suggested to be due to the varied initial structure of the particles, nanowire growth orientation and concentration of defects within the particles

5.4 Chapter conclusions

The results of this study suggest that the majority of nanowires retain nanowire type morphology after the significant structural rearrangement of the first cycle. When cycled in a composite electrode configuration the structural evolution of SFLS type nanowire particles appeared to be quite dissimilar to that previously observed of silicon nanowires *via* in-situ TEM experiments. Defects are suggested to play a significant role in the structural evolution of the SFLS nanowire particles. Variation in lithium transport within a composite electrode compared to in-situ TEM experiments; in which lithium transport usually occurs *via* the nanowire itself, may also cause contribute to the observed variation in particle structure. A recent report which presents similar axial amorphisation of silicon nanowires has been published by Wang *et al.*[6].

The complex morphology of the particles within the sample causes the structural changes which occur to be difficult to define universally, however, after 1 cycle with a lower potential limit of 0.01 V, the majority of originally straight nanowire particles displayed an amorphous segmented type structure. A possible explanation for the formation of the segmented structure has been suggested to be due to the presence of defects and the preferential reaction of lithium at the site of defects, however further more detailed experiments would be required to confirm the presence and type of defect and develop a clearer understanding of the crystal structure of the nanowire particles. The influence of defects within SFLS type nanowire particles is suggested to play a significant role in the structural evolution of the particles during electrochemical reaction.

It is suggested that axial expansion of nanowire type particles should be avoided to reduce the structural rearrangement of the composite electrode during the initial cycle. Nanowire particles with a growth direction of <110>, as previously reported for nanowire material produced *via* a SFLS method utilising trisilane and gold seed crystals [16], should be avoided as the lithium insertion reaction has been demonstrated to preferentially occur in the <110> direction. Particles with a <111> growth direction would be expected to display preferential radial expansion and hence the first cycle structural rearrangement occurring within a composite electrode would be minimised, the presence of defects normal to the growth direction of the nanowire particles should also be avoided to prevent axial expansion.

5.5 Chapter references

1 U. Kasavajjula, C. Wang and a Appleby, *J. Power Sources*, 2007, **163**, 1003–1039.

2 X. Liu, L. Zhong, S. Huang, S. Mao, T. Zhu and J. Huang, *ACS Nano*, 2012, 1522–1531.

3 H. T. Nguyen, F. Yao, M. R. Zamfir, C. Biswas, K. P. So, Y. H. Lee, S. M. Kim, S. N. Cha, J. M. Kim and D. Pribat, *Adv. Energy Mater.*, 2011, **1**, 1154–1161.

4 K. Karki, E. Epstein, J.-H. Cho, Z. Jia, T. Li, S. T. Picraux, C. Wang and J. Cumings, *Nano Lett.*, 2012, **12**, 1392–7.

5 Y. Zhang, Y. Li, Z. Wang and K. Zhao, *Nano Lett.*, 2014, 7161–7170.

6 L. Wang, D. Liu, S. Yang, X. Tian, G. Zhang, W. Wang, E. Wang, Z. Xu and X. Bai, *ACS Nano*, 2014, 8249–8254.

7 X. H. Liu, J. W. Wang, S. Huang, F. Fan, X. Huang, Y. Liu, S. Krylyuk, J. Yoo, S. a. Dayeh, A. V. Davydov, S. X. Mao, S. T. Picraux, S. Zhang, J. Li, T. Zhu and J. Y. Huang, *Nat. Nanotechnol.*, 2012, **7**.

8 I. Ryu, J. W. Choi, Y. Cui and W. D. Nix, *J. Mech. Phys. Solids*, 2011, **59**, 1717–1730.

9 Y. Yan, M. Page, T. H. Wang, M. M. Al-Jassim, H. M. Branz and Q. Wang, *Appl. Phys. Lett.*, 2006, **88**, 1–4.

10 L. a. Berla, S. W. Lee, I. Ryu, Y. Cui and W. D. Nix, *J. Power Sources*, 2014, **258**, 253–259.

11 X. H. Liu, H. Zheng, L. Zhong, S. Huang, K. Karki, L. Q. Zhang, Y. Liu, A. Kushima, W. T. Liang, J. W. Wang, J.-H. Cho, E. Epstein, S. a Dayeh, S. T. Picraux, T. Zhu, J. Li, J. P. Sullivan, J. Cumings, C. Wang, S. X. Mao, Z. Z. Ye, S. Zhang and J. Y. Huang, *Nano Lett.*, 2011, **11**, 3312–8.

12 Y. S. Choi, M. Pharr, C. S. Kang, S.-B. B. Son, S. C. Kim, K.-B. B. Kim, H. Roh, S.-H. H. Lee, K. H. Oh and J. J. Vlassak, *J. Power Sources*, 2014, **265**, 160–165.

13 F. Wang, L. Wu, B. Key, X.-Q. Yang, C. P. Grey, Y. Zhu and J. Graetz, *Adv. Energy Mater.*, 2013, **3**, 1324–1331.

14 C. Cayron, M. Den Hertog, L. Latu-Romain, C. Mouchet, C. Secouard, J.-L. Rouviere, E. Rouviere and J.-P. Simonato, *J. Appl. Crystallogr.*, 2009, **42**, 242–252.

15 V. Schmidt, J. V. Wittemann, S. Senz and U. Gósele, *Adv. Mater.*, 2009, **21**, 2681–2702.

16 A. T. A. Heitsch, V. A. Akhavan and B. A. B. Korgel, *Chem. Mater.*, 2011, **23**, 2697–2699.

17 S. W. Lee, M. T. McDowell, J. W. Choi and Y. Cui, *Nano Lett.*, 2011, **11**, 3034–3039.

18 V. B. Shenoy, P. Johari and Y. Qi, *J. Power Sources*, 2010, **195**, 6825–6830.

19 K. Zhao, G. a. Tritsaris, M. Pharr, W. L. Wang, O. Okeke, Z. Suo, J. J. Vlassak and E. Kaxiras, *Nano Lett.*, 2012, **12**, 4397–4403

20 V. a. Sethuraman, M. J. Chon, M. Shimshak, V. Srinivasan and P. R. Guduru, *J. Power Sources*, 2010, **195**, 5062–5066.

Chapter 6: Development of composite electrode performance

6.1 Introduction

This chapter describes experiments conducted to investigate factors influencing the performance of composite electrodes containing silicon nanowire based active material. The chapter is divided into four sections. The first section investigates the effect of removing gold from batch-1 material. The second investigates the influence of formulation on the electrochemical performance of composite electrodes containing batch-1 material (post gold removal process). The third section investigates the performance of electrodes containing batch-2 material (post gold removal). The fourth section investigates the influence of capacity and voltage limited cycling regimes on the cycle life of composite electrodes containing batch-1 material (Au-removed).

6.2 Gold removal from nanowire material

Gold removal was conducted for two reasons; first the inferior lithium storage properties of gold reduces the specific capacity of the nanowire material as a whole (theoretical capacity of gold is 510 mA h g^{-1} assuming formation of $Li_{15}Au_4$) [1], second, the cost of gold makes its presence within a lithium-ion battery electrode material commercially unviable, chemical removal and reprocessing of the gold seed material would allow for the gold to be recycled and reused.

Gold removal was conducted *via* a series of etching steps as previously reported by Chockla *et al.*[2]. Briefly the gold removal process consisted of a HF etching step to remove any surface oxide, followed by dissolution of gold using an aqua regia solution, followed by washing and drying stages, see Chapter 2 for full details. After gold removal the colour of the nanowire material changed from brown to dark yellow.

6.2.1 Characterisation of batch-1 material after gold removal

Powder X-ray diffraction was conducted to monitor the removal of gold from the nanowire sample (**Figure 6-1**). Prior to gold removal batch-1 material displayed reflections associated with the presence of crystalline silicon and gold. The processed sample displayed a pattern consistent with the removal of gold.

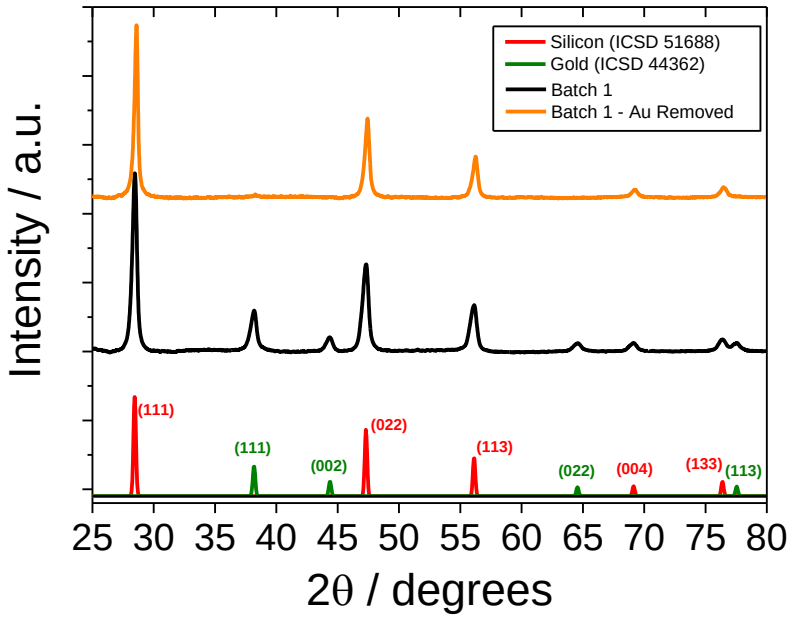

Figure 6-1 – Powder X-ray diffraction patterns of silicon nanowire batches before and after gold removal steps.

SEM imaging of a sample of processed batch-1 confirmed the retention of the morphology of the sample (**Figure 6-2**). Agglomerations of spherical amorphous silicon particles were observed throughout the sample (**Figure 6-2**).

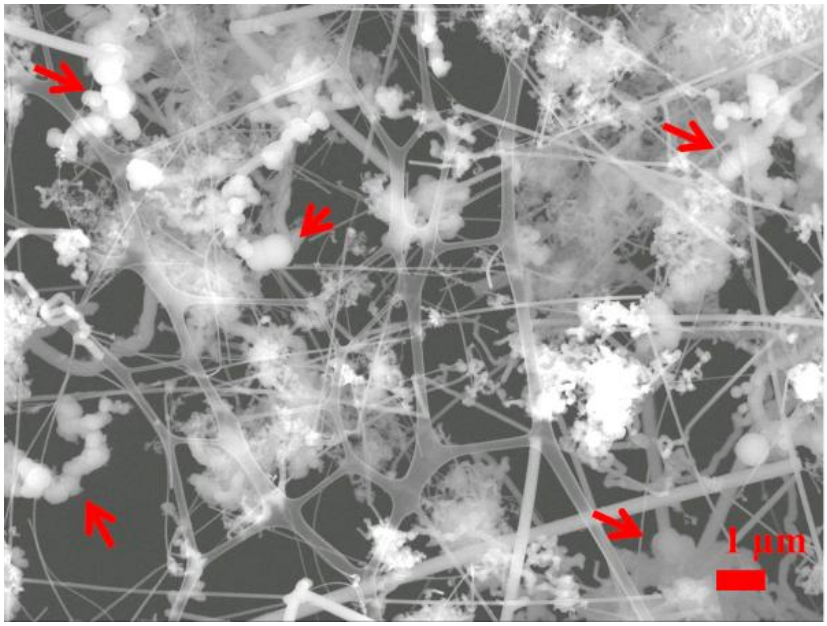

Figure 6-2 – Secondary electron SEM image of processed batch-1 silicon nanowire material. The sample was dispersed on a lacey carbon film supported on a copper TEM grid. The netted type structure in the background of the image is the carbon support. Red arrows highlight the presence of amorphous silicon particles. Image obtained with an accelerating voltage of 10 kV.

TEM imaging of the sample confirmed the removal of gold particles previously observed attached to the surface of silicon nanowire particles (**Figure 6-3**). The surface of nanowire particles was specifically investigated to observe possible changes caused by the etching and highly oxidative conditions used to remove gold from the sample (**Figure 6-3b** and **Figure 6-4**).

a) 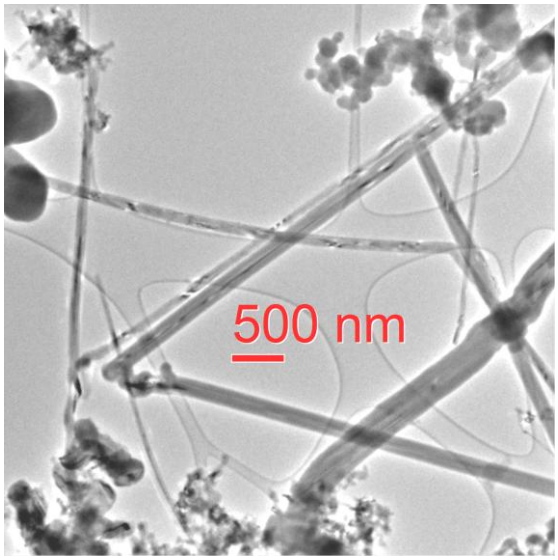

b) 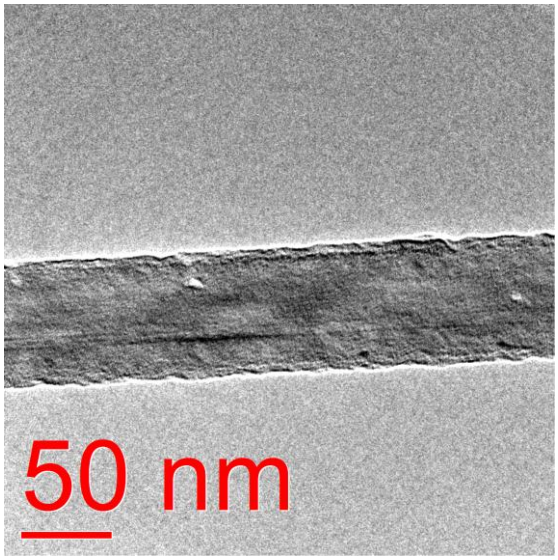

Figure 6-3 – TEM images of batch-1 material after gold removal process Images at various magnifications are displayed. The sample was dispersed on a lacey carbon film supported on a copper TEM grid. An accelerating voltage of 300kV was used to image the samples.

The surface of the particles was observed to consist of a rough amorphous layer, ~3 nm thick, visible in **Figure 6-3b** and **Figure 6-4**. A number of indentations and pores were visible in some of the particles. The presence of the amorphous layer is attributed to oxidation of the silicon

surface either during processing to remove gold or subsequent exposure to ambient conditions. An electron diffraction pattern obtained from the imaged nanowire confirmed the crystallinity of the particle (**Figure 6-4**). The spacing of the lattice fringes observed within the particle were measured to correspond to the (111) lattice planes of crystalline silicon. A stepped crystalline edge was observed at the interface between the crystalline nanowire and the amorphous surface.

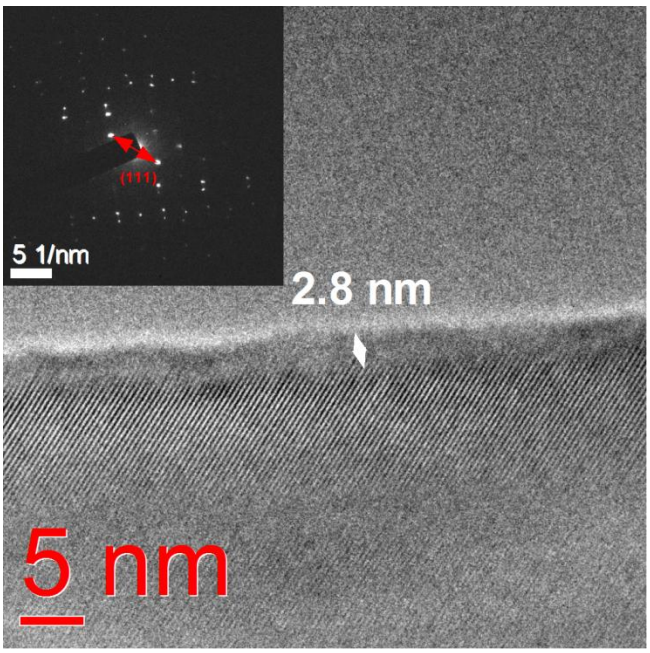

Figure 6-4 – High magnification image of a processed batch-1 silicon nanowire particle, an amorphous layer at the surface of the particle is highlighted by white arrows. A diffraction pattern of the nanowire is inset, the red arrow highlights the direction normal to the (111) plane.

6.2.2 Electrochemical characterisation

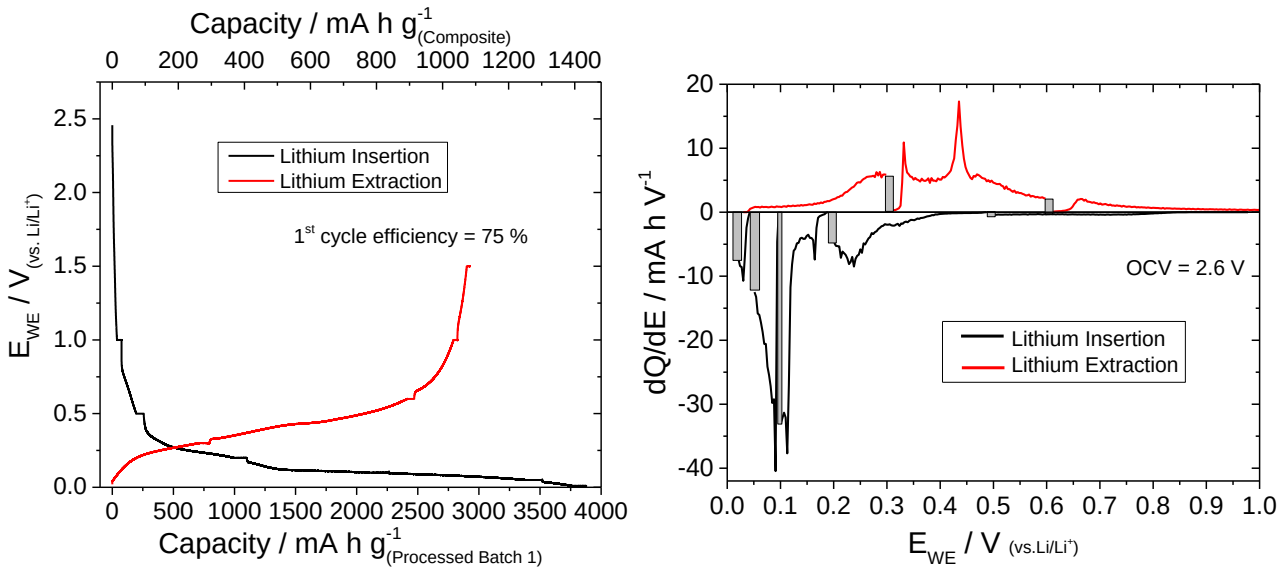

Figure 6-5 – First cycle of a composite electrode containing processed batch-1 silicon nanowire material. Formulation 37:37:26, cycled utilising a two electrode cell. Due to the cycling conditions used the cycle was conducted in stages with a voltage hold corresponding to flat regions in the voltage profile and sharp peaks in the dQ/dE plot, these are artefacts of the experimental conditions. Grey squares were added to the dQ/dE plot to highlight the location of the voltage holds.

Electrochemical analysis of a composite electrode containing processed batch-1 material was conducted. **Figure 6-5** displays the voltage profile and corresponding dQ/dE plot of the initial electrochemical cycle. The performance in terms of insertion capacity, reversible capacity and coulombic efficiency was observed to be very similar to that of an electrode containing batch-1 material prior to gold removal.

6.2.2.1 Comparison of as-received and processed batch-1 material

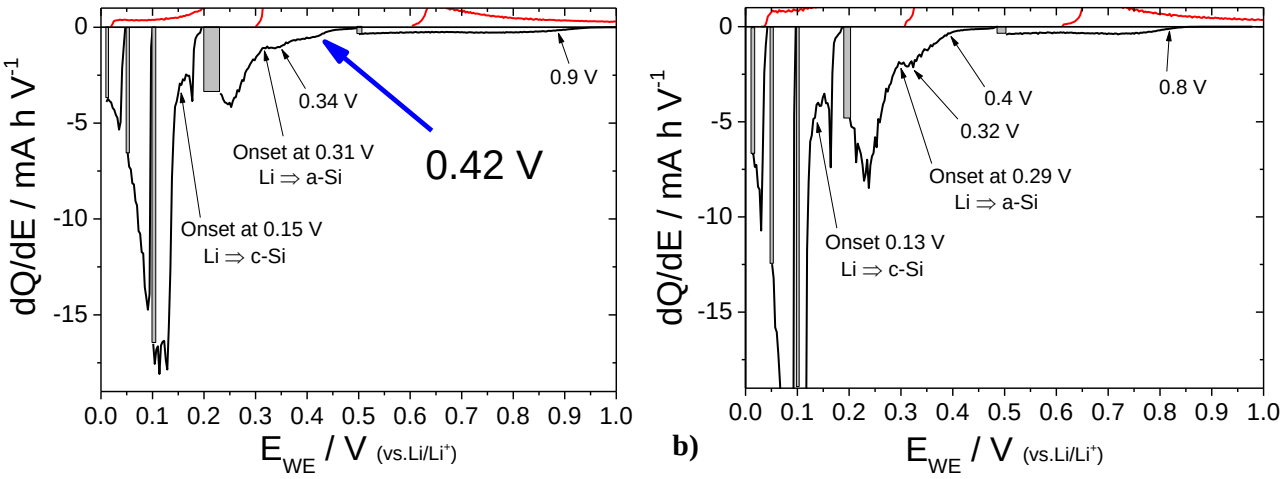

Figure 6-6 – Comparison between insertion profiles of a) batch-1 material and b) processed batch-1 material, points for comparison are highlighted with arrows. Due to the cycling conditions used, staged cycling with potential holds, sharp peaks are visible after a potential hold, these are artefacts of the experimental conditions. Grey squares were added to the dQ/dE plot to highlight the location of voltage hold conducted during cycling.

Closer comparison of the initial reduction processes which occur in the first cycle highlighted a difference between the samples. **Figure 6-6** compares dQ/dE plots; an insertion process, highlighted at around 0.42 V in **Figure 6-6a** (electrode containing as-received batch-1 material), was not present in **Figure 6-6b** (electrode containing processed batch-1 material). The process is unlikely to be associated with lithium insertion into gold as previous reports have suggested lithium insertion into gold occurs at a potential of around 0.25 V [2b]. The absence of the process in **Figure 6-6b** suggests that the species associated with the process were removed during the etching stages. It is unlikely that the process is associated with SiO_x as the aqua regia etching stage is known to result in surface oxidation; as such the processed material would be expected to contain a similar if not higher content of SiO_x as the as-received material.

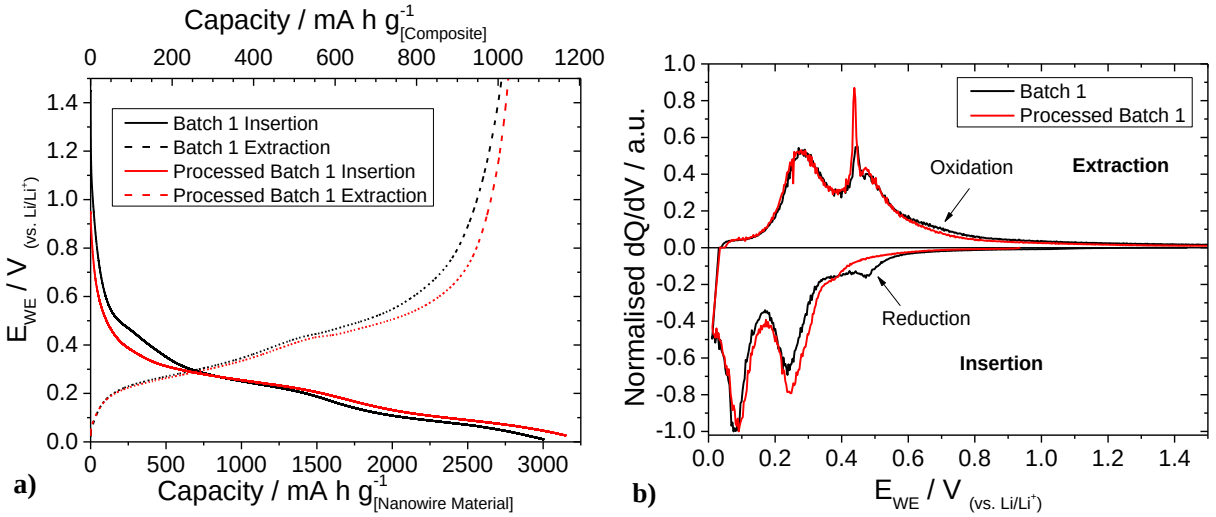

Figure 6-7 – Comparison between cells containing as-received material and processed material throughout the second electrochemical cycle a) voltage capacity plot b) normalised differential charge plot

Comparison of the second electrochemical cycle further confirmed a difference in the voltage profile of electrodes containing the two materials and suggested that the process occurring during insertion at around 0.45 V was partially reversible (**Figure 6-7**). Less charge was passed in the voltage region between 0.55 and 0.4 V during insertion and between 0.6 and 0.8 V during extraction in the electrode containing the processed material (**Figure 6-7b**). Possible explanations include either a catalytic process due to the presence of gold or the removal of a significant content of SiO_x during the HF etching stage which is not reformed during the aqua regia stage.

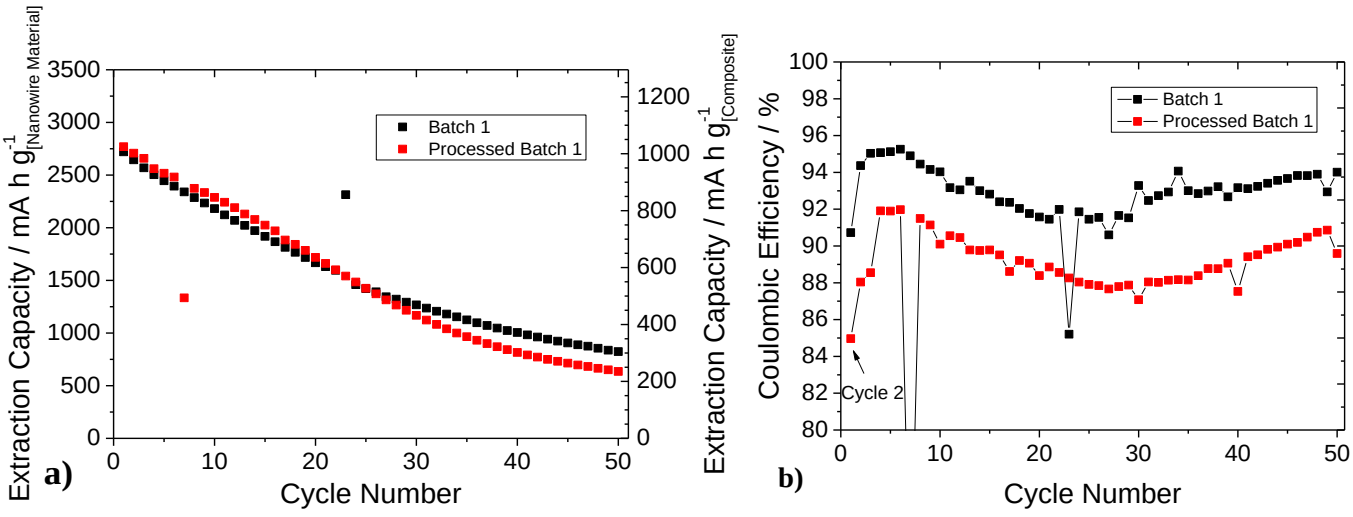

Figure 6-8 – a) Capacity vs. cycle number plot for half cells containing composite electrodes incorporating as received silicon nanowire material and composite electrodes incorporating processed silicon nanowire material b) Coulombic efficiency vs. cycle number of the half cells shown in a)

The extended cycling performance was observed to be similar for both materials (**Figure 6-8**). The reversible capacity of both electrodes was observed to be less than 30% of the initial value

within 50 cycles. The coulombic efficiency of the electrodes displayed a similar pattern of variation: efficiency increased over the initial 5 cycles and then decreased to a minimum by around cycle 30 after which the efficiency increased (**Figure 6-8b**). The electrode containing processed material displayed a lower efficiency throughout cycling.

6.3 Composite electrode formulation

The performance of composite electrodes containing large volume change materials have been reported to be especially sensitive to the composite electrode formulation. High ratios of carbon additives and CMC binder have been suggested to improve 1st cycle efficiency and cycle-life performance of composite electrodes containing silicon [3, 4]. Initial characterisation of nanowire material was conducted utilising a formulation of 37 wt. % nanowire material, 37 wt. % acetylene black, and 26 wt. % poly-acrylic acid, however the cycle life of composite electrodes was observed to be poor and the specific capacity of the resulting electrodes was low, maximum volumetric capacity was around 650 mA h cm^{-3} and maximum gravimetric capacity was around 1000 mA h g^{-1}. Capacity values of around 620 mA h cm^{-3} are reported for commercial graphite based negative electrodes [5]. To be of commercial interest the specific capacity and cycle life of composite electrodes needed to be improved. The influence of the composite electrode formulation on the performance of composite electrodes was investigated with the aim of increasing the specific capacity and cycle life.

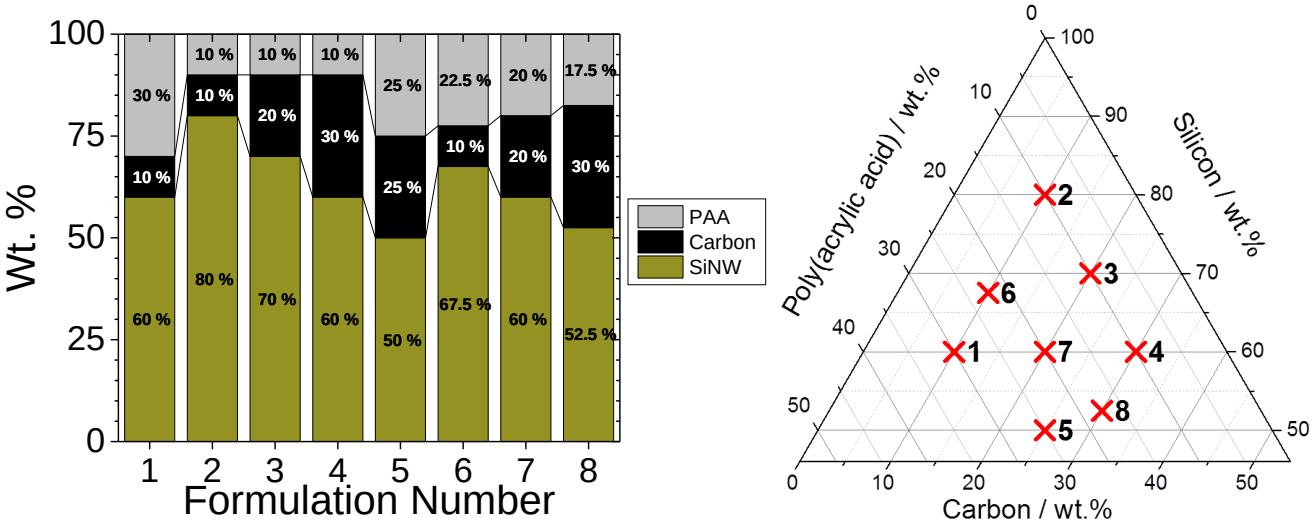

Figure 6-9 – Visual representations of the composite electrode formulations investigated.

Eight formulations were chosen for investigation (**Figure 6-9**). Active material content was kept at or above 50 wt. % to ensure a high energy density for the resulting electrode. Carbon content was selected between 10 and 30 wt. %. Poly-acrylic acid binder content was varied between 10 and 30 wt. %, a minimum of 10 wt. % being required to produce a structurally viable composite electrode. **Table 6-1** details the chosen electrode formulations and the associated theoretical capacity and expected reversible carbon contribution.

Table 6-1 – Details of selected formulations of composite electrode

Formulation	Silicon / wt. %	Carbon / wt. %	PAA / wt. %	Theoretical capacity of electrode† / mA h g^{-1}	Carbon contribution* / %
1	60	10	30	2147.4	0.92
2	80	10	10	2863.2	0.69
3	70	20	10	2505.3	1.57
4	60	30	10	2147.4	2.72
5	50	25	25	1789.5	2.72
6	67.5	10	22.5	2415.8	0.82
7	60	20	20	2147.4	1.83
8	52.5	30	17.5	1879.0	3.09

† assumes Q_T of silicon = 3579 mA h g^{-1}, carbon = 200 mA h g^{-1} and PAA = 0 mA h g^{-1}
** Carbon contribution calculated assuming carbon delivers 200 mA h g^{-1}(Appendix 3).*

6.3.1 Characterisation of composite electrodes

Composite electrodes were produced to the selected formulations. Processed batch-1 silicon nanowire material was used as the active silicon material. SEM images of the microstructure of composite electrodes are displayed in *Appendix 5*, subtle differences were observed, specifically the dispersion of nanowire particles and the observable binder content.

Electronic conductivity was calculated from impedance measurements obtained from the composite electrodes (**Figure 6-10**). The conductivity was observed to correspond generally with the conductive carbon content of the electrode; however the binder content also influenced the electronic conductivity of the electrodes, generally formulations containing a high ratio of binder were observed to display lower electronic conductivity (formulation 1 and 6).

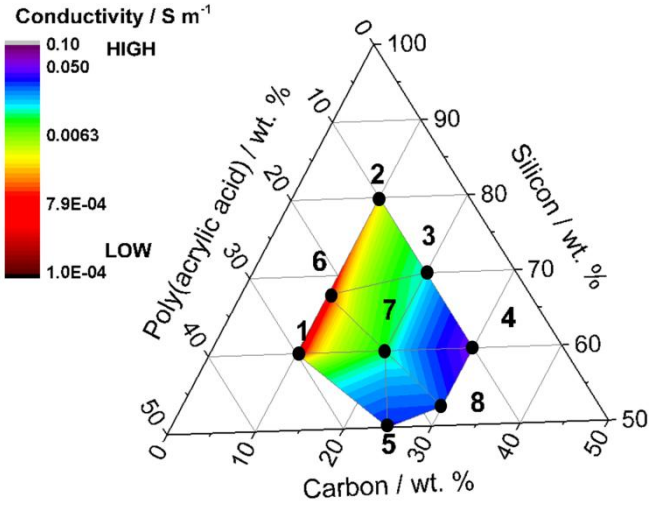

Figure 6-10 - Electronic conductivity of formulations of composite electrode, measured *via* impedance analysis of dry composite electrodes sandwiched between two metal current collectors. The conductivity was calculated utilising Equation 1-10, the measured resistance values of composite electrodes and the measured dimensions (geometrical area = 1 cm^2, thickness varied between 25 and 40 µm).

Electrochemical analysis of the 8 formulations was conducted. Prior to cycling impedance measurements of the 2 electrode cells were conducted. The double layer capacitance of each cell was calculated *via* curve fitting of the measured impedance spectra. The capacitance values give an indication of the electronically active surface area within each cell (**Figure 6-11**). The capacitance values suggest that the formulations 2, 3 and 8 displayed the highest surface area and formulations 1 and 6 displayed the lowest surface area. When considering the capacitance (hence surface area) expected from of the formulations (Carbon = 45 m^2 g^{-1}, silicon = 30m^2 g^{-1} PAA = expected to reduce the capacitance/surface area), the results generally conform, however, formulation 4 does not display the highest capacitance (hence surface area) as would be expected. The result suggests that formulation 4 may not have been structurally viable and a proportion of component particles may have been isolated from the substrate. High concentrations of PAA were generally observed to act to reduce the measured capacitance.

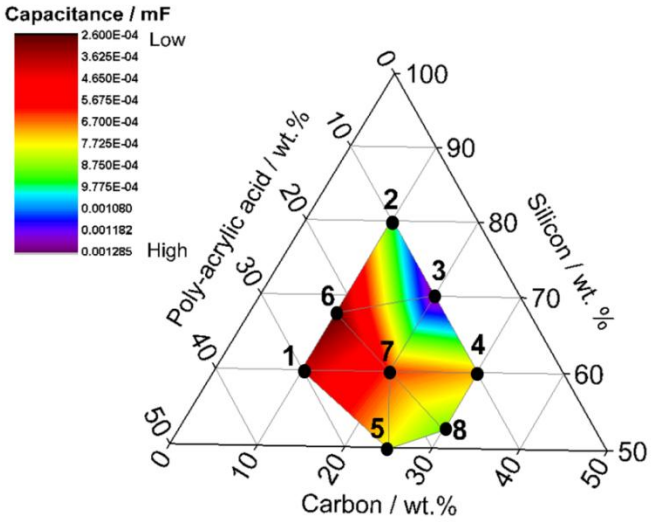

Figure 6-11 – Double layer capacitance values calculated *via* curve fitting of impedance measurements taken from electrochemical cells at OCV prior to cycling.

The voltage profiles of composite electrodes during the first galvanostatic cycle are displayed in *Appendix 6*. The results of the initial electrochemical cycle of all formulations are summarised in **Table 6-2** and **Table 6-3**.

Table 6-2 – Results of initial electrochemical cycle of formulations

Formulation No.	Ratio of electrode (SiNW:C:PAA)	Insertion / mA h $g^{-1}_{(Silicon)}$	Extraction / mA h $g^{-1}_{(Silicon)}$	Coulombic efficiency / %
1	60: 10:30	3108	2292	74
2	80:10:10	2536	1550	61
3	70:20:10	3037	2314	76
4	60:30:10	3149	2184	69
5	50:25:25	2977	2521	85
6	67.5:10:22.5	3276	2394	73
7	60:20:20	3453	2848	83
8	52.5:30:17.5	3430	2468	72

Analysis of the results show that formulation 5 provided the highest first cycle coulombic efficiency at 85 %, however, the highest extraction capacity in terms of both electrode mass and nanowire material mass was observed for formulation 7. The poorest performance in terms of both first cycle coulombic efficiency and extraction capacity was observed for formulation 2. None of the formulations achieved theoretical capacity. The results indicate the significant influence a relatively small variation in formulation can have on the performance of composite electrodes.

Table 6-3 – Comparison of theoretical electrode capacity with achieved capacity for all 8 formulations.

Formulation No.	Ratio of electrode (SiNW:C:PAA)	Maximum electrode capacity / mA h $g^{-1}_{Composite}$	Insertion / mA h $g^{-1}_{Composite}$	Extraction / mA h $g^{-1}_{Composite}$	Extraction capacity / % of Max.
1	60: 10:30	2147	1865	1375	64
2	80:10:10	2863	2029	1240	43
3	70:20:10	2505	2126	1620	65
4	60:30:10	2147	1889	1310	61
5	50:25:25	1790	1489	1261	70
6	67.5:10:22.5	2416	2211	1616	67
7	60:20:20	2147	2072	1709	80
8	52.5:30:17.5	1879	1801	1296	69

Results of extended cycling of formulations 1-8 are displayed in **Figure 6-12** and **Figure 6-13**. **Figure 6-12** displays the extraction capacity per gram of silicon nanowire material, providing a measure of the utilisation of the silicon material within the electrodes. The formulation of the composite electrode was found to significantly influence the cycle-life performance. It was observed that formulations 1 and 6 displayed the most stable performance. Formulations 5 and 7 displayed inferior performance. Formulations 2, 3, 4 and 8 displayed an almost complete capacity loss over 50 cycles. Formulation 4 displayed the poorest performance. The initial capacity values were lower than that previously observed for batch-1 material when a formulation of 37wt. % batch-1, 37 wt. % carbon, 26 wt. % PAA was used (**Figure 5-1**). The lower capacity was suggested to be due to incomplete electrical connection of all of the active material particles when high ratios of active material were used in the formulations. Evidence for this suggestion can be observed in the general trend of initial capacity values measured for the formulations tested; formulations 7, 5 and 8 displayed the highest initial capacity values.

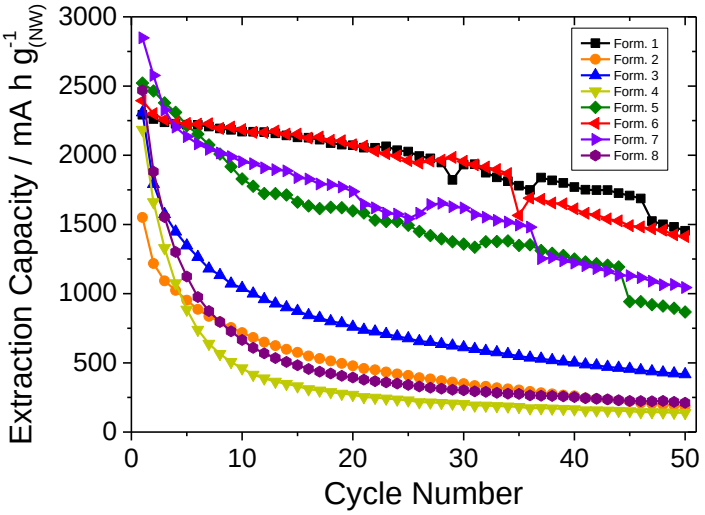

Figure 6-12 - Cycle life plot displaying variation in performance of the composite electrode formulations

Figure 6-13 displays the extraction capacity per gram of composite electrode allowing for direct comparison of capacity between formulations. Analysis suggests that formulation 6 displays the best performance over 50 cycles. Formulation 6 displayed similar stability to formulation 1, however due to the higher ratio of silicon within formulation 6 an increased capacity per gram of composite electrode was achieved.

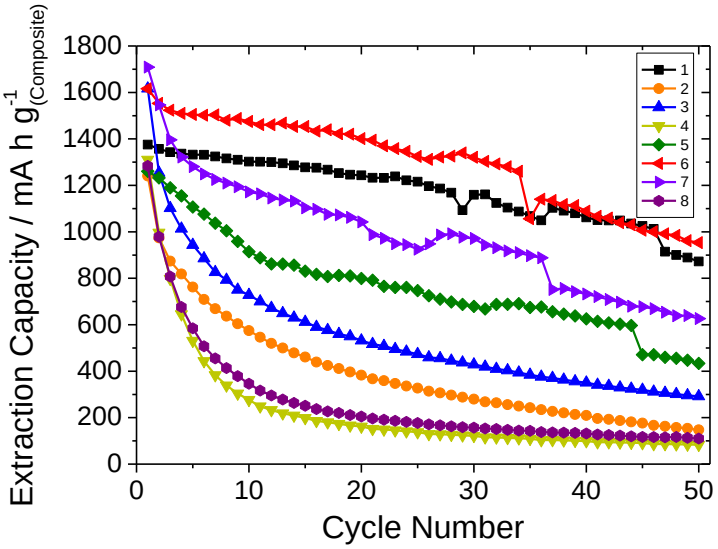

Figure 6-13 – Cycle life plot displaying large variation in performance for the various formulations capacity displayed per gram of composite electrode.

Figure 6-14 displays a ternary diagram constructed to allow visualisation of the relationship between the electrodes formulation and extraction capacity after 50 cycles. The formulations highlighted in purple display the highest capacity, these formulations represent greater than 20 wt. % poly-acrylic acid, less than 20 wt. % carbon additive and less than 70 wt. % silicon nanowire material.

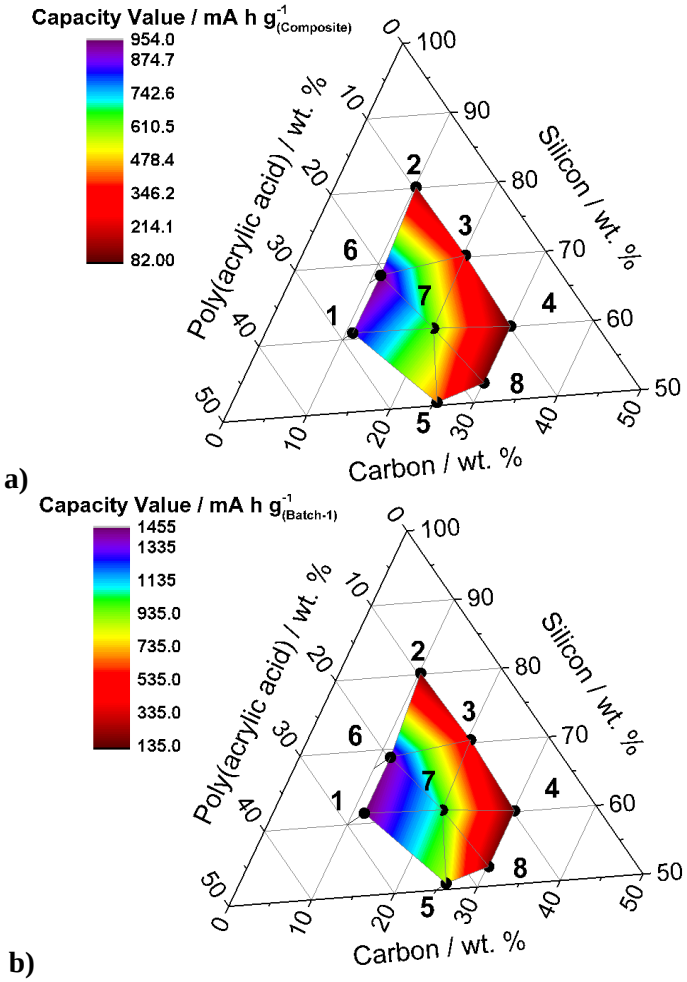

Figure 6-14 – Ternary plots of a) capacity per gram of electrode after 50 cycles, b) capacity per gram of batch-1 material after 50 cycles. Region of highest capacity shown in purple.

From the results obtained, formulation 6 was highlighted as the best performing formulation. The formulation region of less than 20 wt. % carbon, greater than 10 wt. % PAA and greater than 50 wt. % silicon nanowire material has been highlighted for future investigation. Initial capacitance and electrical conductivity measurements made of the composite electrode formulations suggest that low surface area is beneficial to extended stable cycling, and that high electrical conductivity is not required. High electrical conductivity was however observed to influence the first cycle efficiency as formulations 5, 7 and 8 displayed high electrical conductivity and high first cycle efficiency values. The poor performance of formulation 4 is suggested to be caused by poor mechanical stability produced by the high total surface area of the components and the low binder content.

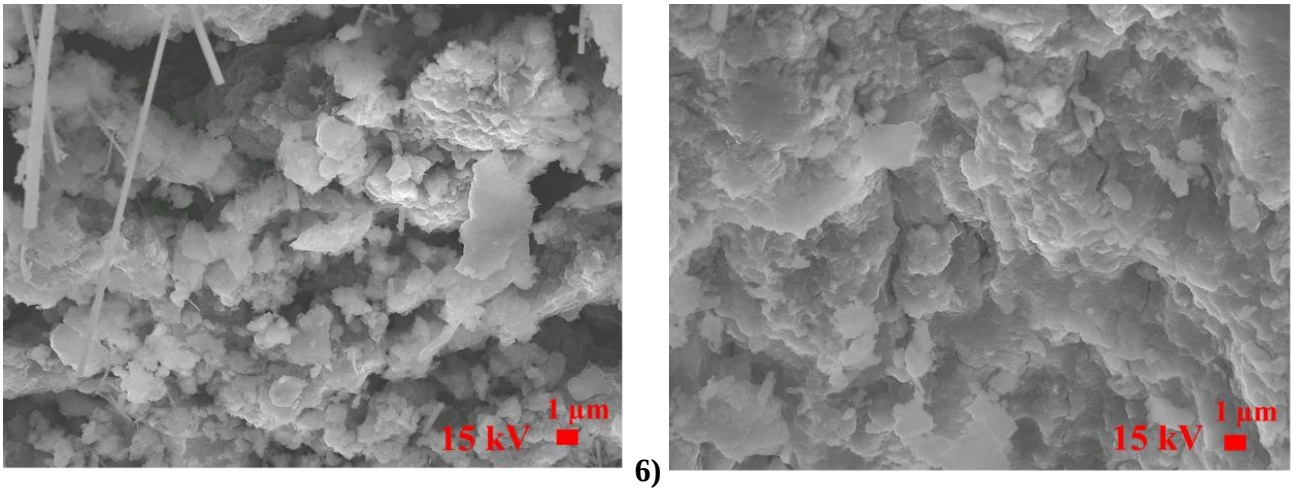

Figure 6-15 – SEM Images of formulation 4 and 6 composite electrodes after 100 cycles. Imaged directly after removal from the electrochemical cell. 15 kV accelerating voltage.

The structure of formulation 4 and formulation 6 composite electrodes after 100 cycles are compared in **Figure 6-15**. Formulation 4, which displayed a rapid loss of capacity in the initial 10 cycles, displayed a fragmented electrode structure. The electrode appeared to have completely broken apart into small fragments. Formulation 6, which displayed the most stable capacity, displayed a more homogenous structure. The images suggest that structural integrity of the composite electrode structure is essential to allow for stable electrochemical performance, and that structural integrity was not achieved in formulation 4.

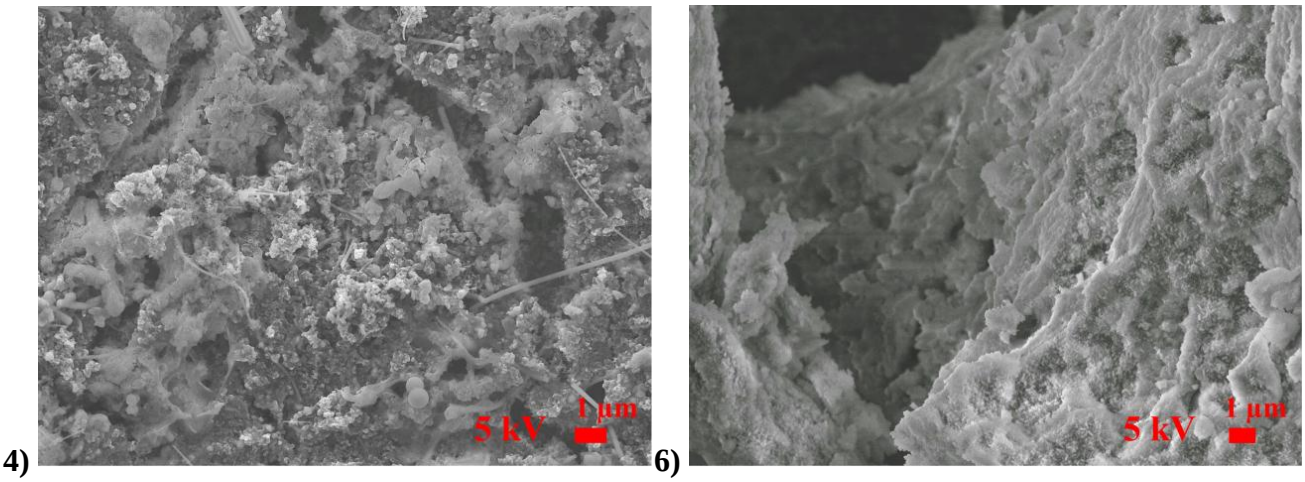

Figure 6-16 – SEM Images of formulation 4 and 6 electrodes after acetonitrile and 0.01M nitric acid washing steps to remove residual electrolyte and electrolyte breakdown products.

Figure 6-16 displays the structure of the same electrodes after washing steps to remove residual electrolyte and electrolyte breakdown products. The components of the formulation 4 composite electrode were easily visible after washing steps. The components of formulation 6 were not visible after washing steps suggesting either the electrolyte breakdown products were not removed completely or that the electrode had become a dense mass of material with indistinguishable component particles.

6.4 Characterisation of processed batch-2 material

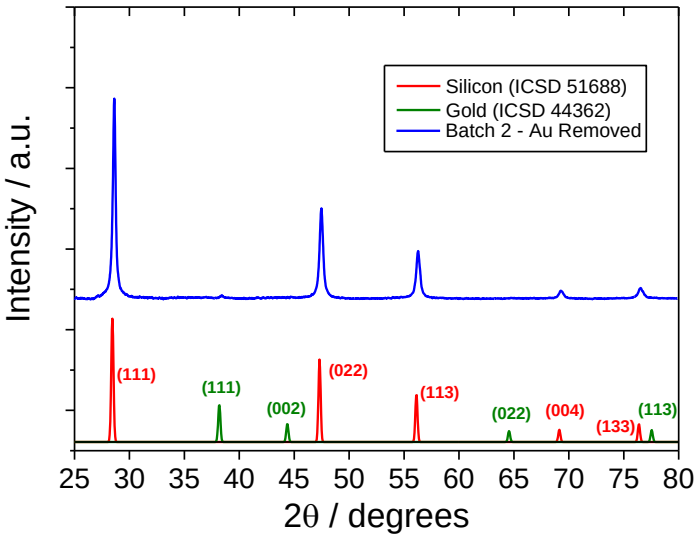

Figure 6-17 - Powder X-ray diffraction pattern of batch-2 nanowire material after gold removal.

Batch-2 material was processed to remove gold *via* the procedure detailed Chapter 2. An XRD pattern obtained from the processed material confirmed the removal of gold (**Figure 6-17**).

a) 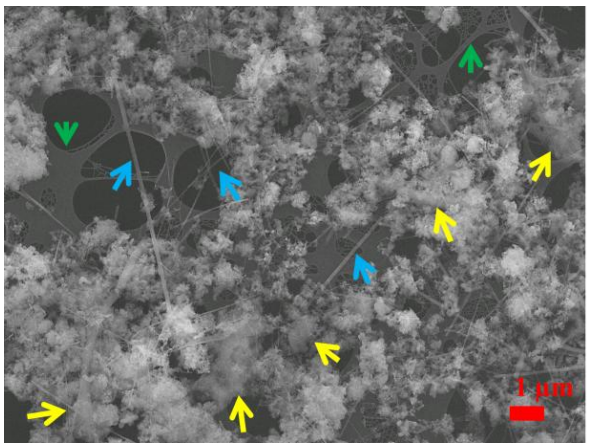

b) 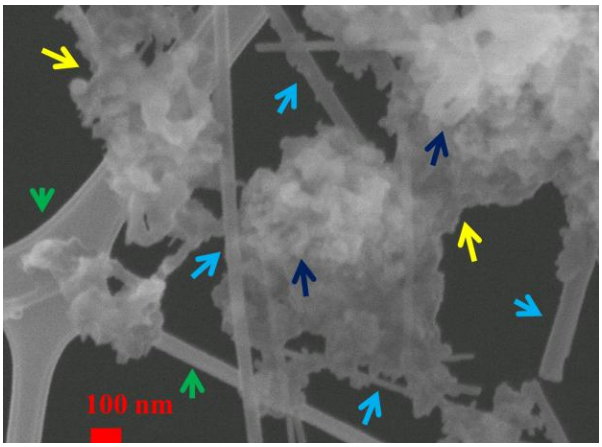

Figure 6-18 – Secondary electron SEM images of processed batch-2 silicon nanowire material. Green arrows highlight a carbon support grid on which the nanowire material was held to allow imaging. Light blue arrows highlight the location of silicon nanowire particles. Yellow arrows highlight the presence non-nanowire material. Dark blue arrows highlight particles within non-nanowire material.

Figure 6-18 displays secondary electron SEM images obtained of a sample of batch-2 material after processing. Bright regions corresponding to gold were not observed within the sample. The SEM sample preparation method (dispersal on a lacey carbon support coated TEM grid) highlighted the large quantity of non-nanowire material within the sample. Non-nanowire material was observed as agglomerated particles throughout the sample.

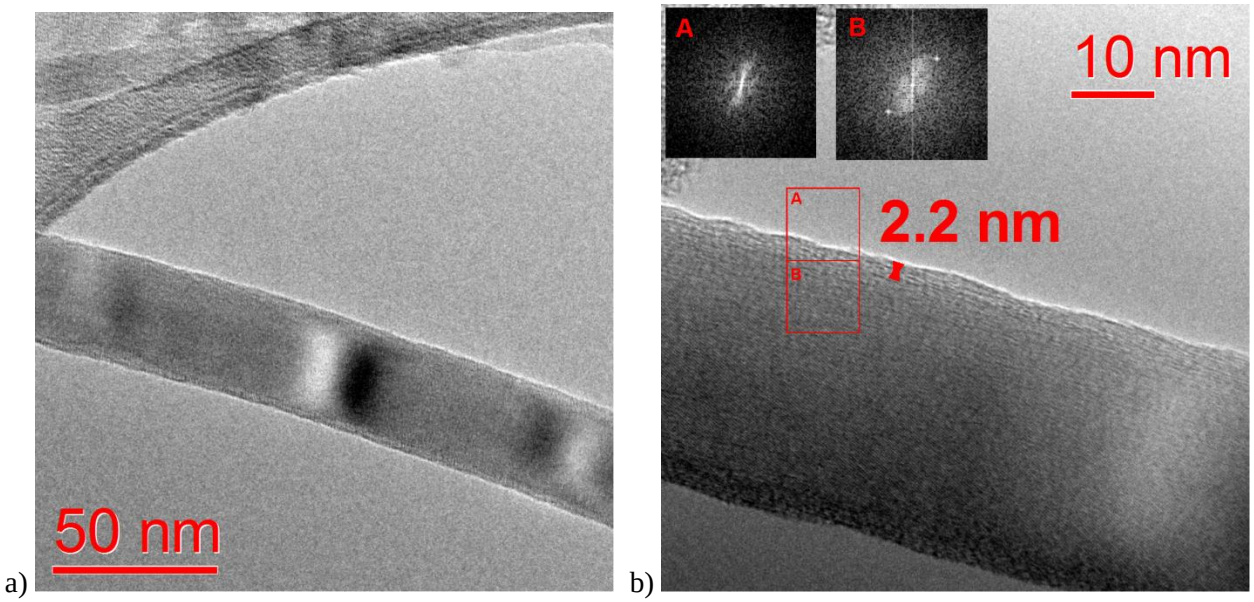

Figure 6-19 – a) TEM image of a nanowire particle from a sample of processed batch-2 material b) higher magnification image highlighting a rough amorphous surface layer.

Figure 6-19 displays high magnification images of nanowire particles present within the processed sample. The particles were observed to display a structure similar to that observed for batch-1 material (**Figure 6-3**). Nanowire particles displayed a crystalline structure with an amorphous surface layer, observed by the presence of bend contours in **Figure 6-19a** which did not extend to the surface of the nanowire and by the inset fast Fourier transforms of regions of the image in **Figure 6-19b**. The amorphous layer was measured to be around 2 nm thick (**Figure 6-19b**).

6.4.1 Electrochemical analysis of processed batch-2 material

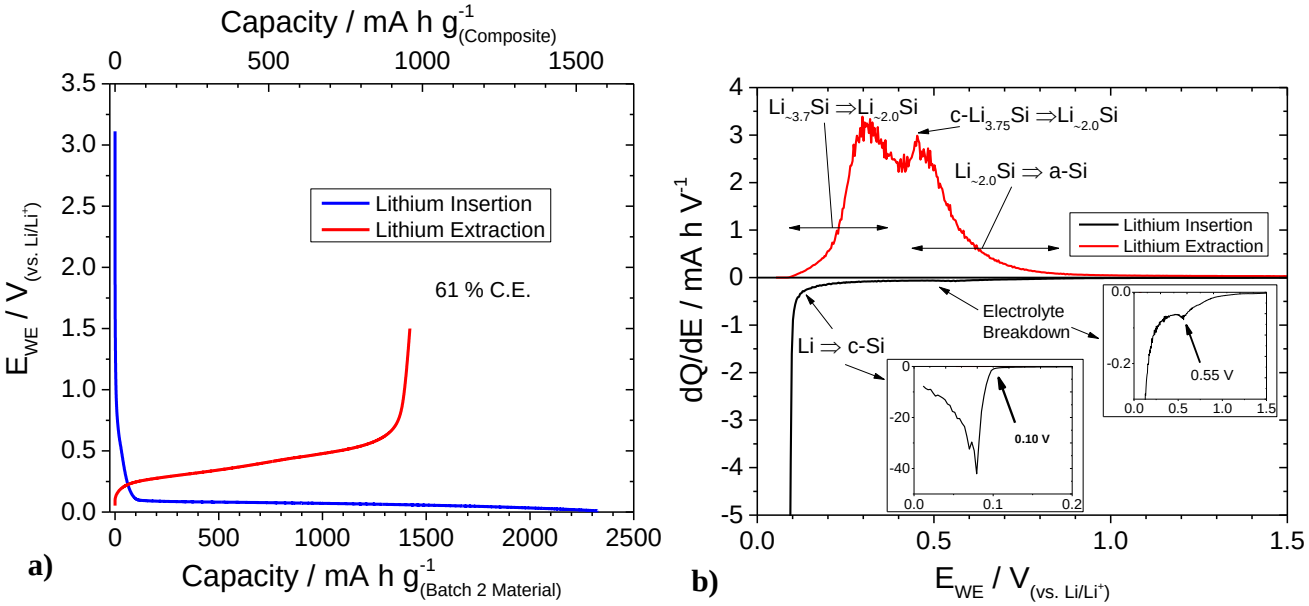

Figure 6-20 - a) Voltage profile of a composite electrode containing processed batch-2 material during the first cycle b) dQ/dE plot of the first cycle displayed in a). Cycled at a rate of C/10 between 0.01 and 1.5 V.

Composite electrodes containing processed batch-2 material were produced to formulation 6 (67.5 wt. % batch-2, 22.5 wt. % PAA and 10 wt. % carbon). Electrochemical analysis was conducted, the voltage profile and corresponding dQ/dE plot of the first cycle of a composite electrode is displayed in **Figure 6-20**. The electrochemical performance observed was characteristic of lithium insertion into nano-scale particles of crystalline silicon. The reversible capacity was observed to be below that of electrodes containing batch-1 material. Notably the electrode containing batch-2 material did not display any capacity which could be attributed to lithium insertion into amorphous silicon. No charge was observed to pass at around 0.4 V during insertion suggesting gold was successfully removed from the sample.

6.4.1.1 Comparison of processed batch-1 and 2 material

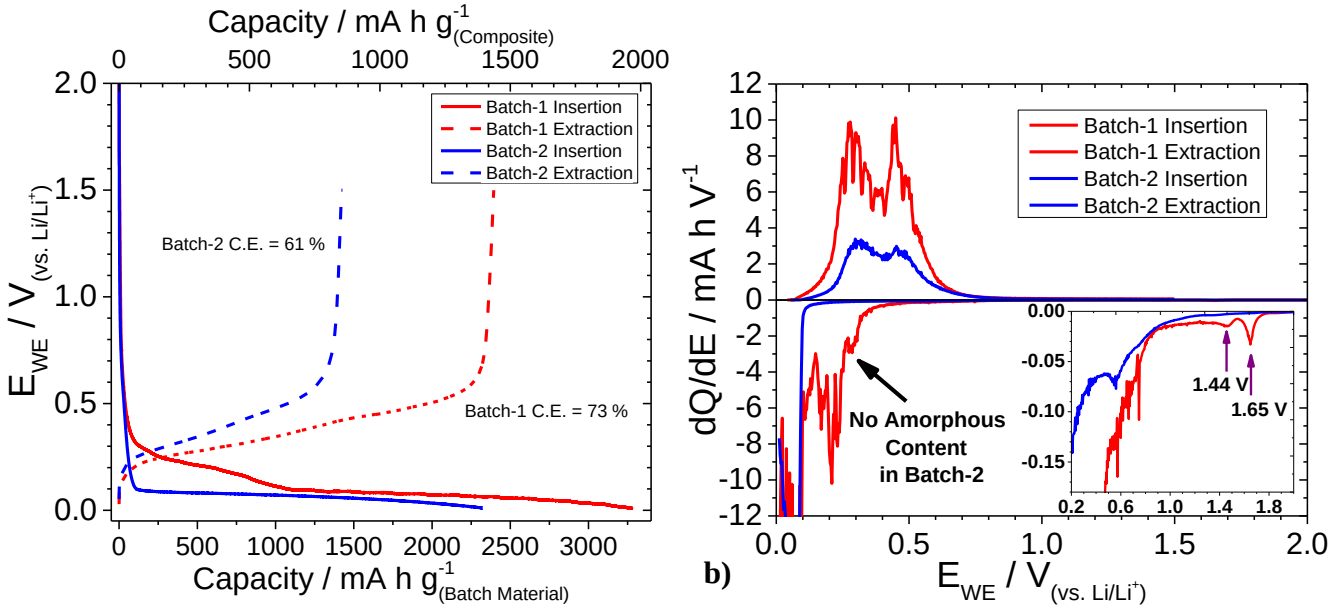

Figure 6-21 - a) Voltage profiles of the first cycle of composite electrodes containing processed batch-1 and 2 material b) dQ/dE plot comparing of the first cycle of electrodes containing processed batch-1 and 2 material. Cycled at a rate of C/10 between 0.01 and 1.5 V.

Via comparison of the first cycle of composite electrodes containing processed batch-1 and 2 material it was observed that the electrodes displayed different processes (**Figure 6-21**). Batch-2 did not display reduction processes at 1.65 and 1.44 V as observed for batch-1 material; this observation suggests that the processes are associated with reduction of surface species present within batch-1 material. Batch-2 material did not display the large reduction process occurring at around 0.3 V previously associated to lithium insertion into amorphous silicon present within batch-1. Little lithium extraction from the crystalline $Li_{15}Si_4$ phase was observed in both electrodes, the lack of lithium extraction suggests that the formulation of the electrode may influence the formation of $Li_{15}Si_4$.

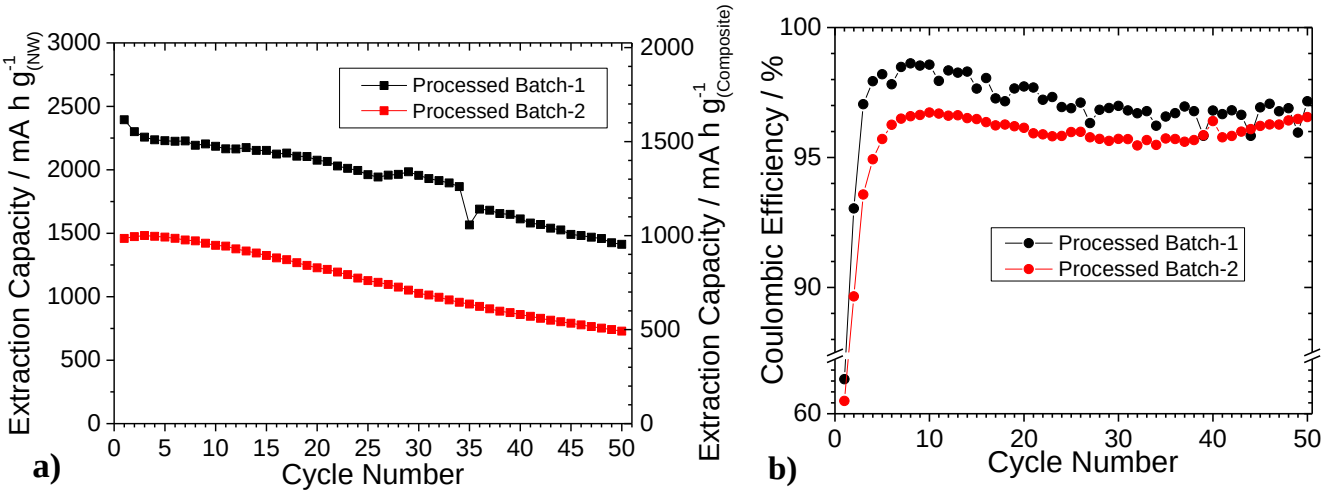

Figure 6-22 – Extended cycling data of composite electrodes containing processed batch-1 and batch-2 silicon material galvanostatically cycled at a rate of C/10 between 0.01 and 1.5 V.

Comparison of extended cycling performance of processed batch-2 and processed batch-1 material is displayed in **Figure 6-22**. A SEM Image of the composite electrode cycled in **Figure 6-22** is displayed in *Appendix 7*. Lower capacity was observed throughout cycling for a composite electrode containing processed batch-2 material. Similar capacity fade was observed for both types of composite electrode. The high content of inactive non-nanowire material within the sample is suggested to be the cause of the low capacity. The non-nanowire material is expected to be formed *via* breakdown of the silicon precursor during synthesis, resulting in formation of inactive poly-phenylsilane material.

6.5 Extending the cycle life of composite electrodes *via* limitation

A common method used to extend the cycle life of lithium ion battery electrodes is *via* capacity and voltage limitation. Capacity and voltage limitation are used to restrict the variation in structural and chemical change of the electrode materials with the aim of increasing the number of cycles an electrode can conduct prior to failure. The effect of limitation on the cycle life performance of composite electrodes containing processed batch-1 material produced to formulation 6 was investigated.

Due to the large volume change associated with lithium insertion into silicon active particles, limitation of the capacity of an electrode reduces the volume expansion of the active material particles within an electrode, assuming even reaction throughout an electrode. Reduction in volume expansion of the active material may improve retention of the structural integrity of the electrode and also reduce the requirement for re-passivation of the active material particle surface. These two effects may also contribute to retention of the ionic mobility of lithium throughout the composite electrode, *via* less formation of electrolyte breakdown products, and help to retain electronic contact between the active material and the current collector by reducing the physical motion of particles within the electrode.

An electrochemical cycle without limitation was conducted for each test cell prior to limited-cycling to allow for amorphisation of the silicon active material. The initial cycle allowed for a significant proportion of capacity to be accessed above 0.2 V. Limitation was applied only to the insertion process. Capacity limitation was introduced by restricting the time of a galvanostatic discharge. Voltage limitation was introduced as a lower cut-off potential.

6.5.1 Analysis of normal voltage window galvanostatic cycling

The first cycle of an electrode galvanostatically cycled at 0.1C is displayed **Figure 6-23**, the voltage window within which the electrode is cycled is highlighted.

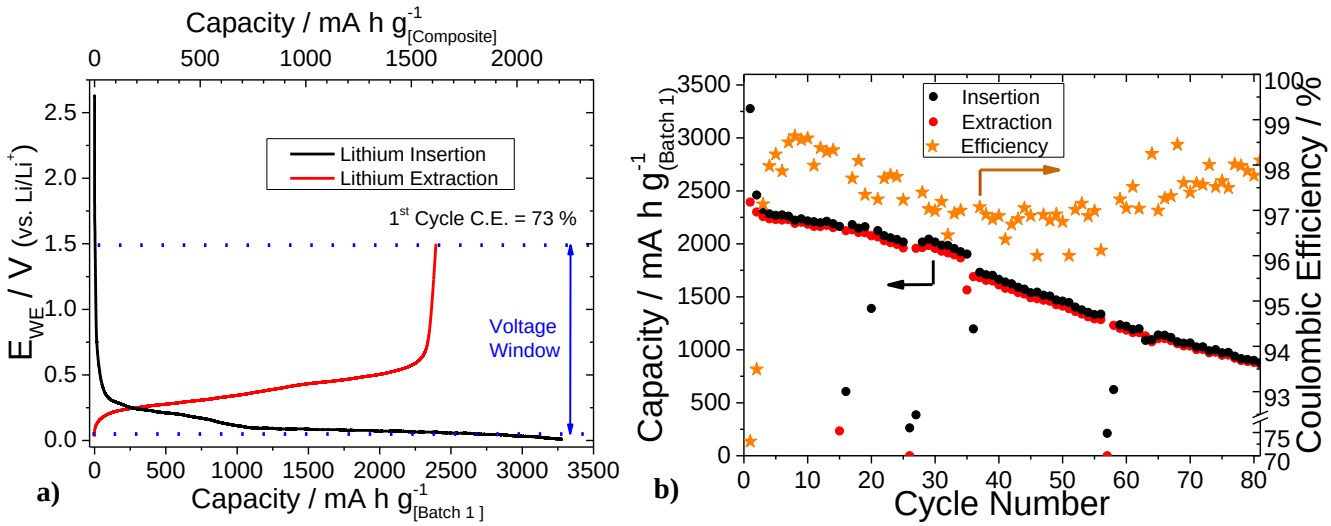

Figure 6-23 – a) Initial cycle of a composite electrode cycled within a wide voltage window (between 0.01 and 1.5 V). b) Extended cycling data, the coulombic efficiency of each cycle is also displayed. Black is lithium insertion capacity, red is lithium extraction capacity and orange is the coulombic efficiency. Cycled at a rate of C/10.

The extended cycling of an electrode between the voltage limits of 0.01 and 1.5 V is displayed in **Figure 6-23b**. Significant capacity fade was observed during cycling. After 80 cycles a reversible capacity of 822 mA h $g^{-1}_{(Batch\text{-}1)}$ was achieved, 34 % of the initial reversible capacity. The coulombic efficiency of the electrode was observed to vary between around 96 and 99 %.

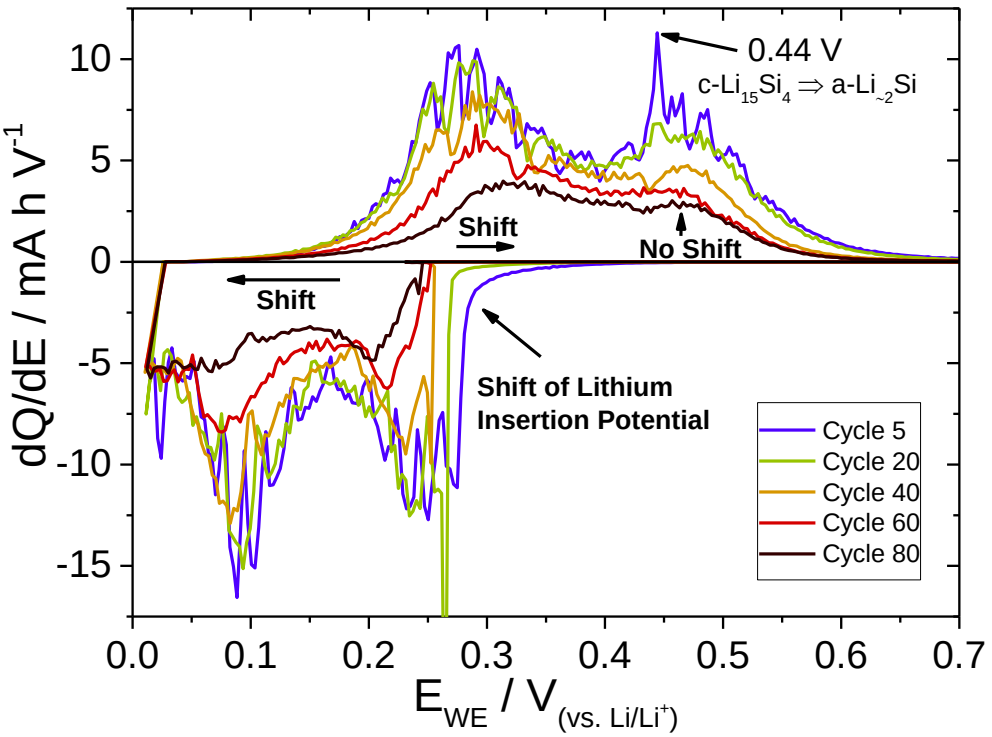

Figure 6-24 – dQ / dE plot of selected cycles during extended galvanostatic cycling at a rate of C/10 between 0.01 and 1.5 V.

Analysis of a selection of cycles was conducted utilising dQ/dE plots (**Figure 6-24**). The decrease in the charge passed during cycling was observed as a reduction in the area between the trace and the Y = 0 line. The potential of lithium insertion was observed to shift to lower

potential throughout cycling. The first extraction peak associated with lithium extraction from high lithium content amorphous silicon phases displayed a positive shift in potential however the second extraction peak, associated with lithium extraction from low lithium content amorphous silicon phase, did not appear to shift significantly.

The observations suggest that polarisation of the electrode caused the voltage of the insertion process to shift to lower potential throughout cycling. The polarisation which occurs during cycling appears to result in a IR drop up to cycle 60, observed as a reduction in the potential of the insertion process. During the latter cycles the gradient of the trace during insertion becomes distorted suggesting a concentration type polarisation, resulting in reduced ionic mobility with the electrode. As the insertion potential shifts, formation of the high lithium content amorphous lithium silicide phase does not occur significantly before the cut-off potential is reached, therefore lithium extraction from the higher lithium content amorphous lithium silicide phase, normally occurring at around 0.25V, was observed to decrease. Formation of the low lithium content silicide phase occurred throughout cycling as lithium insertion to form the lower lithium content amorphous phase occurs at a potential well above the lower cut off potential (0.3 - 0.2 V) and as such was fully formed throughout.

The observed polarisation during cycling is suggested to result from the failure mechanism recently described by Oumellal *et al.* [4], a build-up of electrolyte breakdown products within the composite electrode structure. Additionally, initial poor reversibility is suggested to result from electronic isolation of a proportion of active particles active particles.

6.5.2 Capacity limitation

Two capacity limitation values were selected, 2000 mA h g^{-1} and 1000 mA h g^{-1}. The higher value was selected to represent, lithium insertion involving formation of both high and low amorphous lithium silicide phases (2000 mA h g^{-1}) and the lower limitation to represent formation of only the low lithium content phase (1000 mA h g^{-1}).

6.5.2.1 Capacity limitation of 2000 mA h $g^{-1}_{\text{(Batch-1)}}$

The initial cycle and first limited cycle are displayed in **Figure 6-25a**. The initial performance of the composite electrode was consistent with that previously observed. Extended cycling of the composite electrode under capacity limited conditions is displayed in **Figure 6-25b**.

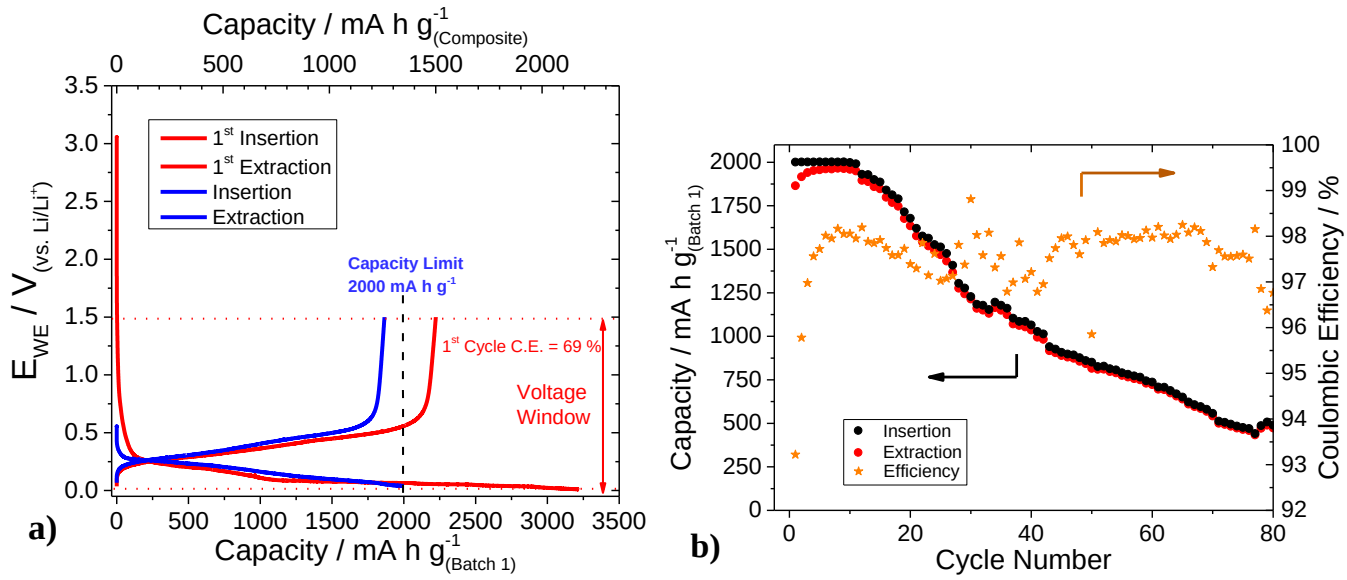

Figure 6-25 – a) Voltage profile of an electrode. The initial cycle with no limitation (cycled between 0.01 and 1.5 V) is displayed in red, the 1st limited cycle displayed in blue (insertion capacity limited to 2000 mA h g^{-1}). b) Extended cycling of a composite electrode containing processed batch-1 material. Cycled at C/10.

Lithium insertion to the capacity limit of 2000 mA h g^{-1} was achieved in the first 13 cycles. Beyond the 13th cycle the voltage of the electrode reached the lower cut-off potential of 0.01V prior to achieving 2000 mA h g^{-1}. The observed cycle life performance of the electrode was comparable to that of an electrode cycled without limitation reaching around 500 mA h $g^{-1}_{(batch1)}$ by the 80th cycle.

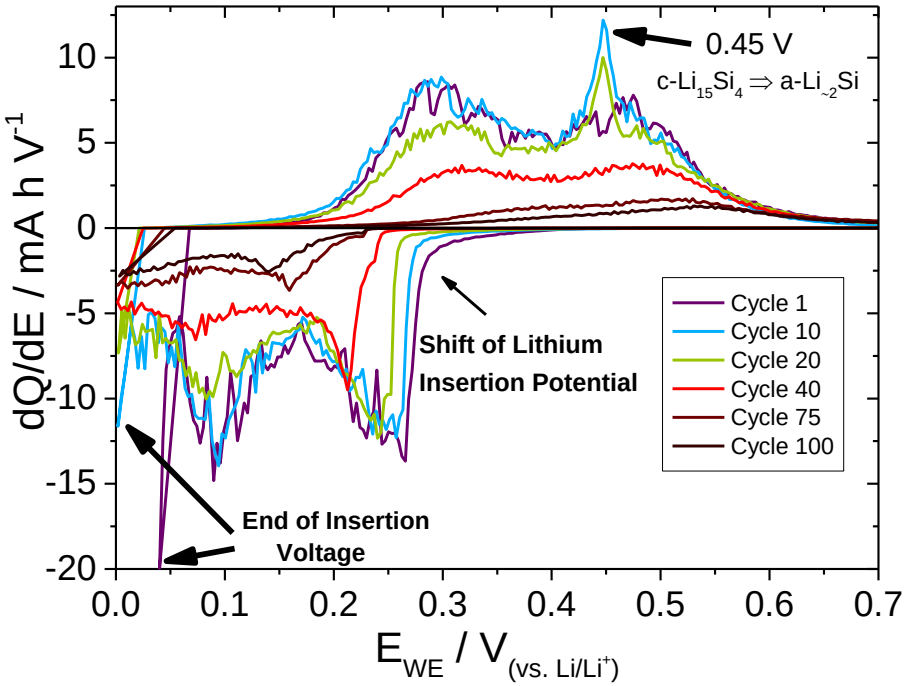

Figure 6-26 – dQ / dE plot of selected cycles during the extended galvanostatic cycling of an electrode with a capacity limitation of 2000 mA h g^{-1}. Cycled at C/10.

The dQ/dE plot of a selection of cycles throughout the extended cycling of a 2000 mA h g^{-1} capacity limited electrode is displayed in **Figure 6-26** . Lithium extraction from the $Li_{15}Si_4$ phase was not observed in cycle 1 but was observed in cycle 10. Within the initial cycles the 2000 mA h g^{-1} limit could be achieved without the formation of the high lithium content phase. Loss of activity required formation of $Li_{15}Si_4$ to achieve the 2000 mA h g^{-1} limit by the 10th cycle. By the 14th cycle the capacity limit could not be achieved above the lower cut-off of 0.01V.

By the 40th cycle formation of $Li_{15}Si_4$ was not observed this was attributed to an increase in polarisation preventing formation of $Li_{15}Si_4$ occurring prior to the electrode reaching the cut-off potential. After cycle 75 the first lithium insertion process dominates the reversible capacity, the reduced contribution of the second insertion process was caused by further polarisation of the electrode.

6.5.2.2 Capacity limitation of 1000 mA h $g^{-1}_{(Batch-1)}$

The initial cycle without limitation and the first limited cycle are displayed in **Figure 6-27a**. The initial cycle of the electrode was consistent with previously tested electrodes. Extended cycling of an electrode limited to 1000 mA h g^{-1} is displayed in **Figure 6-27b**. Stable cycling was observed for 130 cycles prior to the 'end of insertion voltage' reaching the lower cut-off potential of 0.01V. The extraction capacity of the electrode decreased during cycling from a maximum of 990 mA h g^{-1} in cycle 10 to 972 mA h g^{-1} in cycle 130. The coulombic efficiency was observed vary, decreasing during effective capacity limitation and increasing once the voltage of the electrode reached the lower cut-off potential prior to the capacity limit being reached. The drastic decrease in capacity after cycle 130 was caused by the fact the insertion potential plateau began to reach the cut-off potential.

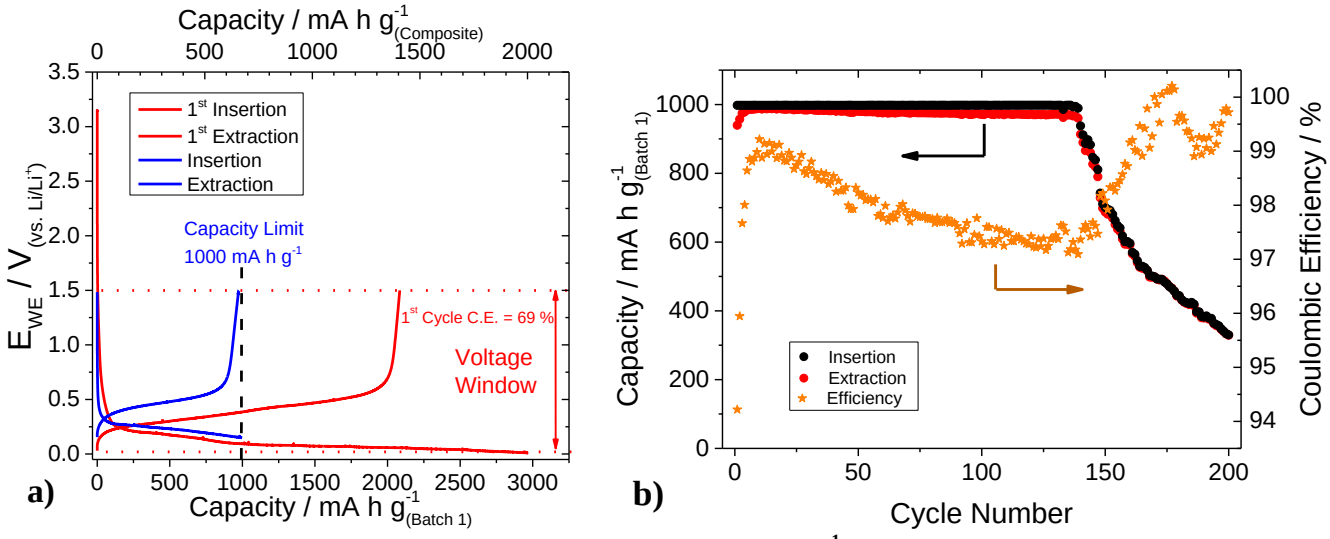

Figure 6-27 – a) Voltage profile of an electrode with 1000 mA h g^{-1} capacity limitation .The initial cycle with no limitation (cycled between 0.01 and 1.5 V) displayed in red, the 1st limited cycle displayed in blue (limited to an insertion capacity of 1000 mA h g^{-1}). b) Extended cycling of a composite electrode limited to an insertion capacity of 1000 mA h g^{-1}. Cycled at C/10.

Significant changes to the voltage at which charge was passed during both insertion and extraction were observed throughout extended cycling of the 1000 mA h g^{-1} limited electrode (**Figure 6-28**). Initially the 1000 mA h g^{-1} capacity limit was satisfied by the 1st lithium insertion process and the formation of low lithium content amorphous lithium silicide. Upon continued cycling formation of higher lithium content phases associated with the 2nd lithium insertion process were observed to contribute to the reversible capacity. The requirement for higher lithium content phases to be produced must have been caused by a lack of active material within the electrode. Formation of higher lithium content phases corresponds to an increased volume expansion of the active particles. Beyond cycle 170 the reversible capacity was observed to be dominated by the 1st insertion process, the absence of the second insertion process was caused by an increased polarisation of the cell preventing formation of higher lithium content phases prior to the potential of the electrode reaching the cut-off potential.

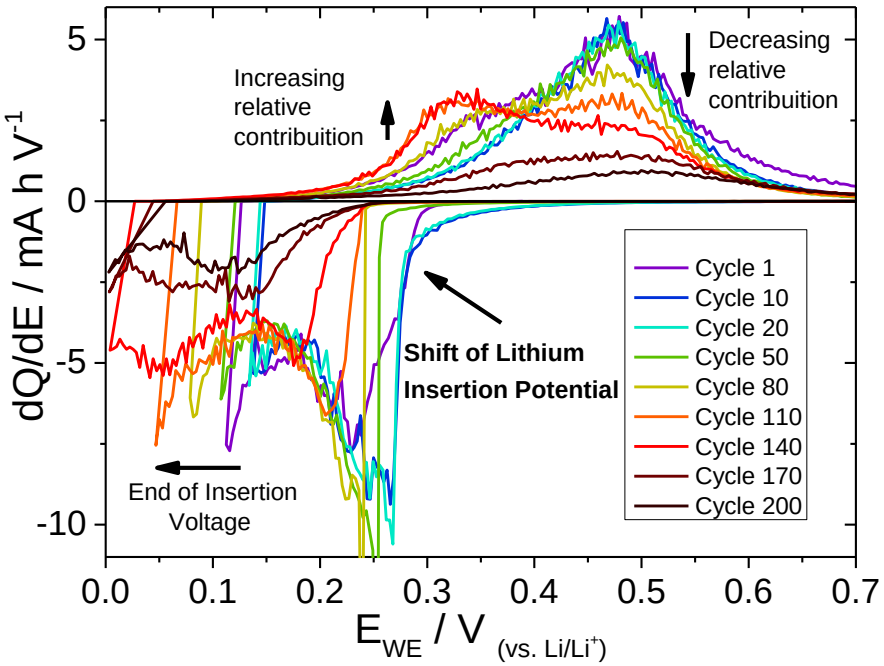

Figure 6-28 - dQ / dE plot of selected cycles during the extended galvanostatic cycling of an electrode with a capacity limitation of 1000 mA h g^{-1}.

The change in the coulombic efficiency observed in **Figure 6-27** can be explained by the relative contribution of the lithium silicide phases formed. As the contribution of the second lithium insertion process increased, the coulombic efficiency decreased, suggesting that the formation of higher lithium content phases result in reduced efficiency, likely due to the associated large volume expansion experienced by the active particles. The contribution of the higher lithium content lithium silicide decreased beyond cycle number 140 and the coulombic efficiency was observed to increase. The correlation between coulombic efficiency and the lithium content of

the silicide phases produced suggests that formation of higher lithium content phases should be avoided to achieve more efficient cycling.

6.5.3 Limitation *via* the lower cut-off voltage

The voltage of the lower cut-off potential was increased above 0.01 V to observe the influence on the cycle life of composite electrodes containing batch-1 material. Two lower voltages were selected, 0.06 V which corresponded to inclusion of the first two lithium insertion processes, and 0.18 V which corresponded to only the first lithium insertion process.

6.5.3.1 Lower cut-off voltage limitation of 0.06 V

Figure 6-29 displays the initial cycle of an electrode in which no limitation was applied as well as the first limited cycle. The electrode displayed similar performance to other previously tested electrodes. Extended cycling of an electrode limited by a lower voltage of 0.06 V is displayed in **Figure 6-29b**. Capacity values were observed to continually decrease throughout cycling. The coulombic efficiency of the electrode was observed to steeply rise, fall and then increase once again. The coulombic efficiency was higher than that observed for a non-limited electrode (**Figure 6-23**). The reversible capacity after the 80th cycle was around 750 mA h g^{-1}, comparable to an electrode cycled without limitation.

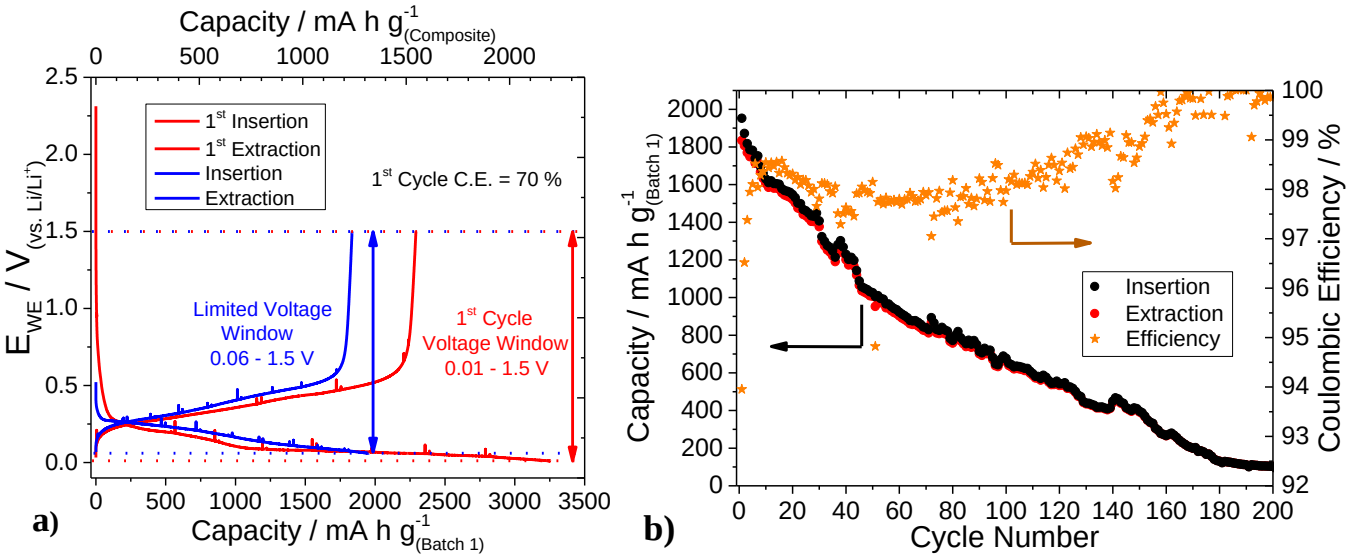

Figure 6-29 – a) Voltage profile of an electrode with a 0.06 V lower voltage limitation .The initial cycle with no limitation displayed in black and red, the 1st limited cycle displayed in blue and orange. b) Extended cycling of a composite electrode containing processed batch-1 material limited to a lower voltage limit of 0.06 V.

Via analysis of the dQ/dE plot (**Figure 6-30**) it was observed that initially both lithium insertion processes occurred, lithium extraction from $Li_{15}Si_4$ was not observed. By the 50th cycle the 1st lithium insertion process began to dominate. An increase in polarisation of the electrode throughout cycling caused the voltage of the insertion process to shift to lower potential. The

shift in insertion potential combined with the 0.06 V cut-off resulted in a reduction in the contribution of the second insertion process to the capacity beyond the 50th cycle.

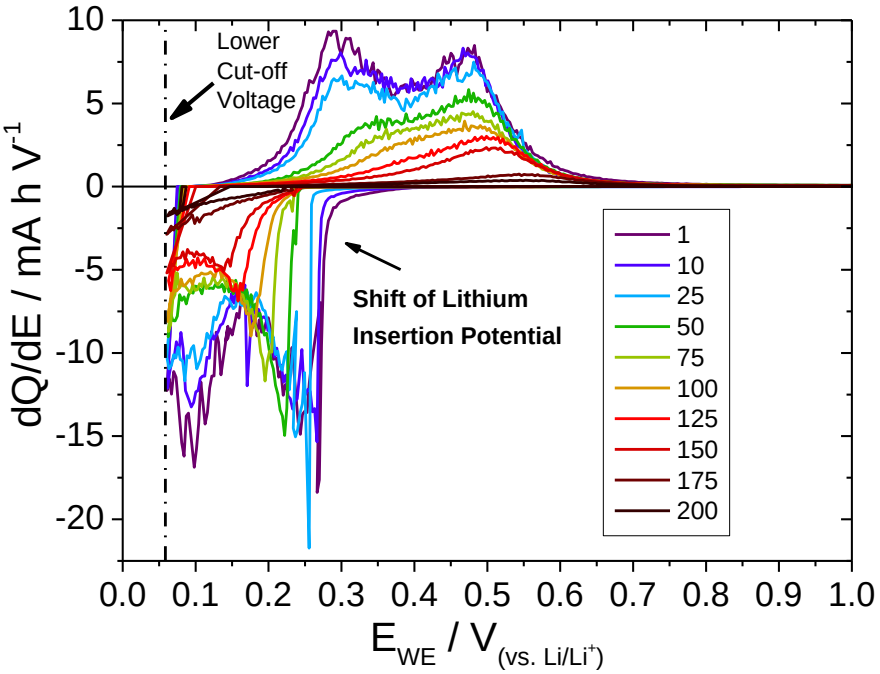

Figure 6-30 – dQ / dE plot of selected cycles during the extended galvanostatic cycling of an electrode with a lower voltage limit of 0.06 V.

As the second insertion process contributed less to the capacity the coulombic efficiency increased (**Figure 6-29**). The observed variation confirmed previous results suggesting formation of the higher lithium content phase *via* the second lithium insertion process was detrimental to coulombic efficiency.

6.5.3.2 Lower cut-off voltage limitation of 0.18 V

The initial cycle and 1st limited cycle of an electrode with a voltage limitation of 0.18 V are displayed in **Figure 6-31**. The electrode displayed lower initial insertion and extraction capacities compared to previously tested electrodes. The difference in capacity may have been caused by an error in mass measurement. The coulombic efficiency of the initial cycle was comparable to previously tested electrodes.

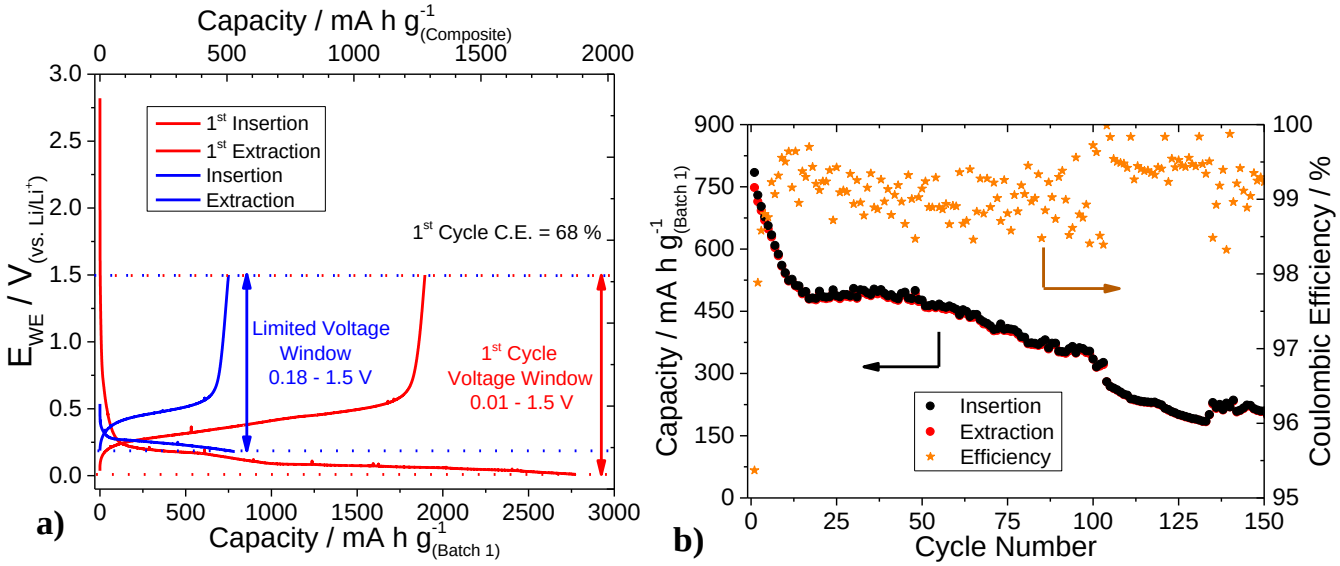

Figure 6-31 – a) Voltage profile of an electrode with a 0.18 V lower voltage limitation .The initial cycle with no limitation displayed in red, the 1st limited cycle displayed in blue. b) Extended cycling of a composite electrode with a lower voltage limit of 0.180 V. Cycled at C/10.

Figure 6-31b displays the extended cycling of an electrode limited to 0.18 V. The electrode displayed a dramatic decrease in capacity over the initial 15 cycles. By the 20th cycle the capacity of the electrode stabilised and remained at around 470 mA h g^{-1} until the 50th cycle. Beyond the 50th cycle the capacity of the electrode decreased. The coulombic efficiency of the electrode throughout cycling was higher than any previously tested electrode (around 99 %).

A dQ/dE plot of selected cycles is displayed in **Figure 6-32**. It was observed that only the first lithium insertion process contributed to obtained capacity. Throughout cycling the voltage of the first lithium insertion process was shifted to lower potential, as the insertion process was shifted towards the lower cut-off voltage of 0.180 V the capacity of the electrode decreased.

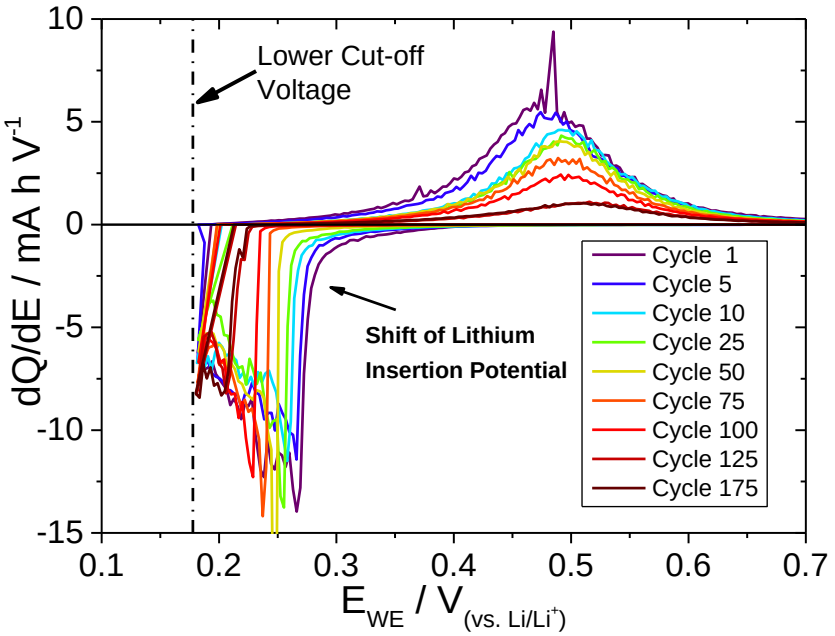

Figure 6-32 – dQ / dE plot of selected cycles during the extended galvanostatic cycling of an electrode with a lower voltage limit of 0.180 V. Cycled at a rate of C/10.

The voltage cut-off of 0.180 V restricted the formation of the high lithium content lithium silicide phase. The restriction of formation of high lithium content phases and hence large volume change of the active particles resulted in higher coulombic efficiency cycling. Despite high coulombic efficiency the capacity of the electrode was observed to decrease. The loss of capacity was attributed to an increase in polarisation throughout cycling.

6.6 Chapter conclusions

Gold removal

Gold removal was confirmed by powder X-ray diffraction. Electrochemical characterisation observed the absence of a reduction process occurring at around 0.42 V in electrodes containing processed nanowire material, the observed voltage of the process did not conform to previous reports on the potential at which lithium alloys with gold [2b], therefore the process was suggested to be associated with surface species such as SiO_x present within the as-received material. The general electrochemical performance of the processed material was observed to be similar to that of the as-received gold removal.

Composite electrode formulation

A number of formulations of composite electrode were evaluated utilising processed batch-1 material as the active component. Formulation 6 was found to provide the highest, most stable capacity over 50 cycles. The superior performance of formulation 6 was attributed to the microstructure of the electrode. Low carbon content reduced excess surface area exposed to the electrolyte, high poly-acrylic acid content promotes proper dispersion of the active material throughout the electrode whilst also ensuring structural stability and reducing the surface area exposed to the electrolyte. A high poly-acrylic acid content was found to be necessary to achieve extended cycling of composite electrodes.

Processed batch-2 material

Processed batch-2 material displayed a lower capacity than processed batch-1 material. The lower capacity of batch-2 was suggested to be due to a high content of non-active, non-silicon material within the batch-2 sample, expected to be composed of breakdown products of the MPS precursor formed during synthesis. Processed batch-2 material did not display a reduction peak associated with lithium insertion into amorphous silicon within the first cycle, unlike batch-1 material.

Limited cycling

Capacity limitation was observed as an effective method to increase the stable cycle life of a composite electrode containing batch-1 material. An electrode limited by an insertion capacity of 1000mA h g^{-1} displayed stable cycling for 130 cycles. In real terms the total amount of charge stored within the limited electrode over the 130 cycles was very similar to that achieved in a non-limited electrode, however the stability and higher coulombic efficiency achieved suggest capacity limitation as an effective method to improve the overall electrochemical performance of composite electrodes. Within a capacity limited electrode the electrochemical

processes contributing to the capacity were observed to vary throughout cycling. The potential of lithium insertion was observed to shift to lower potential as a function of cycle number. The results obtained correspond well to the failure mechanism described by Oumellal *et al.* [4] which suggests that polarisation occurs due to a restriction of lithium ion transport throughout the composite electrode caused by the clogging of the porosity by electrolyte breakdown products.

Voltage limitation was an effective method of restricting formation of higher lithium content phases and restricting the volume expansion of the active material particles. The capacity produced *via* voltage limitation was however unstable and decreased as a function of cycle number. High coulombic efficiencies (> 99 %) were achieved when the potential of the working electrode was restricted to 0.18 V.

Investigations into limited cycling allowed for a more detailed understanding of capacity fade mechanisms including the effect of formation of higher lithium content phases on the coulombic efficiency. Even under significantly restricted conditions electrodes displayed an increase in polarisation throughout testing. The instability suggests that a stable passivation layer was not achieved even when the volume expansion of the active material particles was highly restricted.

6.7 Chapter references

1 Z. Zeng, W.-I. Liang, Y. H. Chu and H. Zheng, *Faraday Discuss.*, 2014, **176**, 95–107.

2 A. M. Chockla, T. D. Bogart, C. M. Hessel, K. C. Klavetter, C. B. Mullins and B. A. Korgel, *J. Phys. Chem. C*, 2012, **116**, 18079–18086.

2b Yuan, L. et al. *J. New Mater. Electrochem.*, 2007, **10**, 95–99.

3 J.-S. Bridel, T. Azaïs, M. Morcrette, J.-M. Tarascon and D. Larcher, *Chem. Mater.*, 2010, **22**, 1229–1241.

4 Y. Oumellal, N. Delpuech, D. Mazouzi, N. Dupré, J. Gaubicher, P. Moreau, P. Soudan, B. Lestriez and D. Guyomard, *J. Mater. Chem.*, 2011, **21**, 6201.

5 I. Kovalenko, B. Zdyrko, A. Magasinski, B. Hertzberg, Z. Milicev, R. Burtovyy, I. Luzinov and G. Yushin, *Science (80-.).*, 2011, **334**, 75–79.

Chapter 7: Influence of electrolyte formulation and rate performance

7.1 Introduction

The large volume expansion of silicon particles during insertion (around 300 % [1]) and subsequent contraction during lithium extraction create a highly dynamic active material. It has been suggested that the dynamic nature of the active material particles prevent the formation of a stable SEI layer at the surface of silicon particles when traditional electrolyte solutions are employed [2, 3].

Electrolyte solutions containing FEC either as an additive [4] or a co-solvent [5, 6] have recently been reported to improve the electrochemical performance of silicon based electrodes. The improvement has been reported to be produced *via* by the formation of improved passivation layers at the surface of active material particles. Electrochemical reduction of FEC has been reported to result in the formation of a number of breakdown products including: poly-carbonate type molecules [5], oxalate type species [7], lithium poly-vinyl carbonate [8] and lithium fluoride [8]. Poly-carbonate and lithium polyvinyl carbonate have been highlighted as breakdown products which may allow for the formation of flexible passivation layers able to withstand the expansion and contraction during lithium insertion and extraction. The flexibility of the layers produced has been suggested to prevent rupture of the passivation layer and the need for re-passivation, restricting growth of SEI layers during cycling.

This chapter aims to investigate the influence of electrolyte on the electrochemical performance of previously produced composite electrodes. The first section tests a number of binary electrolyte solutions containing FEC as a co-solvent. The second section compares, *via* ex-situ SEM and TEM analysis, composite electrodes cycled in traditional electrolytes and FEC containing electrolyte.

7.2 Initial testing of binary solvent electrolytes including FEC

Composite electrodes containing batch-2 material produced to formulation 6 were used to examine the influence of electrolyte on the performance; it was identified that electrodes containing batch-1 material would have been expected to provide superior performance however a lack of material prevented further investigation into the performance of batch-1 material. Simple 1 M $LiPF_6$ binary solvent electrolytes were produced and tested. Binary solvent mixtures were prepared at a 1:1 w/w ratio. The electrolytes produced were compared to commercially sourced LP 30 electrolyte solution. The first cycles of electrochemical cells utilising the prepared electrolyte solutions are displayed in **Figure 7-1** and **Figure 7-2**.

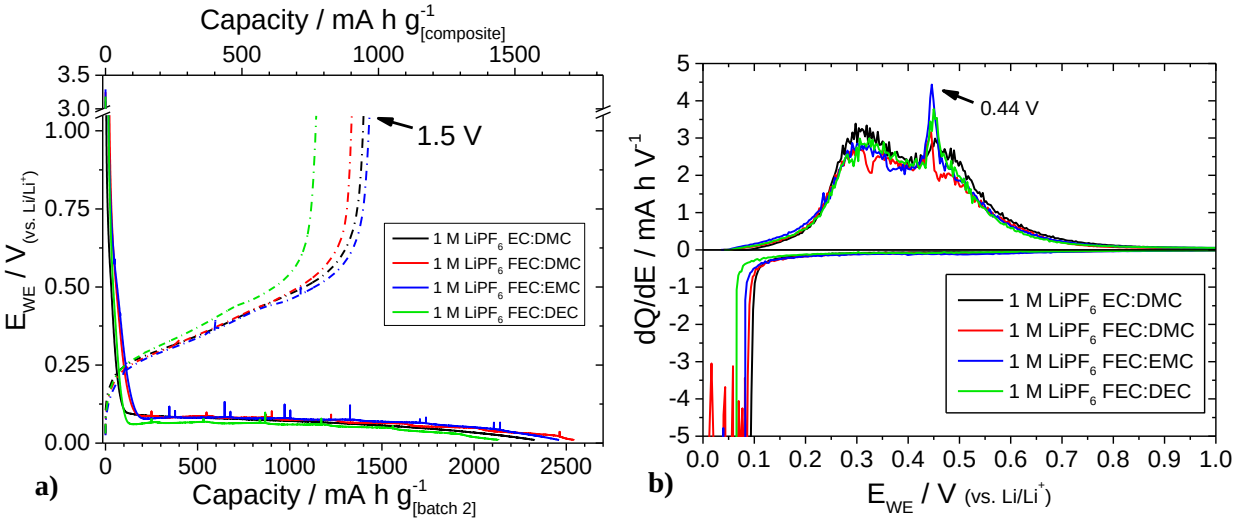

Figure 7-1 – First cycle of composite electrodes in various binary solvent electrolyte solutions a) Voltage profile during lithium insertion and extraction b) dQ/dE plot of the first cycle highlighting lithium insertion and extraction. All electrodes were cycled at C/10.

Electrodes tested in the various electrolyte solutions displayed similar performance. The insertion voltage profile was characteristic of lithium insertion into crystalline silicon beginning at about 0.1 V. The potential at which lithium insertion occurred decreased in the order of LP 30 > FEC: DMC > FEC: EMC > FEC: DEC. Minor differences may have been caused by small differences in water and oxygen content of electrolytes or the use of small samples. Duplicate experiments were not able to be conducted due to a shortage of material during the project. The extraction profile suggested formation of high lithium content amorphous lithium silicide occurred during insertion; a small proportion of lithium extraction from crystalline $Li_{15}Si_4$ was also observed (sharp peak at around 0.44 V). Variation in the performance of the individual composite electrodes used in the experiments may also have contributed to the observed differences.

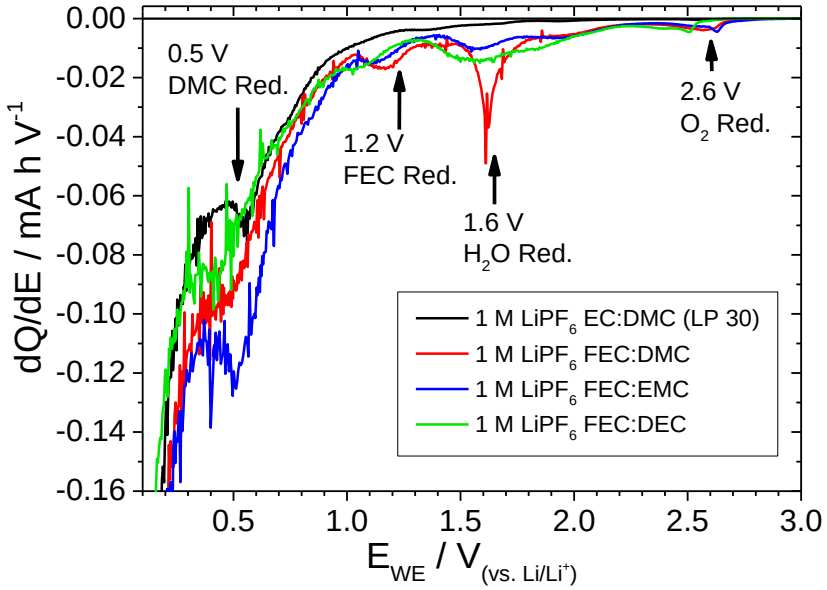

Figure 7-2 – dQ/dE plot highlighting the initial reduction processes occurring between OCV and 0.75 V for each electrolyte solution.

The potential region associated with electrolyte reduction occurring in the first cycle is displayed in **Figure 7-2**. A considerable difference was observed between commercially sourced LP 30 electrolyte and the lab prepared electrolyte solutions. Peaks at observed at 2.6 and 1.6 V in the lab prepared electrolyte solutions are assigned to reduction of dissolved oxygen and water respectively [9]. The profile observed for the commercial electrolyte is typical of that commonly observed in the literature, reduction of EC is commonly reported to initiate at around 1.0 V and a further reduction peak at around 0.5 V is consistent with reduction of DMC [10]. Electrolytes containing FEC were observed to contain a reduction peak at around 1.2 V, consistent with that reported for the reduction of FEC [11,12].

Results of extended cycling of composite electrodes utilising the various electrolyte solutions are displayed in **Figure 7-3**. It was observed that electrolyte solutions containing FEC significantly improved capacity retention and coulombic efficiency of composite electrodes, as previously reported for FEC containing electrolyte solutions [13]. The binary solvent combination was also observed to influence the capacity retention properties of electrodes, 1 M $LiPF_6$ in FEC: DMC displayed a poorer performance in terms of reversible capacity and coulombic efficiency when compared to 1 M $LiPF_6$ in FEC: EMC and 1 M $LiPF_6$ in FEC: DEC (**Figure 7-3**). The variation in performance may have been caused by the presence of water and oxygen contamination within the lab prepared electrolyte solutions.

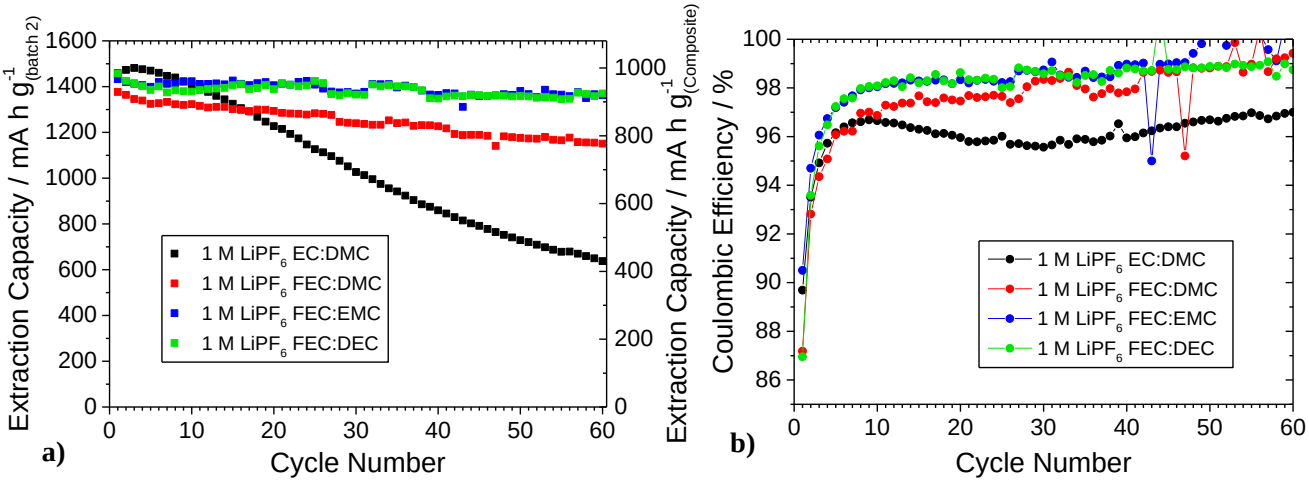

Figure 7-3 – Extended cycling of half cells utilising various electrolyte solutions a) extraction capacity as a function of cycle number b) Coulombic efficiency as a function of cycle number. All cells were cycled utilising a C rate of C/10. (Batch-2).

Over a greater number of cycles, 1 M $LiPF_6$ in FEC: DEC displayed the most stable performance (**Figure 7-4**). 200 cycles were achieved, however the capacity of the electrode was still observed to fade, providing 67 % of the initial extraction capacity after 200 cycles. Erratic coulombic efficiency values were observed for 1 M $LiPF_6$ in FEC: EMC based electrolyte after around 50 cycles, the cause of additional extraction capacity was not clear.

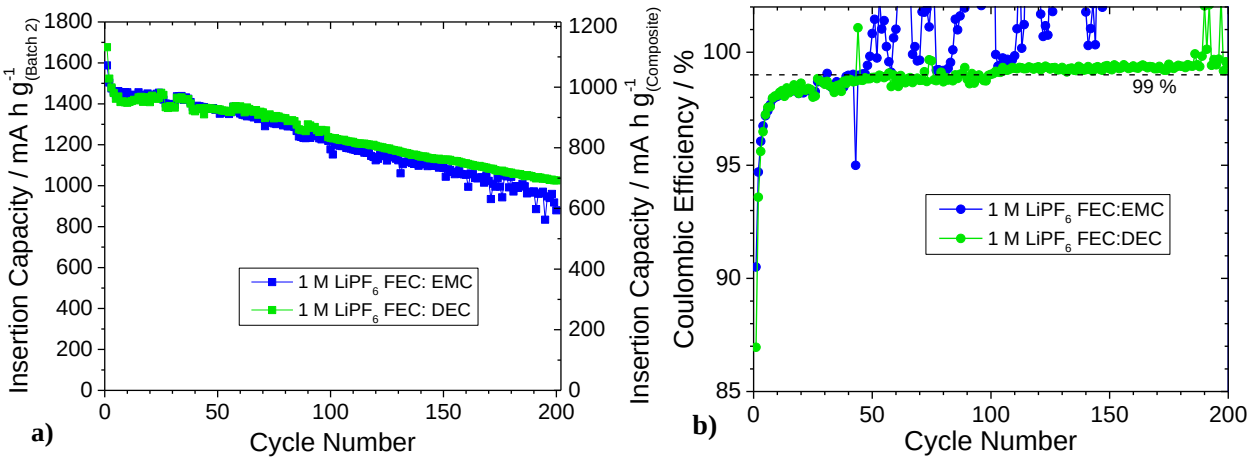

Figure 7-4 – Extended cycling of half cells over 200 cycles in various electrolyte solutions at a C rate of C/10. (Batch-2).

Figure 7-5 displays dE/dE plots of selected cycles of electrodes cycled in 1 M $LiPF_6$ in EC: DMC and 1 M $LiPF_6$ in FEC: DEC. It was observed that the lithium insertion potential decreased as a function of cycle number for the electrode cycled in 1 M $LiPF_6$ in EC: DMC (**Figure 7-5a**). The electrode cycled in 1 M $LiPF_6$ in FEC: DEC displayed a stable lithium insertion potential throughout 150 cycles (**Figure 7-5b**). The observed dependence of the cycling performance on the binary solvent combination requires further work to establish significance.

The onset reduction potential of DEC and DMC have been reported to be very similar at around 1.3 V vs. Li/Li^+ [14]. A possible explanation of the improved performance of the DEC containing

electrolyte may be due to a steric effect and the ability of the solvent molecule to reach the surface of the electrode. Diffusion of solvent molecules through an SEI layer has been suggested as a mechanism for continual SEI growth within carbon based electrodes [15]; a similar process could be expected to occur within silicon based electrodes in which a relatively stable SEI layer has been formed *via* reduction of FEC.

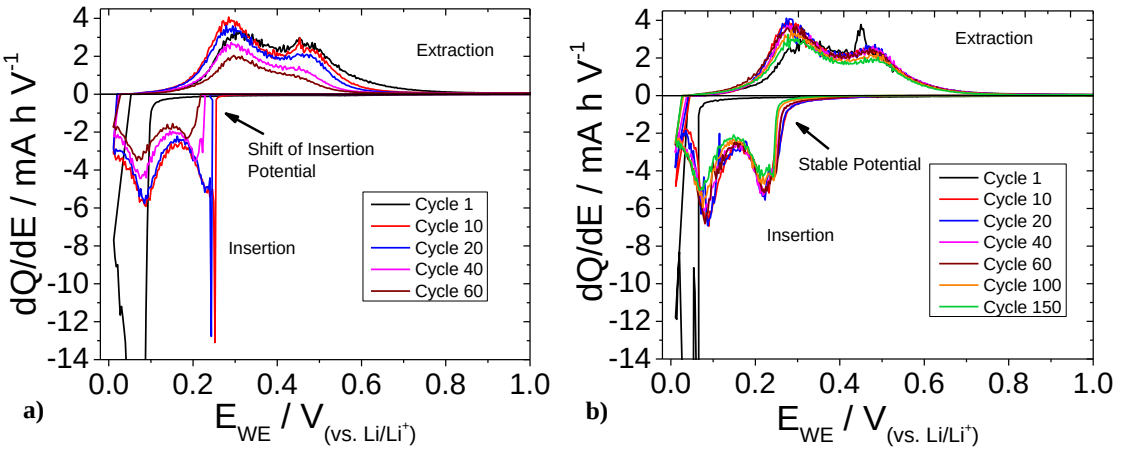

Figure 7-5 – dQ/dE plots of electrodes cycled in a) 1 M $LiPF_6$ EC: DMC and b) 1 M $LiPF_6$ FEC: DEC. Cycled at C/10. (Batch-2)

The performances of all composite electrode formulations previously produced were investigated utilising 1 M $LiPF_6$ FEC: DEC, results of which are displayed in *Appendix 8*. All formulations displayed improved performance when tested utilising 1 M $LiPF_6$ FEC: DEC. Formulation 6 displayed superior performance in both LP 30 and 1 M $LiPF_6$ FEC: DEC electrolyte solutions, suggesting that the physical properties of composite electrodes produced to formulation 6 are conducive to stable cycling of silicon based electrodes irrespective of the electrolyte solution used.

7.3 Investigation into the structural changes of composite electrodes and SFLS nanowire particles cycled in LP 30 and 1 M $LiPF_6$ FEC: DEC electrolyte solutions

A significant difference was observed between the cycle life of composite electrode cycled in commercial LP 30 electrolyte and lab prepared 1 M $LiPF_6$ FEC: DEC. Ex-situ analysis of the electrodes after various cycles was conducted to investigate possible changes occurring within the composite electrode structure and to within the active material particles which may explain the loss of capacity observed in electrodes cycled in LP 30 based electrolyte.

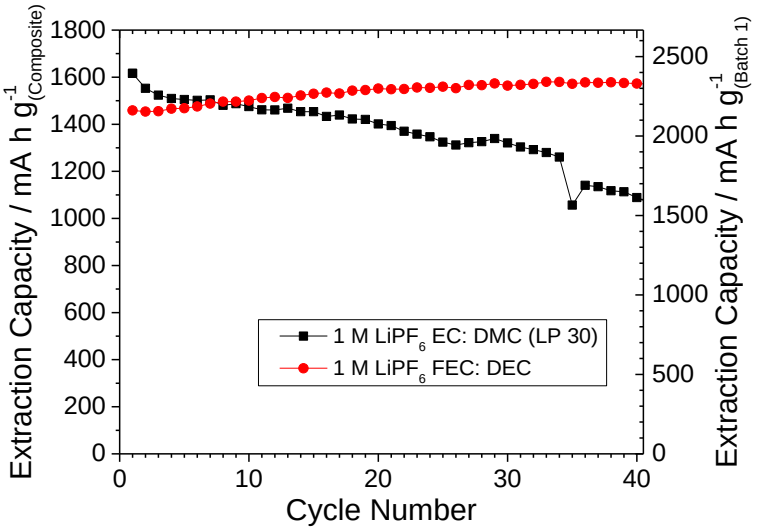

Figure 7-6 – Extended cycling of formulation 6 composite electrodes in LP30 and 1M LiPF6 FEC: DEC cycled at a C rate of C/10. (Batch-1)

The following work was conducted using processed batch-1 material. After electrochemical cycling cells were disassembled and the electrodes were analysed *via* electron microscopy to observe possible changes to the composite electrode structure and active material particles. **Figure 7-6** displayed the variation in performance of batch-1 composite electrodes cycled in the highlighted electrolytes. The electrode cycled in 1 M $LiPF_6$ EC: DMC was observed to considerable capacity fade.

7.3.1 Structure of composite electrodes prior to electrochemical testing

The structure of a composite electrode produced to formulation 6 prior to electrochemical testing is displayed in **Figure 7-7**. The electrode consisted of a ~30 µm thick composite electrode layer (top layer) attached to a copper foil substrate (bottom layer).

a) 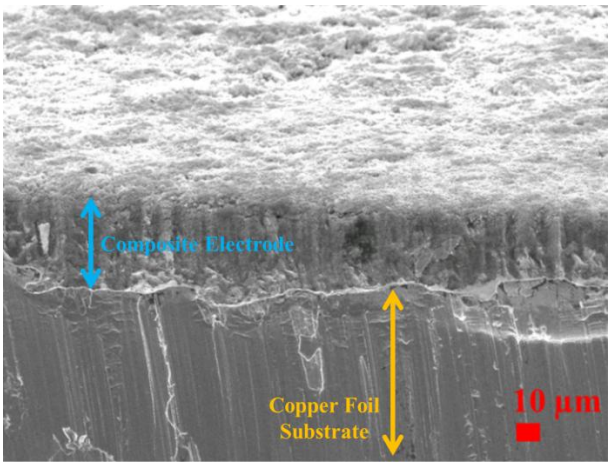

b) 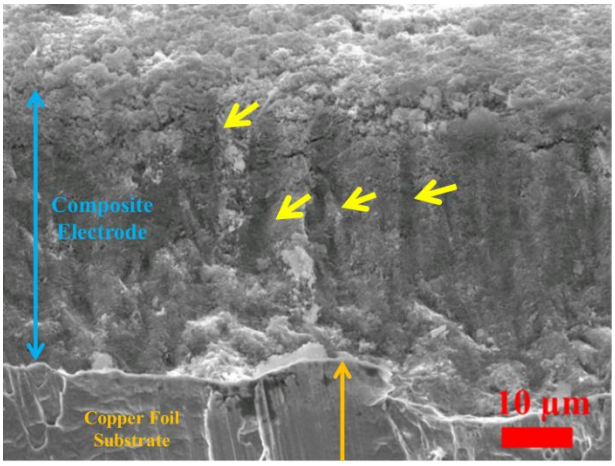

Figure 7-7 – Low magnification SEM images of the cross-section of a composion 6 composite electrode yellow arrows highlight observed vertical cut marks and densification of the composite layer caused by the sample preparation procedure.

A higher magnification image of the micro structure of the composite electrode is displayed in **Figure 7-8**. Silicon nanowire particles, carbon black and spherical amorphous silicon particles were observed within the electrode, poly-acrylic acid binder was difficult to identify.

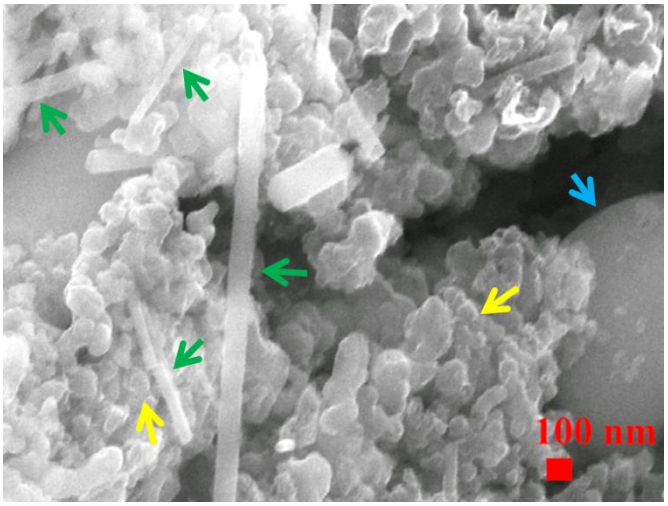

Figure 7-8 – high magnification SEM images of formulation 6 composite electrodes prior to electrochemical testing, green arrows indicate silicon nanowire particles, yellow arrows highlight carbon clack conductive additive particles and the blue arrow highlights an amorphous silicon particle.

7.3.2 Composite electrodes cycled utilising LP 30 electrolyte

7.3.2.1 Imaging of composite electrode structure

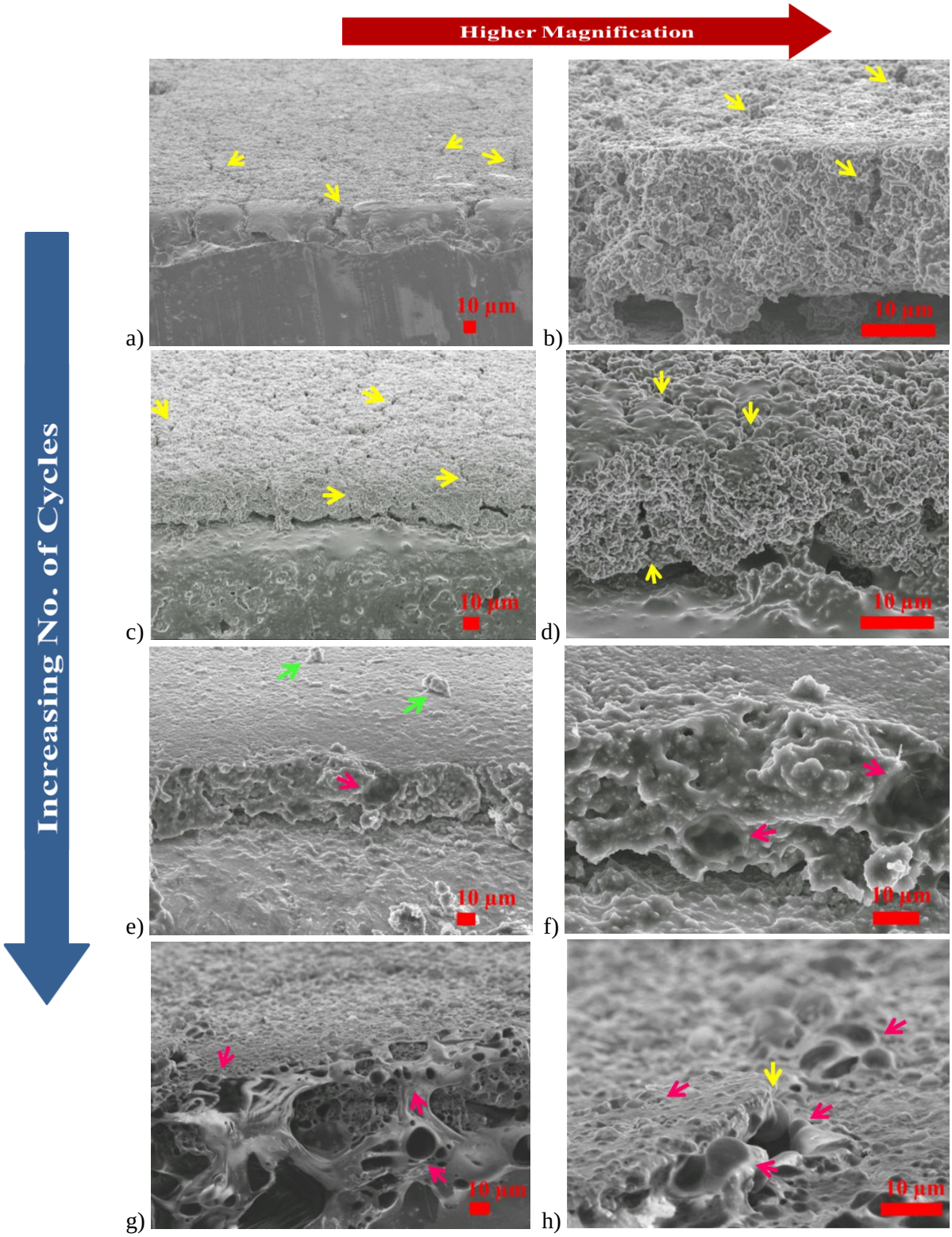

Figure 7-9 – SEM images of formulation 6 composite electrodes cycled in LP 30 electrolyte after various numbers of cycles: a, b) 1 cycle, c, d) 5 cycles, e, f) 10 cycles, g, h) 50 cycles. The electrodes are displayed after full lithium extraction to 1.5 V and washing with DMC to remove any remaining $LiPF_6$. Yellow arrows = cracks, green arrows = protrusions, pink arrows = deflated bubbles.

Figure 7-9 contains SEM images which display the structural changes of a formulation 6 composite electrode during electrochemical cycling in LP 30 electrolyte. **Figure 7-9a, and b** display the structure of a composite electrode after 1 cycle. Cracking of the composite film was observed, fragments of the composite retained contact with the current collector and other fragments of the composite layer. After 5 cycles, (**Figure 7-6c, and d**) smaller fragments of the composite electrode were observed to have been produced. The presence of a smooth surface film covering both the surface of the composite layer and the current collector was observed. The general structure of the composite layer appeared to have deteriorated and become less cohesive.

After 10 cycles (**Figure 7-9e, and f**), the surface of the composite film was observed to be smooth except for regions where material protruded from the surface. No cracks were apparent across the surface. A think smooth layer was also observed covering the entire available surface across the edge of the composite layer. Features which appeared to resemble collapsed bubbles were also observed at the edge of the composite. After 50 cycles (**Figure 7-9g, and h**), a large amount of unknown material was observed to be present across the edges and surface of composite layer. The material appeared to be a polymer type material which was stretched across regions of the electrode. Large deflated bubbles appeared to be present within the material along the edge and surface cracks of the composite layer. Small deflated bubbles were observed to be present within a film of material across the surface of the composite electrode.

The material observed to form across the surface of the electrode in **Figure 7-9** is suggested to be composed of electrolyte breakdown products produced *via* reduction of the electrolyte during cycling. The material was observed to accumulate within the electrode throughout cycling. The observed accumulation of material within the composite electrode structure would be expected to reduce lithium transport throughout the electrode and correspond to the to the observed capacity fade of the composite electrode during electrochemical cycling. The deflated bubbles observed to form after 10 cycles suggests that gas may be produced within the composite and become trapped within the electrolyte breakdown products.

7.3.2.2 Imaging of nanowire particle structure

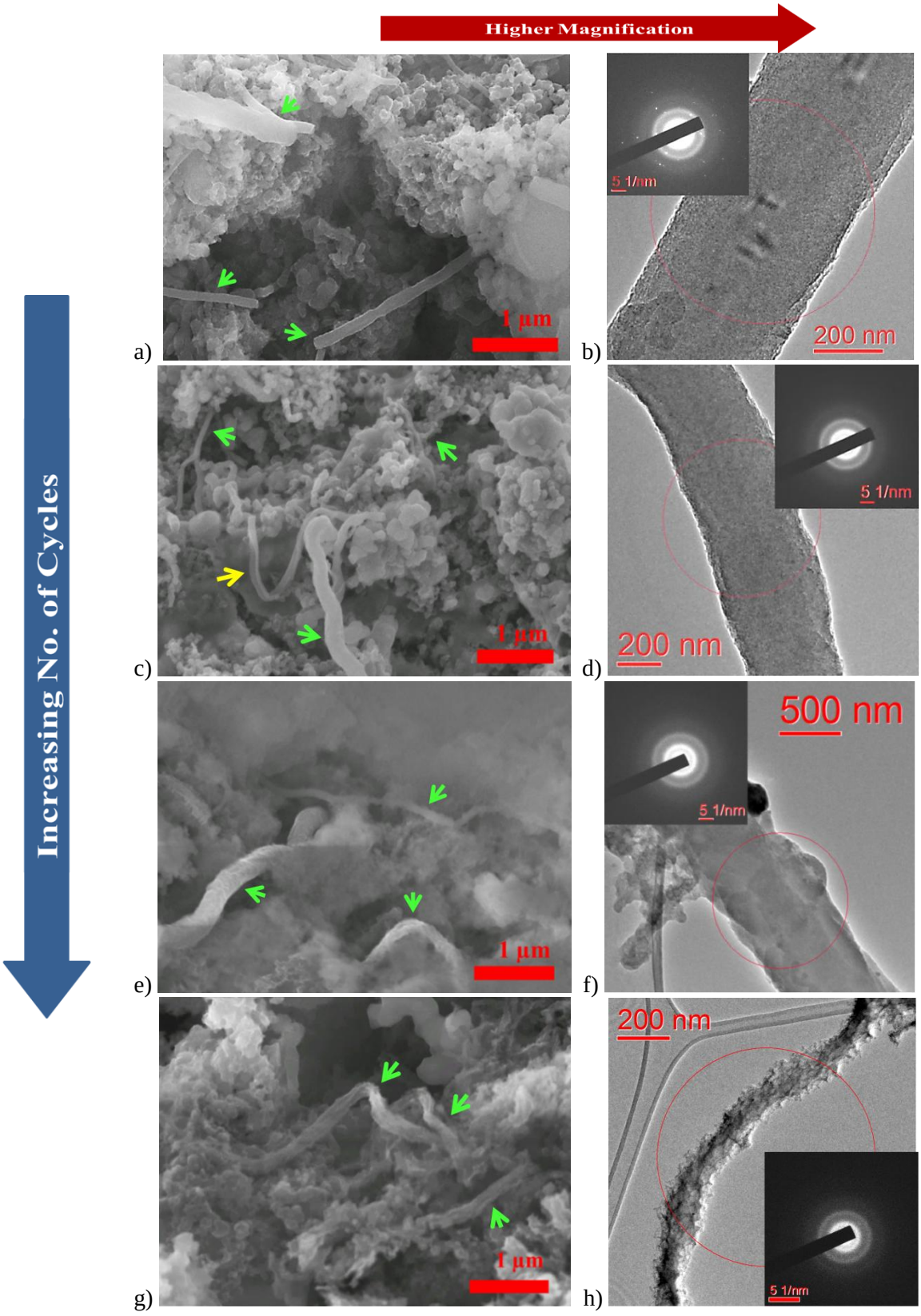

Figure 7-10 – a), c), e) and g) SEM images of active material particles after 1, 5, 10 and 50 cycles in LP 30. Green arrows = nanowire particles, yellow arrows = split nanowire particles. b), d), f) and h) TEM images with inset electron diffraction patterns of active material particles after 1, 5, 10 and 50 cycles respectively. Composite electrodes were washed with acetonitrile and dilute nitric acid to remove electrolyte breakdown products.

Figure 7-10 displays SEM and TEM images of the evolution of the structure of active material particles throughout extended cycling. Composite electrodes were washed to remove electrolyte breakdown products and then imaged. Samples obtained from the washed composite electrodes were also imaged using TEM. After 1 cycle the active material particles remained relatively straight and conformed generally with the structure observed previously in Chapter 4. Nanowire particles however displayed remaining crystallinity within the core, observed *via* the SAED pattern displayed in **Figure 7-10b**. The remaining crystallinity within the structure of the active particles (**Figure 7-10a)** is suggested to be caused by a lack of reaction due to the higher C-rate applied to the sample.

After 5 cycles the nanowire particles were observed to have become curved and distorted (**Figure 7-10c**). A number of nanowire particles were also observed to have split along the length axis of the particle. Electron diffraction conducted on single silicon nanowire particle suggested that after 5 cycles the structure of the nanowire particles was amorphous (**Figure 7-10d**). Full removal of electrolyte breakdown products from an electrode after 10 cycles was not completely achieved (**Figure 7-10e**). Nanowire particles were observed to display retention of nanowire type morphology however the surface of the particle had become rough and distorted. Particles imaged from a sample removed from an electrode after 50 cycles were also observed to have retained nanowire type morphology (**Figure 7-10g, and h**), however the surface of the particles appeared significantly deteriorated and displayed a very rough surface texture.

The nanowire particles were observed to retain nanowire type morphology throughout 50 cycles. The surface structure of the nanowire particles displayed substantial evolution during cycling, the surface became increasingly rough and distorted, and after 50 cycles nanowire particles displayed a porous highly cratered surface. Similar structural evolution of silicon nanowire particles upon electrochemical cycling has been reported in the literature [16]. A recent report suggested a pore collapse and regrowth mechanism during the electrochemical cycling of an amorphous thin film of silicon [17]. Similar structural changes have also been reported to occur in germanium nanowires during electrochemical lithium insertion and extraction [18].

7.3.3 Composite electrodes cycled utilising 1 M $LiPF_6$ FEC: DEC electrolyte

7.3.3.1 Imaging of composite electrode structure

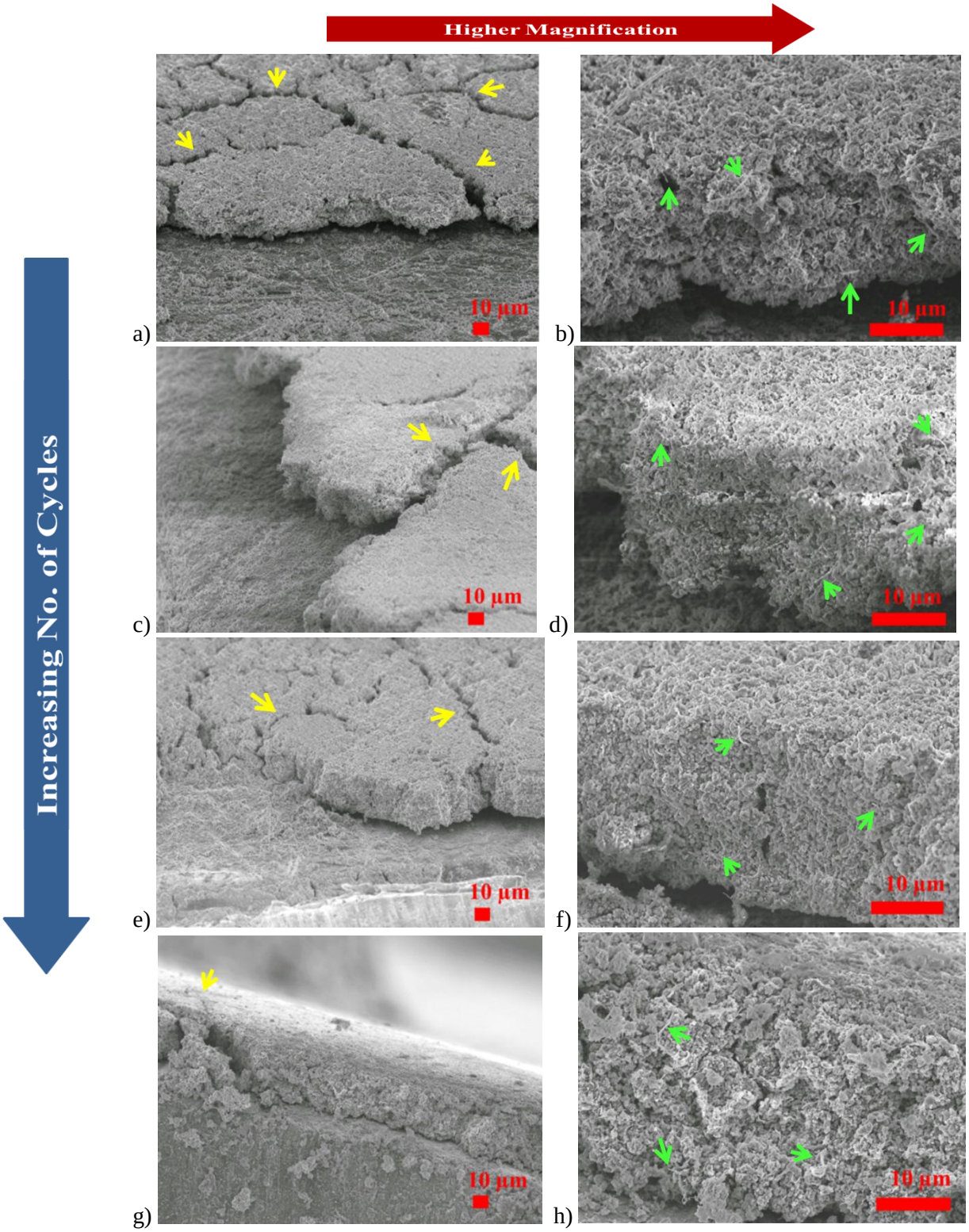

Figure 7-11 – SEM images of formulation 6 composite electrodes cycled in 1 M $LiPF_6$ FEC: DEC electrolyte after various numbers of cycles: a, b) 1 cycle, c, d) 5 cycles, e, f) 10 cycles, g, h) 50 cycles. The electrodes are displayed after full lithium extraction to 1.5 V and washing with DMC to remove $LiPF_6$. Yellow arrows = cracks, green arrows = nanowire particles.

Figure 7-11 displays imaging of composite electrodes cycled in 1 M $LiPF_6$ FEC: DEC after selected numbers of electrochemical cycles. After 1 cycle (**Figure 7-11a, and b**) large cracks were observed to have formed across the composite electrode layer resulting in the formation of large fragments of the composite electrode layer. At higher magnification the porosity and microstructure within the composite electrode layer was easily visible. Nanowire particles were clearly visible throughout the composite structure suggesting limited electrolyte breakdown products had formed.

After 5 electrochemical cycles the structure of a composite electrode displayed a very similar structure to that observed for an electrode after 1 cycle. Large cracks across the surface of the electrode were present. Higher magnification imaging suggested the electrode had slightly reduced in porosity however individual nanowire particles were easily observed within the composite structure. Composite electrodes displayed very similar structures after 10 and 50 electrochemical cycles, large cracks were present within the composite film however the microstructure of the composite displayed a similar appearance. After 50 cycles the microstructure of the electrode appeared slightly denser and more fragmented however the composite electrode remained generally consistent with that observed after 10 cycles.

The structural variation of composite electrodes cycled in 1 M $LiPF_6$ FEC: DEC was observed to be considerably different from electrodes cycled in LP 30 electrolyte. The composite structure did not appear to change significantly between cycle 1 and cycle 50. The visibility of nanowire particles at the surface of an electrode after 50 cycles suggests that the passivation layer remained relatively thin after 50 cycles. The lack of large regions of observable electrolyte breakdown products at the surface of composite electrodes cycled in 1 M $LiPF_6$ FEC: DEC corresponds well to recent reports in the literature of the effect of FEC based electrolytes on the formation of a stable passivation layer on silicon based electrodes[5,19].

The retention of the microstructure of composite electrodes cycled utilising 1 M $LiPF_6$ FEC: DEC corresponds well to retention of the electrochemical performance of the electrodes. The failure mechanism suggested by Oumellal *et al.* appeared to correspond well with observations made of cycled composite electrodes [20].

7.3.3.2 Imaging of Nanowire Particle Structure

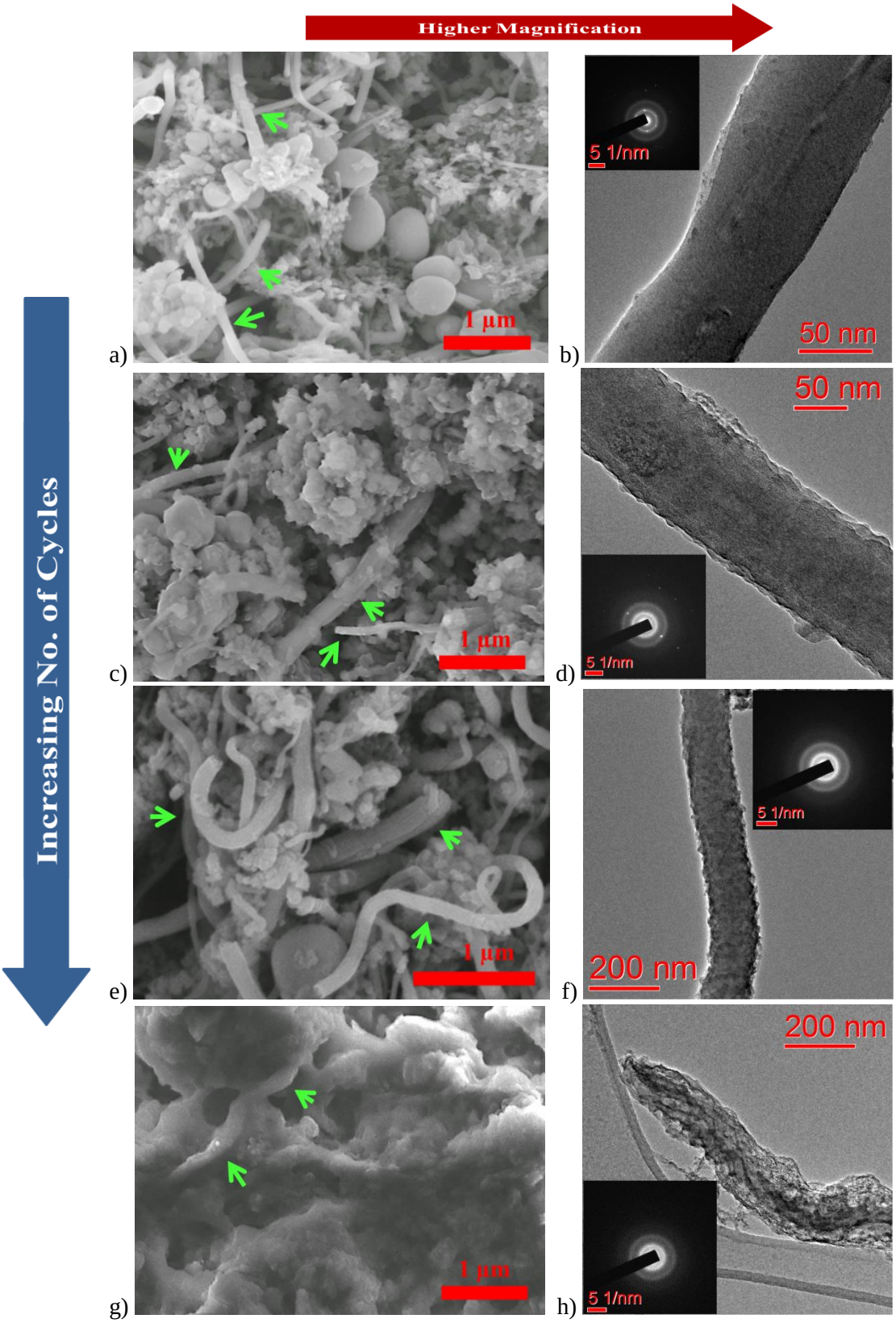

Figure 7-12 – a), c), e) and g) SEM images of active material particles after 1, 5, 10 and 50 cycles respectively in 1 M $LiPF_6$ FEC: DEC. b), d), f) and h) display TEM images with inset electron diffraction patterns of active material particles after 1, 5, 10 and 50 cycles respectively. Composite electrodes were washed with acetonitrile and dilute nitric acid to remove electrolyte breakdown products. Green arrows = nanowire particles.

The structure evolution of nanowire particles when electrochemically cycled using 1 M $LiPF_6$ FEC: DEC was investigated. Images displayed in **Figure 7-12** were obtained *via* SEM and TEM imaging of samples removed from cycled composite electrodes. After 1 cycle the structure of the nanowire particles conformed to that previously observed when cycled in LP30 electrolyte. Nanowire particles were observed to have retained crystalline regions within the core and display axial amorphisation of regions of the crystalline core. The crystalline core is suggested to have been present due to incomplete ration of the active material caused by an initial applied C-rate of 0.1 C.

After 5 cycles nanowire particles were observed to display a rougher surface texture however remained relatively straight (**Figure 7-12)**. Crystalline regions were observed to remain within the core of nanowire particles. The retention of crystalline regions suggests incomplete reaction occurred prior to the 5 cycle; however the nanowire particle imaged after 5 cycles displayed a higher amorphous content than the particle imaged after 1 cycle. The variation in the utilisation of the particles corresponds to the increase in reversible capacity observed for electrodes cycled in 1 M $LiPF_6$ FEC: DEC (**Figure 7-6**). After 10 cycles the nanowire particles were found to be curved and twisted (**Figure 7-12e, and f**). The structure of the nanowire particles was observed *via* electron diffraction to be amorphous. The variation in structure after 5 cycles and 10 cycles suggests that the retention of the crystalline core causes nanowire particles to retain a reasonably straight morphology, however once fully amorphous the particles become more curved. The surface of the nanowire particles was rougher that that previously observed after 5 cycles.

The SEM image of a sample of a composite electrode after 50 cycles displayed the presence of electrolyte breakdown products not removed during washing steps (**Figure 7-12g**). The presence of electrolyte breakdown products after washing steps suggested that after 50 cycles substantial electrolyte breakdown products were present within a composite cycled utilising 1 M $LiPF_6$ FEC: DEC. The structure of a nanowire particle was more clearly observed *via* TEM imaging, nanowire particles were found to display an amorphous, porous structure.

7.3.4 Comparison between LP30 and 1 M $LiPF_6$ FEC: DEC after 50 cycles

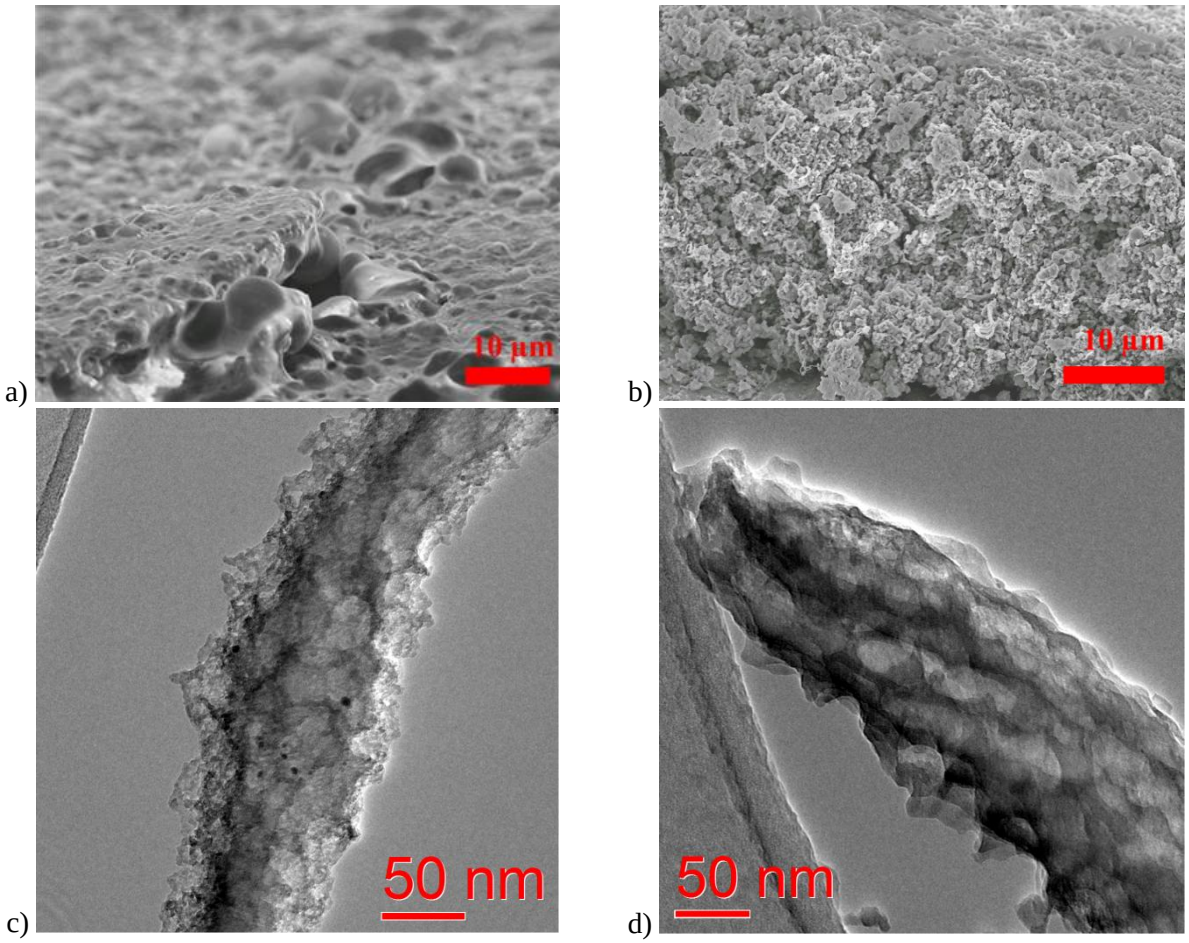

Figure 7-13 – Comparison of composite electrode structure a),b) and nanowire particle structure c),d) after 50 cycles in LP 30 a), c) and 1 M $LiPF_6$ FEC:DEC b), d).

The greatest difference between the electrodes cycled for 50 cycles in the two different electrolyte solutions was that of the structure of the composite electrode, specifically the amount of electrolyte breakdown products formed within the electrode. Vast amounts of electrolyte breakdown products were observed in the composite electrode cycled in LP 30 (**Figure 7-13a, b**). Cracks were observed across the composite electrodes cycled in both electrolyte solutions suggesting that cracking of the composite film was not a cause of capacity fade.

The structure and morphology of nanowire particles were observed to be slightly different, the surface of the particle cycled in LP 30 was rougher and less dense than the particle cycled in 1 M $LiPF_6$ FEC: DEC, however the general structure and morphology of the particles was similar (**Figure 7-13c, d**). The lack of considerable difference suggests the difference in the structural stability of the active material particles was not the cause of the observed capacity fade of electrodes cycled in LP 30.

The major cause of the capacity fade observed for composite electrodes cycled in LP 30 based electrolyte is suggested to be the significant amount of electrolyte breakdown products formed

throughout cycling. The electronically insulating and ionically hindering properties of the electrolyte breakdown products are suggested to effectively smother the composite electrode and restrict and prevent regions of the electrode from operating. The cause of excessive electrolyte breakdown observed in LP 30 based electrolytes is likely to be caused by the need for continual re-passivation of the surface of the active material due to improper passivation produced *via* the reduction of EC and DMC.

7.4 Rate performance utilising 1 M $LiPF_6$ FEC: DEC

The rate performance of formulation 6 based electrodes were investigated utilising a 1 M $LiPF_6$ FEC: DEC electrolyte. The insertion and extraction rate performance of a composite electrode was investigated separately. **Figure 7-14** displays the voltage profile of a composite electrode during rate testing.

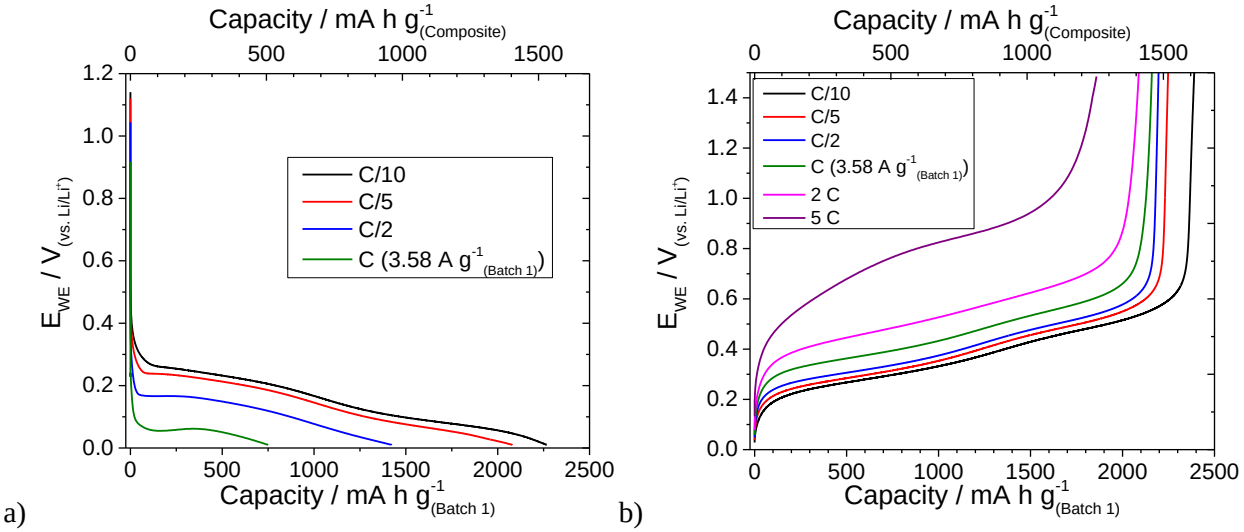

Figure 7-14 – Rate testing of a batch-1 formulation 6 composite electrode cycled in a half-cell configuration utilising 1 M $LiPF_6$ FEC: DEC electrolyte. a) Voltage profile of the insertion process conducted at various C rates, extraction conducted at a rate of C/10. b) Voltage profile of the extraction process conducted at various C rates, insertion conducted at a rate of C/10.

The extraction process displayed a substantially higher performance at increased rate (**Figure 7-14**). Higher polarisation of the potential was observed during lithium insertion. High polarisation combined with a lower cut-off potential close to the potential of lithium insertion restricts the tolerance of the insertion process to polarisation. The observed variation in polarisation between the insertion and extraction processes suggests an intrinsic limitation to the lithium insertion process compared to the lithium extraction process. This observation corresponds with the variation in charge transfer resistance observed during the initial cycle of a composite electrode in Chapter 4 (**Figure 4-14**). A lower charge transfer resistance was observed for the electrode containing lithiated silicon compared to the electrode containing silicon prior to lithium insertion; the same variation was observed in the third cycle of a composite electrode (*Appendix 4)*.

The observed polarisation will be produced by a number of contributing factors including the electronic and ionic wiring within the composite electrode as well as intrinsic properties of the insertion and extraction processes. To investigate the role of electronic and ionic wiring on the observed polarisation a formulation 8 composite electrode was tested at various rates. Formulation 8 displays a lower concentration of active material, a higher conductive carbon

content and lower binder content, all factors which would be expected to improve the electronic and ionic wiring of the resulting composite electrode. **Table 7-1** compares the composition of formulation 6 and 8 electrodes.

Table 7-1 – Details of the composite electrodes produced to formulation 6 and 8.

Formulation No.	Silicon / wt. %	Carbon / wt. %	PAA / wt. %	Theoretical Capacity of Electrode / mA h g^{-1}	Carbon Contribution / %
6	67.5	10	22.5	2415.8	0.82
8	52.5	30	17.5	1879.0	3.09

Rate testing results of a formulation 8 electrode are displayed in **Figure 7-15**. Notably, the polarisation observed during both insertion and extraction at increased rate was lower than that observed for a formulation 6 electrode. A combination of increased carbon content and a higher dilution of active material act to reduce the polarisation of the composite electrode. The extraction process displayed a greater rate performance than the insertion process as previously observed for a formulation 6 composite electrode (**Figure 7-14**).

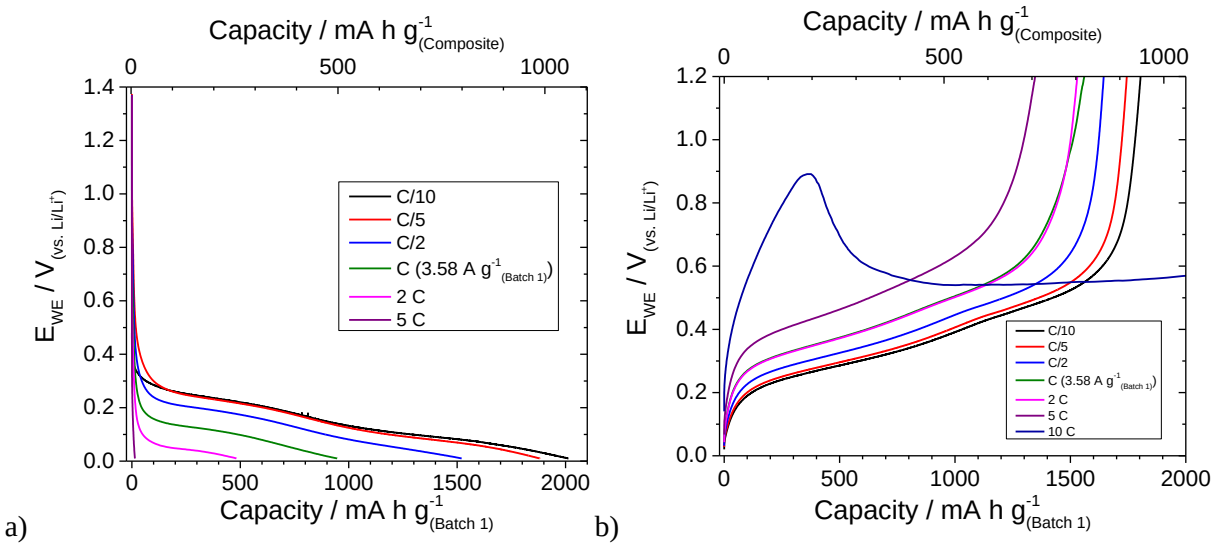

Figure 7-15 – Rate testing of formulation 8 composite electrodes cycled half-cell configuration utilising 1 M $LiPF_6$ FEC: DEC electrolyte. a) Voltage profile of the insertion process conducted at various C rates, extraction conducted at a rate of C/10. b) Voltage profile of the extraction process conducted at various C rates, insertion conducted at a rate of C/10.

When comparing the achieved capacity values of the two formulations, the lower content of silicon within formulation 8 causes the insertion capacity achieved at 1 C in terms of mA h g^{-1} (of composite) to be comparable to that of formulation 6, however due to the lower polarisation of formulation 8 a considerable amount of capacity could be achieved at 2 C whereas no capacity was produced from formulation 6 at 2 C.

a)

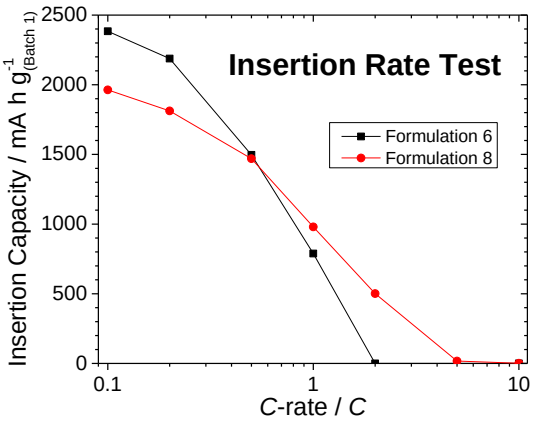

b)

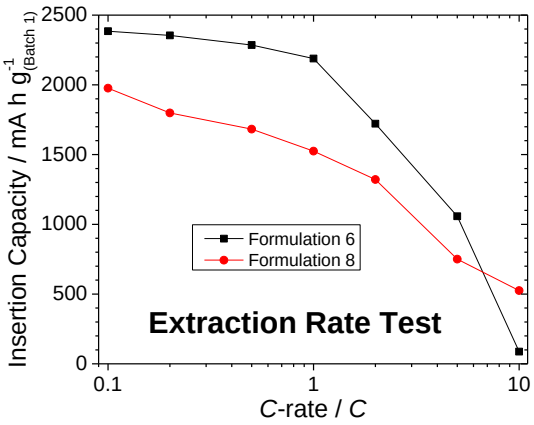

Figure 7-16 – a) Capacity values achieved during insertion rate testing of formulation 6 and 8 composite electrodes, b) capacity achieved on subsequent insertion following extraction rate tests. Insertion capacity values are displayed as they provided the most accurate information.

The influence of the formulation of composite electrodes to the rate performance can be clearly observed in **Figure 7-16**. Improved high rate insertion and extraction performance was observed for formulation 8 electrodes. The results highlight the importance of electrode formulation to the resulting rate performance of the electrode and suggest that *via* optimisation the rate performance of a composite electrode containing SFLS nanowire material may be significantly improved.

7.5 Addition of vinylene carbonate and capacity limited cycling

Vinylene carbonate (VC) has been widely reported to improve the extended cycling performance of composite electrodes and increase the coulombic efficiency of silicon based electrodes. The long term stability of composite electrodes was investigated utilising FEC and VC containing electrolytes.

7.5.1 Addition of vinylene carbonate to 1 M $LiPF_6$ FEC: DEC

The addition of vinylene carbonate to FEC based electrolytes has been reported to improve the performance of silicon based electrodes both in terms of cycle life and coulombic efficiency [21]. Addition of 1 vol. % VC to 1 M $LiPF_6$ FEC: DEC was conducted and the electrolyte solution was tested by cycling a composite electrode containing processed batch-2 material utilising the electrolyte. The first cycle of the cell is displayed in **Figure 7-17**, the initial reduction reactions are highlighted in the corresponding dQ/dE plot in **Figure 7-17b**. The plateau corresponding to lithium insertion into crystalline silicon was observed to occur at around 0.04 V.

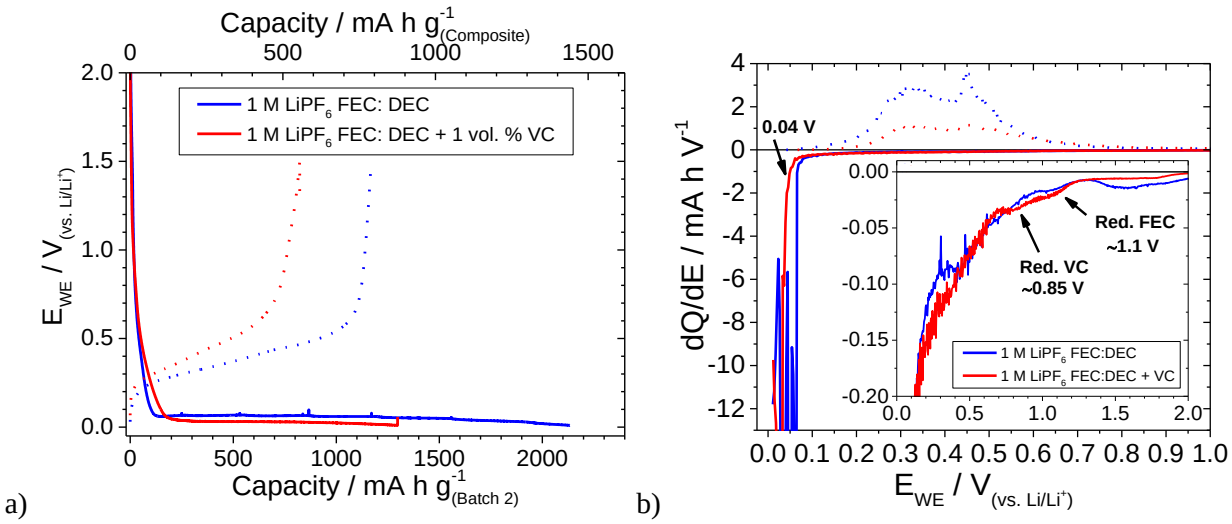

Figure 7-17 – First cycle of formulation 6 composite electrode containing batch-2 silicon nanowire material cycled in 1 M $LiPF_6$ FEC: DEC + 1 vol. % VC. a) Voltage profile of first cycle insertion and extraction process. b) dQ/dE plot of the first cycle, Inset is a zoomed region of the plot highlighting the reduction potential of FEC and VC *via* comparison of the initial reduction processes of composite electrodes cycled in 1M $LiPF_6$ FEC:DEC with and without VC. Cells were cycled between 0.01 and 1.5 V at a rate of C/10.

Two reduction peaks, highlighted in **Figure 7-17b**, occurring at around 1.1 and 0.85 V during the initial insertion process of a composite electrode are assigned to the reduction of FEC and VC respectively. The reduction potentials correspond relatively well to a report of the reduction of FEC and VC measured in separate electrolytes containing either FEC or VC [12]. The low initial insertion capacity achieved for the electrode cycled using VC may be caused by an increase in

resistance of the lithium insertion process caused by the formation of VC reduction products at the surface of the electrode. The increase in resistance caused increased polarisation of the electrode and resulted in a lower insertion potential causing the lower cut-off potential of 0.01 V to be reached prior to complete reaction of the active material.

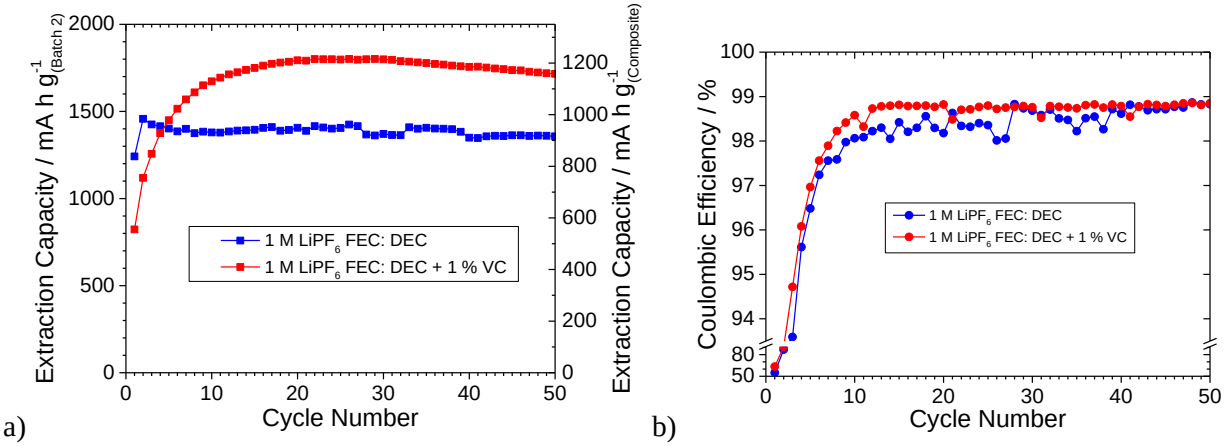

a) b)

Figure 7-18 – Extended cycling of formulation 6 composite electrode cycled in 1 M $LiPF_6$ FEC: DEC + 1 vol. % VC. a) Extraction capacity obtained over 50 cycles. b) Coulombic efficiency values obtained over 50 cycles. Cells were cycled between 0.01 and 1.5 V at a rate of C/10.

Comparison of the extended cycling performance of composite electrodes cycled with and without VC is displayed in **Figure 7-18**. The extraction capacity achieved from the cell containing VC was observed to increase throughout the first 20 electrochemical cycles reaching a capacity of around 1800 mA h $g^{-1}_{(Batch\text{-}2)}$ (**Figure 7-18b**). The capacity was observed to be greater than that achieved in an electrolyte without the presence of VC. The additional capacity maybe caused by an improved initial SEI layer which prevented loss of active material within the electrode during the initial cycles. The difference in capacity may also have been caused by an error in the measurement of the mass of silicon held within the electrode; further work would be required to confirm the capacity improvement.

The electrode cycled in the 1M $LiPF_6$ FEC: DEC + VC electrolyte displayed a higher coulombic efficiency throughout the first 50 cycles. The improved coulombic efficiency is attributed to the formation of an improved SEI layer *via* the reduction of VC. The higher efficiency suggests the SEI layer is more resistant to degradation throughout cycling reducing the need for re-passivation of the interface between the active material and the electrolyte.

7.5.2 Extended cycling

The results of capacity limited cycling of electrodes in FEC containing electrolytes are displayed in **Figure 7-19**. Electrodes were limited at 1000 mA h $g^{-1}_{(Batch\text{-}2)}$ during the insertion process after pre-cycling of the electrodes during which no limitation was applied other than lower and upper cut-off potential of 0.01 V and 1.5 V respectively. Stable cycling was achieved

for around 200 cycles; the cells were prematurely stopped due to the overheating of a temperature controlled unit.

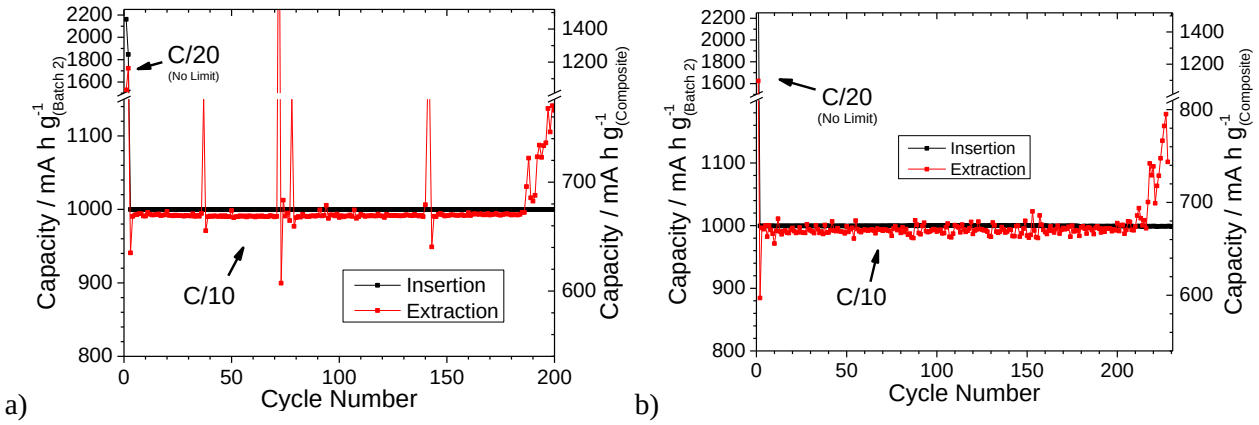

Figure 7-19 – Extended cycling of formulation 6 composite electrodes cycled using a) 1 M $LiPF_6$ FEC: DEC b) 1 M $LiPF_6$ FEC: DEC + 1 vol. % VC. Both cells were pre-cycled at a c rate of C/20 between 0.01 and 1.5 V prior to capacity limited cycling limited to an insertion capacity of 1000 mA h $g^{-1}_{(Batch-2)}$ and cycled at a C-rate of C/10. The C/10 charge and discharge rate combined with the capacity limitation corresponds to maximum insertion in 2 hours 47 min 39 seconds.

Both electrodes displayed stable cycling up to the failure of the temperature controlled unit. To further investigate the cycle life beyond 200 cycles further experiments would need to be conducted, the use of a metallic lithium electrode would be avoided in future experiments to reduce any influence of dendritic lithium on the performance of the electrolyte solution. The major difference in the performance of the two electrodes was the coulombic efficiency achieved throughout cycling (**Figure 7-20**). Both electrodes displayed coulombic efficiency of above 99 % for the majority of the cycles; however the electrode cycled in an electrolyte containing VC overall displayed higher efficiency values. A large variation in the efficiency of the electrode cycled in VC containing electrolyte was observed, further work would need to be conducted to clearly identify the influence of VC on the coulombic efficiency of the composite electrodes over extended cycling. Specifically efficiencies of over 100 % were observed in a number of cycles for both electrodes, suggesting either inactive lithiated material was reactivated or an oxidation process other than lithium extraction from the active material was occurring. Oxidation of material other than lithiated silicon is suggested to be the most likely cause of the additional extraction capacity.

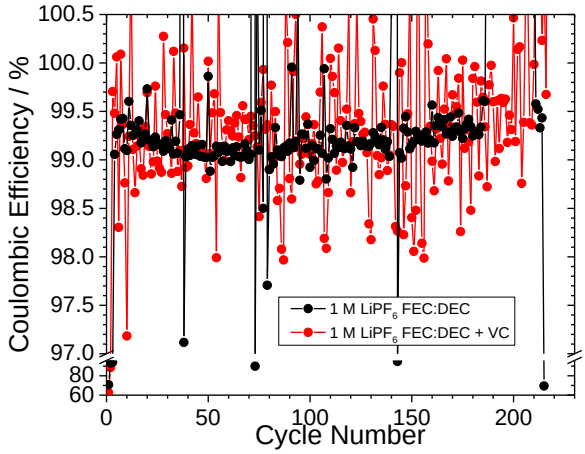

Figure 7-20 – Coulombic efficiency values of electrodes cycled under capacity limitation in electrolytes of 1 M $LiPF_6$ FEC: DEC and 1 M $LiPF_6$ FEC: DEC + 1 vol. % VC. The coulombic efficiency values correspond to the cycling data displayed in Figure 7-19. The coulombic efficiency data recorded displayed significant noise, the cause was unknown.

Results of higher rate capacity limited cycling are displayed in **Figure 7-21**. It was observed that the initial capacity of a formulation 1 electrode cycled in 1 M $LiPF_6$ FEC: DEC + 1 vol. % VC was lower than that that achieved for formulation 1 electrodes cycled in both LP 30 (Chapter 4) and 1 M $LiPF_6$ FEC: DEC (*Appendix 8*), the capacity did not increase during the first 3 cycles unlike that previously observed for formulation 6 electrodes containing batch-2 material cycled in VC containing electrolytes (**Figure 7-18**). The low capacity of the electrode resulted in a capacity limitation close to the practical capacity of the electrode without limitation.

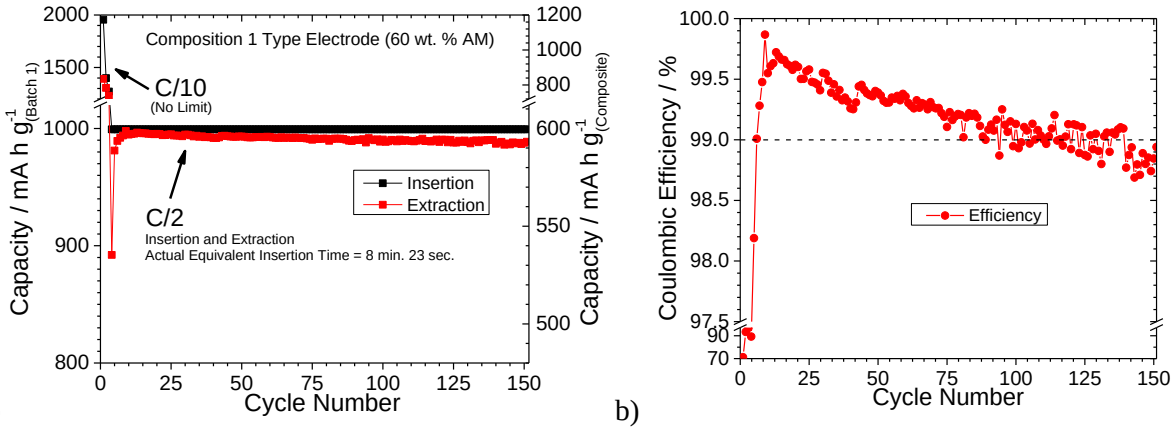

a) b)

Figure 7-21 – Extended cycling of formulation 1 composite electrodes containing batch-1 silicon nanowire material cycled using 1 M $LiPF_6$ FEC: DEC + 1 vol. % VC electrolyte. The cell was cycled at a C rate of C/10 between 0.01 and 1.5 V prior to capacity limited cycling limited at an insertion capacity of 1000 mA h $g^{-1}_{(Batch-1)}$ and cycled at a C-rate of C/2. The C/2 charge and discharge rate combined with the capacity limitation corresponds to maximum insertion in 8 min 23 seconds. a) Capacity as a function of cycle number displayed per gram of active material and per gram of composite. b) Coulombic efficiency values corresponding to the cycle data displayed in a).

Over the capacity limited cycles the electrode displayed stable capacity values and high coulombic efficiency. The very high initial efficiency values are suggested to be due to the shorter length of time the lithiated composite electrode was exposed to the electrolyte prior to

lithium extraction. Throughout capacity limited cycling of the electrode the efficiency of the electrode decreased, this is suggested to be caused by the requirement of the composite electrode to form higher lithium content lithium silicide phases throughout cycling to achieve the capacity limit. Although the results are not directly comparable with other previously cycled electrodes the results suggest that the length of time over which the electrode is lithiated and delithiated influences the reversibility of the electrode.

7.6 Chapter conclusions

Comparison of binary electrolyte solvents including FEC

Electrolyte formulation was observed to play a crucial role in the extended cycling performance of composite electrodes. The investigated binary solvent formulations which contained FEC were found to increase the cycle life of composite electrodes. The cycle life was observed to depend on the linear carbonate contained in the electrolyte, the trend in cycle life was DMC < EMC < DEC. The trend suggests the possibility of a correlation between linear carbonate and performance however further work would be required to confirm the role of linear electrolyte breakdown within binary solvent electrolytes on the long term performance.

Ex-situ imaging of composite electrodes in LP 30 and 1M $LiPF_6$ FEC: DEC

Substantial electrolyte breakdown products were observed to accumulate within composite electrodes when cycled utilising commercial LP 30 electrolyte. No obvious excessive electrolyte breakdown was observed within electrodes cycled utilising 1 M $LiPF_6$ FEC: DEC electrolyte. Nanowire particles were observed to display similar general structural changes throughout cycling in both electrolyte systems. The surface of nanowire particles cycled in LP30 electrolyte was observed to display a slightly less homogenous structure than particles removed from an electrode cycled in FEC containing electrolyte. The formation of a more stable SEI layer in FEC based electrolytes is suggested to be the cause of the lower electrolyte breakdown and improved performance.

Rate performance

The rate performance of a formulation 6 composite electrode was investigated, large polarisations were observed, a capacity of around 500 mA h $g^{-1}_{(Composite)}$ was achieved during insertion at a rate of 1C. The voltage of the composite electrode was less sensitive to increased current density during extraction, displaying lower polarisation. The polarisation of a composite electrode during rate testing was observed to be dependent on the formulation of the electrode. A formulation 8 electrode was observed to display lower polarisation at increased rate resulting in higher achieved capacity at higher rates of both insertion and extraction, a combination of increased electronic conductivity combined with a higher dilution of active material were suggested to be the cause of the reduced polarisation of formulation 8 electrodes.

Addition of vinylene carbonate and capacity limited cycling

The addition of vinylene carbon to 1 M $LiPF_6$ FEC: DEC was observed to increase the capacity and coulombic efficiency of electrodes over extended cycling. The combination of FEC and VC containing electrolytes with a capacity limited cycling regime allowed electrodes to deliver around 675 mA h $g^{-1}_{(Composite)}$ for around 200 cycles with a coulombic efficiency of around

99 %. Capacity limited cycling at a C-rate equivalent to C/2 allowed for high coulombic efficiency values to be obtained. The high efficiency values suggest time dependence to the magnitude of inefficiency. Further work would be required to gain a deeper understanding the cycle time efficiency correlation.

7.7 Chapter references

1 M. N. Obrovac and L. J. Krause, *J. Electrochem. Soc.*, 2007, **154**, A103.

2 S. D. Beattie, D. Larcher, M. Morcrette, B. Simon and J.-M. Tarascon, *J. Electrochem. Soc.*, 2008, **155**, A158.

3 J. R. Szczech and S. Jin, *Energy Environ. Sci.*, 2011, **4**, 56.

4 N.-S. Choi, K. H. Yew, K. Y. Lee, M. Sung, H. Kim and S.-S. Kim, *J. Power Sources*, 2006, **161**, 1254–1259.

5 V. Etacheri, O. Haik, Y. Goffer, G. a. Roberts, I. C. Stefan, R. Fasching and D. Aurbach, *Langmuir*, 2012, **28**, 965–976.

6 Y.-M. Lin, K. C. Klavetter, P. R. Abel, N. C. Davy, J. L. Snider, A. Heller and C. B. Mullins, *Chem. Commun.*, 2012, **48**, 7268–70.

7 S. Dalavi, P. Guduru and B. L. Lucht, *J. Electrochem. Soc.*, 2012, **159**, A642.

8 X. Chen, X. Li, D. Mei, J. Feng, M. Y. Hu, J. Hu, M. Engelhard, J. Zheng, W. Xu, J. Xiao, J. Liu and J. G. Zhang, *ChemSusChem*, 2014, **7**, 549–554.

9 M. Moshkovich, Y. Gofer and D. Aurbach, *J. Electrochem. Soc.*, 2001, **148**, E155.

10 P. Verma, P. Maire and P. Novák, *Electrochim. Acta*, 2010, **55**, 6332–6341.

11 C. Xu, F. Lindgren, B. Philippe, M. Gorgoi, F. Björefors, K. Edstrom and T. Gustafsson, *Chem. Mater.*, 2015, **27**, 2591-2599.

12 I. a. Profatilova, C. Stock, A. Schmitz, S. Passerini and M. Winter, *J. Power Sources*, 2013, **222**, 140–149.

13 A. M. Chockla, T. D. Bogart, C. M. Hessel, K. C. Klavetter, C. B. Mullins and B. A. Korgel, *J. Phys. Chem. C*, 2012, **116**, 18079–18086.

14 X. Zhang, R. Kostecki, T. J. Richardson, J. K. Pugh and P. N. Ross, *J. Electrochem. Soc.*, 2001, **148**, A1341.

15 H. J. Ploehn, P. Ramadass and R. E. White, *J. Electrochem. Soc.*, 2004, **151**, A456.

16 J. W. Choi, J. McDonough, S. Jeong, J. S. Yoo, C. K. Chan and Y. Cui, *Nano Lett.*, 2010, **10**, 1409–13.

17 S. C. DeCaluwe, B. M. Dhar, L. Huang, Y. He, K. Yang, J. Owejan, Y.-P. Zhao, a. A. Talin, J. a Dura and H. Wang, *Phys. Chem. Chem. Phys.*, 2015,**17**, 11301–11312

18 X. H. Liu, S. Huang, S. T. Picraux, J. Li, T. Zhu and J. Y. Huang, *Nano Lett.*, 2011, **11**, 3991–3997.

19 A. Bordes, K. Eom and T. F. Fuller, *J. Power Sources*, 2014, **257**, 163–169.

20 Y. Oumellal, N. Delpuech, D. Mazouzi, N. Dupré, J. Gaubicher, P. Moreau, P. Soudan, B. Lestriez and D. Guyomard, *J. Mater. Chem.*, 2011, **21**, 6201.

21 M. Gauthier, D. Mazouzi, D. Reyter, B. Lestriez, P. Moreau, D. Guyomard, L. Roué and L. Roue, *Energy Environ. Sci.*, 2013, **6**, 2145–2155.

Chapter 8: Conclusions and further work

8.1 Conclusions

Batch-1 silicon nanowire (trisilane precursor) material was found to consist of straight nanowires with a range of diameters from 20nm to > 350 nm diluted with a high proportion of twisted nanowires and amorphous silicon particles. Such complexity was unexpected given reports of SFLS nanowire growth utilising gold seed crystals and trisilane precursor had reported formation of straight nanowire particles without formation of amorphous silicon [1]. Formation of amorphous silicon under supercritical conditions has been reported to occur *via* thermal decomposition of trisilane [2]. The presence of amorphous silicon within the batch-1 sample therefore suggested inefficient conversion of the silicon precursor into nanowire particles during synthesis. Gold was observed to be present not only as nanowire seed crystals but also distributed between particles.

Batch-2 silicon nanowire material (MPS precursor) was observed to contain a high proportion of straight nanowire particles as expected from previous reports of nanowire growth utilising similar conditions [3]. The material contained crystalline silicon and gold in the form of seed crystals present at the end of nanowire particles. Carbon was found *via* EDS and EFTEM imaging analysis, as reported previously and attributed to a poly-phenylsilane shell formed by breakdown of the MPS precursor [3].

Results of IR spectroscopy obtained from dried mixtures of batch-1 and PAA suggested that PAA interacted with the surface of batch-1 material. The presence of batch-1 material was observed to prevent formation of anhydride type functionality between carboxylic groups of the PAA. A peak observed to form at around 1540 cm^{-1} was attributed to the anti-symmetrical stretch of a carboxylate functional group. The presence of carboxylate functionality suggested that a bidentate type interaction formed between the carboxyl functional group of the poly-acrylic acid and the oxidised surface of a nanowire particle, formed *via* a condensation reaction between the acidic PAA and the hydrated silicon oxide surface. Formation of ester type functionality may also have occurred as a broad carbonyl adsorption band was observed in the spectra of the dried mixture at round 1725 cm^{-1}. Further characterisation would be required to definitively confirm the functionality present.

Initial electrochemical characterisation of batch-1 material revealed the characteristic processes during lithium insertion and extraction usually associated with silicon nanowire based electrodes and also confirmed the presence of amorphous silicon within the sample. Impedance spectroscopy conducted throughout the first cycle of a composite electrode (cycled in LP30 electrolyte) suggested a non-conventional adsorption type electrolyte breakdown process at the surface of lithiated batch-1 material within the electrode as previously reported by Radvanyi *et*

al. [4]. Composite electrodes containing batch-1 material initially displayed a reversible capacity of around 2750 mA h $g^{-1}_{(Batch-1)}$ followed by a significant capacity fade over 50 cycles.

The external nanowire morphology was preserved on the initial electrochemical cycle. However, an unexpected amorphisation process was observed *via* ex-situ studies following the initial electrochemical cycle of composite electrodes. In the case of partially reacted electrodes partial amorphisation due to lithium insertion towards the centre of the particles was accompanied by complete amorphisation at random locations along the length of the particles. This resulted in the formation of amorphous nanowires with a segmented type structure after full reaction to 0.01V.

The axial amorphisation pattern observed has not been previously described for SFLS nanowires within a composite electrode. In a recent report of axial amorphisation of nanowire particles [5], it was suggested that a segmented structure arose from the presence of defects within the particles running perpendicular to the growth direction, and the preferential reaction of lithium with silicon at the defect. Further work to investigate the presence and role of defects in the batch-1 silicon nanowire material would be required to confirm this hypothesis. The reaction pattern suggests that the presence of defects within the structure of SFLS nanowire particles may be beneficial to the initial lithium insertion process and reduce the effect of self-limitation during reaction [6, 7].

Gold removal was conducted from both batches of silicon nanowire material. Under the conditions tested gold removal from the sample was not observed to have a significant influence on the performance of the material. The formulation of the composite electrode was found to substantially influence the performance of composite electrodes. The major requirement for stable cycling of composite electrodes was suggested to be the mechanical stability of the electrode layer. Low content of high surface area carbon additive and higher contents of binder enabled the most stable reversible cycling. Of the formulations tested a formulation containing 67.5 wt. % silicon nanowire material, 22.5 wt. % PAA binder and 10 wt. % acetylene black (formulation 6) displayed the best performance.

The performance of processed batch-1 and batch-2 materials was compared; batch-2 material displayed an inferior performance. The difference in performance was attributed to the precursor used for the synthesis of the nanowire material. Batch-1 produced utilising trisilane contained electrochemically active amorphous silicon. Batch-2 material, produced utilising MPS, was observed to contain carbon based material expected to be poly-phenylsilane [8] which simply contributed inactive mass to batch-2 material.

Capacity limitation was found to be an effective method to improve the extended cycling performance of SFLS based composite electrodes. It was found that capacity limitation of 1000 mA h g^{-1} allowed for 130 cycles of stable cycling with coulombic efficiency values of over 95 % when using LP30 electrolyte. Insertion voltage limitation to 0.18 V allowed for high coulombic efficiency values of over 98 % to be achieved when cycling SFLS composite electrodes in LP30.

Binary solvent electrolyte solutions incorporating FEC and a linear carbonate solvent considerably improved the cycle life performance of SFLS composite electrodes, 1 M $LiPF_6$ FEC: DEC allowed for the most stable capacity values to be achieved. The linear carbonate solvent was observed to affect the long term performance of composite electrodes however further work would be required to confirm the influence. 1 M $LiPF_6$ FEC: DEC was previously reported to improve the performance of SFLS based composite electrodes utilising a NaAlg binder by Chockla *et al.* [1]. Composite electrodes containing processed batch-2 material (formulation 6) displayed over 200 cycles at a C rate equivalent to 0.1 C between 0.01V and 1.5 V when cycled with 1 M $LiPF_6$ FEC: DEC, the highest number of cycles reported for a composite electrode containing SFLS nanowire particles.

Ex-situ imaging of composite electrodes (processed batch-1, formulation 6) cycled in LP 30 and 1 M $LiPF_6$ FEC: DEC displayed a significant difference in rate of formation of electrolyte breakdown products. Electrodes cycled in LP 30 appeared clogged with electrolyte breakdown products by the 10^{th} cycle, by the 50^{th} cycle the entire electrode was covered in a thick deposit. Electrodes cycled in 1 M $LiPF_6$ FEC: DEC displayed only slight increases in electrolyte breakdown products between the 1^{st} and 50^{th} cycles.

TEM imaging of silicon nanowire particles removed form composite electrodes cycled in both electrolytes suggested that the structural changes experienced by the active material was similar when cycled in either electrolyte. Formation of large pores within the active nanowire particles were observed by the 50^{th} cycle. Minor differences to the density and surface structure of particles cycled in each electrolyte suggested the electrolyte may influence stability of the active material however the effect is suggested to be secondary to the observed electrolyte breakdown within the composite electrode as a cause of capacity fade.

Formulation 6 was found to be able to deliver around 600 mA h $g^{-1}_{(Batch\text{-}1)}$ / 405 mA h $g^{-1}_{(Composite)}$ at a charge rate equivalent to 1 C (3.58 A $g^{-1}_{(Batch\text{-}1)}$) and able to deliver 1700 mA h $g^{-1}_{(Batch\text{-}1)}$/ 1100 mA h $g^{-1}_{(Composite)}$ at a discharge rate of 5 C (17.89 A $g^{-1}_{(Batch\text{-}1)}$). Improved rate performance in terms of reduced polarisation was observed for formulation 8 electrodes, the combination of increased conductive additive and reduced binder content are suggested to have contributed to the reduced polarisation experienced by the electrode and allowed for increased capacity per

gram of active material to be achieved at high rates. Optimisation of the electrode formulation and conductive additive would be expected to allow for further improvements to the high rate performance of SFLS composite electrodes.

Addition of VC to 1 M $LiPF_6$ FEC: DEC improved the coulombic efficiency of composite electrodes (processed batch-2, formulation 6). Over 200 capacity limited cycles (675 mA h $g^{-1}_{(Composite)}$) with a coulombic efficiency of over 99 % were achieved. Capacity limited cycling of a composite electrode (processed batch-1, formulation 1) at increased rate (C/2) in an electrolyte solution containing VC allowed coulombic efficiency values of over 99.5 % to be achieved for a limited number of cycles. Increased cycle life performance would be expected to be achieved from composite electrodes containing processed batch-1 material produced to formulation 6 cycled under capacity limited conditions.

From the results obtained throughout this project, the mechanism of capacity fade observed in SFLS based composite electrodes can be stated to be similar to that observed for other silicon nanoparticle based composite electrodes [9, 10]. Within optimised electrodes the continual formation of electrolyte breakdown products during cycling appeared to gradually reduce the ionic connectivity throughout the composite electrode. The electronic and ionic conduction path present across the surface of SFLS nanowire particles did not appear to counteract the effect of reduced electrode porosity to an extent that the performance of SFLS material was observed to be considerably greater than that other silicon nanoparticle materials reported in the literature. The most relevant comparison of the performance of SFLS nanowire material in this work can be made with the work of Chockla *et al.*[13].

8.2 Further work

Investigate the influence of processing pH on interaction of PAA with SFLS material. A more detailed understanding of the interaction of poly-acrylic acid binder with the surface of silicon based materials is required, an in-situ FTIR study of the drying of composite electrode inks should be considered. The influence of polymer chain length on the performance of composite electrodes and the rheological properties of the slurry mixture should be investigated and optimised. Various other binders and binder combinations should also be investigated.

A detailed understanding of the growth direction and defect structure of SFLS silicon nanowire particles should be sought; correlation of defect structure with lithium insertion mechanisms may allow for a clearer understanding of the kinetics of lithium insertion and potentially allow for improved first cycle performance.

An understanding of the role of linear carbonate reduction during cycling may be crucial to improving the stability of silicon based electrodes utilising carbonate solvents. A clear understanding of the reactivity of lithiated SFLS material with linear carbonates under various conditions should be sought. An investigation into the time dependence of irreversible capacity should be conducted, long term storage of lithiated silicon in various discharged states in various electrolyte solutions should be considered. The presence, type and quantity of solvent reduction products and the relation to the electrolyte composition should be investigated further, monitoring gas evolution at the surface of lithiated silicon and throughout cycling in various electrolyte solutions may provide insight into linear carbonated reduction processes.

Further formulation optimisation should be conducted. The electronic conductivity and initial capacitance of the composite electrode were generally observed to correlate to the first cycle efficiency and long term stability. Further optimisation in terms of electrochemically active surface area, electronic conductivity and porosity would be expected to further increase the performance. The influence of the conductive additive surface area and morphology should be investigated; the use of multiple types of conductive additive has been reported to play a significant role in the performance of composite electrodes containing silicon [11].

A clear understanding of the possible gains in energy density when using silicon nanowire based composite electrodes is required. Accurate measurements and optimisation of composite electrode thickness and porosity are required to obtain an accurate understanding of the volumetric energy density which could be achieved. A clear understanding of the expansion and contraction of the composite electrode throughout cycling must also be developed. Direct comparison between SFLS type material and other types of silicon materials should be

conducted to understand the magnitude of the potential benefit of the use of SFLS type material within composite electrodes.

8.3 Chapter references

1 A. M. Chockla, T. D. Bogart, C. M. Hessel, K. C. Klavetter, C. B. Mullins and B. A. Korgel, *J. Phys. Chem. C*, 2012, **116**, 18079–18086.

2 L. E. Pell, A. D. Schricker, F. V. Mikulec and B. a. Korgel, *Langmuir*, 2004, **20**, 6546–6548.

3 H. Y. Tuan and B. a. Korgel, *Chem. Mater.*, 2008, **20**, 1239–1241.

4 E. Radvanyi, K. Van Havenbergh, W. Porcher, S. Jouanneau, J. S. Bridel, S. Put and S. Franger, *Electrochim. Acta*, 2014, **137**, 751–757.

5 L. Wang, D. Liu, S. Yang, X. Tian, G. Zhang, W. Wang, E. Wang, Z. Xu and X. Bai, *ACS Nano*, 2014, 8249–8254.

6 M. T. McDowell, I. Ryu, S. W. Lee, C. Wang, W. D. Nix and Y. Cui, *Adv. Mater.*, 2012, **24**, 1–8.

7 X. H. Liu, F. Fan, H. Yang, S. Zhang, J. Y. Huang and T. Zhu, *ACS Nano*, 2013, **7**, 1495–1503.

8 C. K. C. K. Chan, R. N. R. N. Patel, M. J. O'Connell, B. a. B. a Korgel, Y. Cui, M. J. O'Connell, B. a. B. a Korgel and Y. Cui, *ACS Nano*, 2010, **4**, 1443–50.

9 Y. Oumellal, N. Delpuech, D. Mazouzi, N. Dupré, J. Gaubicher, P. Moreau, P. Soudan, B. Lestriez and D. Guyomard, *J. Mater. Chem.*, 2011, **21**, 6201.

10 E. Radvanyi, W. Porcher, E. De Vito, A. Montani, S. Franger and S. Jouanneau Si Larbi, *Phys. Chem. Chem. Phys.*, 2014, **16**, 17142–17153.

11 B. Lestriez, S. Desaever, J. Danet, P. Moreau, D. Plée and D. Guyomard, *Electrochem. Solid-State Lett.*, 2009, **12**, A76.

Appendices

A.1 – **Binder selection**

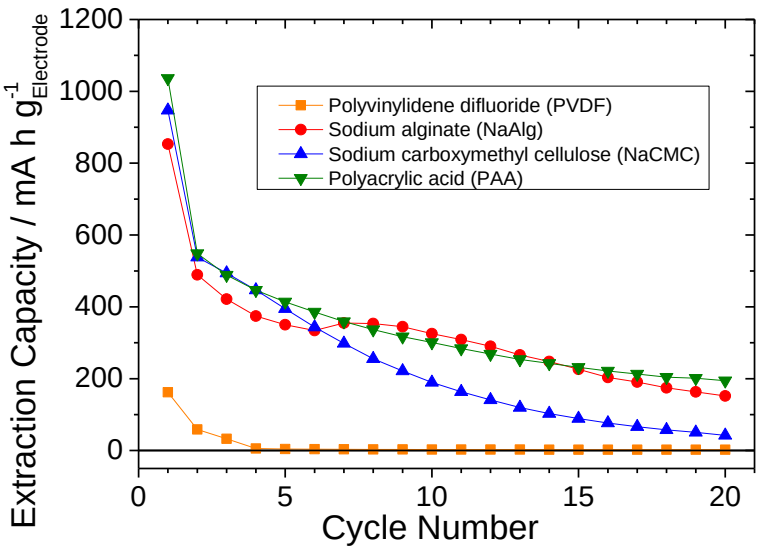

Cycle life testing of PSi325 composite electrodes utilising various polymer binders. All electrodes were cycled at a rate of C/50 in the first cycle followed by C/10 except PVDF which was cycled at C/75 for all 20 cycles.

Initial testing was conducted to evaluate the performance of a number of commercially available polymer binders previously reported in the literature. Composite electrodes were produced however due to cost and limited supply, initial experiments were conducted utilising ball-milled commercially sourced silicon powder (325 mesh, Sigma Aldrich).

Initial experiments comparing various commercially available binders were conducted utilising commercial silicon powder as the active component of composite electrodes. Results highlighted poly-acrylic acid as the superior binder of those tested, in terms of initial reversible capacity and capacity retention after 50 cycles.

A.2 – IR spectra of PAA and powdered silicon

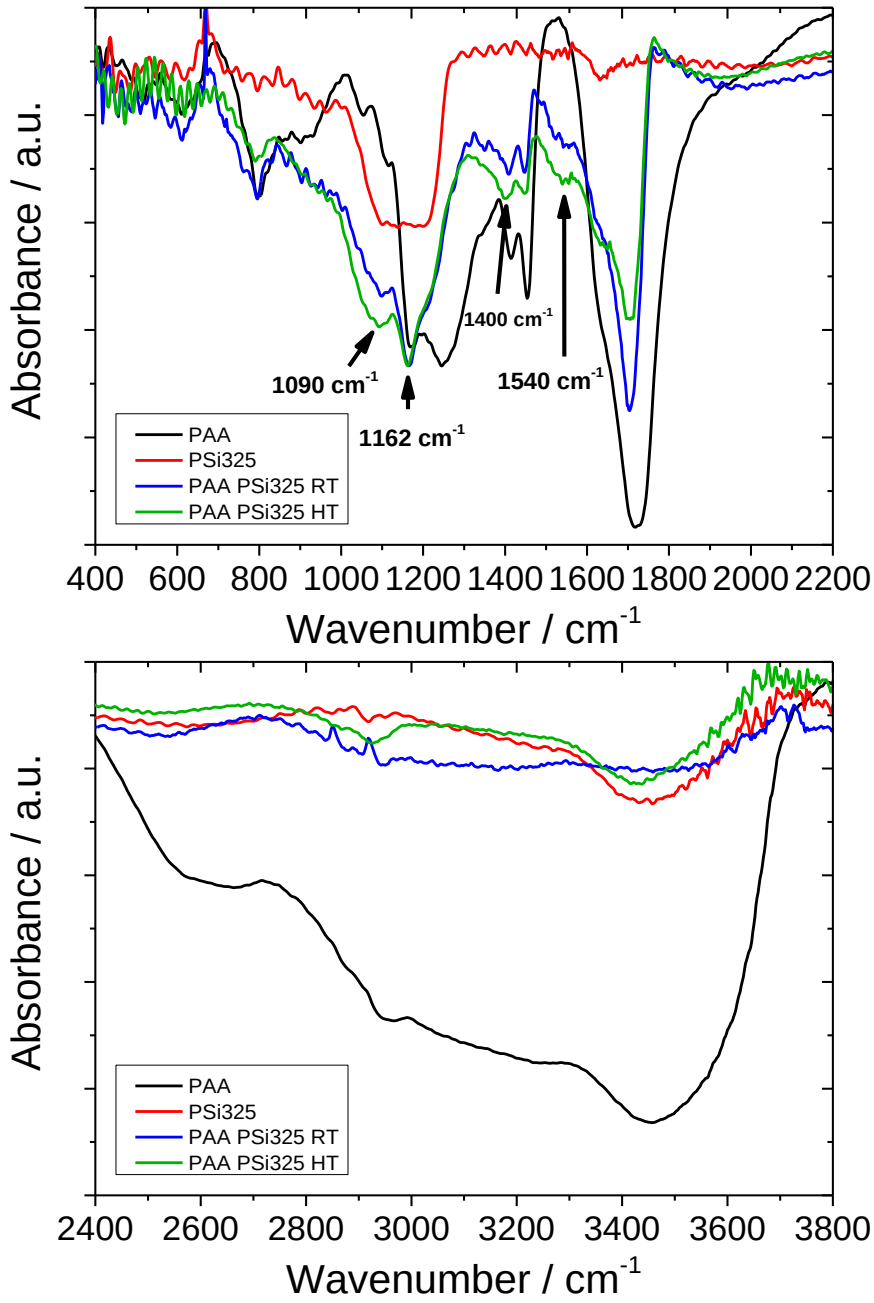

FTIR data of PAA binder – ball milled silicon powder interactions after drying at room temperature (RT) and drying at 120°C under vacuum (HT).

A.3 – Electrochemical testing of control cells

Carbon black and poly-acrylic acid composite electrodes

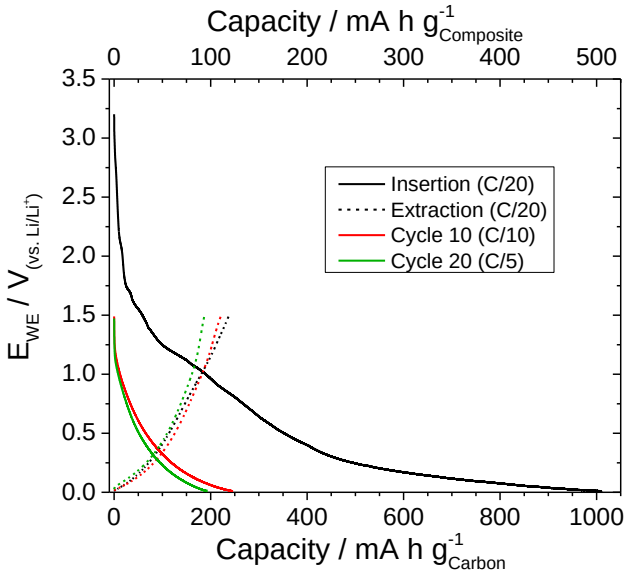

Voltage profile of a carbon black: poly-acrylic acid 1:1 composite electrode cycled vs. a lithium metal counter/reference using LP 30 electrolyte. First cycle in black at C/20.

The current applied to composite electrodes containing silicon active materials was equivalent to a C rate of greater than C/5 for the carbon content, the capacity contribution would therefore be less than 200 mA h g^{-1} (carbon).

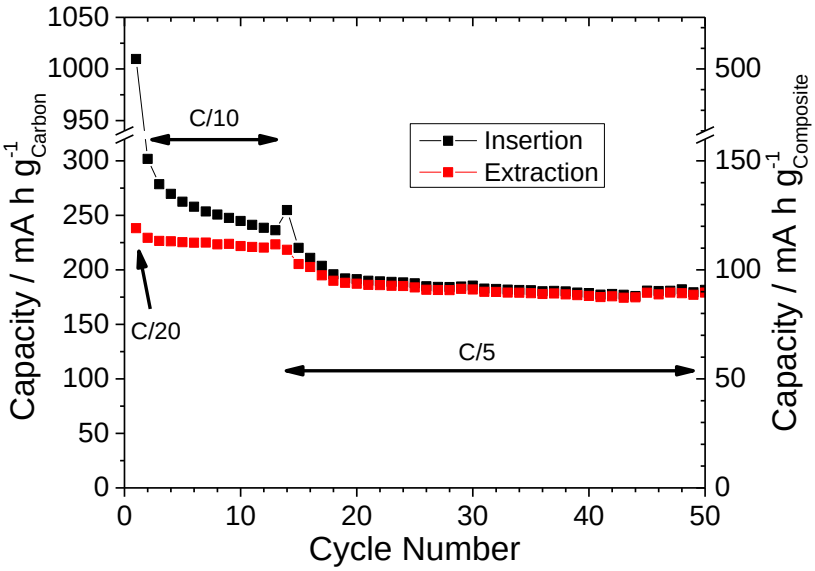

Cycle life plot of carbon black poly-acrylic acid 1:1 composite electrode cycled vs lithium metal counter reference using LP 30 electrolyte.

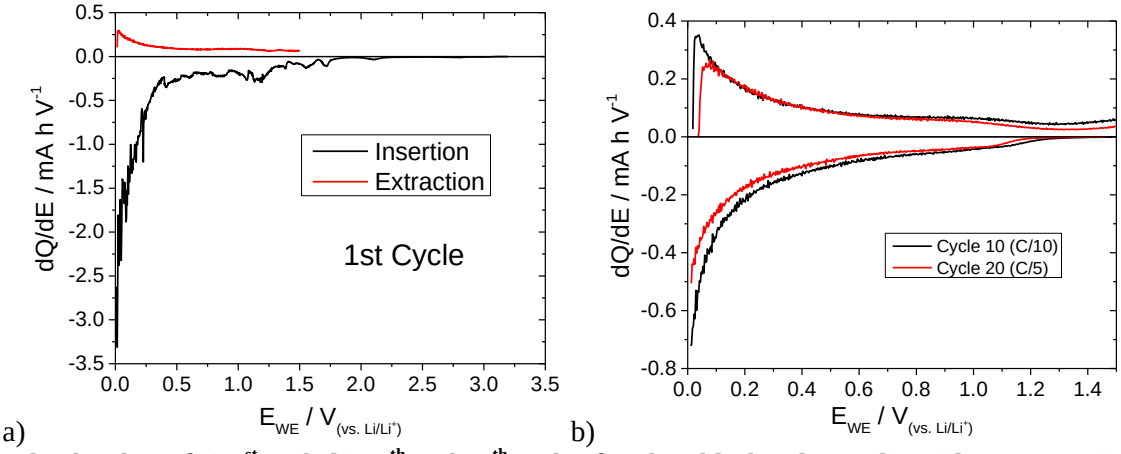

A dQ/dE plots of a) 1st cycle b) 10th and 20th cycle of carbon black poly-acrylic acid 1:1 composite electrode cycled vs lithium metal counter reference using LP 30 electrolyte.

Electrochemical testing of a poly-acrylic acid film

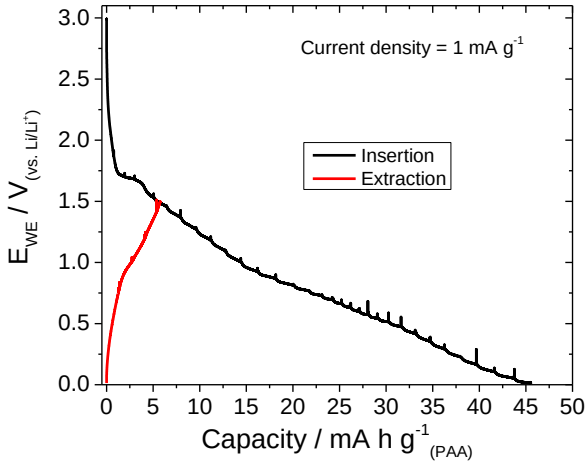

Slow galvanostatic cycle of a poly-acrylic acid film on a copper current collector. Cycled in a half-cell vs. metallic lithium using LP30 as electrolyte. Mass of film = 1.5 mg, applied current of 1.5 µA. No significant reversible capacity observed.

A.4 – **Impedance measurements throughout 3rd cycle**

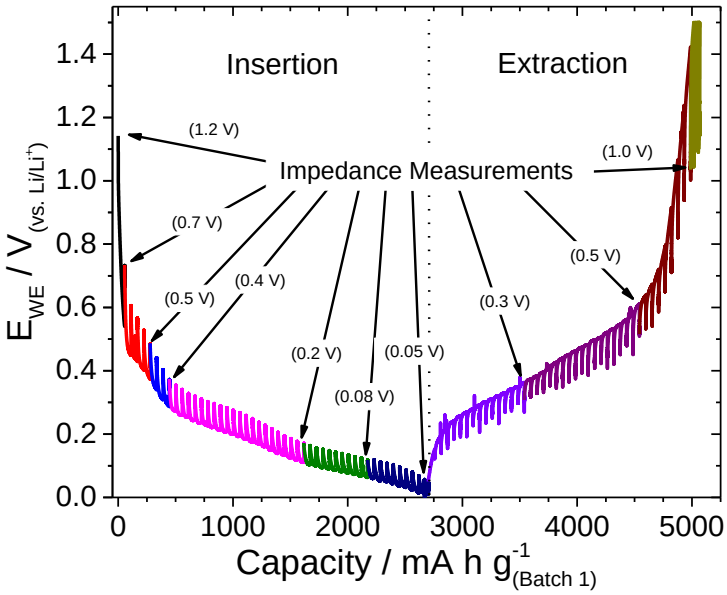

Figure displays the voltage profile of a composite electrode throughout the third electrochemical cycle. A current interruption regime was used to conduct the third cycle of a composite electrode. A current equivalent to 0.05 C was applied for 20 minutes followed by an open circuit time of 1 hour 40 minutes.

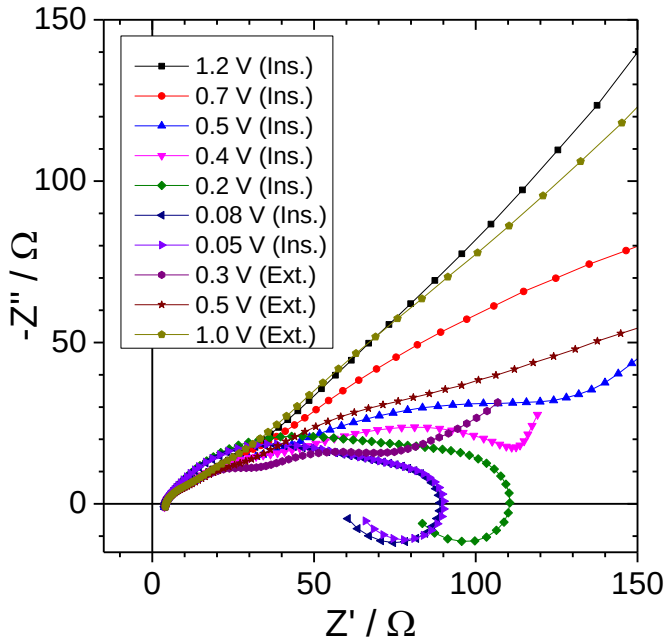

Impedance spectra, displayed in the form of a Nyquist plot, conducted at various potentials throughout the third cycle of a composite electrode over the frequency range 50 kHz to 100 mHz in a three electrode cell configuration at 25°C.

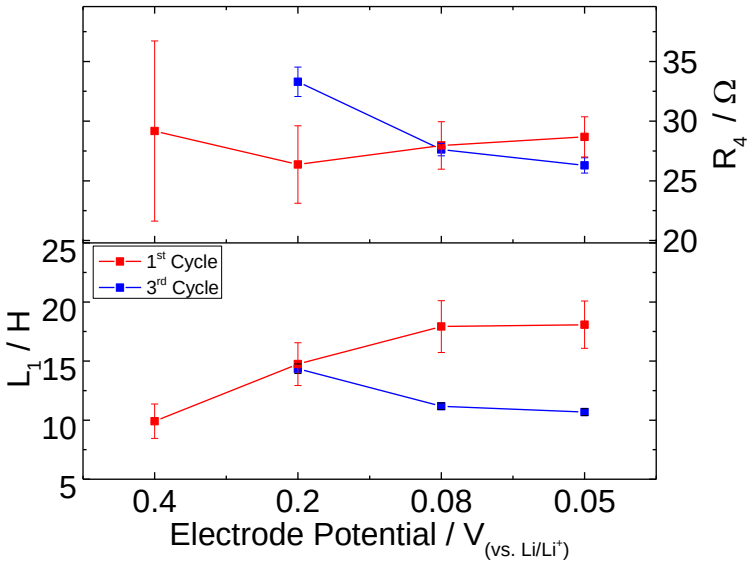

Variation of L_1 and R_4 values measured from impedance spectra which included an pseudo-inductive loop during the third cycle.

A.5 – Cross-sectional SEM images of composite electrode formulations

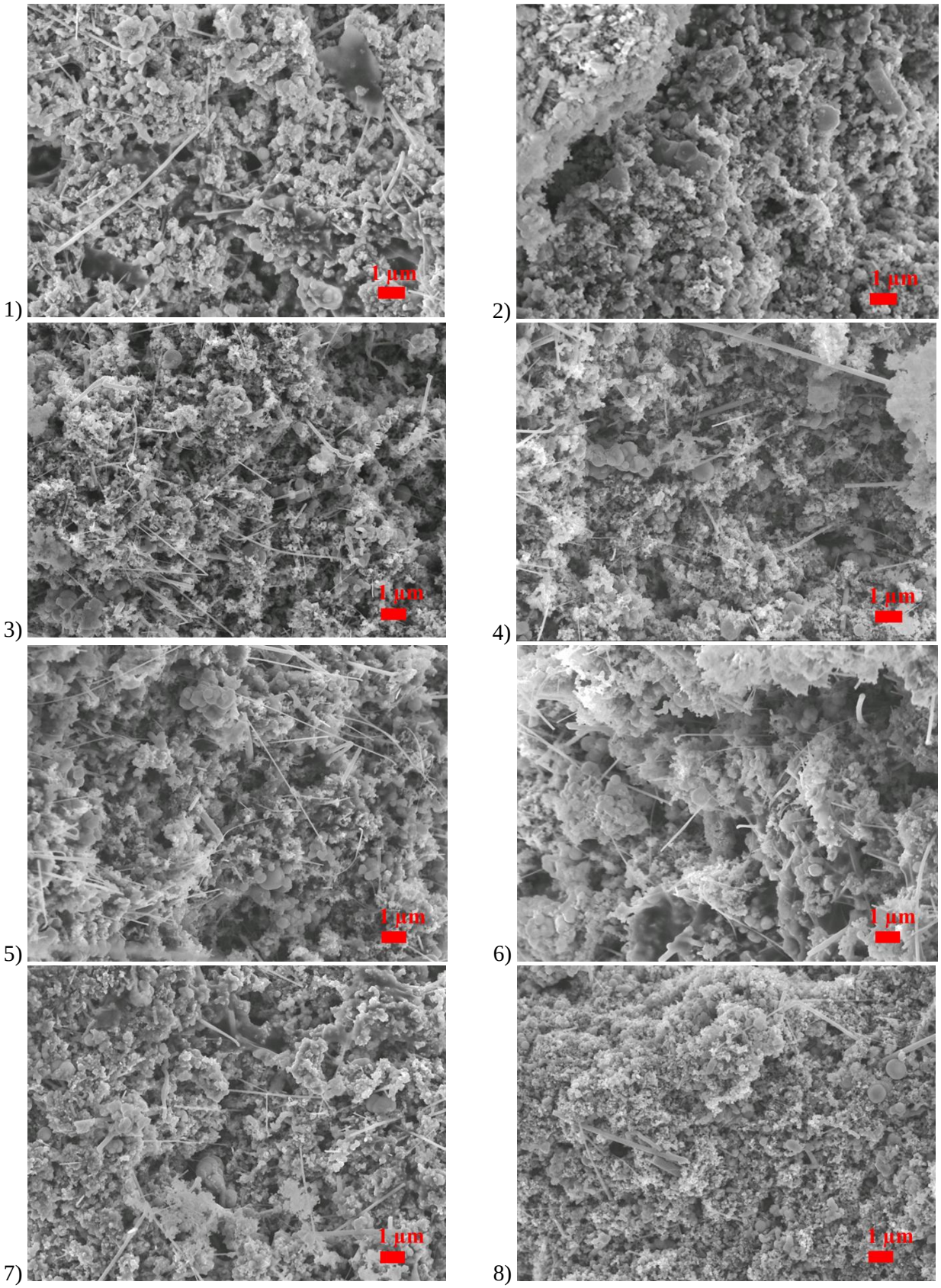

Cross-sectional SEM images of composite electrodes of formulation 1-8. Images display the micro-structure of the composite electrodes produced.

Notably formulation 2 displayed significantly different structure to that of the other formulations, long straight nanowire particles were not observed despite the electrode containing the highest ratio of silicon nanowire particles at 80 wt. %. The cause of the discrepancy is suggested to be due to the low ratio of poly-acrylic acid content to silicon nanowire material. The observation suggested poly-acrylic acid significantly improved the dispersal of nanowire and carbon black particles during slurry processing. Formulations 1, 6 and 7 were observed to contain regions of particles covered in binder; visible regions of binder are suggested to be due to the lower total surface area of the particulate materials within the formulations.

A.6 – First cycle voltage profile of 8 electrode formulations

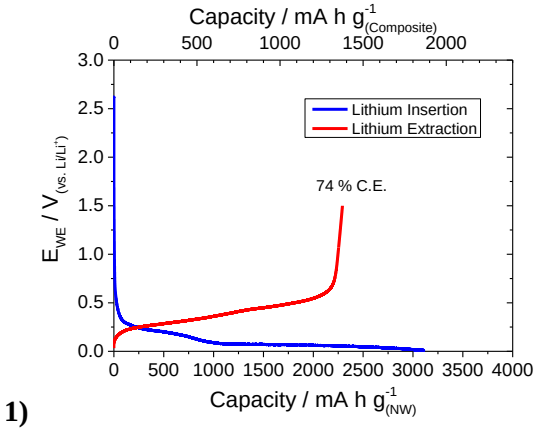

1)

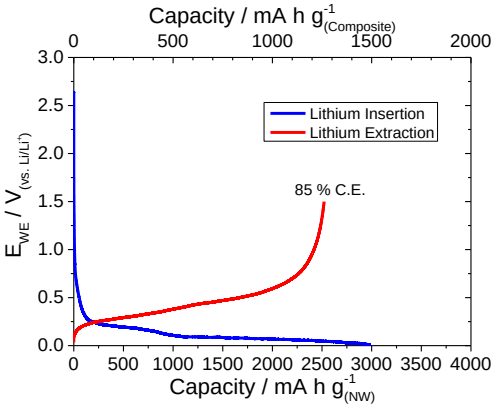

5)

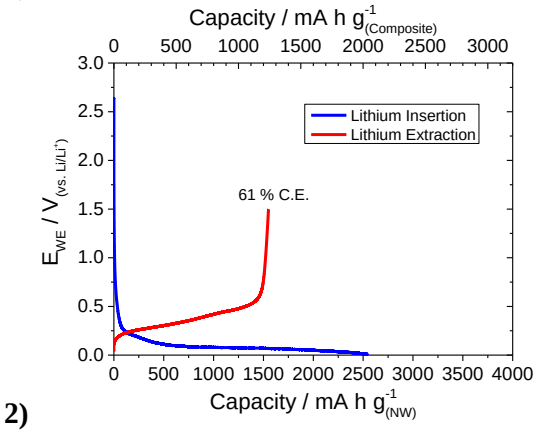

2)

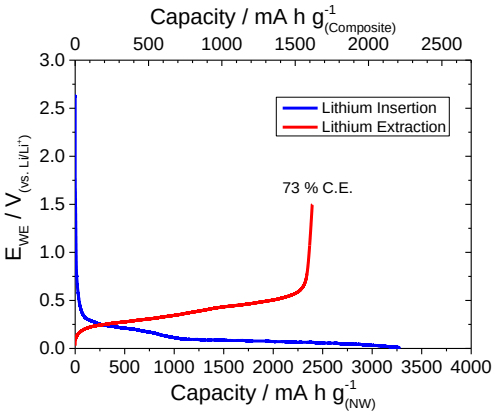

6)

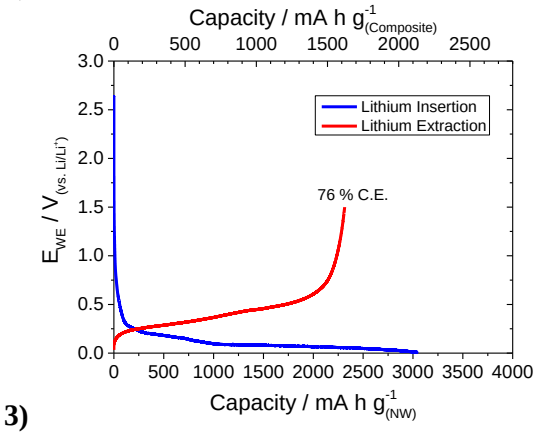

3)

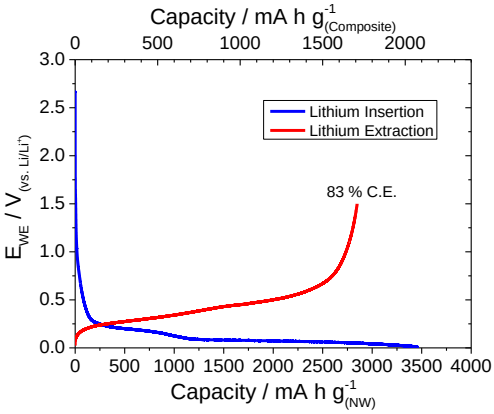

7)

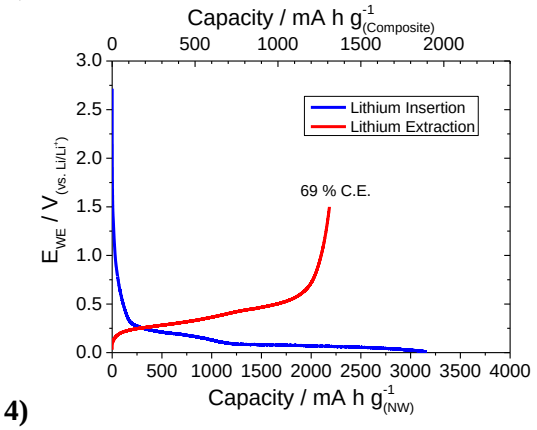

4)

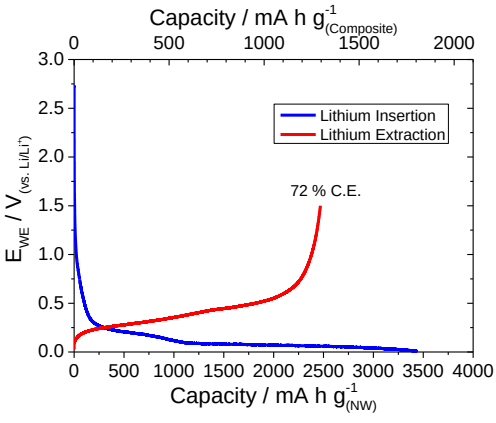

8)

First cycle potentiometric profile of each formulation with 1st cycle efficiency displayed. C/10. LP30.

The charge passed above 0.3 V during insertion in the first cycle, commonly associated with electrolyte breakdown, is displayed for each formulation. Formulation 4 and 8 displayed the highest level of electrolyte breakdown; the formulations represent a high ratio of carbon and low ratio of binder. Notably formulation 5 which contained a relatively high ratio of carbon black displayed low charge associated with electrolyte breakdown, a higher ratio of poly-acrylic acid content in present in the formulation. It is suggested that the poly-acrylic acid binder effectively reduces the surface area of the carbon. Formulation 5 displayed the highest first cycle efficiency. The high 1st cycle efficiency was attributed to the low amount of charge passed above 0.3 V and high carbon content which ensured electronic connectivity throughout the electrode.

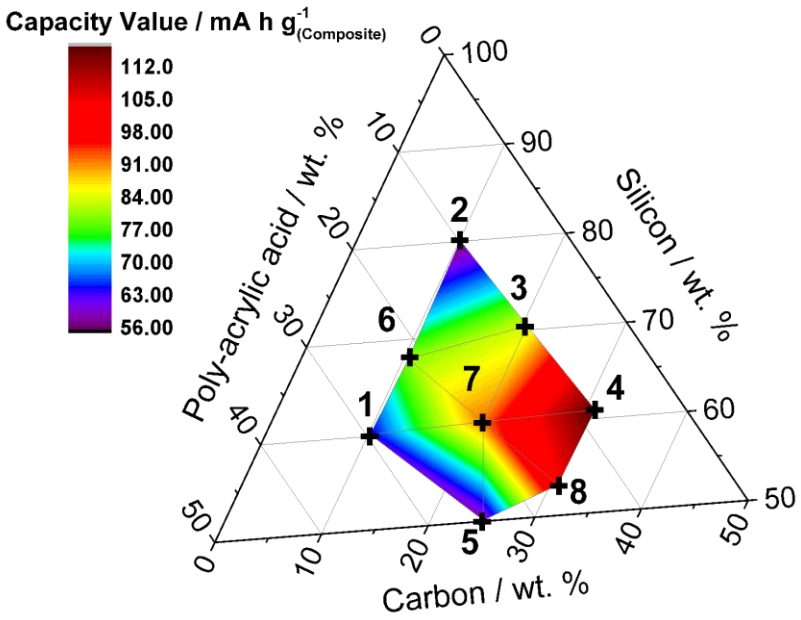

Ternary surface plot displaying capacity passed above 0.3 V during the first cycle insertion for 8 composite electrode formulations.

A.7 – **Processed Batch-2**

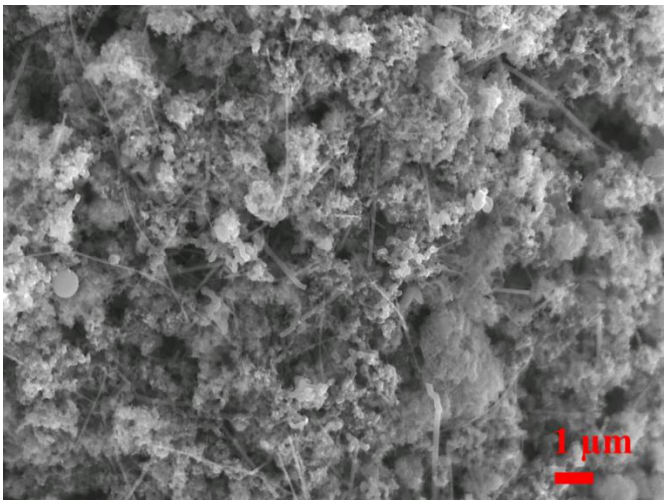

SEM image of a composite electrode cross-section containing processed batch-2 silicon nanowire material produced to formulation 6.

The microstructure of a formed composite electrode is displayed. A porous structure with an even distribution of silicon nanowire particles throughout the electrode was observed.

A.8 – Cycling of all formulations in 1 M $LiPF_6$ FEC: DEC

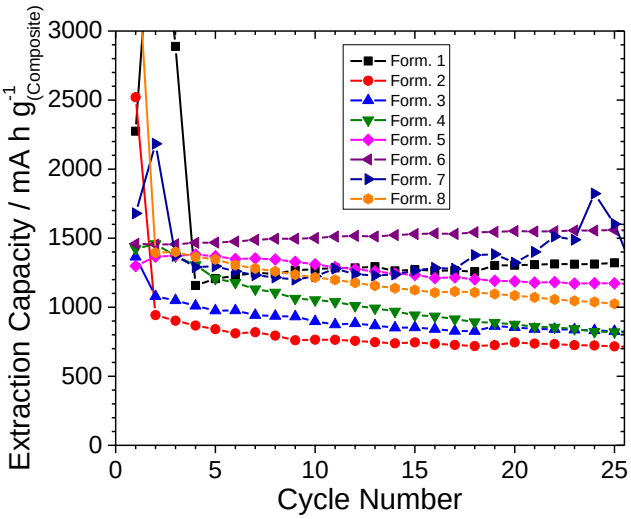

Extended cycling of prepared composite electrodes with varying formulation utilising 1 M $LiPF_6$ FEC: DEC as the electrolyte

Formulation 6 displayed the highest capacity and the most stable performance over 25 cycles. Assuming theoretical capacity of silicon to be 3579 mA h g^{-1}, after cycle 25 formulation 6 displayed around 64 % of the theoretical capacity expected. Formulation 7 was observed to be displaying inconsistent behaviour and erratic capacity values and as such the data was not considered accurate. All electrodes displayed reversible capacity values of over 600 mA h g^{-1} of composite after 25 cycles.

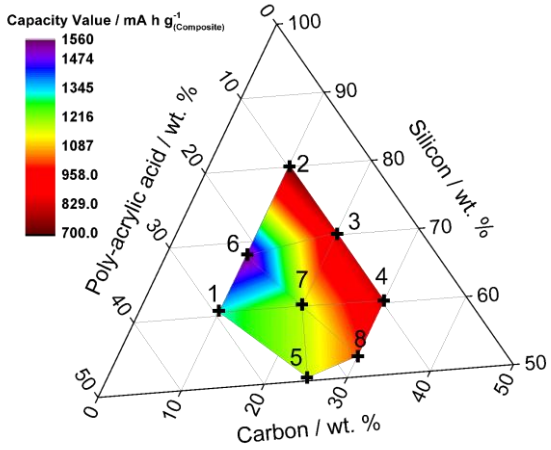

Ternary diagram displaying the extraction capacity values of the formulations tested after 25 electrochemical cycles. (Note the value for formulation 7 was taken from the insertion capacity due to unstable cycling producing inaccurate extraction capacity values).

Formulation 6 displayed superior performance in both LP 30 and 1 M $LiPF_6$ FEC: DEC electrolyte which suggested that the physical properties of the composite electrode are conducive to stable cycling.

A.9 – **Permissions**

Copyright Clearance Center

Welcome, Jacob
Not you?

Log out | Cart (0) | Manage Account | Feedback | Help | Live Help

Get Permission / Find Title
Publication Title or ISBN/ISSN
Go
Advanced Search Options

Order History

View Orders | View Order Details | View RIGHTSLINK Orders

View: Completed | Pending | Canceled | Credited | Denied

Sort orders by: Order Date Ascending Descending

LICENSE #: 3664860561015
Order Date: 07/09/2015
Elsevier Books
Title: Lithium-Ion Batteries
Type of use: reuse in a thesis/dissertation
Fee: 0.00 GBP
View printable order

LICENSE #: 3647160427916
Order Date: 06/13/2015
Journal of Solid State Chemistry
Title: Chemical diffusion in intermediate phases in the lithium-silicon system
Type of use: reuse in a thesis/dissertation
Fee: 0.00 GBP
View printable order

LICENSE #: 3647071454763
Order Date: 06/13/2015
Nature Nanotechnology
Title: A pomegranate-inspired nanoscale design for large-volume-change lithium battery anodes
Type of use: reuse in a dissertation / thesis
Fee: 0.00 GBP
View printable order

LICENSE #: 3647040528239
Order Date: 06/13/2015
Nano Research
Title: Scalable preparation of porous silicon nanoparticles and their application for lithium-ion battery anodes
Type of use: Thesis/Dissertation
Fee: 0.00 GBP
View printable order

LICENSE #: 3647031507530
Order Date: 06/13/2015
Angewandte Chemie International Edition
Title: Three-Dimensional Porous Silicon Particles for Use in High-Performance Lithium Secondary Batteries
Type of use: Dissertation/Thesis
Fee: 0.00 GBP
View printable order

LICENSE #: 3647021255167
Order Date: 06/13/2015
Journal of Materials Chemistry
Title: The failure mechanism of nano-sized Si-based negative electrodes for lithium ion batteries
Type of use: Thesis/Dissertation
Fee: 0.00 GBP
View printable order

LICENSE #: 3647011206665
Order Date: 06/13/2015
Science
Title: A Major Constituent of Brown Algae for Use in High-Capacity Li-Ion Batteries
Type of use: Thesis / Dissertation
Fee: 0.00 GBP
View printable order

LICENSE #: 3647010900898
Order Date: 06/13/2015
ChemSusChem
Title: Reduction Mechanism of Fluoroethylene Carbonate for Stable Solid–Electrolyte Interphase Film on Silicon Anode
Type of use: Dissertation/Thesis
Fee: 0.00 GBP
View printable order

LICENSE #: 3646631247419
Order Date: 06/12/2015
Angewandte Chemie International Edition
Title: A Highly Cross-Linked Polymeric Binder for High-Performance Silicon Negative Electrodes in Lithium Ion Batteries
Type of use: Dissertation/Thesis
Fee: 0.00 GBP
View printable order

LICENSE #: 3646630356556
Order Date: 06/12/2015
Journal of Power Sources
Title: Microscopic model for fracture of crystalline Si nanopillars during lithiation
Type of use: reuse in a thesis/dissertation
Fee: 0.00 GBP
View printable order

LICENSE #: 3646620615374
Order Date: 06/12/2015
Nature Communications
Title: Revealing lithium–silicide phase transformations in nano-structured silicon-based lithium ion batteries via in situ NMR spectroscopy
Type of use: reuse in a dissertation / thesis
Fee: 0.00 GBP
View printable order

LICENSE #: 3646581238364
Order Date: 06/12/2015
Advanced Materials
Title: 25th Anniversary Article: Understanding the Lithiation of Silicon and Other Alloying Anodes for Lithium-Ion Batteries
Type of use: Dissertation/Thesis
Fee: 0.00 GBP
View printable order

LICENSE #: 3646441275795
Order Date: 06/12/2015
Springer eBook
Title: Carbon Anodes
Type of use: Thesis/Dissertation
Fee: 0.00 USD
View printable order

LICENSE #: 3562021062792
Order Date: 02/04/2015
Journal of Alloys and Compounds
Title: First principles study of Li-Si crystalline phases: Charge transfer, electronic structure, and lattice vibrations
Type of use: reuse in a thesis/dissertation
Fee: 0.00 EUR
View printable order

LICENSE #: 3561901072082
Order Date: 02/04/2015
Materials Science and Engineering: R: Reports
Title: Recent developments in lithium ion batteries
Type of use: reuse in a thesis/dissertation
Fee: 0.00 USD
View printable order

PERMISSION LICENSE: COMMERCIAL ELECTRONIC USE [Thesis]

Request ID/Invoice Number: JAC16547

Date: June 15, 2015

To: Jacob Locke
University of Southampton
Chemistry- Building 29
So17 1BJ
United Kingdom
"Licensee"

McGraw-Hill Education Material

Author: D. Linden and T. Reddy
Title: Handbook of Batteries
ISBN: 0071359788
Description of material: Material on page 1081 [only]

Fee: Waived

Licensee Work

Author: Jacob Locke
Title: *Silicon nanowires for high energy*
Publisher: University of Southampton
Publication Date: 2015
Format: Print and the University of Southampton's Library
Distribution/territory: UK
Languages: English

McGraw-Hill Global Education Holdings, LLC (herein after known as "McGraw Hill Education") grants permission for the use described above under the following terms and conditions:

1. McGraw-Hill Education hereby grants Licensee the non-exclusive right to include the McGraw-Hill Education Material in the Licensee Work and to reproduce and distribute the McGraw-Hill Education Material as part of the Licensee Work. The McGraw-Hill Education Material may be used only in the Licensee Work. All use of the McGraw-Hill Education Material is subject to the terms and conditions of this Agreement.
2. No changes may be made to the McGraw-Hill Education Material without the prior written consent of McGraw-Hill Education.
3. Licensee will provide to McGraw-Hill Education the URL and password for the web site in which the McGraw-Hill Education Material appears (if applicable).
4. McGraw-Hill Education makes no representations or warranties as to the accuracy of any information contained in the McGraw-Hill Education Material, including any warranties of merchantability or fitness for a particular purpose. In no event shall McGraw-Hill Education have any liability to any party for special, incidental, tort, or consequential damages arising out of or in connection with the McGraw-Hill Education Material, even if McGraw-Hill Education has been advised of the possibility of such damages. All persons provided with the McGraw-Hill Education Material must be provided with written notice of this disclaimer and limitation liability, either in an end-user license and/or with an on-screen notice that is visible each time the end-user initiates access to the McGraw-Hill Education Material.
5. A credit to McGraw-Hill Education shall be visible each time the end-user initiates access to any screen or page containing any of the McGraw-Hill Education Material. Such credit shall include the title and author of the work and a copyright notice in the name of McGraw-Hill Education.
6. The permission fee of $0 must be received by McGraw-Hill Education on or before , and MUST BE ACCOMPANIED BY A SIGNED COPY OF THIS AGREEMENT. A check should be made payable to McGraw-Hill Global Education Holdings, LLC, Attn: Permissions Department, Wells Fargo Bank , Lockbox #6167, PO Box 8500, Philadelphia, Pa. 19178-6167. Please include the invoice number indicated at the top of this form on your check.
7. This permission does not cover the use of any third-party copyrighted material, including but not limited to photographs and other illustrations, which appears in the McGraw-Hill Education Material with a credit to other sources. Written permission to use such material must be obtained from the cited source.
8. McGraw-Hill Education shall have the right to terminate this Agreement immediately upon written notice to Licensee if Licensee is in material breach of this Agreement.
9. Licensee shall indemnify McGraw-Hill Education from any damages, lawsuits, claims, liabilities, costs, charges, and expenses, including attorney's fees, relating to its use of the McGraw-Hill Education Material.
10. This Agreement incorporates the parties' entire agreement with respect to its subject matter. This Agreement may be amended only in writing and signed by both parties and shall be governed by the laws of New York. Licensee may not assign this Agreement or any rights granted hereunder to any third party.

Please sign and return one copy (with payment,if applicable) to the address above, as outlined in Clause 6 of this agreement.

For McGraw-Hill Education:

DocuSigned by:
Cynthia Aguilera

Cynthia Aguilera
Permissions Department
McGraw-Hill Education

For Licensee:

DocuSigned by:
Jacob Locke

Name

Title Mr

Request for Permission to Reproduce or Re-Publish ECS Material

Please fax this form to: The Electrochemical Society (ECS), Attn: Permissions Requests, 1.609.730.0629. You may also e-mail your request to: copyright@electrochem.org. Include all the information as required on this form. Please allow 3-7 days for your request to be processed.

I am preparing a (choose one): *thesis*

entitled: *Silicon nanowires for high energy lithium-ion battery negative electrodes*

to be published by: *University of Southampton (held within library)*

in an upcoming publication entitled: *N/A*

I request permission to use the following material in the publication noted above, and request nonexclusive rights for all subsequent editions and in all foreign language translations for distribution throughout the world.

Description of material to be used—Indicate what material you wish to use (figures, tables, text, etc.) and give the full bibliographic reference for the source publication. You may attach a separate list, organized by ECS title.

✓ *Figure 13 - Formation of Lithium-Graphite Intercalation Compounds in Nonaqueous Electrolytes and Their Application as a Negative Electrode for a Lithium Ion (Shuttlecock) Cell : doi: 10.1149/1.2220849* J. Electrochem. Soc. *1993 volume 140, issue 9, 2490-2498*

Scheme 1 - Reduction Reactions of Carbonate Solvents for Lithium Ion Batteries : doi: ~~*10.1149/1.2220849*~~ ~~J. Electrochem. Soc. *1993 volume 140, issue 9, 2490-2498*~~ 10.1149/2.002140ecel ECS Electrochemistry Letters 3(9) 2014 A91-A93

✓ *Figure 1 - Advanced Model for Solid Electrolyte Interphase Electrodes in Liquid and Polymer Electrolytes:* doi: 10.1149/1.1837858 *J. Electrochem. Soc. 1997 volume 144, issue 8, L208-L210*

✓ *Figure 9 and 13 - CoO2, The End Member of the LixCoO2 Solid Solution:* doi: 10.1149/1.1836594 *J. Electrochem. Soc. 1996 volume 143, issue 3, 1114-1123*

✓ *Figure 2 - A High Capacity Nano Si Composite Anode Material for Lithium Rechargeable Batteries: doi: 10.1149/1.1390899 Electrochem. Solid-State Lett. 1999 volume 2, issue 11, 547-549*

✓ *Figure 1 and 2 - Structural Changes in Silicon Anodes during Lithium Insertion/Extraction:* doi: 10.1149/1.1652421 *Electrochem. Solid-State Lett. 2004 volume 7, issue 5, A93-A96*

Figure 5 - Understanding the Degradation of Silicon Electrodes for Lithium-Ion Batteries Using Acoustic Emission: doi: 10.1149/1.3489374 *J. Electrochem. Soc. 2010 volume 157, issue 12, A1354-A1360*

Figure 9 - Silicon/Graphite Composite Electrodes for High-Capacity Anodes: Influence of Binder Chemistry on Cycling Stability doi: 10.1149/1.2888173 *Electrochem. Solid-State Lett. 2008 volume 11, issue 5, A76-A80*

Figure 10 - In Situ Observation and Long-Term Reactivity of Si/C/CMC Composites Electrodes for Li-Ion Batteries: doi: 10.1149/1.3581024 *J. Electrochem. Soc. 2011 volume 158, issue 6, A750-A759*

Figure 1 and 7 - Composite Silicon Nanowire Anodes for Secondary Lithium-Ion Cells: doi: 10.1149/1.3251341 *J. Electrochem. Soc. 2010 volume 157, issue 1, A41-A45*

Signature: JACOB LOCKE Date: 15th June 15, 2015

Name: Jacob Locke

Address: Floor 7, Building 29, University of Southampton, Southampton, SO17 1BJ, UK

Telephone: 02380 595 000 Fax: N/A

E-mail: jal406@soton.ac.uk

Permission is granted to reproduce the above-referenced material. Please acknowledge the author(s) and publication data of the original material, and include the words: "Reproduced by permission of The Electrochemical Society."

June 22, 2015

Date

Ann. F. Goedkoop, Publications Production Director